Master Thesis

European Master of Research on Information and Communication Technologies

Multidimensional SAR data representation and processing based on Binary Partition Trees

Author:
Alberto Alonso González

Supervisor:
Carlos López Martínez

Universitat Politècnica de Catalunya

Signal Theory and Communications Department

July 12, 2011

Contents

Chapter 1

Introduction and objectives

Remote sensing allows the extraction of information about an object or phenomenon without having direct contact with it. It is based on the matter interaction with the electromagnetic energy and it covers all the process of acquisition, processing and interpretation of the data.

The utility and interest about remote sensing has experienced an unprecedented boom in recent years, specially with the ability to gather information about the Earth from the space at planetary scales, employing sensors on board satellites and spaceships. Remote sensing can be very helpful to generate, for example, maps and digital terrain models, being of great interest today, but the amount of information that can be extracted does not end here and constantly new applications are appearing. Currently, remote sensing can be employed to perform weather and ocean forecasting, to predict natural disasters, for biological and biophysical monitoring, achieve forest inventory information and biomass measures, desertification control, etc. It is also possible to monitor the vessel traffic, the evolution of the urban areas and, in general, the environmental effects produced by the human beings.

The different technologies employed in remote sensing can be classified according to different criteria. On one hand, they can be classified depending on the electromagnetic source employed for illumination; there are systems having their own illumination source, also called *active systems*, while others are employing an external source to the system, such as either the Sun or just measuring the radiation emitted by the target, which are called *passive systems*. On the other hand, they can be classified according to the range of the electromagnetic spectrum employed, as for instance, microwave, infrared or optical systems. This master thesis deals with Synthetic Aperture Radar (SAR) systems, which

can be classified, according to the previously defined criteria, as active systems working at the microwave frequencies.

The SAR technology was born at the beginning of the '50s, when an important improvement in the spatial resolution of the radars was achieved in the flight direction through a coherent registering of the returned radar echoes for being further processed. Since then, SAR systems have become more popular over the years since they can monitor a great coverage that can increase up to a planetary coverage if they are on board a satellite, and they present a high spatial resolution. Additionally, since it is an active system operating at the microwave wavelengths, it is independent of the weather and the night and day cycles, since the atmosphere is almost transparent at these frequencies. At the beginning, SAR systems only operated at one frequency and polarization state but, rapidly, the technology has evolved greatly with the introduction of multidimensional sensors. These sensors are capable of acquiring simultaneously different images of the scene by changing some parameter, which has enabled the emergence of the SAR polarimetry and interferometry. This thesis has been developed employing Polarimetric SAR (PolSAR) data.

The electromagnetic wave polarization makes reference to the vectorial nature of the electric and magnetic fields conforming it. It is possible to generate waves having the electric field moving over different planes and, thus, having a different interaction with the targets depending in their physical structure and morphology. Polarimetric SAR systems (PolSAR) obtain multidimensional images by combining different polarizations of the incident and reflected waves.

In most of the cases in SAR systems, the size of the resolution cell is much larger than the wavelength and, thus, the measured echo is a coherent combination of all the individual targets within that cell. This coherent combination may be constructive or destructive, and it appears over the SAR images with a characteristic granularity known as *speckle*. Although the speckle is real electromagnetic measure, from the point of view of the acquisition system it is considered as noise, since it can not be predicted accurately and is contaminating the measure of the reflectivity of the resolution cell. The useful information, then, may be extracted from the statistics of the speckle term.

There are a wide number of techniques to extract these statistics and eliminate, as far as possible, the contaminant effect of the speckle term in SAR images. The most basic technique is to average the image values over the image using a particular window, usually a rectangular window, which is also known as the multilook filter. In fact, this estimation corresponds to the Maximum Likelihood Estimator (MLE) of the reflectivity. Then, by applying the multilook, the reduction factor of the speckle is proportional to the number of samples averaged and inversely proportional to the resulting resolution. In this sense, it is not a good technique, since it implies a resolution loss and it is one of the most valuable

advantages of the SAR systems.

The latest speckle filtering techniques are focused in a different direction, since it only makes sense to average pixels over the image having the same statistical distribution, that is, over homogeneous regions. If it were possible to delimit correctly these homogeneous regions over the image, then it would be possible to average over homogeneous regions only, obtaining results with higher quality and also preserving the spatial resolution of the original images. The latest techniques try to adapt to the image structure by employing different methods, however this adaptation is extremely difficult due to the speckle noise, then it seems the classical catch-22 situation, since to filter the speckle noise an adaptation to the image structure is needed but to achieve this adaptation properly some speckle filtering is needed.

Some state-of-the-art techniques try to achieve this adaptation by selecting between different directed windows or by defining an adaptive homogeneous neighborhood around each pixels, however they have some inconveniences in spatial structure adaptation or they introduce some distortion over the estimated data. In this thesis a different technique is proposed, based on generating an image abstraction based on a Binary Partition Tree (BPT), representing the image structure at different scales. This technique has been employed for image processing, achieving good results, but it needs an adaptation to be able to process PolSAR data. This adaptation to the different PolSAR datasets will be analyzed and described and it will be employed for different applications like the speckle filtering, coastline segmentation or change detection.

Then, the objectives for this thesis are the design, implementation and evaluation of different BPT based applications employing polarimetric SAR images. It includes the adaptation and the PolSAR data modeling to be able to generate properly its BPT representation, and the BPT exploitation for different applications. On this thesis, the BPT representation has been employed to process single PolSAR images and also series of images acquired at different dates, to study also the temporal dimension of the data.

In this work, interesting and promising results have been obtained, demonstrating the ability of the technique to adapt to the image structure at different detail levels. It has improved the evaluated speckle filtering techniques by achieving a better estimation of the scene reflection parameters while also having a good preservation of the spatial resolution. Then, it opens the door to apply this technique to different applications, since the BPT representation contains a lot of useful information about the image structure at different scales, making it very useful for other purposes than the ones analyzed in this thesis, as, for instance, classification, information extraction, target location, etc.

This manuscript has been divided into seven different chapters that will be described briefly.

The first chapter, as an introduction, put the reader in position to the scope of this work and its objectives. The second chapter makes a brief description of the concepts related to SAR and PolSAR systems. The problem of the speckle noise is described more elaborately, and some of the state-of-the-art speckle filtering techniques are defined.

In the third chapter, the BPT is presented as a data abstraction. Its structure is defined in detail and all the concepts related to its construction process are presented and described. All the algorithms employed for the BPT construction and its exploitation will be presented and a generic BPT-based processing scheme is proposed. Finally, an analysis of the processing scheme complexity is briefly described.

The fourth chapter particularizes the generic BPT processing scheme to the specific case of the polarimetric SAR data. It presents a region model for this data and different similarity measures that will be employed and analyzed for the BPT construction process.

The fifth chapter is devoted to the definition and analysis of different PolSAR image applications based on the BPT exploitation. Different BPT pruning strategies are proposed and compared and a detailed analysis es performed for the speckle filtering application, by employing real and simulated data. This approach is compared with other state-of-the-art speckle filtering techniques and some qualitative and quantitative analysis are performed to state the performance of the technique. Additionally, the BPT will be employed for a completely different application, that is, coastline segmentation. Although it is not evaluated as in detail as the speckle filtering application, it can give an idea of the BPT exploitation at completely different detail scales and its usefulness for different applications.

The sixth chapter makes an extension of the previously defined approach to the temporal dimension. A set of coregistered PolSAR images acquired at different dates are used to generate a space-time BPT representation, detecting the structure of the dataset in the space and time dimensions simultaneously. Speckle filtering application is considered over this space-time dataset and it is compared with the two-dimensional filtering defined in the previous chapter. Change detection application in the temporal dimension is also considered, generating maps of the number of changes on this dimension, giving an idea of the temporal stability of the different regions on the scene.

Finally, chapter 7 presents the most relevant conclusions after this research work and some possible future research lines are mentioned.

Additionally, in the appendices, a compilation of all the publications related to the subject of this master thesis can be found.

Chapter 2

SAR and PolSAR

This chapter is devoted to make an introduction of the main concepts referring to SAR and PolSAR systems. In Section 2.1 the foundations of SAR will be presented. SAR imaging systems will be presented and a statistical description of SAR data will be described, including the analysis of the speckle term present in this data.

In Section 2.2 polarimetric SAR systems (PolSAR) will be introduced. The electromagnetic wave polarimetry and its exploitation by PolSAR multichannel systems will be described. Under this new framework, the statistical description and modeling of the polarimetric data will be addressed.

2.1 Synthetic Aperture Radar

SAR systems are based on a coherent imaging technique at microwave frequency to generate a high resolution images about the complex reflectivity of the Earth surface. The main difference of the SAR systems in comparison with other remote sensing imaging systems, like the optical imaging sensors, is that SAR systems are active systems, that is, they produce their own illumination source. Thus, they are independent of most of the natural processes, including night and day cycles and weather state, making SAR an all condition imaging system. Additionally, since they are working at microwave frequency, SAR systems can detect some physical phenomenon only seen at these frequencies. Then, SAR technique may be seen as a valuable complement to other remote sensing techniques.

2.1.1 Basic concepts

In a typical radar system, a pulse is generated and conducted to the transmitting antenna, where it is emitted as an electromagnetic wave to the target. When the wave hits the target, part of its energy is re-radiated backwards toward the transmitter. This reflected electromagnetic wave, also known as radar echo, is captured again by the antenna and conducted towards the receiver, where it can be detected and processed.

A SAR system is able to obtain a high resolution image of the observed scene reflectivity by coherently processing the different radar echoes obtained at different positions. Thus, SAR systems are typically onboard a moving platform, usually an airplane or a satellite. In this context, the *azimuth* direction is defined as the flight direction, which defines the movement of the radar. The radar beam is slanted from the nadir direction to a direction perpendicular to the flight direction, known as *range* direction. Since the radar is moving, a footprint is generated by the antenna beam, referred as *swath*.

The resolution δ of an imaging system can be defined as the minimum separation of two targets to be detected and distinguished as two different targets at different positions. In SAR systems, since they are two-dimensional imaging systems, different resolutions can be achieved in range δ_r and azimuth δ_a dimensions. The range resolution δ_r is related with the radar pulse duration τ_p or inversely related with the signal bandwidth B

$$\delta_r = c\frac{\tau_p}{2} = \frac{c}{2B} \tag{2.1}$$

where c stands for the propagation speed of the electromagnetic waves in the medium.

To obtain a good quality in terms of the Signal to Noise Ratio (SNR) with a short pulse duration τ_p high energy pulses must be generated. In practice, with real transmitters, it is not possible to achieve short pulses having high energy at the same time. However, pulse compression techniques can be employed to solve this problem, by transmitting a long modulated pulse wich is processed afterwards by a matched filter [1] [2], compressing it to a duration equivalent to $1/B$. Employing this technique, the pulse energy can be increased and simultaneously a good range resolution can be obtained.

In a classical radar, the azimuth resolution is defined the antenna angular beam width θ_a, which is proportional to

$$\theta_a \propto \frac{\lambda}{D_a} \tag{2.2}$$

where λ refers to wavelength and D_a is the antenna length in the azimuth direction. Then, the resolution in the azimuth direction δ_a will be

$$\delta_a = r_0\frac{\lambda}{D_a} \tag{2.3}$$

where r_0 represents the range distance between the antenna and the target. Note that for radars onboard a satellite platform, good azimuth resolution, in the order of meters,

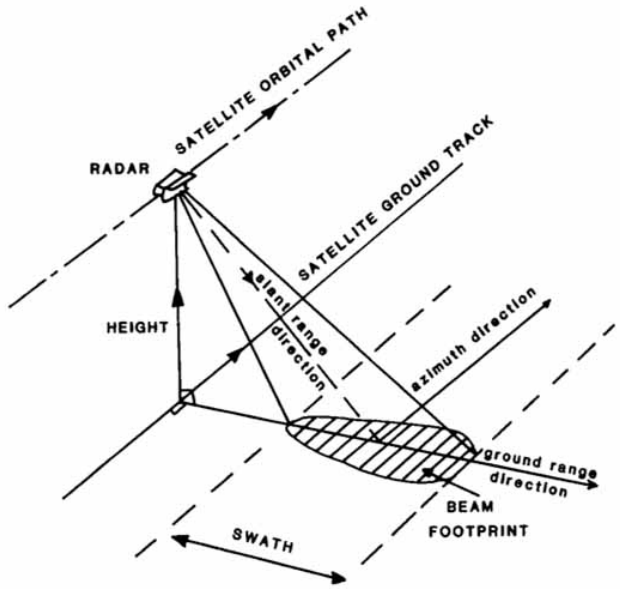

Figure 2.1: Synthetic aperture radar principle

can only be obtained with very large antennas, in the order of kilometers length in the azimuth direction, which is completely unfeasible.

Azimuth resolution can be effectively increased by applying the concept of synthetic aperture [3] [4] [5]. In fact, SAR is based on employing the movement of the platform in the azimuth direction to build an antenna array with an effective length much larger than the physical length of the receiver antenna. Each element of the array is the same receiver antenna which is transported to all of its positions. Fig. 2.1 shows the synthetic aperture principle for a SAR system geometry.

Then, similarly to a real aperture radar, the angular beam width θ_{sa}, corresponding to a synthetic antenna of azimuth length L_e would be

$$\theta_{sa} = \frac{\lambda}{2L_e}. \tag{2.4}$$

The factor 2 is related to the phase difference produced by the two way travel from the antenna to the target. Then, the azimuth resolution δ_a with this synthetic aperture will be

$$\delta_a = r_0 \frac{\lambda}{2L_e}. \tag{2.5}$$

The maximum length L_e of the synthetic aperture for a target at a range distance r_0 will be limited by traveled distance in the amount of time on which the target is illuminated by the antenna. Then, this maximum length can be bounded

$$L_e < \frac{\lambda r_o}{D_a}. \tag{2.6}$$

This limitation is also bounding the maximum azimuth resolution δ_a that can be achieved by the synthetic aperture

$$\delta_a = \frac{D_a}{2}. \tag{2.7}$$

Note that for a SAR system the azimuth resolution δ_a does not depend neither on the distance to the target r_0 nor th wavelength λ. The azimuth resolution only depends on the antenna size in the azimuth dimension D_a and, then, the smaller the antenna the higher the resolution. This surprising result is caused by the fact that, the smaller the antenna, the larger is the angular beam width θ_a, and also the time on which the target is illuminated by the antenna is enlarged, making possible a bigger synthetic aperture. The same can be applied to the distance of the target r_0, having larger synthetic apertures for farther targets.

2.1.2 SAR system impulse response

The SAR imaging process can be separated into two different stages: the data acquisition and the data focusing. At the first stage, the data is acquired, by transmitting a set of electromagnetic pulses that are reflected by the scene, then, the different radar echoes reflected are captured by the system and are finally registered. This type of data is called *raw data* and can not be directly related with the reflectivity of the scene. To obtain this scene reflectivity data a focusing process has to be done over the raw data, by effectively merging all the information referring to each target which is spread across the raw data.

A proper definition of the SAR imaging process can be obtained only if the impulse response of the SAR system is known, that is, the response of the system to a single point target, including both processes: the data acquisition and image focusing. This type of target, assuming that there is only one small target producing only one radar echo at a given resolution cell, is known as a point target or single target. When the impulse response is known, the complete image can be interpreted as a combination of the contributions of an arbitrary number of single targets.

The complex SAR image obtained to the output of the system for a point target at coordinates (x_0, r_0) is

$$S(x,r) = \sigma_s(x_0,r_0) \cdot \exp\left(j\frac{4\pi}{\lambda}(r-r_0)\right) \cdot \operatorname{sinc}\left(\frac{\pi(r-r_0)}{\delta_r}\right) \cdot \operatorname{sinc}\left(\frac{\pi(x-x_0)}{\delta_a}\right) \tag{2.8}$$

where $\sigma_s(x_o, r_0)$ refers to the complex Radar Cross Section (RCS) of the target [6] [7] [8]. From (2.8), it can be seen that the SAR system impulse response, including the acquisition and focusing stages, is proportional to

$$h(x,r) \propto \exp\left(j\frac{4\pi}{\lambda}r\right) \cdot \operatorname{sinc}\left(\frac{\pi r}{\delta_r}\right) \cdot \operatorname{sinc}\left(\frac{\pi x}{\delta_a}\right). \tag{2.9}$$

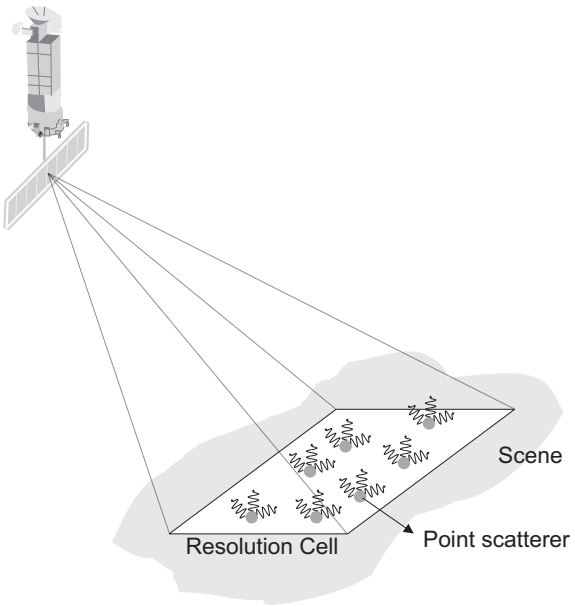

Figure 2.2: Resolution cell representation having multiple individual targets within

Then, from (2.9), the impulse response of the SAR system can be seen as a rectangular filter with a bandwidth in range dimension equal to $2B/c$ and $2/D_a$ in azimuth direction [3] [9] [10]. Additionally, from (2.9) the phase term associated to the range delay can be related to the scene, instead of to the SAR system, producing an impulse response proportional to

$$h(x, r) \propto \operatorname{sinc}\left(\frac{\pi r}{\delta_r}\right) \cdot \operatorname{sinc}\left(\frac{\pi x}{\delta_a}\right). \tag{2.10}$$

2.1.3 SAR data statistical description

In the previous section, the SAR system impulse response has been obtained and, as stated in (2.10), it can be seen as a low-pass filter over the scene reflectivity. The cell resolution concept is tightly related with the impulse response area, which can be considered δ_a by δ_r in size. Typically, in a real situation, the dimensions of this area, that is, the azimuth and range resolution, are much larger than the wavelength λ and then, the resulting echo is a combination of all the echoes produced by the individual targets present within the resolution cell [8] [11], as shown on Fig. 2.2.

These small targets are randomly distributed within the resolution cell and then, the signal received for each resolution cell can be considered as the coherent sum of all the complex reflections for each target, as represented on Fig. 2.3.

Then, the received coherent sum for a given resolution cell, represented as $r\exp(j\theta)$

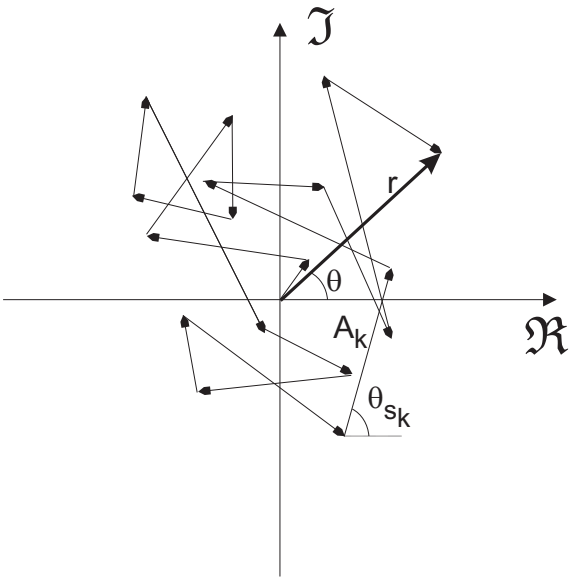

Figure 2.3: The received echo for a resolution cell is the combination of the echoes of the individual targets within this cell

and also known as the random walk, may be expressed as [12] [13]

$$r\exp(j\theta) = \sum_{k=1}^{N} A_k \exp(j\theta_k) \tag{2.11}$$

$$\Re\{S\} = \sum_{k=1}^{N} A_k \cos(j\theta_k) \tag{2.12}$$

$$\Im\{S\} = \sum_{k=1}^{N} A_k \sin(j\theta_k). \tag{2.13}$$

Most of geophysical media, as for instance: rough surfaces, vegetation, ice, snow, etc... have a very complicated structure and composition. Consequently, the knowledge of the exact scattered electromagnetic field, when illuminated by an incident wave, is only possible if a complete description of the scene was available. This type of information is completely unattainable for practical applications. Then, a possible alternative to characterize these scattering processes is through a statistical analysis [8] [14] [15]. These objects are called distributed targets, as opposite to point targets, as defined in Section 2.1.2.

To obtain the statistical description of the complex SAR image $S(x, r)$, some assumptions are taken related to the elemental targets $A_k \exp(j\theta_k)$ [11] [16]:

- The amplitude A_k and phase θ_k of the k-th phasor are statistically independent from each other and from the other phasors. This means that the scattering center of the elemental targets are uncorrelated and that the amplitude is not dependent on the phase.

- The phase of each one of the individual targets are uniformly distributed in the interval $(-\pi, \pi]$.

The first assumption is true since the phase propagation delay is independent of the intensity of the reflected wave. The second assumption is true, considering that the dimensions of the resolution cell δ_a, δ_r are much larger than the wavelength λ, as a wide margin of phase center values is introduced for the different targets within the resolution cell.

If, additionally, the number of individual point targets N within the resolution cell is large enough, then $A_k \cos(\theta_k)$ and $A_k \sin(\theta_k)$ satisfy the Central Limit Theorem [17], and $\Re\{S\}$ and $\Im\{S\}$ are following a normal zero-mean distribution [11] [16] [17] [18]. Their mean value can be calculated as

$$E\left\{\Re\{S\}\right\} = \sum_{k=1}^{N} E\{A_k \cos(\theta_k)\} = \sum_{k=1}^{N} E\{A_k\} E\{\cos(\theta_k)\} = 0 \tag{2.14}$$

$$E\left\{\Im\{S\}\right\} = \sum_{k=1}^{N} E\{A_k \sin(\theta_k)\} = \sum_{k=1}^{N} E\{A_k\} E\{\sin(\theta_k)\} = 0 \tag{2.15}$$

where $E\{\cdot\}$ refers to the expectation operator.

Similarly, the variance value for $\Re\{S\}$ and $\Im\{S\}$ can be obtained

$$E\left\{\Re^2\{S\}\right\} = \sum_{k=1}^{N} E\{A_k^2\} E\{\cos^2(\theta_k)\} = \frac{N}{2} E\{A_k^2\} \tag{2.16}$$

$$E\left\{\Im^2\{S\}\right\} = \sum_{k=1}^{N} E\{A_k^2\} E\{\sin^2(\theta_k)\} = \frac{N}{2} E\{A_k^2\}. \tag{2.17}$$

The correlation between them would be

$$E\left\{\Re\{S\}\Im\{S\}\right\} = \sum_{k=1}^{N} \sum_{l=1}^{N} E\{A_k A_l\} E\{\cos(\theta_k)\sin(\theta_l)\} = 0. \tag{2.18}$$

Renaming x to $\Re\{S\}$ and y to $\Im\{S\}$, their probability density functions can be expressed as

$$p_x(x) = \frac{1}{\sqrt{2\pi\sigma^2}} \exp\left(-\frac{1}{2}\left(\frac{x}{\sigma}\right)^2\right) \qquad x \in (-\infty, \infty) \tag{2.19}$$

$$p_y(y) = \frac{1}{\sqrt{2\pi\sigma^2}} \exp\left(-\frac{1}{2}\left(\frac{y}{\sigma}\right)^2\right) \qquad y \in (-\infty, \infty) \tag{2.20}$$

where $\sigma^2/2 = (N/2)E\{A_k^2\}$.

Then, $p(x)$ and $p(y)$ are zero-mean Gaussian distributions, also expressed as $N(0, \sigma^2/2)$. The probability density function of the amplitude $p_r(r)$ and phase $p_\theta(\theta)$, where $r =$

$\sqrt{x^2+y^2}$ and $\theta = \arctan(y/x)$, can also be obtained

$$p_{r,\theta}(r,\theta) = \frac{r}{2\pi\sigma^2}\exp\left(\frac{-r^2}{2\sigma^2}\right) \tag{2.21}$$

$$p_r(r) = \frac{r}{\sigma^2}\exp\left(\frac{-r^2}{2\sigma^2}\right) \qquad r \in [0,\infty) \tag{2.22}$$

$$p_\theta(\theta) = \frac{1}{2\pi} \qquad \theta \in (-\pi,\pi]. \tag{2.23}$$

As it can be seen, the amplitude and phase distribution are separable. $p_r(r)$ is also known as a Rayleigh distribution, whereas $p_\theta(\theta)$ is a uniform distribution. This means that the phase θ of a target has no information about itself. For a Rayleigh distribution, like $p_r(r)$, the mean value and its variance are

$$E\{r\} = \sigma\sqrt{\frac{\pi}{2}} \tag{2.24}$$

$$\sigma_r^2 = \left(2-\frac{\pi}{2}\right)\sigma^2. \tag{2.25}$$

Another statistical parameter usually employed is the coefficient of variation (CV), defined as the relation between the standard deviation and the mean [19]. From the previously defined expressions, it can be derived as $\sqrt{\frac{4}{\pi}-1}$.

Generally, the study of SAR data is interested in the intensity I, defined as $I = r^2$, which pdf can be expressed as

$$p_I(I) = \frac{1}{\sigma^2}\exp\left(\frac{-I}{\sigma^2}\right) \qquad I \in [0,\infty) \tag{2.26}$$

and then, I is following an exponential distribution. Therefore, its mean value will be $E\{I\} = \sigma^2$ and its variance $\sigma_I^2 = \sigma^4$. The CV of the intensity, then, will be equal to 1.

2.1.4 Multiplicative speckle noise model

From (2.26), the probability density function of the SAR image intensity has been identified as an exponential distribution. If the variable change

$$I = \sigma^2 z \tag{2.27}$$

is introduced on (2.26), then the following distribution $p_z(z)$ is obtained

$$p_z(z) = \exp(-z) \qquad z \in [0,\infty). \tag{2.28}$$

From (2.27), the intensity of a SAR image pixel can be considered as a deterministic value containing information about the incoherent reflected power (σ^2) multiplied by the *speckle noise* (z), having an exponential distribution (2.28) with a mean and variance

values equal to one. This causes that the speckle noise is usually considered as a multiplicative noise respect to to the SAR image intensity [18] [20] [21] [3]. However, note that the speckle noise is not a random process, since it is an electromagnetic measure of the interactions of all the individual targets. Nevertheless, due to the complexity of the reflection process, it can not be predicted for a given pixel and then, it is interpreted as a random process degrading the deterministic component σ^2.

Note that all the information about the scene reflectivity is contained in the term σ^2, and the phase has no information, as stated before. Then, the SAR image $S(x, r)$ can be described over an homogeneous area as

$$S(x, r) = \sqrt{\sigma^0} n \exp(j\theta) \tag{2.29}$$

where n denotes the multiplicative component of the speckle noise in amplitude, characterized by $E\{n\} = 1$ and $\text{var}\{n\} = 1$. The information is contained in $\sqrt{\sigma^0}$ and it is independent of the noise $n \exp(j\theta)$.

2.2 SAR Polarimetry

Polarimetric SAR (PolSAR) systems increase the amount of information extracted from the scene by the acquisition of more than one SAR images referring to the same area. The main feature of an electromagnetic wave is the vectorial nature of its electromagnetic field, also known as polarization. Then, employing different combinations of the polarization of the incident and reflected waves, the amount of information channels can be increased. This option has also an important advantage, the *polarization synthesis* [22], allowing the retrieval of the target response at any polarization by just knowing its response to two orthogonal polarization states.

2.2.1 Wave polarization

From the Maxwell equations, the solution conforming the progressive waves can be extracted, representing the energy transportation from one plane to another [23]. Employing the classical Cartesian coordinates $[\hat{\mathbf{x}}, \hat{\mathbf{y}}, \hat{\mathbf{z}}]$ to describe the electric field of a wave propagating on the $\hat{\mathbf{Z}}$ direction, it can be obtained

$$\vec{E}(\vec{z}, t) = E_x(\vec{z}, t)\hat{\mathbf{x}} + E_y(\vec{z}, t)\hat{\mathbf{y}} = E_{0x}\cos(wt - kz - \delta_x)\hat{\mathbf{x}} + E_{0y}\cos(wt - kz - \delta_y)\hat{\mathbf{y}} \tag{2.30}$$

where δ_x and δ_y are two constant phase terms, E_{0x} and E_{0y} represent the electric field amplitude at directions $\hat{\mathbf{x}}$ and $\hat{\mathbf{y}}$ and k is defined as

$$k = 2\frac{\pi}{\lambda} = \frac{w}{c}. \tag{2.31}$$

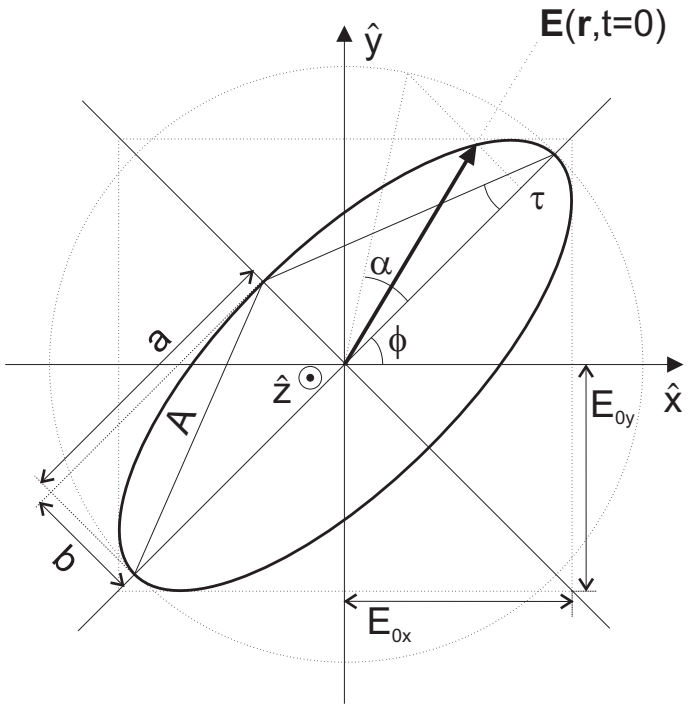

Figure 2.4: Generic polarization ellipse for an electromagnetic wave propagating on $\hat{\mathbf{z}}$ direction

The expression in (2.30) can also be expressed in vectorial form

$$\vec{E}(\vec{z},t) = \begin{bmatrix} E_x \\ E_y \end{bmatrix} = \begin{bmatrix} E_{0x}\cos(wt - kz - \delta_x) \\ E_{0y}\cos(wt - kz - \delta_y) \end{bmatrix}. \tag{2.32}$$

The components E_x and E_y are following the expression

$$\left(\frac{E_x}{E_{0x}}\right)^2 + \left(\frac{E_y}{E_{0y}}\right)^2 - 2\frac{E_x E_y}{E_{0x}E_{0y}} = \sin^2(\delta) \tag{2.33}$$

where $\delta = \delta_x - \delta_y$.

The equation (2.33) defines the geometric figure of the electric field vector $\vec{E}(\vec{z},t)$ along the time dimension for any value of z. This geometric figure, in the most general case, has the shape of an ellipse, also known as polarization ellipse, which shape does not depend neither the space nor the time. The polarization ellipse is shown in Fig. 2.4

A polarization state can be defined by the following parameters

- Orientation in the space of the plane containing the polarization ellipse. It is determined by its normal vector, which is the propagation direction of the electromagnetic wave. On Fig. 2.4 it has been assumed as $\hat{\mathbf{z}}$.

- Orientation angle ϕ of the major axis of the ellipse with respect to the $\hat{\mathbf{x}}$ direction. The values for this parameters are in the interval $[\frac{-\pi}{2}, \frac{\pi}{2}]$.

	Lineal horizontal	Lineal vertical	Circular clockwise	Circular counter-clockwise
ϕ	0	$\frac{\pi}{2}$	$[\frac{-\pi}{2}, \frac{\pi}{2}]$	$[\frac{-\pi}{2}, \frac{\pi}{2}]$
τ	0	0	$\frac{-\pi}{4}$	$\frac{\pi}{4}$

Table 2.1: Some typical polarization states and its associated parameters

- Ellipticity angle τ, representing the aperture of the ellipse and having values in the interval $[\frac{-\pi}{4}, \frac{\pi}{4}]$.

- Polarization direction, indicating the turning direction of the polarization ellipse. It is expressed by the sign of the ellipticity τ. It is determined by the IEEE convention; when looking to the wave towards the propagation direction, if the electric field vector is rotating in clockwise direction then $\tau < 0$, if it is rotating counter-clockwise then $\tau > 0$.

- The amplitude of the polarization ellipse A, defined as $A = \sqrt{a^2 + b^2}$, where a and b are the amplitude of the major and minor axis of the ellipse, respectively.

- The initial phase α with respect to the phase origin for $t = 0$, defined in the interval $(-\pi, \pi]$.

Table 2.1 shows the polarization ellipse values for some typical polarization states.

2.2.2 The scattering matrix

To completely characterize the scattering process of a target when it is illuminated by an electromagnetic wave, the scattering matrix may be employed. However, to define properly the scattering matrix, it is necessary to define properly the global scenario on which it will be described. A Cartesian coordinate system $[\hat{\mathbf{x}}, \hat{\mathbf{y}}, \hat{\mathbf{z}}]$ will be assumed, with the origin located over the target.

On the other hand, the SAR system can be considered as a system containing 2 antennas, the transmitter and the receiver antennas, which can be located at any position in the space. When these antennas are located at different positions, then the reflection process is called bistatic, whereas if they are located at the same point it is called monostatic. A particular case of the bistatic configuration is obtained when the receiver antenna is located behind the target, over the same line from the transmitter to the target.

The electric field vector can be completely described by two orthogonal polarization states [24]. In the following, these two orthogonal polarization states will be assumed as the lineal horizontal $\hat{\mathbf{h}}$ and vertical $\hat{\mathbf{v}}$ polarization states, conforming the polarization basis $\{\hat{\mathbf{h}}, \hat{\mathbf{v}}\}$.

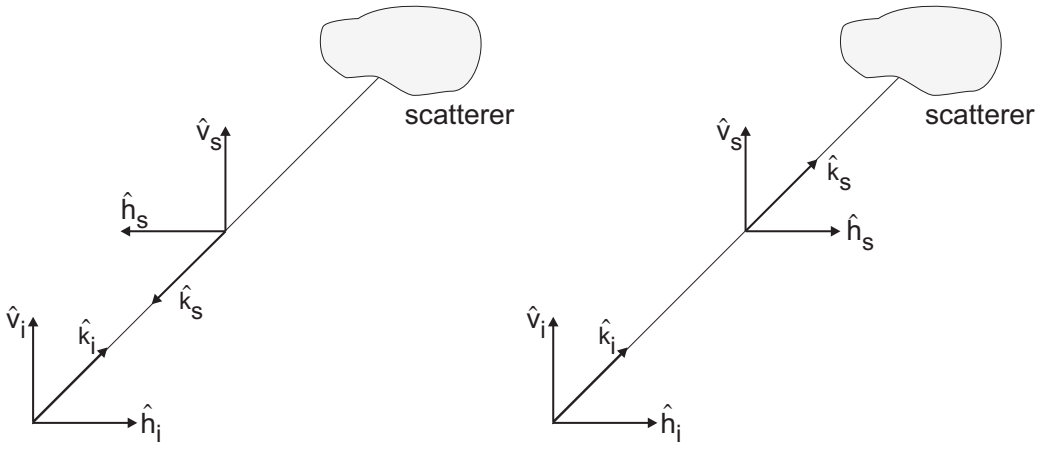

(a) FSA (b) BSA

Figure 2.5: Incident and scattered electric field coordinate reference conventions

Then, the incident electric field has two components E_h^i and E_v^i over this basis, and its coordinate system is centered on the transmitter antenna $[\hat{\mathbf{h}}_\mathbf{i}, \hat{\mathbf{v}}_\mathbf{i}, \hat{k}_i]$. For the scattered electric field $[\hat{\mathbf{h}}_\mathbf{s}, \hat{\mathbf{v}}_\mathbf{s}, \hat{k}_s]$ there are two different conventions depending on the SAR system type. One convention is called Forward Scattering Alignment (FSA), which is referent to the propagating wave. The other convention, called Backward Scattering Alignment (BSA), is defined regarding the radar antennas. Fig. 2.5 shows both conventions for the incident and scattered electric fields.

Then, the equivalence of the different conventions can be extracted for the incident and scattered electric fields; for the FSA convention: $\hat{\mathbf{h}}_\mathbf{s} = -\hat{\mathbf{h}}_\mathbf{i}, \hat{\mathbf{v}}_\mathbf{s} = \hat{\mathbf{v}}_\mathbf{i}$ and $\hat{k}_s = -\hat{k}_i$, whereas for the BSA: $\hat{\mathbf{h}}_\mathbf{s} = \hat{\mathbf{h}}_\mathbf{i}, \hat{\mathbf{v}}_\mathbf{s} = \hat{\mathbf{v}}_\mathbf{i}$ and $\hat{k}_s = \hat{k}_i$.

In the following, the BSA convention will be employed, since the incident and scattered electric fields are expressed over the same coordinate system. Employing the selected polarization basis $\{\hat{\mathbf{h}}, \hat{\mathbf{v}}\}$, the incident and scattered waves can be expressed as

$$E^i = E_h^i \hat{\mathbf{h}}_\mathbf{i} + E_v^i \hat{\mathbf{v}}_\mathbf{i} \tag{2.34}$$

$$E^s = E_h^s \hat{\mathbf{h}}_\mathbf{s} + E_v^s \hat{\mathbf{v}}_\mathbf{s}. \tag{2.35}$$

To relate the different components of the incident and scattered waves, assuming the far field hypothesis, the 2 by 2 scattering matrix $\mathbf{S}$ can be employed. $\mathbf{S}$ is a complex dimensionless matrix, characteristic of the target, and also known as scattering matrix

$$\begin{bmatrix} E_h^s \\ E_v^s \end{bmatrix} = \frac{\exp(-jkr)}{r} \begin{bmatrix} S_{hh} & S_{hv} \\ S_{vh} & S_{vv} \end{bmatrix} \begin{bmatrix} E_h^i \\ E_v^i \end{bmatrix} \tag{2.36}$$

or, equivalently, in matrix notation

$$\mathbf{E^s} = \frac{\exp(-jkr)}{r} \mathbf{S E^i} \tag{2.37}$$

where r represents the distance between the receiver antenna and the target. The expression (2.37) is also known as field equation. In the following, the term $\frac{\exp(-jkr)}{r}$ referring to the wave propagation will be omitted since it is not affecting the polarimetric information. Additionally, a monostatic SAR system case will be assumed, since it is the real situation for most system, where the position of the transmitter and the receiver antennas can be considered the same. Then, under this assumption and applying the reciprocity theorem [25] [26], the following equivalences can be obtained

$$S_{vh} = S_{hv} \tag{2.38}$$

for the BSA convention and

$$S_{vh} = -S_{hv} \tag{2.39}$$

for the FSA case. Then, one of the off-diagonal elements of the **S** matrix is redundant. To express the same information about the target reflectivity without any redundant parameter, the scattering vector **k** may be employed, containing the same relevant information as the scattering matrix **S**

$$\mathbf{k}_{3L} = [S_{hh}, \sqrt{2}S_{hv}, S_{vv}]^T. \tag{2.40}$$

An important parameter of the scattering vector is its squared norm $\|\mathbf{k}\|^2$, also known as *span*, which is referring to the total reflected power by the target. This value must be independent of the polarization basis employed for representation of the electromagnetic waves. The term $\sqrt{2}$ appearing in (2.40) is intended to preserve this information with respect to the scattering matrix. Another scattering vector, representing the same information in a different polarization basis is the Pauli scattering vector

$$\mathbf{k}_{3P} = \frac{1}{\sqrt{2}}[S_{hh} + S_{vv}, S_{hh} - S_{vv}, 2S_{hv}]^T. \tag{2.41}$$

which has the advantage of being easier to relate its components with the elemental physical mechanisms of scattering. Note that both vectors are in the $\mathbb{C}^3$ space.

2.2.3 Covariance and Coherence matrices

In the previous section the scattering matrix and vector have been defined. This information is capable to describe the target scattering properties provided that it is a point scatter. Generally, this is not true, as stated in Section 2.1.3, since within the resolution cell a large number of independent targets are present randomly distributed and, then, the reflected wave is the coherent sum of all these contributions.

Note that in polarimetric SAR images, each one of the elements of the **S** matrix can be considered a individual SAR image. In Section 2.1.3 it has been shown that a SAR

image can be modeled by $N(0, \sigma^2/2)$. Then, each one of the elements of the scattering matrix can be modeled as a zero-mean complex Gaussian distribution with variance $\sigma^2/2$.

Therefore, the useful information about the scene reflectivity, as in the single channel SAR images, is within the data statistics. Assuming that $\mathbf{k}$ is the scattering vector containing all the information of the scattering mechanism in a particular resolution cell, then $\mathbf{k}$ is following a multidimensional Gaussian distribution, which is zero-mean and can be described by its covariance matrix $\mathbf{C}$ [27] [28] [29]

$$p_k(\mathbf{k}) = \frac{1}{\pi^Q |\mathbf{C}|} \exp(-\mathbf{k}^H \mathbf{C}^{-1} \mathbf{k}) \tag{2.42}$$

where $Q = 3$ for a monostatic configuration and ^{H} denotes hermitian transpose of complex vectors and matrices. The zero-mean complex multidimensional Gaussian pdf, as shown on (2.42) is denoted as $N(\mathbf{0}, \mathbf{C})$ and is completely determined by its covariance matrix $\mathbf{C}$, being an hermitian and positive semi-definite matrix [17]. This matrix can be defined as

$$\mathbf{C} = E\{\mathbf{k}_{3L}\mathbf{k}_{3L}^H\} = \begin{bmatrix} E\{S_{hh}S_{hh}^*\} & \sqrt{2}E\{S_{hh}S_{hv}^*\} & E\{S_{hh}S_{vv}^*\} \\ \sqrt{2}E\{S_{hv}S_{hh}^*\} & E\{S_{hv}S_{hv}^*\} & \sqrt{2}E\{S_{hv}S_{vv}^*\} \\ E\{S_{vv}S_{hh}^*\} & \sqrt{2}E\{S_{vv}S_{hv}^*\} & E\{S_{vv}S_{vv}^*\} \end{bmatrix}. \tag{2.43}$$

Note that $E\{\mathbf{k}\} = \mathbf{0}$ and, then, no information can be extracted directly from the scattering vector $\mathbf{k}$ or matrix $\mathbf{S}$. All the information is contained in the higher order statistics, that are completely characterized by $\mathbf{C}$ [17] [30] [31]. This matrix contains in the diagonal elements the RCS value of the region in the polarimetric basis, that is, $|\sigma_{hh}|^2$, $|\sigma_{hv}|^2$ and $|\sigma_{vv}|^2$, but, additionally, in the off-diagonal elements it contains information about the correlation between the different elements of the scattering matrix, that are very useful for the PolSAR data interpretation.

Similarly, the coherence matrix $\mathbf{T}$ can be defined, by employing the Pauli scattering vector $\mathbf{k}_{3P}$, defined in (2.41), instead of the conventional scattering vector $\mathbf{k}_{3L}$ [32]

$$\mathbf{T} = E\{\mathbf{k}_{3P}\mathbf{k}_{3P}^H\}. \tag{2.44}$$

Again, the advantage of this coherence matrix is that its values can be easily related with the physical scattering mechanisms. Anyway, since the conventional scattering vector $\mathbf{k}_{3L}$ and the Pauli vector $\mathbf{k}_{3P}$ contains the same information, expressed in a different polarization basis, the covariance and coherence matrices also contain the same information. In fact, they are related by the following expression [32]

$$\mathbf{T} = \frac{1}{2} \begin{bmatrix} 1 & 0 & 1 \\ 1 & 0 & -1 \\ 0 & \sqrt{2} & 0 \end{bmatrix} \mathbf{C} \begin{bmatrix} 1 & 1 & 0 \\ 0 & 0 & \sqrt{2} \\ 1 & -1 & 0 \end{bmatrix}. \tag{2.45}$$

2.2.4 Speckle noise in PolSAR data

For distributed targets, as stated in the previous section, the characterization of their scattering process can only be done by the second order moments, since the scattering vector is following a $N(\mathbf{0}, \mathbf{C})$ distribution. In this section, the covariance matrices $\mathbf{C}$ will be referred, but the same may be applied for the coherence matrices $\mathbf{T}$, since they are related through expression (2.45).

The estimation process of the covariance matrix is performed by averaging the matrices of n pixels, and is called *multilook*. In the following, the estimated covariance matrix, also known as sample covariance matrix, will be denoted as $\mathbf{Z}$, and can be expressed as [19] [27] [28] [33]

$$\mathbf{Z} = \langle \mathbf{k}\mathbf{k}^H \rangle_n = \frac{1}{n} \sum_{i=1}^{n} \mathbf{k}_i \mathbf{k}_i^H. \tag{2.46}$$

where a $\{\hat{\mathbf{h}}, \hat{\mathbf{v}}\}$ polarization basis is assumed and, then, $\mathbf{k}$ refers to $\mathbf{k}_{3L}$. This matrix $\mathbf{Z}$ estimated over n samples is also referred as *n-look* PolSAR data.

The multilook estimator corresponds to the Maximum Likelihood Estimator (MLE) of the covariance matrix. However, this estimator has some important drawbacks. On one hand, the estimated covariance matrix $\mathbf{Z}$ depends on the number of averaged pixels n, resulting in a better estimation as n increases [34]. Equivalently, the variance of the estimator will be lower and the amount of speckle noise reduction will be better for larger n. On the other hand, this estimation only makes sense over homogeneous areas, that is, areas having the same distribution (with the same covariance matrix $\mathbf{C}$), otherwise a spatial resolution loss will be observed over the image.

The probability distribution of the sample covariance matrix $\mathbf{Z}$, assuming the zero-mean complex Gaussian distribution for the scattering vector $\mathbf{k}$, can be expressed as a complex Wishart distribution $W(\mathbf{C}, n)$ [33]

$$p_{\mathbf{Z}}(\mathbf{Z}) = \frac{n^{Qn} |\mathbf{Z}|^{n-Q}}{|\mathbf{C}|^n \widetilde{\Gamma}_Q(n)} \mathrm{etr}(-n\mathbf{C}^{-1}\mathbf{Z}) \tag{2.47}$$

where $\mathrm{etr}(\mathbf{X})$ is the exponential of the matrix trace and

$$\widetilde{\Gamma}_Q(n) = \pi^{\frac{1}{2}Q(Q-1)} \prod_{i=1}^{Q} \Gamma(n-i+1). \tag{2.48}$$

where Q is the dimension of the $\mathbf{k}$ vector and Γ is the gamma function. For a monostatic SAR radar $Q = 3$.

Note that the determinant of the estimated covariance matrix $|\mathbf{Z}|$ appears in the numerator of the expression (2.47) and, then, the matrix $\mathbf{Z}$ must be full-rank or the Wishart

distribution $p_{\mathbf{Z}}(\mathbf{Z})$ can not be defined. Then, a minimum averaging over at least Q different pixels must be done to get a full-rank $\mathbf{Z}$ matrix.

From Section 2.1.4, each element of the scattering matrix can be defined as

$$S_{pq} = \sqrt{\sigma_{pq}} n_{pq} \exp(j\theta_{pq}) \tag{2.49}$$

where n refers to the speckle noise, σ_{pq} is the local RCS and p and q refer to the orthogonal polarization basis $p, q \in \{\hat{\mathbf{h}}, \hat{\mathbf{v}}\}$. Then, for the estimated covariance matrix elements

$$\langle S_{pq} S_{rs}^* \rangle = \langle \sqrt{\sigma_{pq}\sigma_{rs}} \exp(j(\theta_{pq} - \theta_{rs})) \rangle \langle n_{pq} n_{rs}^* \rangle. \tag{2.50}$$

To recover all the useful information from the multilook, it is needed that $\langle n_{pq} n_{rs}^* \rangle = 1$ when $pq = rs$ and zero otherwise. A Gaussian variable having this distribution will be defined by a diagonal covariance matrix, producing the same speckle noise for all the SAR images, which is not true [19].

In [35] a speckle noise model is proposed for multichannel SAR images based on the study of the complex hermitian product of a pair of SAR images. Given two SAR images, S_1 and S_2, the single-look covariance matrix $\mathbf{Z}$ is defined as

$$\mathbf{Z} = \begin{bmatrix} S_1 S_1^* & S_1 S_2^* \\ S_2 S_1^* & S_2 S_2^* \end{bmatrix}. \tag{2.51}$$

Each element of this matrix can be expressed as

$$S_k S_l^* = |S_k S_l^*| \exp\left(j(\theta_k - \theta_l)\right) = z \exp(j\phi) \tag{2.52}$$

which amplitude z and phase ϕ are following the probability distributions [28]

$$p_z(z) = \frac{4z}{\varphi^2(1-|\rho|^2)} I_0\left(\frac{2|\rho|z}{\varphi(1-|\rho|^2)}\right) K_0\left(\frac{2z}{\varphi^2(1-|\rho|^2)}\right) \tag{2.53}$$

$$p_\phi(\phi) = \frac{1-|\rho|^2}{2\pi}\left(\frac{\beta\left(\frac{1}{2}\pi + \arcsin(\beta)\right)}{(1-\beta^2)^{3/2}} + \frac{1}{1-\beta^2}\right) \tag{2.54}$$

where ρ is the complex correlation coefficient between the pair of images, φ represents the average power from both channels, calculated as $\varphi = \sqrt{\sigma_1\sigma_2}$, being σ_1 and σ_2 the backscattering coefficients of the images S_1 and S_2, β is defined as $\beta = |\rho|\cos(\phi - \phi_x)$ with ϕ_x as the effective phase difference between the image pair, I_0 is the modified Bessel function of the first kind whereas K_0 is the modified Bessel function of the third kind.

Introducing the speckle noise model of the difference phasor [36] [27] it can be seen that real and imaginary parts of the hermitian product of a pair of SAR images can be divided into three additive terms

$$z\exp(j\phi) = [zN_c + (zv_1' + jzv_2')]\exp(j\phi_x). \tag{2.55}$$

Analyzing separately the contribution to the global noise of each one of the terms, a speckle noise model can be defined for the hermitian product of a pair of SAR images

$$S_k S_l^* = \varphi N_c \bar{z}_n n_m \exp(j\phi_x) + \varphi(|\rho| - N_c \bar{z}_n) \exp(j\phi_x) + \varphi(n_{ar} + j n_{ai}) \tag{2.56}$$

where n_m is a multiplicative noise component associated to the first term, n_{ar} and n_{ai} are additive noise components associated to the real and imaginary parts of the hermitian product, $\bar{z}_n$ is the expected value of amplitude normalized of the hermitian product, obtained for the case $\varphi = 1$, and N_c contains approximately the same information as the coherence $|\rho|$. The terms of (2.56) can be classified as

$$S_k S_l^* = \underbrace{\varphi N_c \bar{z}_n n_m \exp(j\phi_x)}_{\text{Multiplicative term}} + \underbrace{\varphi(|\rho| - N_c \bar{z}_n) \exp(j\phi_x) + \varphi(n_{ar} + j n_{ai})}_{\text{Additive term}}. \tag{2.57}$$

Then, the first term of (2.56) is called multiplicative term, since the useful signal is multiplied by a multiplicative speckle term n_m. The second and third terms are contaminated by the additive components of the speckle noise n_{ar} and n_{ai}.

Note that (2.56) may be seen as a generalization of the speckle noise models obtained in Section 2.1.4, by making $k = l$, and, consequently, $|\rho| = 1$ and $\phi_x = 0$ radians. Then (2.56) is simplified to

$$S_k S_k^* = |S_k|^2 = \varphi n_m \tag{2.58}$$

where $\varphi = E\{|S_k|^2\}$. As it can be seen, this result matches with the multiplicative speckle noise model defined in Section 2.1.4.

2.2.5 H/A/$\bar{\alpha}$ polarimetric decomposition

A wide number of different polarimetric decompositions are available, for the extraction of useful information from PolSAR data as, for instance: Huynen [37], Krogager [38], Cameron [39], Freeman-Durden [40] or TSVM [41]. In [42], Cloude and Pottier proposed a decomposition based on the projection of the coherence matrix $\mathbf{T}$ in the polarization basis formed by its eigenvectors. Then, a coherence matrix may be expressed as the sum of three unitary matrices having rank equal to 1, that is, three pure scattering mechanisms $\mathbf{T}^i$

$$\mathbf{T} = \sum_{i=1}^{3} \lambda_i \mathbf{v}_i \mathbf{v}_i^H = \sum_{i=1}^{3} \lambda_i \mathbf{T}^i \tag{2.59}$$

where $\lambda_1 > \lambda_2 > \lambda_3$ are the ordered eigenvalues and $\mathbf{v}_i$ are the corresponding eigenvectors.

Then, the entropy H and anisotropy A parameter can be defined as

$$H = \sum_{i=1}^{3} -P_i \log_3 P_i \tag{2.60}$$

$$A = \frac{\lambda_2 - \lambda_3}{\lambda_2 + \lambda_3} \tag{2.61}$$

where the pseudo-probabilities P_i are defined as

$$P_i = \frac{\lambda_i}{\sum_{j=1}^{3} \lambda_j}. \tag{2.62}$$

Note that the eigendecomposition of the covariance matrix may be interpreted as the identification of the different pure scattering mechanisms, denoted by the eigenvectors, and their associated reflected power, denoted by the eigenvalues. Then, the entropy H parameter is related with the uncertainty associated with the different scattering mechanisms, being equal to 1 when all the mechanisms are equally probable, that is, all of them have the same reflected power, and equal to 0 when only one mechanism is present. Anisotropy A gives and idea of the dominance of the second pure mechanism, in terms of reflected power (λ_2), versus the third one (λ_3), being equal to 0 when both have the same power ($\lambda_2 = \lambda_3$) and equal to 1 if there is no reflected power for the third mechanism ($\lambda_2 \gg \lambda_3$).

On the other hand, the $\bar{\alpha}$ parameter is referring to the weighted average of the different pure scattering mechanism angles α_i

$$\bar{\alpha} = \sum_{i=1}^{3} P_i \alpha_i \tag{2.63}$$

where the angle α_i refers to the type of reflection, from surface scattering $\alpha_i = 0°$ to volume scattering $\alpha_i = 45°$ and double bounds in conductive surfaces $\alpha_i = 90°$.

2.3 PolSAR speckle filtering techniques

As seen in previous sections, an initial averaging over the sample covariance matrix $\mathbf{Z}$ is needed to obtain a well defined and full rank matrix. However, this averaging process only makes sense when it is performed over homogeneous regions of the image, that is, pixels having the same statistical distribution. This process of estimating the covariance or coherence matrix from the PolSAR data is also known as speckle filtering, since the effect of the speckle noise over the data is also diminished, enabling a better estimation of the parameters of these matrices.

In this section, some of the state-of-the-art polarimetric speckle filtering techniques will be presented.

2.3.1 Multilook and Boxcar filter

In Section 2.2.3 the multilook concept was introduced as the sample covariance matrix estimation process from the data of n different pixels, as stated in (2.46). The Boxcar

filter, also referred to as multilook filter by extension, is the application of this averaging process over a rectangular window around a given pixel [34].

The Boxcar filter is the simplest filter and, since the multilook corresponds to the MLE of the covariance matrix, it does not introduce systematically any bias or distortion. However, as stated before, this filtering technique has some drawbacks, since this averaging process should be done employing homogeneous pixels following the same statistical distribution. When applying the Boxcar filter inside large homogeneous regions, the sample covariance matrix $\mathbf{Z}$ can be estimated properly, but, near region contours or for small point targets, this is not the case. As a result, region contours will appear blurred and point targets will be enlarged by the filter window size, which may be seen as a spatial resolution loss. Then, in this kind of filtering there is always a compromise between the amount of speckle filtering and the spatial resolution loss.

2.3.2 Lee adaptive filter

In [43] a polarimetric SAR data filtering technique was introduced, with an adaptive filter to improve the precision of the estimated coherence. In order to overcome the drawbacks of the multilook filter, as stated before, it tries to adapt to the image morphology and average only homogeneous pixels. To achieve this adaptation, 8 different directional windows are defined, containing different neighborhoods for a given pixel, and the one containing the most homogeneous pixels is selected for averaging. The most homogeneous window selection is based on the average of the span, that is, the total received power calculated as $\mathrm{tr}(\mathbf{Z})$. Then, only the information contained in the diagonal elements of the covariance matrix is employed. The pixels within the most homogeneous directional window are employed for the estimation of the covariance matrix $\tilde{\mathbf{Z}}$ employing the Local Linear Minimum Mean Squared Error (LLMMSE)

$$\tilde{\mathbf{Z}} = \bar{\mathbf{Z}} + b(\mathbf{Z} - \bar{\mathbf{Z}}) \tag{2.64}$$

where $\bar{\mathbf{Z}}$ refers to the sample covariance matrix averaged over the selected directional window, $\mathbf{Z}$ refers to the value of the sample covariance matrix for the central pixel and $b \in [0, 1]$ is a weighting factor calculated with the degree of local stationarity.

Assuming a multiplicative noise

$$y = xn \tag{2.65}$$

where y is the value of the central pixel, x is the value we want to estimate and n represents the multiplicative noise, with an expectation equal to one and variance γ_n^2. Then, the weighting factor b can be calculated as

$$b = \frac{\mathrm{var}(x)}{\mathrm{var}(y)} \tag{2.66}$$

and

$$\mathrm{var}(x) = \frac{\mathrm{var}(y) - \bar{y}^2\sigma_n^2}{1 - \sigma_n^2} \tag{2.67}$$

where $\bar{y} = E\{y\}$.

Over homogeneous areas $\mathrm{var}(x) = 0$, then $b = 0$ and $\tilde{\mathbf{Z}} = \bar{\mathbf{Z}}$, corresponding to the result for the multilook filter over the oriented window. On the contrary, for point targets or very heterogeneous areas $b = 1$ and then $\tilde{\mathbf{Z}} = \mathbf{Z}$. In this case, the intensity of the given pixel is not affected and the original value is preserved.

The Lee adaptive filter tries to adapt to the image morphology with a set of predefined directional windows, which increase the contour and details preservation with respect to the multilook filter. However, the directional windows are fixed and the capabilities to adapt and preserve the the image morphology are very limited.

2.3.3 IDAN filter

As stated before, the Lee adaptive filter tries to adapt to the image morphology by defining a set of directional windows, having, then, a very limited adaptation capability in this sense. A new approach in the same direction is the Intensity Driven Adaptive Neighborhood (IDAN) [44] which estimates an arbitrary homogeneous neighborhood for each pixel. It defines an Adaptive Neighborhood (AN) around each pixel employing the Region Growing (RG) technique. Finally, the estimated covariance matrix $\mathbf{Z}$ is obtained by averaging all the pixels within the homogeneous neighborhood.

The adaptive neighborhood concept was introduced in [45] for applications employing medical images. For each pixel, called seed, a neighborhood is constructed employing the region growing process, having a variable shape and dimensions and containing only pixels with the same distribution than the seed. The seed is calculated by applying a median filter to the adjacent pixels to the pixel of interest [44]. The median filter is employed to avoid as much as possible the spatial resolution loss. The IDAN has the advantage of being able to achieve a stronger filtering and a better adaptation to the image structure than the Lee filter. However, since intensity SAR images are not following a symmetric distribution, as stated in Section 2.1.3, it introduces an important bias over the estimated values [46]. This bias makes impossible employing the IDAN filter for SAR applications employing quantitatively the estimated information.

The IDAN employs only the information contained in the diagonal elements of the coherence matrix

$$p(m,n) = \begin{bmatrix} T_{11}(m,n) \\ T_{22}(m,n) \\ T_{33}(m,n) \end{bmatrix} = \begin{bmatrix} p_1(m,n) \\ p_2(m,n) \\ p_3(m,n) \end{bmatrix} \tag{2.68}$$

where m and n are the coordinates of the image pixels.

Similarly to the Lee sigma filter [47], only are added to the AN the pixels differing less than two times the coefficient of variation (CV) from the seed. Consequently, the interval $\pm 2\sigma/\mu$ ensures that the AN population is significant. This process is iterated for each component until no more pixels can be added to the AN or a limit number of pixels is achieved

$$\frac{\|p_i(k,l) - \hat{p}_i(m,n)\|}{\|\hat{p}_i(m,n)\|} \leq 2\frac{\sigma}{\mu} \tag{2.69}$$

where $p_i(k,l)$ represents the pixel to add, $\hat{p}_i(m,n)$ refers to the seed value and the subindex i refers to each one of the three SAR intensity images, as defined in (2.68).

The CV σ/μ is a well-known parameter for SAR images, as shown on Section 2.1.3, and is theoretically constant for homogeneous areas, taking the value $1/\sqrt{L_{eq}}$, where L_{eq} is the number of independent pixels averaged.

As a refinement, to avoid the excessive enlargement of the AN and the inclusion of pixels having a different statistical distribution, the process of generating the AN has been divided into two steps. In the first step only are added the pixels having This process is iterated for each component until no more pixels can be added to the AN or a limit number of pixels is achieved

$$\frac{\|p_i(k,l) - \hat{p}_i(m,n)\|}{\|\hat{p}_i(m,n)\|} \leq \frac{2}{3}\frac{\sigma}{\mu} \tag{2.70}$$

and in the second step the pixels fulfilling (2.69) are added to the AN. However, on the second step only are evaluated the pixels that have been rejected previously by (2.70), which will be neighbors of some pixel of the AN.

Once the neighborhood for each pixel is known, then the covariance matrix can be estimated by averaging all the pixels within the AN or also applying the LLMMSE within the AN, as described in Section 2.3.2.

Fig. 2.6 shows an example of a PolSAR image and the results obtained after applying different speckle filters defined in this chapter. As it can be seen, Fig. 2.6a represents the original PolSAR image and the effect of the speckle noise can be seen as a granular texture over the image. On Fig. 2.6b the 7x7 Boxcar multilook filter has been applied and an important reduction of the speckle noise can be seen. However, all the contours and small details of the image appear blurred, resulting a spatial resolution loss. Figs. 2.6c and 2.6d show results after applying the adaptive Lee filter, defined in Section 2.3.2, and the IDAN filter, defined in this section. These filter achieve a relatively good speckle reduction while also maintain the spatial resolution better than the multilook filter. However, as it will be seen, they may introduce some bias or distortion over the filtered images.

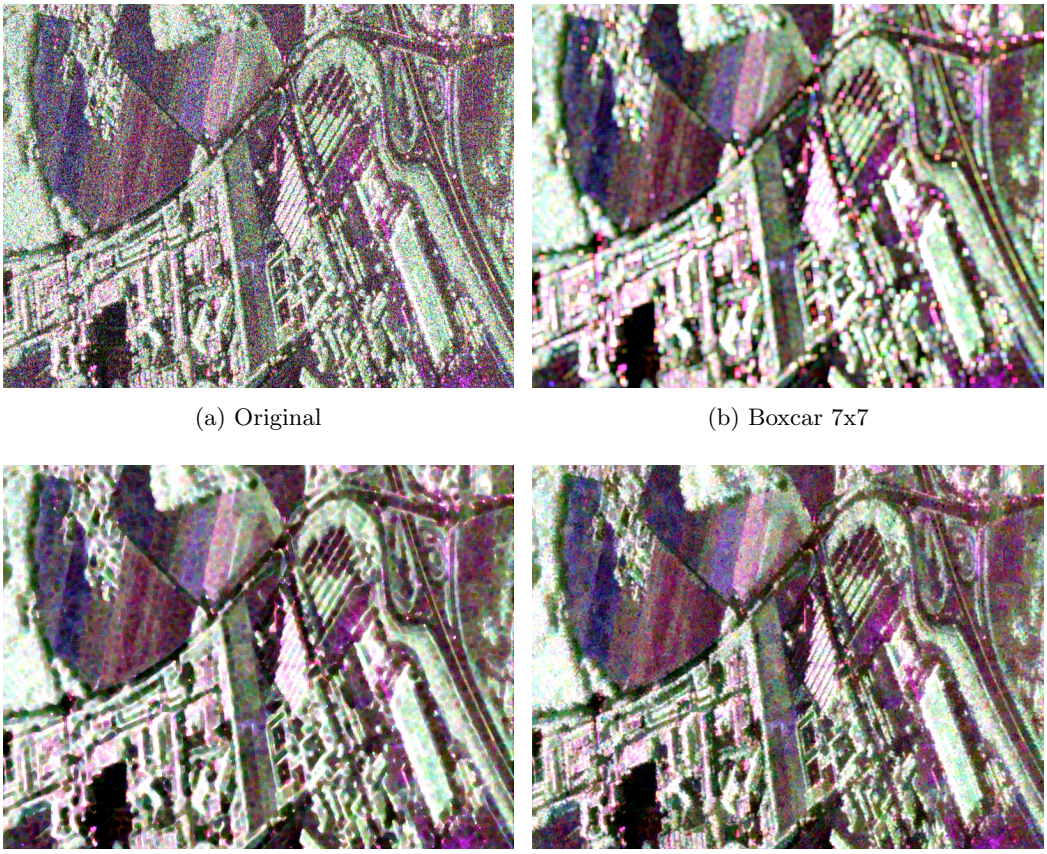

(a) Original (b) Boxcar 7x7

(c) Lee filter (d) IDAN filter

Figure 2.6: PolSAR images filtered employing different speckle filters. The Pauli vector $\mathbf{k}_{3P}$ is represented, assigning its components to the RGB channels ($|S_{hh} + S_{vv}|$, $|S_{hv} + S_{vh}|$, $|S_{hh} - S_{vv}|$)

Chapter 3

Binary Partition Tree representation

3.1 BPT hierarchical data representation

The Binary Partition Tree (BPT) was introduced in [48] as a hierarchical region-based image representation. In this manuscript, it will be presented as a general concept, concerning the generic term *data* instead of *image*.

A BPT is a region-based and multi-scale data representation. This representation contains all the information present in the original data plus additional information related to the data structure. This information is conformed by aggregated regions at different scales arranged into a hierarchical structure conforming a binary tree.

The BPT may be considered as an abstraction of the original data, making possible its analysis at different scales to find meaningful information that can be very difficult to extract by analyzing the data elements (e.g. the samples or pixels in a two dimensional image) individually.

In this context, a region will be considered as a *connected* area of a dataset. Consequently, a connectivity scheme has to be defined for every data element. Under this assumption, a connected region is a region on which any pair of data elements contained are connected through a path that lies completely within the region itself.

3.1.1 Graphs and trees

In Graph theory [49], a graph G is defined as a mathematical structure containing a set V of *vertices* or *nodes* and a set E of *edges* or *lines*, and it is denoted as $G = (V, E)$. The set of edges E contains 2-element subsets of V, since an edge is related with two nodes. In this work only *undirected* graphs will be employed, which means that the edges of the graph

do not have a particular direction and then, the set E can be defined as an unordered pair of vertices. Fig. 3.1 shown a representation of a simple graph with 4 vertices and 4 edges.

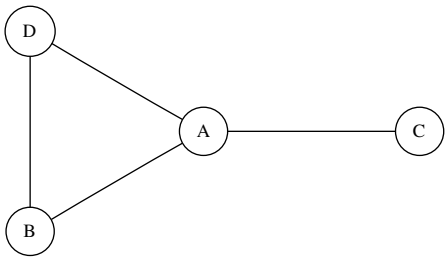

Figure 3.1: A graph $G = (V, E)$ representation with $V = \{A, B, C, D\}$ and $E = \{\{A, B\}, \{A, C\}, \{A, D\}, \{B, D\}\}$

A *weighted graph* is a graph having a value (the weight) associated with each edge. A representation of a wighted graph is presented in Fig. 3.2.

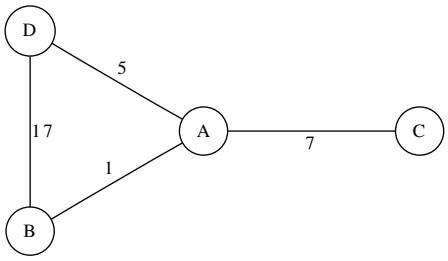

Figure 3.2: A weighted graph $G = (V, E)$ representation, having $V = \{A, B, C, D\}$ and $E = \{\{A, B, 1\}, \{A, C, 7\}, \{A, D, 5\}, \{B, D, 17\}\}$

A *tree* is a special case of graph, in which every two nodes are connected by *exactly one* path. This means that there are no cycles inside a tree, also known as closed paths, and that a tree is a connected graph, having a path that connects any pair of nodes. Typically, trees are represented hierarchically in a top-down scheme. Then, a *root* node has to be defined, which is represented on top of the drawing. Recursively, the nodes connected to each node are represented in a level below it and they are called its *sons*. The nodes of the tree having no sons are called *leaves*. Fig. 3.3 shows a representation of a tree with 4 leaves and 6 nodes.

Property 3.1. *A tree with n nodes has always $n - 1$ edges.*

A *binary tree* is a special case of tree having exactly 2 sons per node except for the tree leaves. In this case, the two sons can be named left and right sons. Fig. 3.4 represents a binary tree with 4 leaves $\{A, B, C, D\}$.

Property 3.2. *A binary tree with n leaves has $2n - 1$ nodes and, applying Property 3.1, $2n - 2$ edges.*

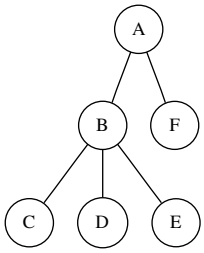

Figure 3.3: A tree representation having 4 leaves $\{C, D, E, F\}$. The root node A has 2 sons $\{B, F\}$ whereas the node B has 3 sons $\{C, D, E\}$

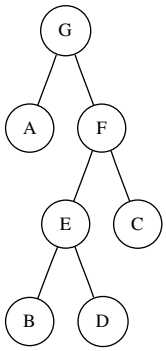

Figure 3.4: A binary tree representation

3.1.2 Binary Partition Tree

As stated before, a BPT is a hierarchical data representation. This representation is presented in form of a binary tree. Each node of the tree represents a region of the original data. The leaves of the tree represent each one of the original data elements whereas other nodes represent the merging of its two child nodes. Consequently, the root node of the tree represents the whole data. Between the leaves and the root nodes there are a wide number of nodes representing the data structure at different detail levels that can be exploited for different applications. Fig. 3.5 represents a BPT generated from a 4 elements $\{A, B, C, D\}$ dataset, corresponding to the tree leaves.

Note that the BPT is not balanced, and then regions with different sizes in terms of the original dataset elements contained are merged. In the Fig. 3.5 BPT representation this effect can be clearly seen by the fact that the leaves appear at different levels of the tree.

Since each node of the tree represents a region of the original data, a region model is introduced into every node. This region model should be complete enough to be able to represent properly all the regions within the tree, ranging from single element regions (the tree leaves) to the whole dataset (the root node). The definition of this region model can be an arduous task but, in fact, a good region model is essential to obtain a good BPT

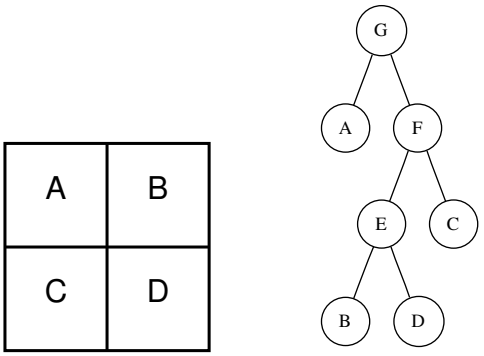

(a) Original data elements

(b) BPT representation

Figure 3.5: BPT representation of a dataset containing 4 elements $\{A, B, C, D\}$

data representation, as it will be seen on the following sections.

3.2 BPT construction process

In the previous section, the BPT data representation has been presented, but a construction process needs to be defined to generate a BPT from the original dataset, that is, generate the structure presented in Fig. 3.5b from Fig. 3.5a. To define an efficient construction algorithm an iterative approach is proposed by decomposing the whole process into small steps corresponding to the inclusion of one hierarchical relation. Then, there are two main approaches to construct the BPT structure in an iterative manner:

1. Focused on division, or *top-down* approach: at each construction step one region is divided into two smaller ones, becoming the child nodes of the original region. Note that these two regions must be connected and mutually disjoint to preserve the BPT structure as it has been defined previously. The process is started from the root node of the tree and ends when all the remaining regions are individual data elements, that is, the tree leaves.

2. Focused on fusion, or *bottom-up* approach: at each construction step two regions are merged conforming a new node of the tree which becomes their father. In this case, the two regions merged must be neighboring regions to form a connected region. This process starts from the tree leaves, that are the individual data elements of the dataset and ends when the root node is generated.

However, for computational reasons, it is more feasible to address a *bottom-up* tree construction algorithm since the number of possible different fusions is more limited than the number of possible different divisions for a given construction step. In fact,

an iterative BPT construction algorithm is defined in [48] in a bottom-up approach. The complete sequence of regions that are merged during the construction process is called *merging sequence*. For the example presented in Fig. 3.5 the complete merging sequence will contain the initial regions and the sequence of regions merged at each step: $(\{A, B, C, D\}, (B, D)|(E, C)|(A, F))$. Note that the final BPT generated is completely defined by the merging sequence.

A decision mechanism has to be defined to choose which two regions have to be merged at each step. Since the ultimate goal is to represent within the BPT regions containing data elements with similar structure, a *similarity criterion* is proposed. Then, at each step, the two most similar regions are merged [48]. This measure is the centerpiece of the tree construction process since it will define the merging sequence and then, the final BPT representation generated.

A similarity-based measure d has to be defined on the region model space $d : X \times X \mapsto \Re$, where X represents the region model space. A mathematical distance on X can be employed as a similarity-based measure for the construction process, merging at each step the pair of regions A and B having the minimum distance, expressed as $d(A, B)$. However, for the construction process, only the ordering defined over the neighboring regions is relevant, not the value of the measure itself, since two measures producing the same merging sequence will produce the same BPT. Then, the mathematical properties of d can be relaxed and, in the following, it will be called *dissimilarity measure*, as a more general concept. The required properties for a dissimilarity measure d are [50]:

1. $d(A, B) \geq d_0$ (generalized non-negativity)
2. $d(A, B) = d_0 \Leftrightarrow A = B$ (identity of indiscernibles)
3. $d(A, B) = d(B, A)$ (symmetry)

All the information about each data element neighborhood can be expressed in a Region Adjacency Graph (RAG). In this graph every node represents a data element and each edge represents a neighboring relation. This information can be enriched by the dissimilarity measure value over each edge of the graph, conforming a Weighted Region Adjacency Graph (WRAG). For every two neighboring data elements A and B, an edge is added to the weighted graph, with the dissimilarity measure value $d(A, B)$ over the two nodes, as shown in Fig. 3.6.

Algorithm 3.1 describe an algorithm to construct the WRAG $\mathbf{W}$ from the original dataset $\mathbf{D}$. Note that a neighborhood has to be defined for each element of the dataset.

When the WRAG has been generated, the proposed BPT construction algorithm in [48] can be applied. At each step, the edge e with minimum weight of the WRAG $\mathbf{W}$ is selected

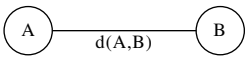

Figure 3.6: Weighted Region Adjacency Graph. An edge is added for every neighboring relation weighted by the dissimilarity measure

Algorithm 3.1 WRAG generation algorithm

Require: dataset **D**, dissimilarity measure d

Ensure: WRAG **W** is generated

```
for each elem i ∈ data_elems(D) do
    I ← create_node(i)
    add_node(W, I)
    for each node K ∈ neighborhood(I) do
        e ← create_weighted_edge(I, K, d(I, K))
        add_edge(W, e)
    end for
end for
```

and its two end nodes, A and B, are merged. The father node F is added to the BPT **B** and the edges to its child nodes. At this point, **W** has to be updated to represent the new state; the two nodes merged, A and B, are removed and the father F is added. Additionally, all the edges involving A and B have to be removed and replaced with the updated edges towards the new region F. Finally, this process is repeated until no more edges are contained in **W**.

The complete sequence of states for the described algorithm during the BPT construction of the Fig. 3.5 is represented in Fig. 3.7 for the Algorithm 3.2. The BPT **B** structure, the WRAG **W** and the remaining regions over the original dataset are shown for each iteration. Over **W** the edge with the minimum weight is colored in blue. The nodes corresponding to this edge are the regions merged at each step.

3.3 BPT pruning

On the previous section, the BPT has been defined as a representation of the original data. The idea is to tackle a large number of data processing applications by performing an initial step of abstraction from the original dataset, which contains a wide number of data elements, making difficult its direct interpretation. This abstraction step is performed by computing the BPT representation of the data which makes possible the data interpretation at different scales. This process has been detailed in Section 3.2. Note that this abstraction step depends only on the dataset itself and, thus, it is completely application

Algorithm 3.2 BPT construction algorithm

Require: WRAG $\mathbf{W}$, dissimilarity measure d

Ensure: BPT $\mathbf{B}$ is constructed

1: $\mathbf{B} \leftarrow \emptyset$
2: **for each** node $K \in$ nodes($\mathbf{W}$) **do** {Initialize $\mathbf{B}$}
3: add_node($\mathbf{B}$, K)
4: **end for**
5: **while** edges($\mathbf{W}$) $\neq \emptyset$ **do** {begin BPT construction}
6: $e \leftarrow$ min(edges($\mathbf{W}$))
7: $A, B \leftarrow$ nodes(e)
8: $F \leftarrow$ merge(A, B)
9: add_node($\mathbf{W}, F$)
10: **for each** node $K \in$ neighbors($\mathbf{W}$, A) $\cup$ neighbors($\mathbf{W}$, B) **do**
11: $n \leftarrow$ create_weighted_edge(F, K, $d(F, K)$)
12: add_edge($\mathbf{W}$, n)
13: **end for**
14: remove_nodes($\mathbf{W}, \{A, B\}$)
15: remove_edges($\mathbf{W}$, edges_from(A) $\cup$ edges_from(B))
16: add_node($\mathbf{B}, F$)
17: $l \leftarrow$ create_edge(F, A)
18: $r \leftarrow$ create_edge(F, B)
19: add_edge($\mathbf{B}$, l)
20: add_edge($\mathbf{B}$, r)
21: **end while**

independent.

Once we have the BPT data abstraction, we need to exploit this representation to extract useful information for a specific application. BPT exploitation can be challenging since its internal structure is larger and more complex than the structure of the original dataset. However, it also contains a large amount of additional information related with the data structure at different detail levels, which is an opportunity to develop more complex applications or to improve existing ones. Nonetheless, all the BPT structure is arranged hierarchically, making easier its navigation and interpretation and empowering the use of efficient algorithms for its exploitation.

In this manuscript, the BPT exploitation will be based on a BPT pruning process [48]. This process can be seen as a data simplification, by removing some branches of the tree that represent small details of the data that are not interesting for the particular

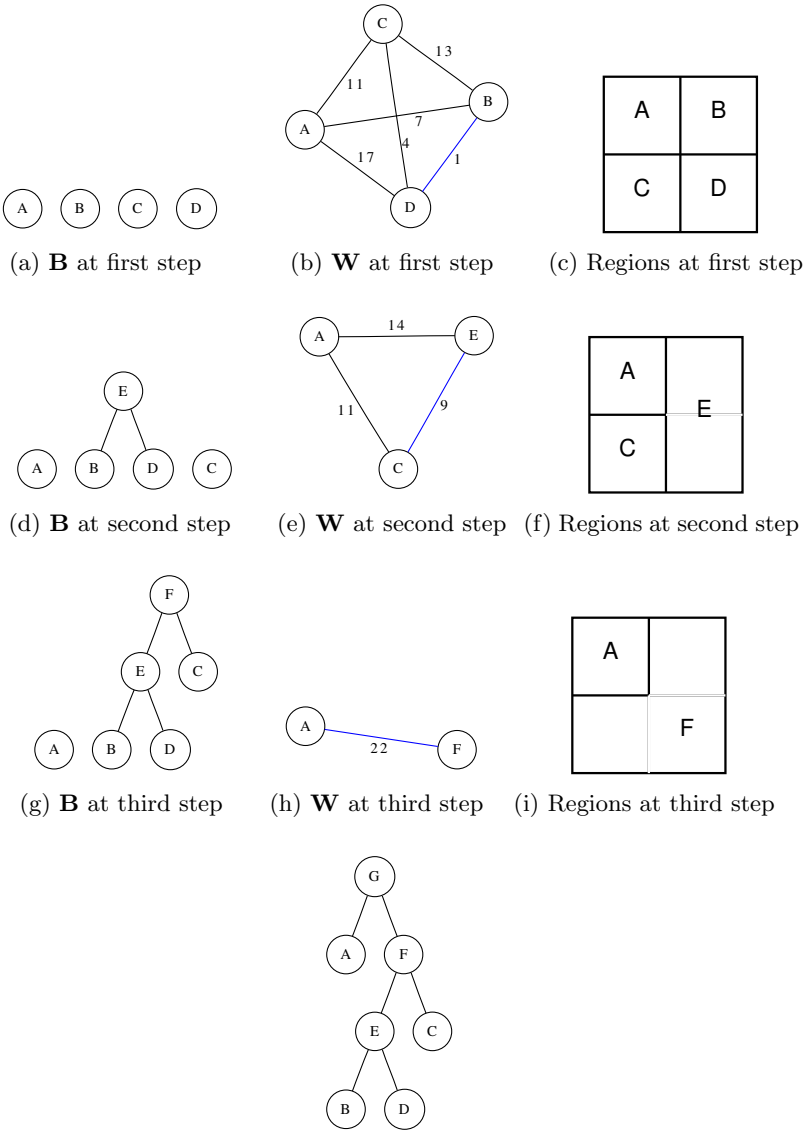

(a) **B** at first step (b) **W** at first step (c) Regions at first step

(d) **B** at second step (e) **W** at second step (f) Regions at second step

(g) **B** at third step (h) **W** at third step (i) Regions at third step

(j) Final BPT **B** generated

Figure 3.7: BPT construction process step-by-step. WRAG and regions for each step is also represented. The edge for the two most similar regions is colored in blue

application. On the other hand, it can also be seen as a node selection of the tree; the useful regions for our application are extracted from the tree.

Note that the BPT pruning process is completely application dependent, as opposed to the BPT construction process. Then, the BPT data representation has to be generated only once, and this abstraction can be employed multiple times for different applications by applying different pruning strategies.

To apply a BPT pruning some pruning criterion, denoted as Υ, has to be defined. This criterion can be evaluated for every region of the BPT, which will be fulfilled for *interesting*

regions and not fulfilled otherwise. The BPT pruning process, then, will select each node A from the tree if $\Upsilon(A)$ is fulfilled. Strictly speaking, to conform a valid tree pruning, that is, the resulting graph is also a binary tree, only the biggest regions from each tree branch that fulfill Υ will be selected. Consequently, within a node A selected from a BPT pruning process can be other regions that fulfill Υ but region A is not contained within any bigger region B that fulfills $\Upsilon(B)$.

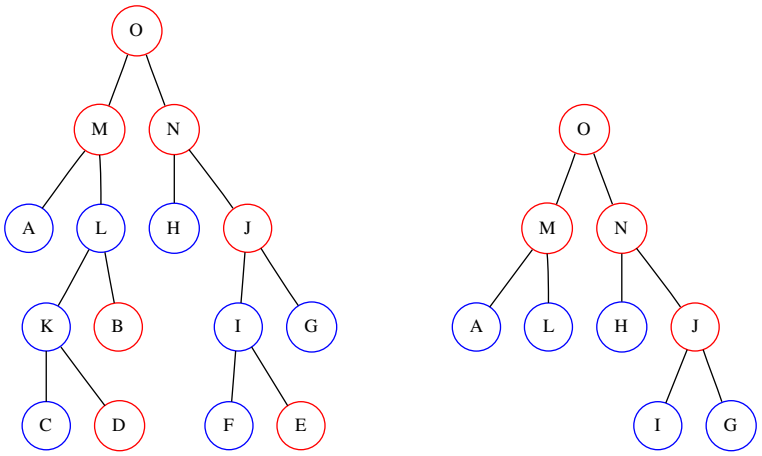

(a) Original BPT (b) Pruned BPT

Figure 3.8: BPT pruning process. Nodes that fulfill Υ are colored in blue whereas nodes that not fulfill it are colored in red

Fig. 3.8 shows an example of BPT pruning. The nodes that fulfill the pruning criterion Υ are colored in blue, whereas the nodes that not fulfill Υ are colored in red. As it can be seen, inside a node (for example L) can be different nodes than fulfill Υ or not but, to conform a valid tree pruning, only the biggest regions that fulfill Υ are selected, as shown in Fig. 3.8b.

An algorithm to achieve this behavior can be efficiently implemented in a top-down approach. Starting from the root R of the tree, the pruning criterion Υ is checked for every node A. If $\Upsilon(A)$ is fulfilled the subtree below node A is pruned. If $\Upsilon(A)$ is not fulfilled, then its two child nodes are checked. An implementation of this algorithm is presented in Algorithm 3.3. The set of nodes to check are stored in $\mathbf{Q}$ whereas the nodes found that fulfill Υ are stored in the set Θ. This set of pruned regions Θ fulfilling Υ corresponds to the leaves of the pruned tree. For the example presented in Fig. 3.8 the Algorithm 3.3 will compute $\Theta = \{A, L, H, I, G\}$.

Note that a BPT pruning process is closely related with a data segmentation, as stated in [48]. In fact, the set of pruned regions Θ generated by Algorithm 3.3 conforms a data segmentation that can be governed by the pruning criterion Υ.

Algorithm 3.3 BPT pruning algorithm

Require: BPT completely generated with root R, pruning criteria Υ

Ensure: The set Θ contains the pruned regions

1: $\Theta \leftarrow \emptyset$
2: $\mathbf{Q} \leftarrow \{R\}$
3: **while** $\mathbf{Q} \neq \emptyset$ **do**
4: $K \leftarrow$ get_and_remove_first_node($\mathbf{Q}$)
5: **if** $\Upsilon(K)$ **or** is_leaf(K) **then**
6: $\Theta \leftarrow \Theta \cup \{K\}$
7: **else**
8: $A, B \leftarrow$ sons(K)
9: $\mathbf{Q} \leftarrow \mathbf{Q} \cup \{A, B\}$
10: **end if**
11: **end while**

3.4 Data processing scheme based on BPT

The previous sections have described the BPT representation as a data abstraction, have defined an iterative algorithm to generate this representation and have presented the BPT pruning as a simple mechanism to exploit the BPT structure. In this section, the whole scheme for a BPT-based application is outlined and a first analysis of the complexity [51] of the presented algorithms is described.

The generic BPT-based processing scheme is presented in Fig. 3.9. As mentioned before, the first step is to generate a Weighted RAG from the original data elements. This step can be computed by the WRAG generation algorithm, described in Algorithm 3.1.

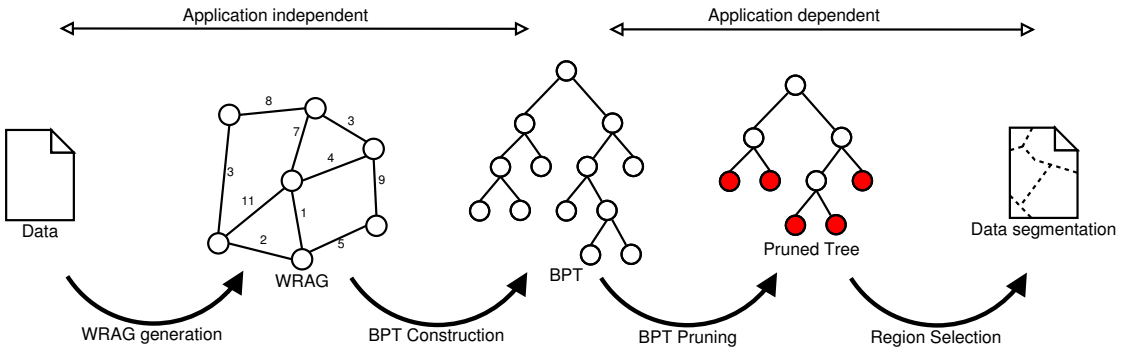

Figure 3.9: Typical BPT-based processing scheme, where a data segmentation is obtained. Note that the whole BPT generation process is application independent, whereas the BPT exploitation is application dependent

To be able to apply Algorithm 3.1, it is assumed that the original data can be decomposed into individual data elements and that a neighborhood can be defined over them. This term can also be referred as the *element connectivity*. The regions represented within the BPT structure will be connected regions based on this element connectivity.

Algorithm 3.1 is a generation algorithm, containing only statements to create iteratively all the nodes and edges of the WRAG $\mathbf{W}$. Assuming $\mathbf{W} = (\mathbf{V_W}, \mathbf{E_W})$, where $\mathbf{V_W}$ and $\mathbf{E_W}$ represent the set of nodes and edges of $\mathbf{W}$, respectively, the complexity of the algorithm should be in the order

$$O(|\mathbf{V_W}| + |\mathbf{E_W}|) \tag{3.1}$$

where $|\mathbf{S}|$ represent the number of elements into the set $\mathbf{S}$. Note that the cost of computing the dissimilarity measure d has been assumed to be constant.

The number of nodes in $\mathbf{W}$, $|\mathbf{V_W}|$ is directly the number of elements n within the dataset. On the other hand, the number of edges $|\mathbf{E_W}|$ depends on the element connectivity defined. However, it can be assumed that, generally, the number of neighbors for each data element does not depend on the dataset size, since it is a local property of each data element. Then, the number of edges $|\mathbf{E_W}|$ can be assumed as a constant factor k on the number of edges $|\mathbf{E_W}| = k|\mathbf{V_W}| = kn$, and the complexity of the WRAG generation Algorithm 3.1 can be expressed as

$$O\left((k+1)|\mathbf{V_W}|\right) = O\left((k+1)n\right) \equiv O(n) \tag{3.2}$$

being linear on the number of data elements present on the dataset.

The next step on the processing chain presented in Fig. 3.9 is the BPT construction. The proposed Algorithm 3.2 to construct a BPT representation is an iterative algorithm that adds a new node to the BPT $\mathbf{B}$ at each iteration. The initialization of the BPT $\mathbf{B}$ (lines 1-4) has a linear cost with the number of data elements $O(n)$. By applying Property 3.2 it can be easily seen that the number of iterations computed by the algorithm are $n-1$. However, inside the BPT construction main loop, lines 5-21, there is an inner loop iterating over the neighbors of the two nodes A, B being merged. On the best case, the total number of iterations will be a constant factor p of the number of iterations, and then the total cost of Algorithm 3.2 will be

$$O\left(n + (p+1)(n-1)\right) \equiv O(n) \tag{3.3}$$

which is also linear with the number of data elements. It has been assumed that all the operations within the BPT construction loop can be executed in constant time, including region merging and graph updates.

However, within this loop the minimum edge of **W** is selected, which suggests that the edges of this graph have to be stored within some sorted structure. Unfortunately, there is no sorted structure having, at the same time, constant cost for finding the minimum value and for insertion-deletion operations. Consequently, some of the operations within the main loop can not be implemented with constant cost. This will lead to a logarithmic factor on the number of edges in **W** and the cost will be:

$$O\left(n + (p+1)(n-1)log(kn)\right) \equiv O(n\ log\ n) \tag{3.4}$$

The BPT pruning process, as described in Algorithm 3.3, at most traverses all the BPT **B** nodes. If the pruning criteria Υ can be computed in constant time, the maximum complexity of this algorithm will be equivalent to the number of nodes in **B**, that is $2n-1$

$$O\left(2n-1\right) \equiv O(n) \tag{3.5}$$

which is again a linear cost on the number of data elements from the dataset.

The last step represented in Fig. 3.9 represents a node selection over the pruned tree and its interpretation over the original dataset. In the proposed processing scheme it corresponds to the selection of the leafs of the pruned tree, represented in red color, which represent a data segmentation over the original dataset, as stated before.

As it can be seen, the BPT construction is the most computational expensive step of the chain. Fortunately, this is an application independent process, since it depends only on the data itself, not on the application. As a consequence, the BPT construction needs to be computed only once. When it is generated, the same BPT can be exploited for different applications, through different pruning processes, for example.

Chapter 4

PolSAR data BPT Representation

In the previous section, the BPT has been presented as a region-based and multi-scale data representation. It may be seen as a data abstraction that can be employed to extract useful information about data structure. As mentioned in Section 3.4, the BPT based processing scheme can be separated basically into two steps: the BPT construction and its exploitation.

As mentioned in Chapter 2, SAR images are strongly non-stationarity, as they reflect the complexity of the scene. In this case, a BPT PolSAR image abstraction can be very useful to identify homogeneous regions at different scales.

In this chapter, the generic BPT data representation presented in Chapter 3 will be adapted to the concrete case of PolSAR images [52] [53] [54] [55]. All the elements needed to be able to construct a PolSAR image BPT representation by employing Algorithm 3.1 and Algorithm 3.2 will be defined in the following sections.

4.1 Connectivity for PolSAR images

When dealing with PolSAR data, an image will be considered as a dataset and then, each pixel of the image will be considered as a data element. The first concept that has to be defined is the data connectivity or, in this case, the *pixel connectivity*. This decision will define the shape of the regions represented within the BPT, since they will be connected regions under the defined pixel connectivity.

Typically, in image processing two types of pixel connectivity are employed: 4-connectivity and 8-connectivity, depending on the number of neighbors per pixel. They are represented on Fig. 4.1. The 4-connectivity scheme, Fig. 4.1a, has the advantage of being simpler.

However, the fact that diagonal pixels are not neighbors imposes a limitation on the possible connected regions represented by the BPT, since diagonal thin structures can not be represented because their pixels are not connected. In this work, an 8-connectivity scheme will be assumed, as represented in Fig. 4.1b, in order to avoid this limitation.

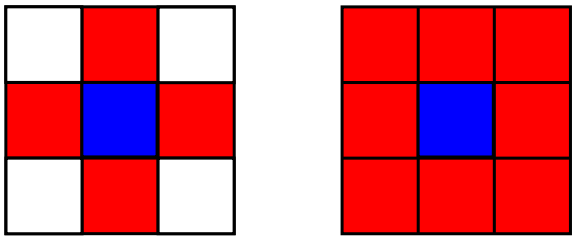

(a) 4-connectivity (b) 8-connectivity

Figure 4.1: Possible pixel connectivity schemes for a PolSAR image. Every image pixel, in blue, has 4 or 8 neighbors, represented in red

4.2 Region model for PolSAR data

As mentioned in Section 3.1 each node of the BPT represents a region of the image with a region model. A region model has to be selected capable of representing PolSAR image regions. In Section 2.2, the structure and distribution of PolSAR data has been described. Since it is affected by the speckle term, an statistical model is needed to represent a region.

Assuming the complex Gaussian scattering model, as presented in Section 2.2, an homogeneous region can be completely defined by its complex covariance matrix $\mathbf{C}$. Then, an appropriate region model for a given region A will be estimated covariance matrix $\mathbf{Z}$ [52] [53]

$$\mathbf{Z} = \langle \mathbf{k}\mathbf{k}^H \rangle_{n_A} = \frac{1}{n_A} \sum_{i \in A} \mathbf{k}_i \mathbf{k}_i^H \tag{4.1}$$

where n_A represents the number of pixels within region A. Note that this equation is very similar to the one defined in (2.46), the only difference is that the average is computed over the pixels within region A.

The estimated covariance matrix $\mathbf{Z}$ is a good region model to characterize an homogeneous region of a PolSAR image, as described before. Unfortunately, this can not be always true for all the nodes of the BPT, since it contains regions of the image at different scales. The root node of the tree, for example, contains all the PolSAR image that, probably, can not be properly represented by its estimated covariance matrix $\mathbf{Z}$.

In this manuscript, the estimated covariance matrix $\mathbf{Z}$, as defined in (4.1), will be employed. This decision will have a negative effect on the upper nodes of the tree, that is, the nodes closer to the root, that are strongly non-homogeneous. However, as it will be

seen, if the applications for which this BPT representation will be employed are looking for homogeneous regions over the tree, then the impact of this decision can be negligible, since these regions can be appropriately modeled with $\mathbf{Z}$.

Moreover, the estimated covariance matrix $\mathbf{Z}$ (4.1) has an additional inconvenient. When calculating it over the single pixels i of the original PolSAR image, the resulting covariance matrix $\mathbf{Z}_i$ is rank-deficient. In fact, this issue will affect all the regions A of the tree containing a number of pixels n_A smaller than the covariance matrix $\mathbf{Z}$ size. This circumstance can be a problem for some dissimilarity measures, resulting in the need for an initial filtering process to get full rank covariance matrices as region models for the individual pixels.

4.3 Dissimilarity measures

Once a region model has been selected to represent the regions of the PolSAR data, a dissimilarity measure d has to be defined over the region model space. The dissimilarity measure is the keystone of the BPT construction process. It defines completely the data representation obtained and, depending on its ability to measure the similarity between different regions, the resulting BPT will be able to represent and extract useful information of the original dataset correctly.

Note that the dissimilarity measure is tied to the region model employed, in this case the estimated covariance matrix $\mathbf{Z}$. Consequently, as stated in the previous section, all the limitations of this model representing the different regions will be transfered to the dissimilarity measure. In this case, the dissimilarity measure will not be capable to evaluate properly the similarity of strongly non-homogeneous regions, since they are not accurately characterized.

Additionally, the estimated covariance matrix $\mathbf{Z}$ can be rank-deficient, which could be a problem for some dissimilarity measures, as mentioned previously. In this direction, the dissimilarity measures will be divided into two types: measures employing the full covariance matrix $\mathbf{Z}$ and measures employing only the diagonal elements of $\mathbf{Z}$ [52] [53]

1. Dissimilarity measures employing the full covariance matrix $\mathbf{Z}$ have the advantage of being sensitive to the complete polarimetric information, under the complex Gaussian model assumption. This will lead to a more precise and powerful dissimilarity measure. However, these measures need to have all the elements of the estimated covariance matrix well defined, that is, they need full-rank matrices. As stated before, this will lead to the need for an initial filtering of the data which also may result in a resolution loss.

2. On the other hand, the dissimilarity measures that employ only the diagonal elements do not need an initial filtering. They can deal properly with rank-deficient matrices eliminating the need for an initial filtering. On the contrary, these dissimilarity measures can not employ all the polarimetric information, since they are ignoring the off-diagonal elements of $\mathbf{Z}$, resulting in a poorer estimation of the similarity between regions than the full matrix measures. Mathematically, they are assuming uncorrelated data since all off-diagonal elements are assumed to be 0.

4.3.1 Full-matrix dissimilarities

This section will present some dissimilarity measures that employ the full estimated covariance matrix $\mathbf{Z}$. Then, it will be assumed that for two nodes A, B they have the estimated covariance matrices $\mathbf{Z}_A, \mathbf{Z}_B$ that are full-rank matrices.

- Symmetric revised Wishart dissimilarity d_{sw}. This dissimilarity measure, defined in [52] is based on a statistical test assuming a Wishart probability distribution [56] over the estimated covariance matrix. It assumes that the two region models follow a Wishart pdf and that one of them is known. Then, it tests if the other can be considered as a realization of the same distribution. The problem of this measure d_w itself is that it is not symmetric, since it depends on which region is assumed to have the known distribution. Hence, a modified symmetric version d_{sw} is obtained by applying $d_{sw}(A,B) = d_w(A,B) + d_w(B,A)$ and by introducing a term depending on the region size

$$d_{sw}(A,B) = \left(tr(\mathbf{Z}_A^{-1}\mathbf{Z}_B) + tr(\mathbf{Z}_B^{-1}\mathbf{Z}_A)\right)(n_A + n_B) \tag{4.2}$$

  where $tr(.)$ denotes the matrix trace and n_A denotes the number of pixels within the region A.

- Geodesic dissimilarity d_{sg}, defined in [53], is following a completely different approach. It is based on the positive definite matrix cone geometry [57], that is, the geometry of the region model space. It measures the distance over the geodesic path, instead of the euclidean path, that follow the curvature of the matrix cone space. A modified version is generated by adding a term depending on the region size

$$d_{sg}(A,B) = \|log\left(\mathbf{Z}_A^{-1/2}\mathbf{Z}_B\mathbf{Z}_A^{-1/2}\right)\|_F + ln\left(\frac{2n_An_B}{n_A+n_B}\right) \tag{4.3}$$

  where $\|.\|_F$ represents the Frobenius matrix norm, $log(.)$ represents the matrix logarithm and $ln(.)$ represents the natural logarithm.

- Ward relative dissimilarity d_{wr}, from Ward hierarchical clustering [58]. An error measure based on the error sum-of-squares (ESS) was introduced to quantify the amount of information loss when two clusters are joined. This measure can also be used to measure the information loss when merging two neighboring regions. A normalization matrix is introduced to tackle the multiplicative nature of the speckle noise. Then, the Ward relative dissimilarity measure is defined as

$$d_{wr}(A,B) = n_A \cdot \|\mathbf{N}_{AB}^H(\mathbf{Z}_A - \mathbf{Z}_{AB})\mathbf{N}_{AB}\|_F^2 + n_B \cdot \|\mathbf{N}_{AB}^H(\mathbf{Z}_B - \mathbf{Z}_{AB})\mathbf{N}_{AB}\|_F^2 \quad (4.4)$$

  where $\mathbf{Z}_{AB}$ denotes the covariance matrix of the region $A \cup B$, $\mathbf{A}^H$ denotes matrix $\mathbf{A}$ hermitian transpose, $\mathbf{N}_A$ denotes the normalization matrix of $\mathbf{Z}_A$, defined as

$$\mathbf{N}_A = \begin{pmatrix} \sqrt{Z_{A11}} & 0 & 0 \\ 0 & \sqrt{Z_{A22}} & 0 \\ 0 & 0 & \sqrt{Z_{A33}} \end{pmatrix}, \quad (4.5)$$

  and $\|\mathbf{A}\|_F$ denotes the Frobenius matrix norm.

The term depending on the region sizes is required since during the BPT construction regions of different sizes will be compared. The idea represented by this term is that it is assumed that bigger regions will have less noisy estimations of the region model and then, the dissimilarity over them may be more restrictive than with smaller regions.

To understand the geodesic dissimilarity d_{sg} approach, an example with a simplified space is presented to show its adaptation to the space geometry. The real symmetric 2 by 2 covariance matrix space will be assumed to be able to represent it graphically

$$\mathbf{C} = \begin{bmatrix} C_{11} & \sqrt{C_{11}C_{22}}\rho \\ \sqrt{C_{11}C_{22}}\rho & C_{22} \end{bmatrix} \quad (4.6)$$

where $-1 \leq \rho \leq 1$ represent the correlation coefficient. Note that the real covariance matrices are symmetric and, then, its three independent components C_{11}, C_{12}, C_{22} can be represented graphically. This space is represented in Fig. 4.2. As it can be seen, the space is confined within a cone, conforming the positive definite matrix cone.

To see the adaptation of the geodesic dissimilarity d_{sg} to this space, it will be compared with the euclidean distance $\|\mathbf{Z}_A - \mathbf{Z}_B\|_F$. In the following, only the first term of (4.3), $\|log\left(\mathbf{Z}_A^{-1/2}\mathbf{Z}_B\mathbf{Z}_A^{-1/2}\right)\|_F$, corresponding to the dissimilarity of the covariance matrix, will be employed. The term corresponding to the region sizes will be ignored since in this example we are comparing only covariance matrices, not regions of the image.

The euclidean path γ_e, which length is measured by the euclidean distance, can be defined as

$$\gamma_e(t) = \mathbf{Z}_A + t(\mathbf{Z}_B - \mathbf{Z}_A) \quad (4.7)$$

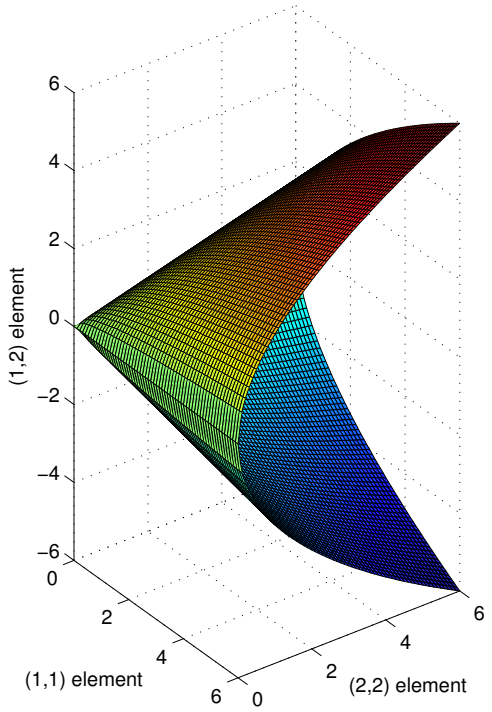

Figure 4.2: The 2 by 2 real symmetric covariance matrix space cone

with $0 \leq t \leq 1$.

On the other hand, according to [57], the geodesic path γ_g is defined by

$$\gamma_g(t) = \mathbf{Z}_A^{\frac{1}{2}} \left(\mathbf{Z}_A^{-\frac{1}{2}} \mathbf{Z}_B \mathbf{Z}_A^{-\frac{1}{2}} \right)^t \mathbf{Z}_A^{\frac{1}{2}} \tag{4.8}$$

for $0 \leq t \leq 1$.

As an example, assuming the values for $\mathbf{Z}_A$ and $\mathbf{Z}_B$

$$\mathbf{Z}_A = \begin{bmatrix} 2 & -1 \\ -1 & 1 \end{bmatrix}, \quad \mathbf{Z}_B = \begin{bmatrix} 1 & 1 \\ 1 & 2 \end{bmatrix} \tag{4.9}$$

then the euclidean path γ_e and geodesic path γ_g are represented in Fig. 4.3, in black and magenta colors, respectively. The plot over the original space is presented in Fig. 4.3a over the positive definite matrix cone bounds. As it can be seen, the euclidean path γ_e follows a straight line from $\mathbf{Z}_A$ to $\mathbf{Z}_B$ but the geodesic path γ_g is following a curved line adapted to the positive definite matrix cone. Since the geodesic dissimilarity d_{sg} is based on the Frobenius norm in the logarithmic space, the euclidean and geodesic paths γ_e γ_g have been represented also in this space in Fig. 4.3b. Note that, as mentioned before, the logarithm applied is the matrix logarithm, not the logarithm to each element of the

matrix individually. In this space, the bounds of the positive definite matrix cone can not be represented since when an eigenvalue tends to 0 the matrix logarithm tend its elements to infinity. Then, the positive definite matrix cone is unbounded in the logarithmic space. As it can be seen in Fig. 4.3b, in the logarithmic space the euclidean path γ_e appears as a curved line whereas the geodesic path develop a straight line behavior.

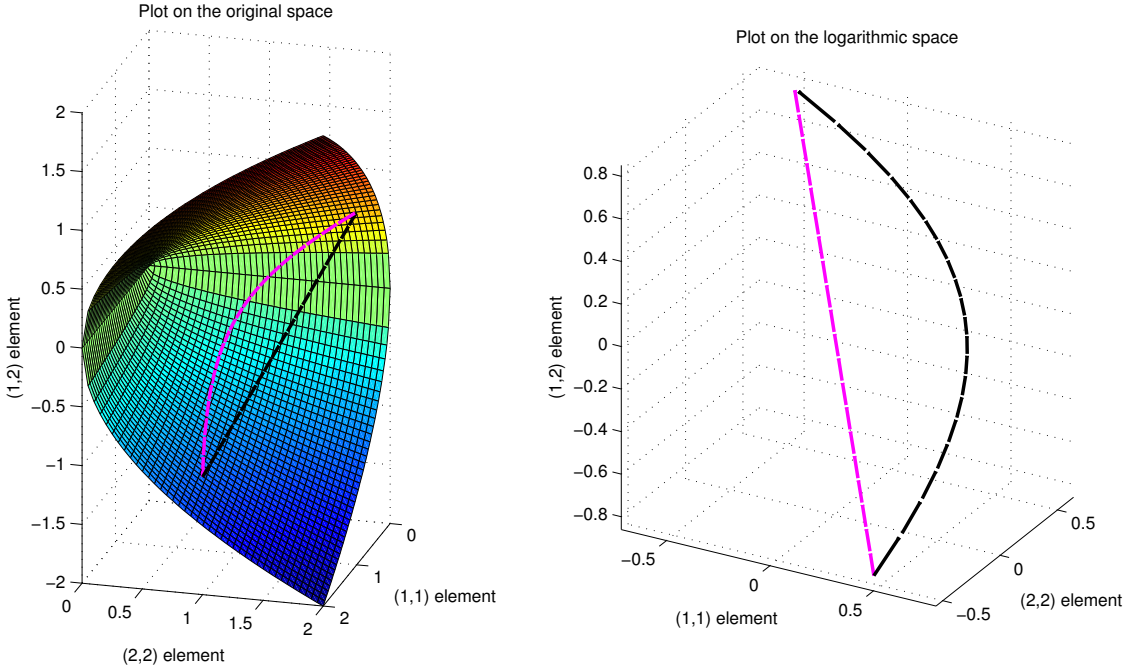

(a) Original space

(b) Logarithmic space

Figure 4.3: Euclidean (black) and geodesic (magenta) paths over the original and logarithmic spaces

4.3.2 Diagonal dissimilarities

The dissimilarity measures presented in this section will employ only the elements in the diagonal of the covariance matrix. The proposed measures are the same measures presented in Section 4.3.1 but assuming that all the off-diagonal elements equal to 0, that is, they are assuming uncorrelated data.

- Diagonal revised Wishart dissimilarity d_{dw} is the same measure as (4.2) but assuming that $\mathbf{Z}_A$ and $\mathbf{Z}_B$ are diagonal N by N matrices

$$d_{dw}(A,B) = \left(\sum_{i=1}^{N} \left(\frac{Z_{Aii}^2 + Z_{Bii}^2}{Z_{Aii} Z_{Bii}} \right) \right) \cdot (n_A + n_B) \tag{4.10}$$

  where Z_{Aij} and Z_{Bij} represent the (i,j)-th element of the estimated covariance matrices $\mathbf{Z}_A$ and $\mathbf{Z}_B$, respectively.

- Diagonal geodesic dissimilarity d_{dg}, as for the d_{dw} case, is based on (4.3) but assuming that $\mathbf{Z}_A$ and $\mathbf{Z}_B$ are diagonal N by N matrices

$$d_{dg}(A,B) = \sqrt{\sum_{i=1}^{N} ln^2\left(\frac{Z_{Aii}}{Z_{Bii}}\right)} + ln\left(\frac{2n_An_B}{n_A+n_B}\right) \tag{4.11}$$

The fact that full matrix and diagonal dissimilarity measures are based on the same principles will be very useful when comparing the benefit of employing the full matrix information to employing only the diagonal information, assuming that all off-diagonal elements equal to 0.

Additionally, the following diagonal dissimilarities can be defined, based on a relative comparison of the matrix diagonal elements.

- Diagonal relative normalized dissimilarity d_{dn} is based on the euclidean norm of the normalized difference of the matrix diagonal vector. Then, the difference of the diagonal vectors is normalized by their sum, which results in a result bounded in the interval $[-1,1]$ for each diagonal element. The d_{dn} dissimilarity measure is obtained as the euclidean norm of the resulting vector. Finally, a term depending on the region size is added

$$d_{dn}(A,B) = \left(\sum_{i=1}^{N}\left(\frac{Z_{Aii}-Z_{Bii}}{Z_{Aii}+Z_{Bii}}\right)^2\right)^{1/2} \cdot (n_A+n_B). \tag{4.12}$$

- Diagonal relative dissimilarity d_{dr}, computed as the euclidean norm of the sum of relative errors respect to to both regions. Note that this comparison, as opposite to d_{dn} is not bounded, taking values on the interval $[0,\infty)$. A term depending on the region size is also added

$$\begin{aligned} d_{dr}(A,B) &= \left(\sum_{i=1}^{N}\left(\frac{Z_{Aii}-Z_{Bii}}{Z_{Bii}}+\frac{Z_{Bii}-Z_{Aii}}{Z_{Aii}}\right)^2\right)^{1/2} \cdot (n_A+n_B) \\ &= \left(\sum_{i=1}^{N}\left(\frac{(Z_{Aii}-Z_{Bii})^2}{Z_{Aii}Z_{Bii}}\right)^2\right)^{1/2} \cdot (n_A+n_B). \end{aligned} \tag{4.13}$$

Chapter 5

PolSAR BPT-based applications

The previous chapter has defined all the necessary elements to generate a BPT representation from a PolSAR image. At this point, a BPT can be generated by applying the processes and algorithms described in Chapter 3. Now, some BPT exploitation mechanism will be described for different applications. Note that, as stated in Chapter 3, the whole BPT construction process is application independent and, thus, the same applies for all the concepts defined in the previous chapter. On the contrary, the concepts introduced in this chapter are focused on one concrete application and then, this Chapter is divided into different subsections according to different applications.

In this Chapter some applications that exploit the BPT will be described: speckle filtering and coastline segmentation. The speckle filtering application will be analyzed in detail, defining different pruning methods and criteria and testing them with real and simulated data. Finally, the coastline segmentation application will be described briefly. As it will be seen, the two mentioned applications are completely different and they will exploit distinct information contained within the same BPT.

5.1 Speckle filtering

SAR images are corrupted by the speckle noise and, due to its multiplicative nature, it makes SAR image processing difficult. This effect is caused by the coherent essence of radar images and it has been analyzed in detail in Chapter 2. Usually, any process of information extraction from PolSAR data needs some speckle filtering. The main problem for filtering over these data is that it is strongly non-homogeneous. Some state-of-the-art techniques, refer to Section 2.3, tend to define an homogeneous neighborhood around a

given pixel to avoid mixing non-homogeneous data.

As mentioned in Chapter 3, the BPT is a region-based and multi-scale data representation. This representation may be useful to identify homogeneous regions over the PolSAR image and to be able to apply a speckle filtering without mixing non-homogeneous pixels. Two BPT pruning processes are defined in the following sections, attempting to extract homogeneous regions over the image. When the image is segmented into its homogeneous regions, the filtering application comes out easily, since all the pixels within each region can be represented by the estimated covariance matrix over the whole region that, indeed, corresponds to the region model.

5.1.1 BPT pruning based on the number of regions

The first approach to extract homogeneous regions from the BPT is to extract a fixed number N of regions corresponding to the N *most different* regions from the tree. To apply this criterion, a measure needs to be defined to evaluate how different are two given regions. However, as stated in Chapter 3, the dissimilarity measure is employed exactly for this purpose and then, the same dissimilarity measure d employed for the BPT construction process can be employed for pruning.

Note that when the same dissimilarity measure is employed for BPT construction and for this tree pruning then, it is equivalent to construct the BPT up to a given number of regions N is achieved. Then, there is no need to generate the full BPT nor to apply the pruning process defined in Section 3.3, which may result in a faster processing chain. However, if different tree pruning processes will be done over the same tree, or it will be employed for different applications, then generating the full BPT only once may be faster.

Fig. 5.1 and Fig. 5.2 show examples of a 256 by 256 pixel PolSAR image crops, corresponding to some agricultural fields and an urban area, respectively, processed with the 9x9 multilook and the mentioned BPT pruning based on the number of regions. Data, acquired by the DLRs ESAR system at L-band, will be presented in detail in the following sections devoted to analyze the obtained results in detail. Fig. 5.1a and Fig. 5.2a present the original data crop whereas Fig. 5.1c to Fig. 5.1e and Fig. 5.2c to Fig. 5.2e show the results for different number of regions N. As mentioned before, each region has been represented with its estimated covariance matrix employing a Pauli RGB composition. For the BPT construction process and, hence, for the pruning process, the geodesic dissimilarity measure d_{sg} described in (4.3) has been employed. Note that, since the d_{sg} measure is employing the full covariance matrix information, an initial filtering is needed. In this case, an initial 3 by 3 multilook filtering has been employed.

As it can be seen in Fig. 5.1 and Fig. 5.2, the contour preservation of BPT processed images is much better than with the 9x9 multilook. Since it is a region-based filtering, the

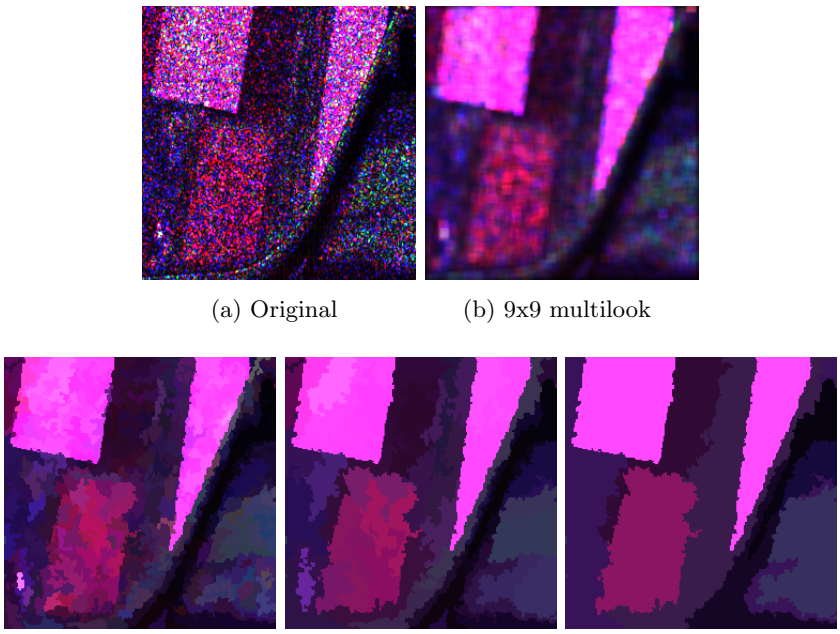

(a) Original (b) 9x9 multilook

(c) $N = 250$ (d) $N = 50$ (e) $N = 10$

Figure 5.1: 9x9 multilook and BPT pruning based on the number of regions of an agricultural fields image for different values of N. The BPT has been constructed employing the geodesic d_{sg} dissimilarity. Images are represented using Pauli RGB composition ($|S_{hh} + S_{vv}|$, $|S_{hv} + S_{vh}|$, $|S_{hh} - S_{vv}|$)

region edges appear perfectly clear, instead of blurred, as for the multilook filter, which is a linear filtering. Additionally, the regions obtained from the BPT respect the main contours of the original image, unless the fixed number of regions N is established too small. Increasing the number of regions N results in smaller regions and more details of the original image preserved. However, it is difficult to establish the optimal N for the images and this number will be completely different for images presented in Fig. 5.1a and Fig. 5.2a since the urban environment is much more complex.

Fig. 5.3 presents the region size histograms for the pruned regions in the results shown in Fig. 5.1 and Fig. 5.2, for the number of regions $N = 250$ and $N = 50$. Analyzing the differences between the two environments, it can be seen that the dynamic range of the pruned region sizes is much more narrow in the agricultural area than in the urban area, mainly because the difference in complexity of both scenes. Additionally, it can be seen that the region sizes obtained are very dependent on the pruning parameter N. For $N = 250$ the maximum region size density for agricultural area is between 150-400 pixels, with around 80% of total regions, whereas for $N = 50$ only 8% of regions are within these values. One would expect that, since the structure of the image is the same, those values should be more similar for both cases. However, the underlying problem is that

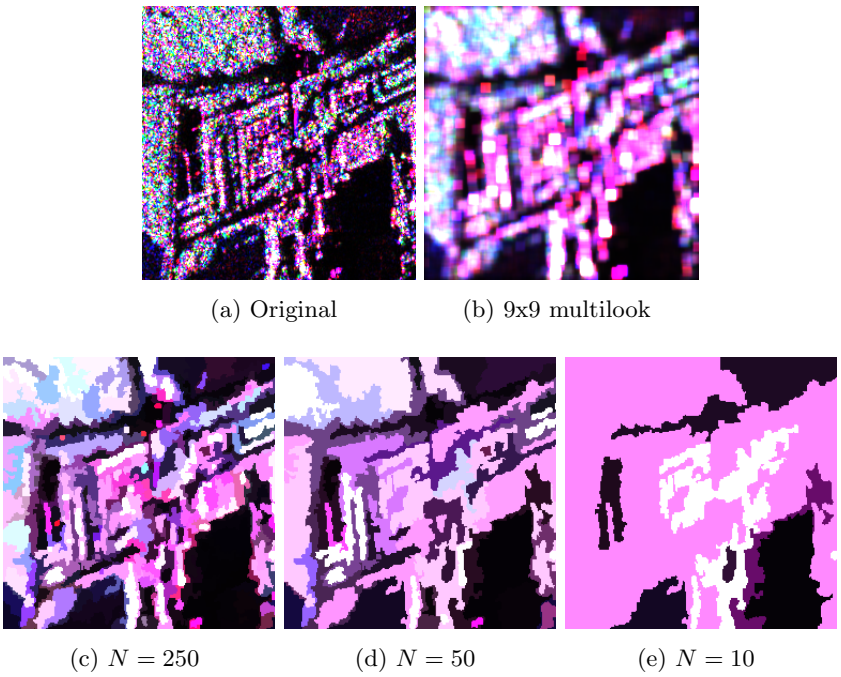

(a) Original (b) 9x9 multilook

(c) $N = 250$ (d) $N = 50$ (e) $N = 10$

Figure 5.2: 9x9 multilook and BPT pruning based on the number of regions of an urban image for different values of N. The BPT has been constructed employing the geodesic d_{sg} dissimilarity. Images are represented using Pauli RGB composition ($|S_{hh} + S_{vv}|$, $|S_{hv} + S_{vh}|$, $|S_{hh} - S_{vv}|$)

the number of regions is highly dependent on the image structure and then, it can not be used as a pruning parameter when we want to obtain a segmentation that adapts to this image structure.

	Agricultural zone			Urban zone		
Number of regions N	250	50	10	250	50	10
Minimum region size	44	157	1693	1	45	45
Maximum region size	570	2539	12094	918	4948	40430

Table 5.1: Pruned regions and region sizes in pixels over urban and agricultural areas for BPT pruning based on the number of regions with different N

The BPT pruning based on the number of regions has the advantage that it does not need to introduce any new criteria, since the same dissimilarity measure employed for the BPT construction is applied for tree pruning. Additionally, as stated before, it can be simpler and faster if it is generated by stopping the BPT construction process when N regions are achieved. On the other hand, fixing the number of regions N is its major drawback, since this factor is strongly dependent on the image structure and it is not easy to find a priori. Additionally, as shown in Section 4.3, the dissimilarity measures have a strong dependence with the region sizes and thus, it will be difficult to obtain in the

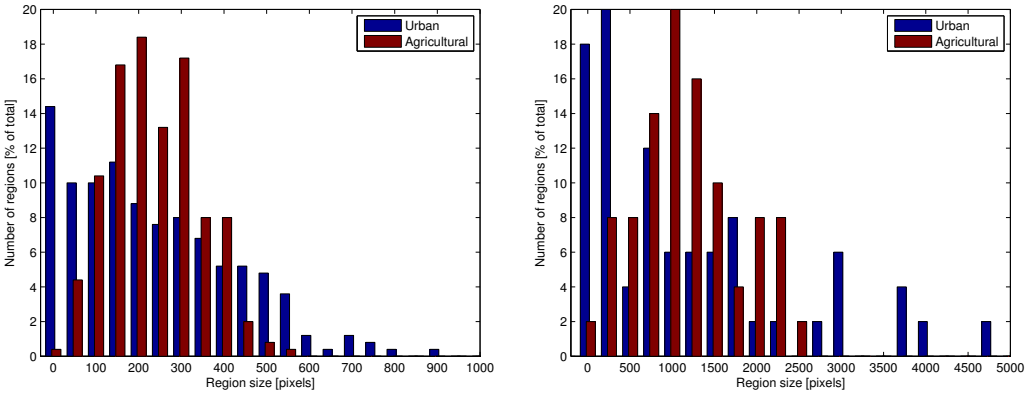

(a) $N = 250$ (b) $N = 50$

Figure 5.3: Region size histograms for $N = 250$ and $N = 50$ over agricultural and urban area images presented in Fig. 5.1 and Fig. 5.2

same image regions with substantially different sizes, even if the original data presents this structure.

Moreover, note that the dissimilarity measure employed for BPT construction is based only on the region model. If it is also applied for BPT pruning then the pruning accuracy will depend on the accuracy of the model to represent properly the region pixels. As mentioned in Section 4.2, the estimated covariance matrix $\mathbf{Z}$ defined in (4.1) is a good model only for homogeneous regions, which means that the BPT pruning based on the number of regions may not perform properly when N is small enough to obtain inhomogeneous regions.

5.1.2 Homogeneity based pruning

The BPT pruning based on the number of regions has been defined in Section 5.1.1 and some of its important drawbacks have been described. In order to overcome its inconveniences, the following guidelines should be accomplished

1. The pruning factor should be completely independent of the image structure, to avoid the trouble of defining a different value for each image.

2. The pruning criterion should be independent of the region size, making possible that regions with completely different sizes appear at the same tree pruning.

3. The pruning criterion should depend on all the pixel values contained within the region, not only on the region model, to mitigate the problems induced when the region model can not represent properly the whole region.

A new BPT pruning criterion Υ_h is introduced based on the region homogeneity to overcome the problems of the pruning based on the number of regions. Then, a homogeneity measure ϕ has to be defined to asses the homogeneity of a given node A. The biggest nodes of the tree being more homogeneous than a given threshold δ_p will be pruned. Note that, in this case, the BPT pruning Algorithm 3.3 should be used and it can not be simplified to avoid the whole BPT construction, since both processes have nothing in common. Consequently, it can be slower than the BPT pruning based on the number of regions.

According to the previously defined guidelines, the following homogeneity measure ϕ is defined

$$\phi(A) = \frac{1}{n_A} \sum_{i \in A} \frac{\|\mathbf{Z}^i - \mathbf{Z}_A\|_F^2}{\|\mathbf{Z}_A\|_F^2} \tag{5.1}$$

where $\mathbf{Z}^i$ represents the covariance matrix of pixel i within region A, $\mathbf{Z}_A$ represent its estimated covariance matrix and n_A its total number of pixels.

Note that (5.1) measures the homogeneity of a given region A, being independent of the image structure and, since it is an average on all the pixels within the region A, it does not depend on the region size or on the region model only. Then, this homogeneity measure ϕ is following the previously defined guidelines.

The homogeneity measure ϕ can also be viewed as the relative Mean Squared Error (MSE) when representing a region A by its model $\mathbf{Z}_A$. The only difference with the traditional MSE is that it is divided by the squared norm of the region model $\|\mathbf{Z}_A\|_F^2$. This normalization is needed due to the multiplicative nature of the speckle noise.

The region homogeneity pruning criterion Υ_h can be defined, then, as the test for a region having a homogeneity measure ϕ below the pruning factor δ_p

$$\Upsilon_h(A): \quad \phi(A) < \delta_p. \tag{5.2}$$

Usually, the pruning factor δ_p is expressed in dB, corresponding to the pruning criterion

$$\Upsilon_h(A): \quad 10 \cdot log_{10}\left(\phi(A)\right) < \delta_p(dB). \tag{5.3}$$

Notice that employing this new pruning criteria Υ_h the number of pruned regions will be automatically established. For complex images the number of regions will be higher since all the regions pruned have to accomplish the pruning criteria (5.3).

Fig. 5.4 and Fig. 5.5 show the same images presented in Fig. 5.1a and Fig. 5.2a, corresponding to agricultural and urban areas, respectively, filtered employing the defined region homogeneity based pruning for different pruning factors δ_p.

As it can be seen, by comparing Fig. 5.4 and Fig. 5.5, employing the region homogeneity based pruning, with Fig. 5.1 and Fig. 5.2, employing the pruning based on the number of regions, the region sizes over an agricultural area can take more different values. Note

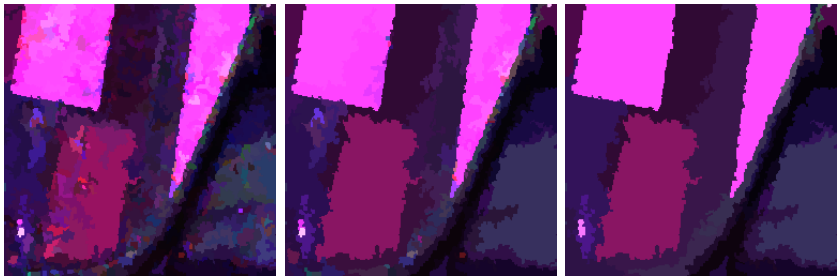

(a) $\delta_p = -2dB$ (b) $\delta_p = -1dB$ (c) $\delta_p = 0dB$

Figure 5.4: BPT homogeneity based pruning of an agricultural fields image for different values of δ_p. The BPT has been constructed employing the geodesic d_{sg} dissimilarity. Images are represented using Pauli RGB composition ($|S_{hh} + S_{vv}|$, $|S_{hv} + S_{vh}|$, $|S_{hh} - S_{vv}|$)

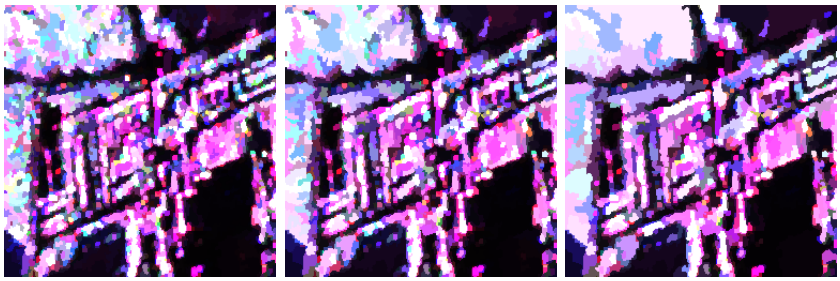

(a) $\delta_p = -2dB$ (b) $\delta_p = -1dB$ (c) $\delta_p = 0dB$

Figure 5.5: BPT homogeneity based pruning of an urban area image for different values of δ_p. The BPT has been constructed employing the geodesic d_{sg} dissimilarity. Images are represented using Pauli RGB composition ($|S_{hh} + S_{vv}|$, $|S_{hv} + S_{vh}|$, $|S_{hh} - S_{vv}|$)

the small details on the bottom part of the image whereas big regions are obtained inside the agricultural fields. Additionally, with the same pruning parameter values, the urban area can be filtered preserving all the small details. To show this feature numerically, Table 5.2 represents the number of regions and the region size dynamic range for each pruning processes.

	Agricultural zone			Urban zone		
δ_p	$-2dB$	$-1dB$	$0dB$	$-2dB$	$-1dB$	$0dB$
Number of regions	502	116	32	2652	1696	1043
Minimum region size	2	4	11	1	1	1
Maximum region size	3602	8697	8698	898	1403	3052

Table 5.2: Pruned regions and region sizes in pixels over urban and agricultural areas for homogeneity based pruning with different pruning thresholds δ_p

Analyzing Table 5.2, the number of regions over the urban area is much higher than over the agricultural area. This is needed to obtain homogeneous regions having a similar relative MSE (5.1) in both cases, since the structure of the urban area is much more complex. Additionally, when comparing Table 5.2 with Table 5.1, the region size dynamic range obtained is much higher than with number of regions based pruning, since the homogeneity measure ϕ is independent on the region size.

Fig. 5.6 presents the region size histograms for different pruning thresholds δ_p over agricultural and urban areas. It is worth to notice that for urban area, Fig. 5.6a, the maximum density of region sizes is around 20 pixels for all the pruning factor values whereas for the agricultural area, Fig. 5.6b, this value is around 100 pixels, but it is also maintained for different δ_p values.

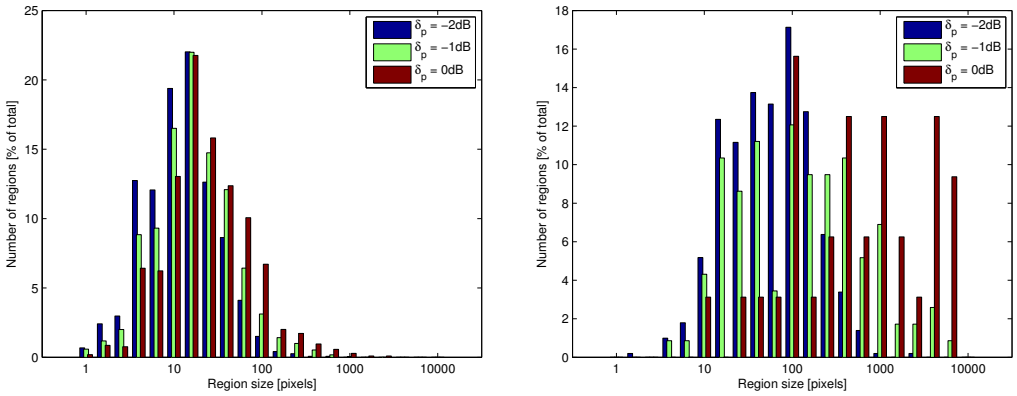

(a) Urban area

(b) Agricultural area

Figure 5.6: Region size histograms for agricultural and urban area images presented in Fig. 5.1 and Fig. 5.2 with different pruning factors δ_p

The BPT homogeneity based pruning can improve all the disadvantages of the pruning based of the number of regions. It can obtain a wider range of region sizes since it is independent of the region size, generating bigger regions over homogeneous areas of the image while, at the same time, it preserves the small details of the image. It does not depend on the image complexity or size; fixing a pruning factor δ_p it will obtain the bigger homogeneous regions that fulfill the pruning criterion (5.3). Additionally, it ensures that the pruned nodes represent regions having a relative MSE below a given factor δ_p. On the other hand, its main inconvenience of being more complex, since the full BPT construction is needed, is not a major drawback when different pruning strategies are needed over the same tree, since the BPT construction only has to be computed once. Note that the same concept applies to the region homogeneity values $\phi(A)$ for each node A of the tree.

An important point is that all the images presented in Fig. 5.2c to Fig. 5.2e and Fig. 5.5a to Fig. 5.5c are generated from the same BPT through different pruning thresholds and consequently, all this information is represented within the same BPT structure of the urban area image (the BPT generated employing the d_{sg} dissimilarity measure, 8-connectivity and the estimated covariance matrix $\mathbf{Z}$ as the region model, as described previously in Chapter 4). The same can be applied to Fig. 5.1c to Fig. 5.1e and Fig. 5.4a to Fig. 5.4c of the agricultural area. This can give an idea of the amount of information present within a PolSAR image BPT representation and its usefulness.

5.1.3 Results with real data

In this section, the proposed BPT-based speckle filtering schemes will be analyzed in detail with two real datasets, corresponding to two different Polarimetric SAR sensors: the ESAR airborne system and the RADARSAT-2 spaceborne system.

The first dataset corresponds to a measuring campaign conducted by DLR in 1999 with its experimental ESAR system over the Oberpfaffenhofen test-site, southern Germany. Data were collected at L-band, with a spatial resolution of 1.5m x 1.5m in fully polarimetric mode. The whole image has 2816 rows by 1540 columns and its Pauli RGB image is presented in Fig. 5.7a.

Fig. 5.7b presents the filtered image obtained by applying the defined BPT region homogeneity based pruning with a pruning factor $\delta_p = -2dB$ over a BPT constructed employing the revised Wishart d_{sw} dissimilarity, defined in (4.2). As it can be seen, qualitatively the colors of the original image are maintained whereas the level of noise is strongly reduced. The contours and the small details of the original image are preserved and, due to the speckle filtering effect, they appear more clear in Fig. 5.7b.

The previous dataset has been processed, for comparison purposes, with a 7x7 multilook as a reference, the IDAN[1] [44] filter, and the discussed BPT pruning approaches: pruning based on the number of regions and region homogeneity based pruning. To perform a more detailed analysis of the filtering techniques, they will be studied over a 512 by 512 pixel crop of the full dataset, presented in Fig. 5.8a. The selected area contains large agricultural fields at the bottom part of the image and a urban area with small details in the center and right parts. Additionally, a forest area can be found at the top part of the image. Fig. 5.8b and Fig. 5.8c present the same area filtered with the multilook and IDAN filters, respectively.

The multilook filter can achieve a good speckle filtering results, however its spatial resolution loss may be important, blurring the contours and enlarging point scatters to

[1]The PolSARPro [59] IDAN implementation has been employed for this work, with a maximum window size parameter of 100 pixels.

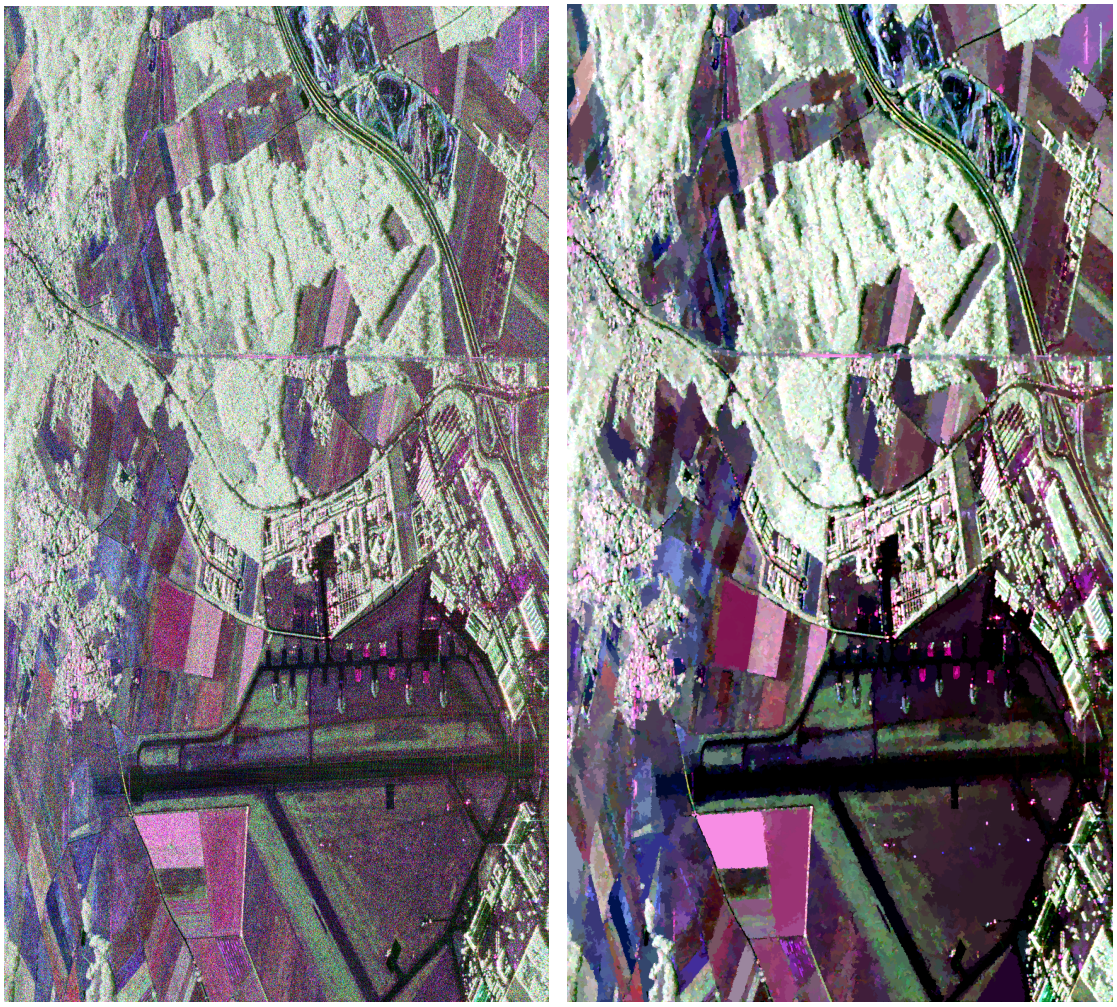

(a) Original (b) $d_{sw}, \delta_p = -2dB$

Figure 5.7: Pauli original and BPT-based filtered images of Oberpfaffenhofen. The revised Wishart dissimilarity measure d_{sw} has been employed for BPT construction and region homogeneity based pruning with $\delta_p = -2dB$ ($|S_{hh} + S_{vv}|$, $|S_{hv} + S_{vh}|$, $|S_{hh} - S_{vv}|$)

the window size. On the other hand, the IDAN filter has a very good spatial resolution preservation both in contours and in point scatters. However, the amount of speckle reduction achieved by the IDAN filter is smaller when compared to the multilook filter.

Fig. 5.9 shows results over the same area processed with the BPT approach. The figures on the left column (Figs. 5.9a, 5.9c, 5.9e) correspond to BPT pruning based on the number of regions[2] whereas the right column (Figs. 5.9b, 5.9d, 5.9f) show results of region homogeneity based pruning. All the images have been generated by pruning over the

[2]Note that the results are shown over a detailed area of 512 by 512 pixel, but the whole image, presented in Fig. 5.7a is processed. Then, the number of regions N refers to the whole image, and only a small subsets of regions appear over the crop shown.

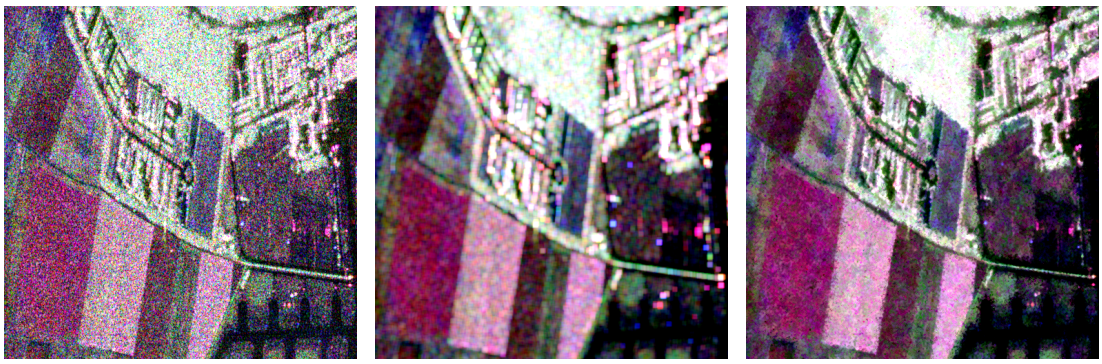

(a) Original (b) 7x7 multilook (c) IDAN

Figure 5.8: Detail Pauli RGB images. (a) Original, (b) filtered with 7x7 multilook and (c) filtered with IDAN ($|S_{hh} + S_{vv}|$, $|S_{hv} + S_{vh}|$, $|S_{hh} - S_{vv}|$)

same BPT, constructed with the revised Wishart d_{sw} dissimilarity over the whole image, presented in Fig. 5.7a.

The BPT-based speckle filtering results, shown in Fig. 5.9, exhibit their ability to achieve strong filtering over large homogeneous areas, for example in the agricultural fields on the bottom part of the image. It can achieve stronger filtering than the multilook while also preserving the field contours. The same effect can be observed over the forest zone, where large filtering can be attained. Additionally, the small details of the urban area are preserved, specially with the region homogeneity based pruning, obtaining within the same image regions with very different sizes. It can be seen also the effect of the pruning factor for both pruning criteria. When decreasing the number of regions N or increasing the homogeneity threshold δ_p larger regions appear over the image. Note that, when increasing δ_p or decreasing N, the pruned regions change, but no new contours appear, since within the BPT structure the new regions are always generated by merging of two smaller ones.

Fig. 5.9 also shows the differences between the two pruning criteria defined. When comparing both BPT pruning strategies, the disadvantages mentioned in Section 5.1.1 of the pruning based on the number of regions appear clearer when processing the whole dataset. It can be seen that it is not possible to fix an appropriate number of regions N to obtain in the same image all the small details of the urban area and large regions over the agricultural fields. This drawback is produced by the strong dependence of the dissimilarity measures with the region sizes, which is necessary for a good BPT construction but makes them not suitable as pruning criteria. The homogeneity based pruning can adapt better to the spatial information and obtain regions with very different sizes, ensuring that they have a relative MSE below the pruning factor δ_p.

To show the ability of the region homogeneity based pruning to preserve small details

(a) $d_{sw}, N = 50000$ (b) $d_{sw}, \delta_p = -2dB$

(c) $d_{sw}, N = 10000$ (d) $d_{sw}, \delta_p = -1dB$

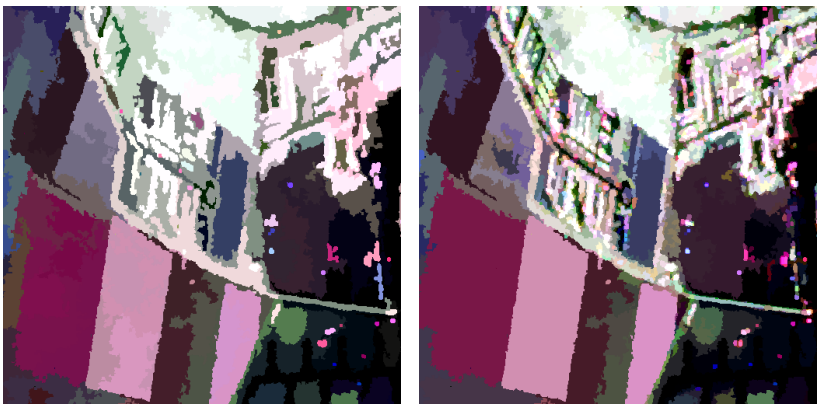

(e) $d_{sw}, N = 2000$ (f) $d_{sw}, \delta_p = 0dB$

Figure 5.9: Detail Pauli RGB images. (a), (c), (e) filtered with pruning based on the number of regions and (b), (d), (f) filtered with region homogeneity based pruning ($|S_{hh} + S_{vv}|$, $|S_{hv} + S_{vh}|$, $|S_{hh} - S_{vv}|$)

of the original image and, at the same time, perform strong filtering over homogeneous areas, an image crop containing five corner reflectors over an homogeneous field, near to the main runway of the airport, is processed with different filtering techniques. The results

are shown in Fig. 5.10.

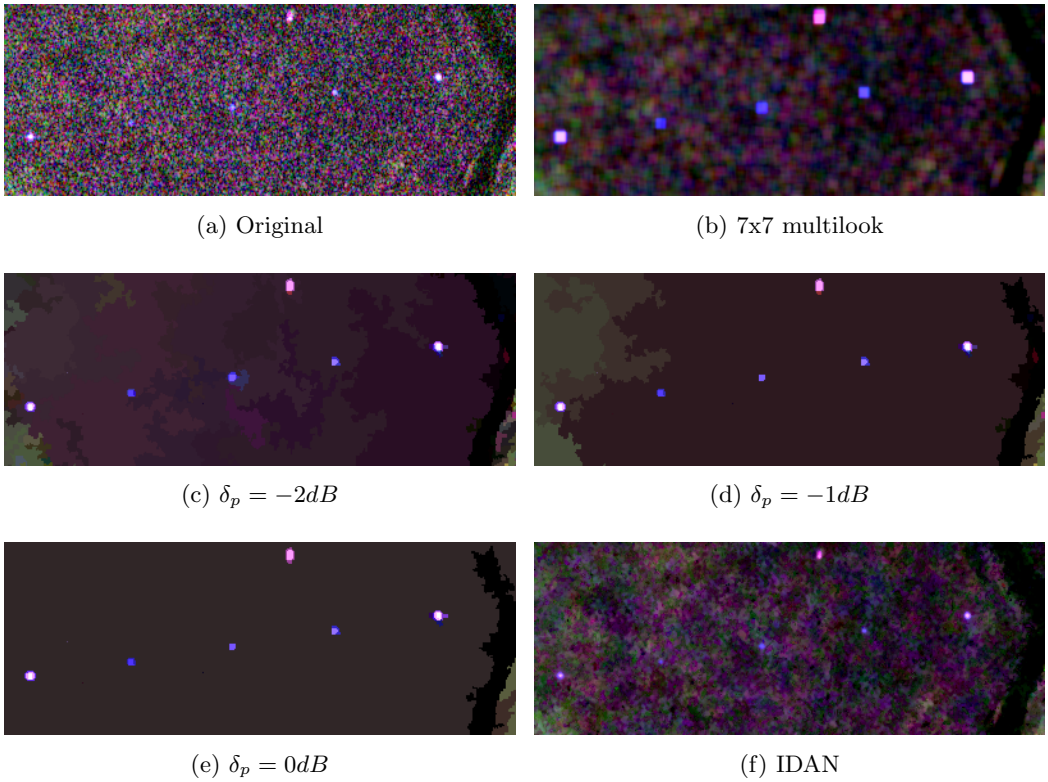

(a) Original (b) 7x7 multilook

(c) $\delta_p = -2dB$ (d) $\delta_p = -1dB$

(e) $\delta_p = 0dB$ (f) IDAN

Figure 5.10: Detail Pauli RGB images of corner reflectors preservation ($|S_{hh} + S_{vv}|$, $|S_{hv} + S_{vh}|$, $|S_{hh} - S_{vv}|$)

The original crop image is shown in Fig. 5.10a, where the corner reflectors appear as small bright dots. When processing the image with the 7x7 multilook filter, presented in Fig. 5.10b, the corner reflectors appear more clear but, due to the spatial resolution loss, they appear enlarged with the multilook window shape. The IDAN filter has a better spatial resolution preservation, Fig. 5.10f, maintaining the original shape of the corner reflectors. However, the amount of speckle filtering over the field is lower, when compared with the multilook. BPT-based filtering is presented in Figs. 5.10c to 5.10e. The region homogeneity based pruning has been employed over the previously BPT generated with the revised Wishart d_{sw} dissimilarity (4.2). As it can be seen, the corner reflectors are preserved, almost with the same shape as in the original image, for all the values of δ_p presented. The level of filtering on the field changes, from $\delta_p = -2dB$ where some regions are detected inside showing its internal structure, to $\delta_p = 0dB$ where a big region covers the whole field. Note that the level of filtering attained is then, much higher with the BPT-based approach than with the other presented speckle filtering techniques, resulting in a better estimation of the polarimetric information. This example illustrates the ability of the region homogeneity based pruning to extract regions with very different sizes from

within the tree, adapting to the data structure and preserving small details.

Fig. 5.11 shows different results obtained pruning different BPTs with the same pruning mechanism: the region homogeneity based pruning with a pruning factor $\delta_p = 0dB$. The BPTs have been constructed employing different dissimilarities defined in Section 4.3 over the original image Fig. 5.7a. An initial 3x3 multilook has been employed to be able to apply the full matrix dissimilarities, as described before. Again, instead of representing the full image, the 512x512 crop image presented in Fig. 5.8a is shown.

Although the BPTs have been constructed employing different dissimilarity measures during the construction process, similar regions are obtained corresponding to the same agricultural fields and representing the urban structure. This results can give an idea of robustness of the BPT construction process respect to the dissimilarity measure employed. Different dissimilarities have been employed, with completely different approaches; ones are based on a statistical test, others on the covariance matrix cone geometry; ones employing the full covariance matrix, others only the diagonal information and the regions obtained seem to adapt qualitatively to the image structure in all the cases. A more detailed analysis of the results is much more complex by the absence of ground truth, but in Section 5.1.4 a more detailed analysis will be done with simulated data to overcome this inconvenience.

The morphology of the pruned trees for different dissimilarity measures are presented in Fig. 5.12. However, to obtain a small enough tree to be representable, instead of the full image, a small crop has been processed corresponding to an area of agricultural fields, presented in Fig. 5.1a. As in the previous example, all the trees have been pruned employing the region homogeneity based pruning with $\delta_p = 0$. The pruned nodes are colored in green if they are tree leaves, that is, single pixels of the image, or in red otherwise.

The task to analyze and evaluate the BPT structure is a very difficult mission and will not be addressed in this work. However, looking at the different pruned trees in Fig. 5.12 it can be seen that typically diagonal dissimilarities obtain more linear trees, whereas BPTs obtained by full matrix dissimilarities are more balanced and thus, their representation appears wider. Additionally, the revised Wishart dissimilarity d_{sw}, is the only one having individual pixels, represented in green, being pruned and also they appear in the upper nodes of the tree. This is not the desired structure, since one would expect to get individual pixels not so close to the root node. However, these results are not very significant since they are obtained from a small and simple image (Fig. 5.1a), having large homogeneous regions. To obtain a representative pruned tree structure, the whole image tree should be employed but, in this case, the resulting tree will be too large to be properly represented.

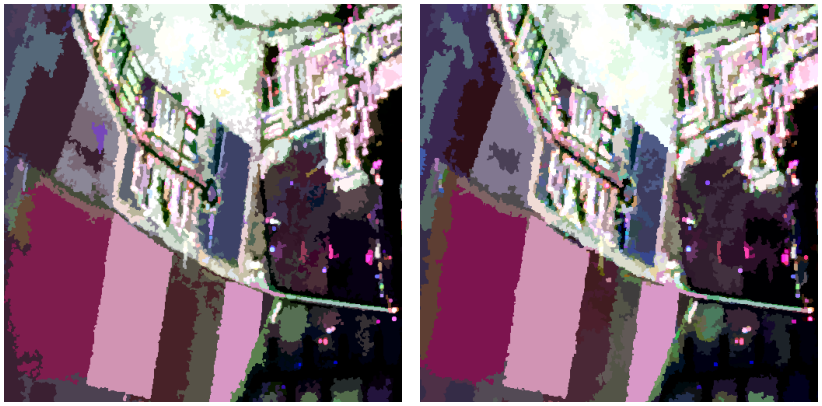

(a) $d_{dg}, \delta_p = 0dB$ (b) $d_{sg}, \delta_p = 0dB$

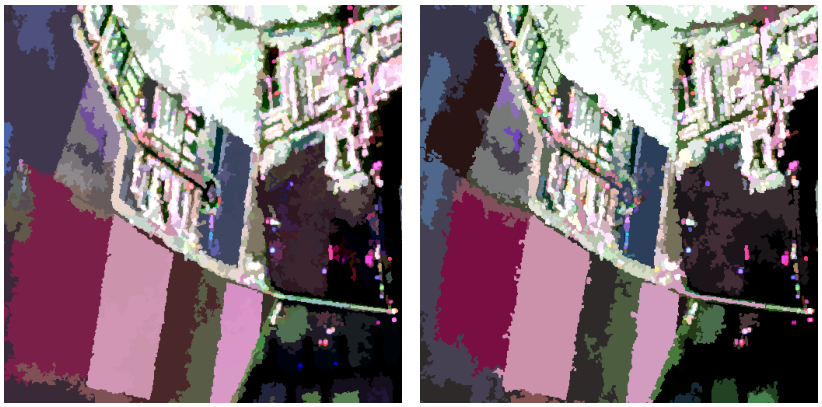

(c) $d_{dw}, \delta_p = 0dB$ (d) $d_{wr}, \delta_p = 0dB$

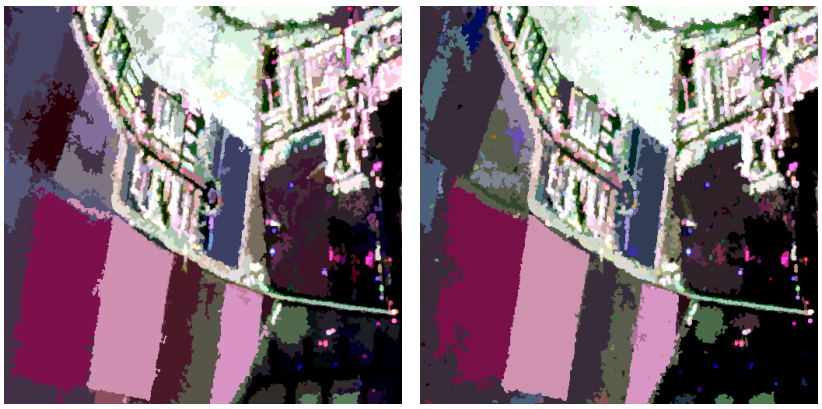

(e) $d_{dn}, \delta_p = 0dB$ (f) $d_{dr}, \delta_p = 0dB$

Figure 5.11: Detail Pauli RGB images processed using region homogeneity based pruning with $\delta_p = 0dB$ over different trees constructed employing various dissimilarity functions ($|S_{hh} + S_{vv}|$, $|S_{hv} + S_{vh}|$, $|S_{hh} - S_{vv}|$)

In the previous examples, a qualitative analysis has been made of the proposed BPT-based filtering schemes. However, although the BPT construction and pruning is taking into account all the polarimetric information within the covariance matrix, only the di-

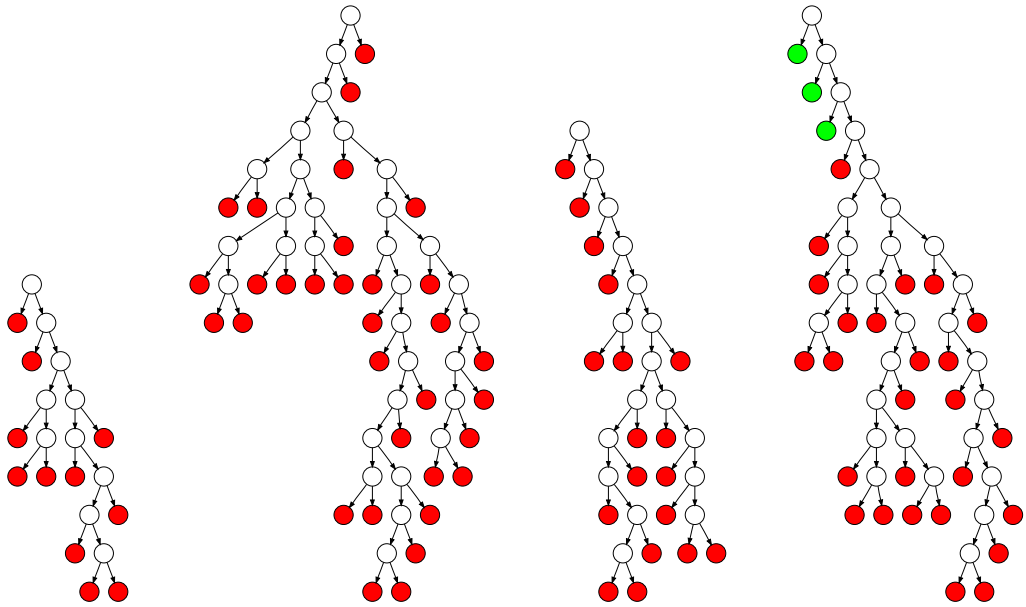

(a) d_{dg} (b) d_{sg} (c) d_{dw} (d) d_{sw}

Figure 5.12: Pruned BPTs using region homogeneity based pruning with $\delta_p = 0dB$ over different trees constructed employing various dissimilarity functions. Pruned nodes are colored in green if they are leaves or in red otherwise

agonal elements have been represented, since the Pauli RGB composition has been employed to represent the data. To analyze the fully polarimetric information preservation, some complementary analysis are needed. In the following analysis, the Entropy (H), Anisotropy (A) and averaged alpha angle ($\bar{\alpha}$) decomposition will be employed, as defined in Section 2.2. Note that these parameters can not be defined over the original image, since their calculation needs full-rank matrices, then the 7x7 multilook filtered image will be employed as a reference.

Fig. 5.13 presents the H/A/$\bar{\alpha}$ decomposition parameters over the image crops employed before. The entropy and anisotropy are represented from 0, in blue, to 1, in red colors; the averaged alpha angle is represented from 0°, in blue, to 90°, in red. Results are shown for the 7x7 multilook filter, as a reference, the IDAN filter and the BPT homogeneity based pruning for $\delta_p = -2dB$ and $\delta_p = 0dB$. An initial qualitative evaluation shows that the colors are maintained for all the filtering processes, meaning that the H/A/$\bar{\alpha}$ parameters are maintained. However, when results are analyzed in detail some differences are observed. The BPT-based filtering can take profit of estimating the covariance matrix over large homogeneous areas, reducing the noise and estimation errors. This effect is specially clear over agricultural fields, in the bottom part of the image. In the forest, at the top part of the image, a similar effect can be observed; increasing the pruning factor

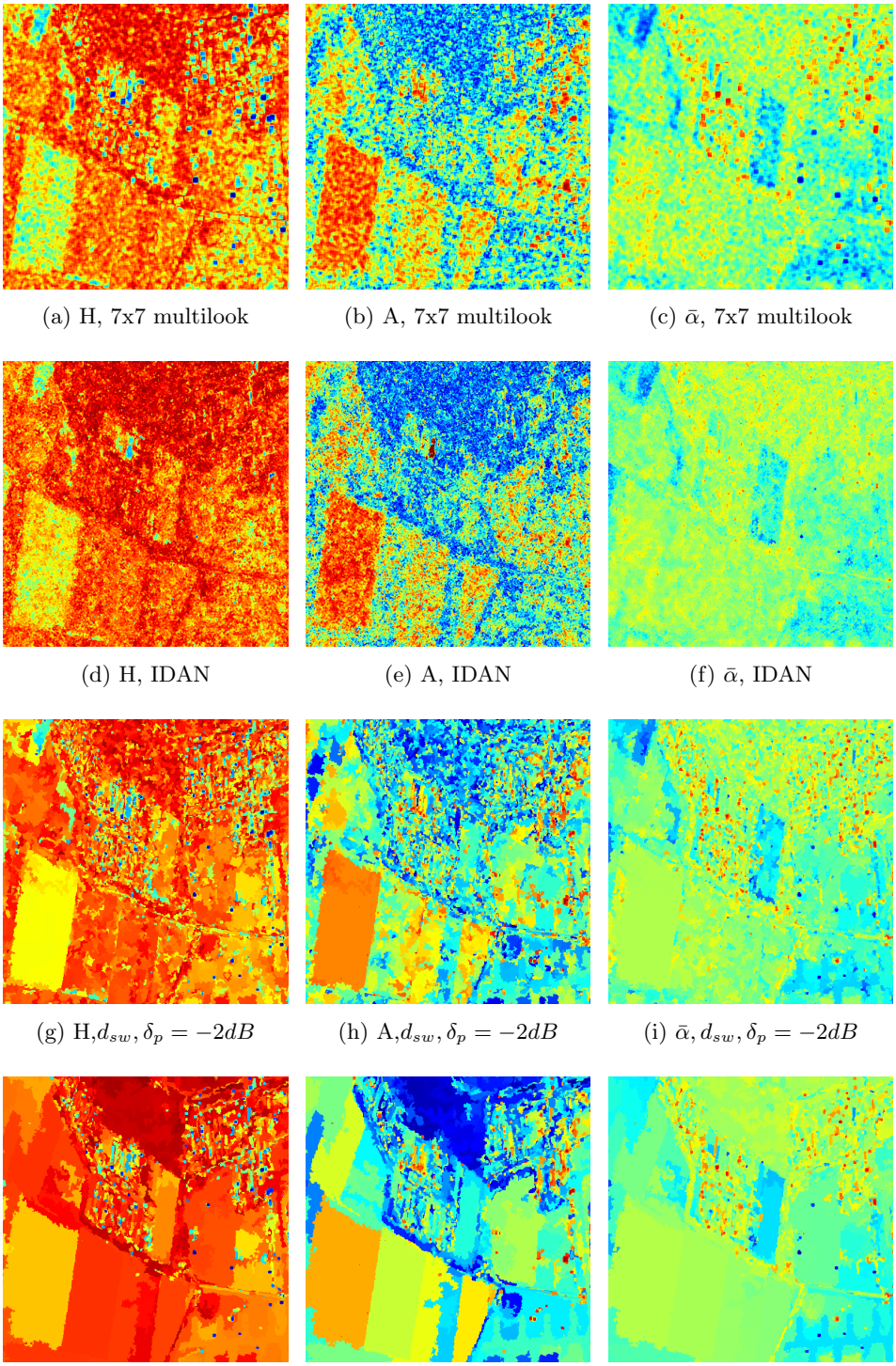

(a) H, 7x7 multilook (b) A, 7x7 multilook (c) $\bar{\alpha}$, 7x7 multilook

(d) H, IDAN (e) A, IDAN (f) $\bar{\alpha}$, IDAN

(g) H,$d_{sw}, \delta_p = -2dB$ (h) A,$d_{sw}, \delta_p = -2dB$ (i) $\bar{\alpha}, d_{sw}, \delta_p = -2dB$

(j) H,$d_{sw}, \delta_p = 0dB$ (k) A,$d_{sw}, \delta_p = 0dB$ (l) $\bar{\alpha}, d_{sw}, \delta_p = 0dB$

Figure 5.13: H/A/$\bar{\alpha}$ of processed images with multilook, IDAN and using region homogeneity based pruning

to $\delta_p = 0dB$ results in a better estimation, where entropy H tends to 1 and anisotropy A

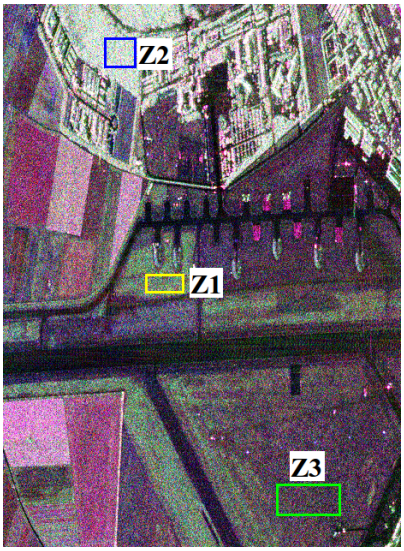

Figure 5.14: Homogeneous zones selected over the original image ($|S_{hh} + S_{vv}|$, $|S_{hv} + S_{vh}|$, $|S_{hh} - S_{vv}|$)

tends to 0, which fits with the theoretical response for a random volume scattering, as it is supposed to occur over forest. On the other hand, the ability of the region homogeneity BPT pruning to preserve small details can be clearly seen over urban areas, at the center of the image, where the small structures corresponding to buildings and other human-made targets are preserved. Note that, as a consequence, the proposed filtering scheme improves the estimation of the polarimetric information both, in point as well as in distributed scatters, with respect to the multilook filter.

To make a quantitative evaluation of the polarimetric information preservation, a set of three homogeneous test regions have been manually selected over the original image, presented in Fig. 5.14. Different parameters, covering the covariance matrix elements and the H/A/$\bar{\alpha}$ polarimetric decomposition, are estimated over these regions for the original image and the images filtered employing different filtering strategies. The results over these areas are presented in Table 5.3 for 7x7 multilook, IDAN filter and BPT-based filtering.

Table 5.3 shows that the multilook and the region homogeneity BPT pruning estimate the elements of the covariance matrix properly, obtaining results very similar to the original ones. However, on some regions the BPT pruning employing $\delta_p = 0dB$ start to diverge from the original values due to inhomogeneous region mixture. Then, probably fixing the pruning factor to $\delta_p = 0dB$ can be an excessive value for the filtering application. On the other hand, the IDAN filter introduces an important bias on the covariance matrix elements. The presence of this bias has been discussed in [60] and compensated up to a certain point by the authors [61]. The last three columns of Table 5.3 show the H/A/$\bar{\alpha}$

Region	Filtering	C_{11}	C_{22}	C_{33}	$\Re(C_{13})$	$\Im(C_{13})$	H	A	$\bar{\alpha}$
Z1 5000 px	Original	28.27	16.06	18.34	5.242	5.504	-	-	-
	ML 7x7	28.21	15.97	18.36	5.321	5.465	0.8012	0.3543	48.29
	IDAN	18.73	9.661	12.03	2.471	2.595	0.8558	0.3050	49.48
	BPT -2dB	28.15	16.10	18.17	5.466	5.605	0.8271	0.2873	48.27
	BPT -1dB	28.20	15.20	18.08	5.558	5.612	0.8618	0.2036	47.91
	BPT 0dB	27.76	14.47	16.96	5.813	5.211	0.8694	0.1630	47.74
Z2 5950 px	Original	279.3	159.1	172.8	49.80	-14.37	-	-	-
	ML 7x7	280.8	159.3	172.9	49.18	-15.27	0.8598	0.2907	49.06
	IDAN	173.0	102.4	105.8	20.59	-7.978	0.9003	0.2501	51.29
	BPT -2dB	278.1	158.4	171.5	48.05	-16.12	0.8475	0.2984	49.50
	BPT -1dB	280.4	157.7	172.4	50.24	-15.42	0.8925	0.2269	49.41
	BPT 0dB	292.2	160.8	177.0	50.74	-13.42	0.9305	0.1307	49.61
Z3 18000 px	Original	10.70	2.782	13.13	2.644	5.599	-	-	-
	ML 7x7	10.70	2.789	13.14	2.662	5.593	0.6781	0.4248	42.62
	IDAN	7.123	1.864	8.678	1.433	2.896	0.7438	0.4505	44.39
	BPT -2dB	10.33	2.713	12.94	2.498	5.255	0.7370	0.3755	43.32
	BPT -1dB	10.36	2.799	13.23	2.434	5.136	0.7445	0.3881	43.60
	BPT 0dB	11.76	3.405	13.59	2.556	5.351	0.7852	0.3471	44.34

Table 5.3: Mean estimated values over homogeneous areas for different filtering strategies

parameters. These parameters can not be calculated over the original data since they need full-rank matrices and then, they not appear over the corresponding rows. The values obtained for all the filters are similar, including the IDAN filter. In this case, the bias over the covariance matrix is not so important over H/A/$\bar{\alpha}$ parameters since they have a relative nature, covering bounded intervals of $[0, 1]$ for H/A and $[0°, 90°]$ for $\bar{\alpha}$. Note that, since these parameters are calculated indirectly from the covariance matrix, their estimation is biased. This bias has been studied in detail in [62], depending on the number of samples (looks) employed for the covariance matrix estimation. As stated in [62], the entropy H and anisotropy A are always underestimated and overestimated, respectively, and increasing the number of looks reduces the bias. This effect can be seen on Table 5.3 while increasing the pruning factor δ_p means incrementing the number of looks as regions obtained are larger and then, H and A are incremented and reduced, respectively.

5.1.4 Results with simulated data

In the previous section, a qualitative analysis of the filtering results with real data has been addressed. A quantitative evaluation has also been done by selecting manually some homogeneous areas over the data and comparing estimated values over original and filtered images. However, a more detailed analysis can not be done since the ground truth of the

data is not known. In fact, the ground truth can not be obtained for a real image and then, a new evaluation process is defined in this section, based on generating simulated PolSAR images from a given synthetic ground truth.

To make a detailed assessment of the filtering process, a simulated 128x128 pixels PolSAR image is proposed in Fig. 5.15 with four square regions of equal size. Simulated data have been generated using the complex Gaussian polarimetric model presented in [63], assuming a reflection symmetric target since most of natural targets follow this model, with covariance matrix $\mathbf{C}$ of the form

$$\mathbf{C} = \sigma_{HH} \begin{pmatrix} 1 & 0 & \rho\sqrt{\gamma} \\ 0 & \varepsilon & 0 \\ \rho^*\sqrt{\gamma} & 0 & \gamma \end{pmatrix} \tag{5.4}$$

where * denotes complex conjugate.

Three sets of images have been simulated according to (5.4) with $\gamma_i = 1$ and $\varepsilon_i = 0.1$ and variations for σ_{HHi} and ρ_i in different regions $i = 1 \dots 4$ as denoted in Fig. 5.15a

1. Variations in intensity: $\rho_i = 0.5$; $\sigma_{HH} = \{1,\ 9,\ 25,\ 49\}$
2. Variations in correlation: $\rho = \{0,\ 0.25e^{j\pi},\ -0.5,\ 0.75e^{-j\pi}\}$; $\sigma_{HHi} = 1$
3. Variations both in correlation and in intensity: $\rho = \{0,\ 0.25e^{j\pi},\ -0.5,\ 0.75e^{-j\pi}\}$; $\sigma_{HH} = \{1,\ 9,\ 25,\ 49\}$

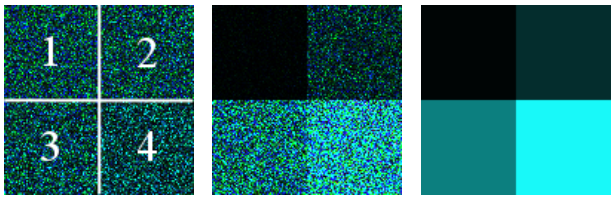

(a) (b) (c)

Figure 5.15: Simulated PolSAR images with 4 equal size zones. Z_{11}, Z_{22} and Z_{33} are assigned to blue, red and green channels, respectively. (a) Zones shape and numeration, (b) and (c) one realization of the image with intensity variations and image ground-truth, respectively

Some matrix measure is needed to asses numerically the accuracy of the filtered image X with respect to the simulated ground truth Y. The matrix relative error E_R measure is proposed

$$E_R(X,Y) = \frac{1}{n_h \cdot n_w} \sum_{i=1}^{n_h} \sum_{j=1}^{n_w} \frac{\|\mathbf{X}^{ij} - \mathbf{Y}^{ij}\|_F}{\|\mathbf{Y}^{ij}\|_F} \tag{5.5}$$

where n_h and n_w are the image height and width in pixels, respectively, $\mathbf{X}^{ij}$ represents the (i,j)th pixel value of image X and $\|\cdot\|_F$ denotes Frobenius matrix norm. Note that

the relative error measure defined in (5.5) is based on the inverse signal to noise ratio (SNR^{-1}) averaged for all the pixels in the image.

Fig. 5.16 presents a filtering quality comparison, in terms of E_R (5.5), of the BPT pruning based on the number of regions, presented in Section 5.1.1, with some of the dissimilarity measures defined in Section 4.3.2. The number of regions N is shown in the upper horizontal axis with logarithmic scale. In the lower horizontal axis, the mean region area in pixels is stated, calculated as $(n_h \cdot n_w)/N$. The plot also compares the BPT pruning based on the number of regions with the multilook filter (2.46), for different window sizes. In this case, the mean region size corresponds to the nominal window size, i.e. n in (2.46). For the BPT based filtering, an initial 3x3 multilook has been applied in order to get full rank matrices needed for d_{sw} (4.2) and d_{wr} (4.4) dissimilarities. The results have been obtained averaging 25 different realizations of the simulated image. For the multilook and the d_{sw} cases the standard deviation values resulting from the 25 realizations are also included. The rest of the curves present similar standard deviation values to the d_{sw} case.

The aim to simulate synthetic images with variations on intensity and correlation is to compare the behavior of diagonal and full matrix dissimilarity measure and to asses the performance of the BPT-based speckle filtering in comparison with the multilook filter, as a reference. When variations on intensity are present, Figs. 5.16a and 5.16c, for small values of the average region size the results for the BPT pruning based on the number of region are very close to the multilook filter, since the region mixture for the multilook filter near the region contours is negligible. For larger values of region size, in the order of 50-100 pixels, equivalent to a 9x9 Boxcar filter, the E_R measure starts to increase rapidly for the Boxcar filter, as the region mixture near contours becomes noticeable. The BPT based filtering, on the contrary, is able to adapt to the image spatial morphology, avoiding the region mixture near contours and achieving a constant improvement on the ground truth estimation as the region size increases, reflected by a decrease on the relative error measure. The best value in terms of E_R is achieved near the 4 regions for almost all the dissimilarity measures, except the d_{dr} measure, when reducing the region number implies an unavoidable region mixture, since the ground truth is composed by exactly 4 square regions.

When there are no variations on intensity, results are completely different, as shown on Fig. 5.16b. Note that in this case only the dissimilarity measures employing the full matrix information are sensitive to the region contours. Then, the regions generated employing d_{dn} (4.12), d_{dr} (4.13) and d_{dw} (4.10) rapidly start mixing non-homogeneous regions, since they can not adapt to the spatial morphology, and never improve the multilook filter performance. On the other hand, full matrix dissimilarities d_{sw} (4.2) and d_{wr} (4.4) can adapt to the image spatial morphology, avoiding the region mixture effect, and achieving

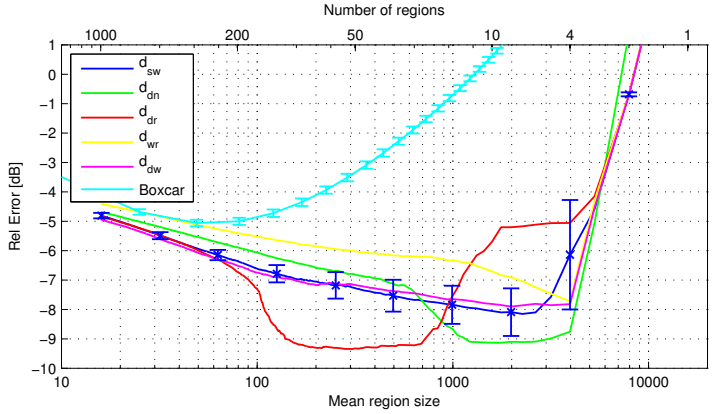

(a) Variation in intensity

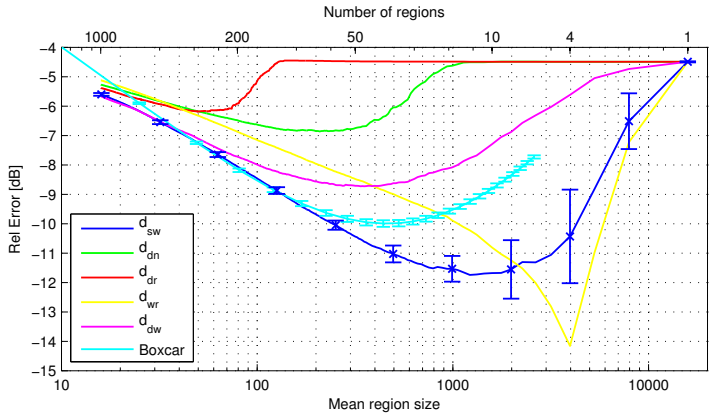

(b) Variation in correlation

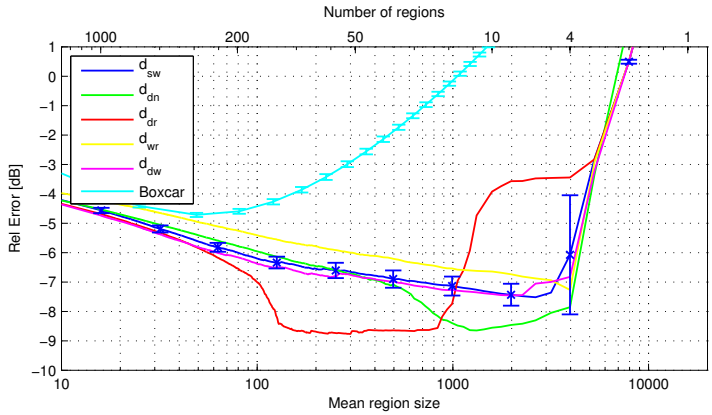

(c) Variations both in correlation and in intensity

Figure 5.16: Relative matrix error for simulated images with 4 equal size zones filtered with a BPT pruning based on the region number. Results have been obtained averaging 25 realizations

better results than the multilook filter. Note that, in Fig. 5.16b, the intensity is constant over the entire image. As a result, the mixing of different regions has not as a dramatic

impact in E_R as in Fig. 5.16a and 5.16c. This also explains why the minimum of the Boxcar relative error occurs at region sizes about 400-500 pixels, equivalent to a 21x21 multilook filter.

Comparing the results obtained for the different dissimilarity measures over the three plots, it can be seen that each dissimilarity measure has a different behavior respect to the number of regions N. The Wishart based dissimilarities have an almost stable and constant decrease in terms of E_R as N increases, and achieving the best values of E_R near the ideal value $N = 4$. On the contrary, the d_{dn} and d_{dr} dissimilarities have a strong decrease of E_R before $N = 4$, achieving the best value far from its ideal value, although they can achieve better performance in terms of E_R. Ward relative dissimilarity d_{wr} have a poorer performance in terms of E_R when compared to other dissimilarities, but it has the advantage of presenting a clear minimum at exactly 4 regions for all the cases. When there are no variations in intensity, the full matrix dissimilarities are the only ones that can adapt to the spatial contours and improve the Boxcar filter, as shown on Fig. 5.16b.

Fig. 5.17 shows some examples of the results of the Boxcar filter and the BPT pruning based on the number of regions for different N and different BPTs constructed employing various dissimilarity measures. As it may be seen in Fig. 5.17a, 5.17b and 5.17c, as the Boxcar filter size increases the amount of speckle noise reduction and the quality of the estimation increases. However, the spatial resolution is degraded considerably as the filter size increases, blurring completely the region contours. In Fig. 5.17d, 5.17e and 5.17f, the number of regions N is fixed to 100 and different dissimilarity measures for BPT construction are compared. All of them are able to detect the main contours of the four zones with this number of regions. The contours detected inside the main regions are completely random and they are due to the speckle noise present on the image. In Fig. 5.17g, 5.17h and 5.17i, the symmetric revised Wishart dissimilarity measure d_{sw} (4.2) has been employed and the results are shown for different number of regions. For $N = 4$, as it may be observed, there is a good preservation of the spatial resolution, but also of the polarimetric information under the Gaussian hypothesis. A comparison between Fig. 5.15c and Fig. 5.17i exhibits that the filtered image is quite close to the ideal one. This similarity is also supported by the fact that the relative error function (5.5), which is also sensitive to the polarimetric information, presents very low values. As detailed previously, each region is represented by the average covariance matrix which is the MLE under the Gaussian hypothesis [64]. Furthermore, as N decreases the number of contours in the filtered image decreases, reducing the effect of the speckle noise, but new contours never appear.

The same evaluation process with the simulated 4 region images presented before, has been applied to the BPT region homogeneity based pruning strategy. In this case,

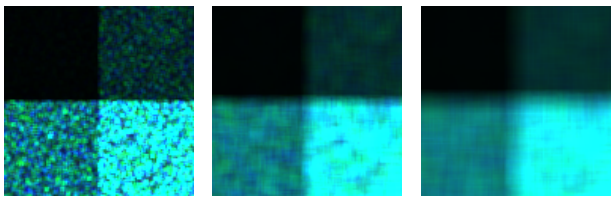

(a) Boxcar 3x3 (b) Boxcar 9x9 (c) Boxcar 15x15

(d) d_{dn}, $N = 100$ (e) d_{dw}, $N = 100$ (f) d_{wr}, $N = 100$

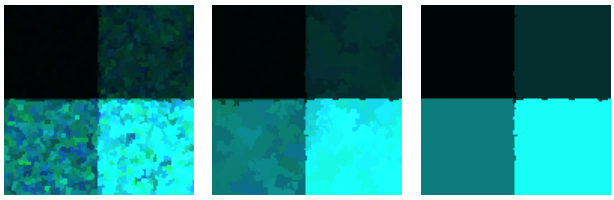

(g) d_{sw}, $N = 1000$ (h) d_{sw}, $N = 100$ (i) d_{sw}, $N = 4$

Figure 5.17: Boxcar and BPT filtering (pruning based on the number of regions) in one of the simulated PolSAR images with variations in both correlation and intensity employing different dissimilarity measures. Z_{11}, Z_{22} and Z_{33} are assigned to blue, red and green channels, respectively

the BPTs employing all the dissimilarity measures defined in Section 4.3 are compared. Results are shown on Fig. 5.18, in terms of the same evaluation measure, the relative error E_R, defined in (5.5). As in the previous case, results have been obtained by averaging the results of 25 different realizations of each simulated image. The values of the standard deviations are shown for the revised Wishart dissimilarity d_{sw}.

As it can be seen on Fig. 5.18, the behavior of the different curves on the plots is very similar, independently of the image structure. There is always a clear minimum, for all the BPTs employing different dissimilarity measures, at the same point, at about $\delta_p = -6dB$. Additionally, when there are variations on intensity, Figs. 5.18a and 5.18c, a wide range of values for δ_p can be selected, approximately $-6dB \leq \delta_p \leq -4dB$, having a near-optimum behavior. This fact is caused since the region mixture produces a strong increase in the region homogeneity measure and then, the pruning factor has to be substantially increased to accept this non-homogeneous regions. When there are only variations on correlation, Fig. 5.18b, there is not such a wide range of near-optimum values for δ_p, but there is also a clear minimum located at $\delta_p = -6dB$.

Comparing Fig. 5.16 and Fig. 5.18, the minimum values in terms of relative error

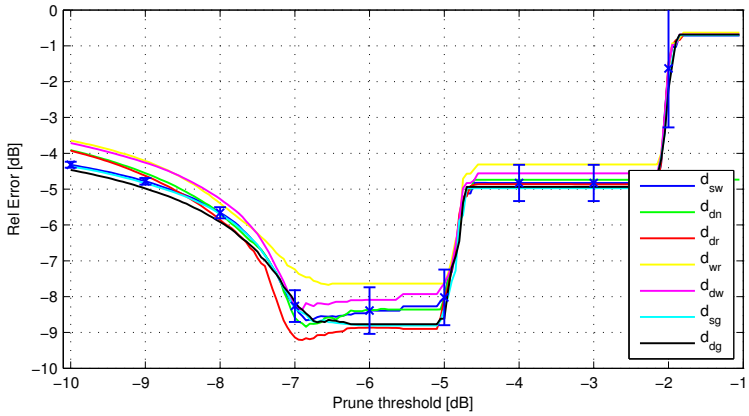

(a) Variation in intensity

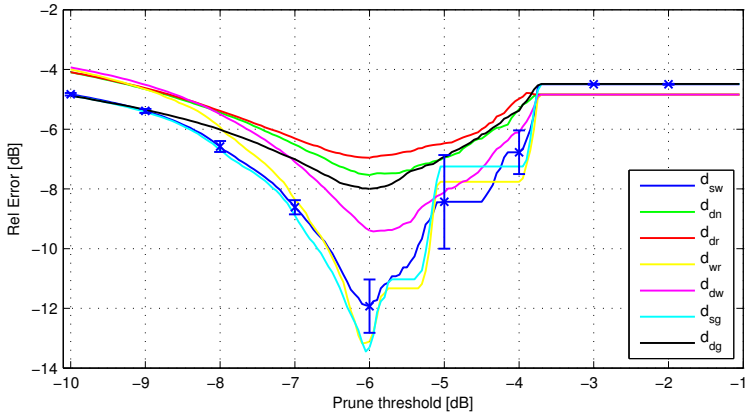

(b) Variation in correlation

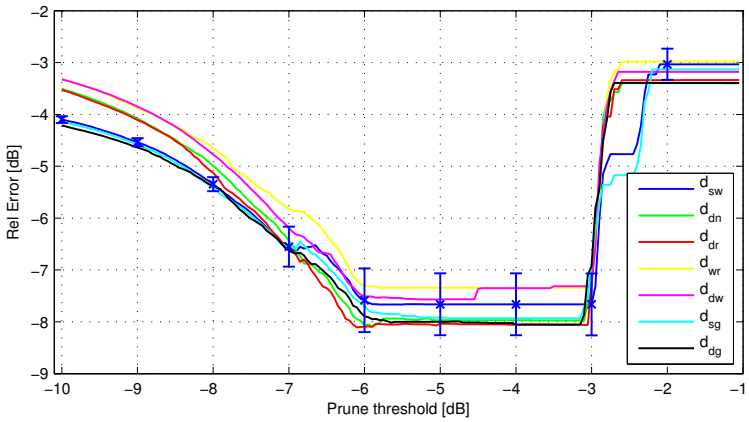

(c) Variations both in correlation and in intensity

Figure 5.18: Relative matrix error for simulated images with 4 equal size zones filtered with a region homogeneity based pruning. Results have been obtained averaging 25 realizations.

obtained in BPT pruning based on the number of regions are approximately preserved in the region homogeneity pruning. However, since the homogeneity measure in which

pruning is based on is sensitive to all the covariance matrix elements, a small improvement can be observed when the dissimilarity measure is not sensitive to region changes, as seen in Fig. 5.18b for diagonal dissimilarities d_{dn} (4.12), d_{dr} (4.13) and d_{dw} (4.10), which contributes making the region homogeneity based pruning more robust. From all the curves presented in Fig. 5.18 employing different dissimilarities, it is clear that the BPTs constructed employing the geodesic family of dissimilarity measures can achieve better results in terms of E_R, specially the d_{sg} measure, since it is a full matrix measure and it also obtains good results when there are only variations in correlation, in Fig. 5.18b.

Fig. 5.19 shows the results of applying the BPT homogeneity based pruning in one realization of the simulated data with variations both in correlation and in intensity. In Figs. 5.19a-5.19f the pruning threshold δ_p has been fixed to -6 dB, which is the optimum value for all the simulated images, as seen in Fig. 5.18. With this pruning threshold, the BPT homogeneity pruning employing all the dissimilarity measures obtain a filtered image very close to the ideal one shown in Fig. 5.15c, obtaining a good preservation of the polarimetric information under the Gaussian hypothesis. There are only small differences in the detected contours, which are more accurate for d_{sw}, d_{wr} and d_{sg}, since they are sensitive to all the covariance matrix information. In Fig. 5.19g-5.19l, the full matrix geodesic dissimilarity measure d_{sg} has been employed and different pruning thresholds are shown. Comparing it with the pruning based on the region number results for the same image, in Fig. 5.17, they achieve similar results, specially for high pruning threshold values. Additionally, the wide range of near-optimum values for δ_p can be seen on Fig. 5.19j-5.19l, obtaining exactly the same result, corresponding to the 4 regions of the image, for values $-6dB \leq \delta_p \leq -4dB$.

Nevertheless, the most important benefits of employing the region homogeneity based BPT pruning versus the pruning based on the number of regions is to overcome the drawbacks stated in Section 5.1.2. These drawbacks appear clearly when homogeneous regions having very different sizes want to be preserved from the image. This fact has been observed evidently when processing real data, on Section 5.1.3. The simulated ground truth, having 4 regions of equal size, does not present this kind of structure. Then, a new simulated ground truth is proposed to reflect more accurately the spatial structure of a real PolSAR image.

To obtain meaningful results, the simulated ground truth may be a realistic representation of a PolSAR image. Ideally, it should contain large homogeneous areas, like agricultural fields, and also small details, like the corner reflectors or the urban area seen before. Additionally, the covariance matrix $\mathbf{C}$ for every region should represent realistic values that can be found in real data. Then, to accomplish the previously mentioned requirements, a ground truth will be generated by a segmentation of a real image. Since

(a) d_{dn}, $\delta_p = -6dB$ (b) d_{dr}, $\delta_p = -6dB$ (c) d_{dw}, $\delta_p = -6dB$

(d) d_{dg}, $\delta_p = -6dB$ (e) d_{sw}, $\delta_p = -6dB$ (f) d_{wr}, $\delta_p = -6dB$

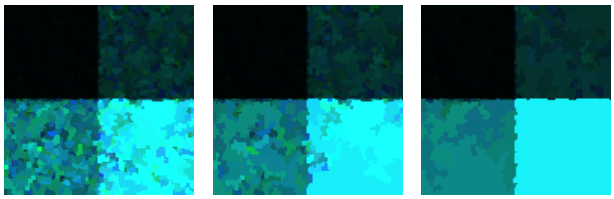

(g) d_{sg}, $\delta_p = -9dB$ (h) d_{sg}, $\delta_p = -8dB$ (i) d_{sg}, $\delta_p = -7dB$

(j) d_{sg}, $\delta_p = -6dB$ (k) d_{sg}, $\delta_p = -5dB$ (l) d_{sg}, $\delta_p = -4dB$

Figure 5.19: BPT homogeneity pruning filtering in one of the simulated PolSAR images with variations in both correlation and intensity employing different dissimilarity measures and prune thresholds. Z_{11}, Z_{22} and Z_{33} are assigned to blue, red and green channels, respectively

a manual segmentation is not affordable, due to the large number of small regions and details of a real image, a segmentation tool will be employed. In this case, the BPT region homogeneity based pruning with a pruning factor $\delta_p = -1dB$ will be employed over the tree constructed with the geodesic dissimilarity d_{sg} presented in (4.3).

This BPT-based filtering has been applied to two different 512 by 512 pixel size image crops presented in Fig 5.20 and Fig 5.21, corresponding to a region dominated by large agricultural fields and a urban area, respectively. For the evaluation process, images Fig 5.20b and Fig 5.21b will be employed as a ground truth and speckle noise will be simulated over them. Note that these images do not correspond to the real ground truth of the images Fig 5.20a and Fig 5.21a due to imperfections and limitations of the BPT-

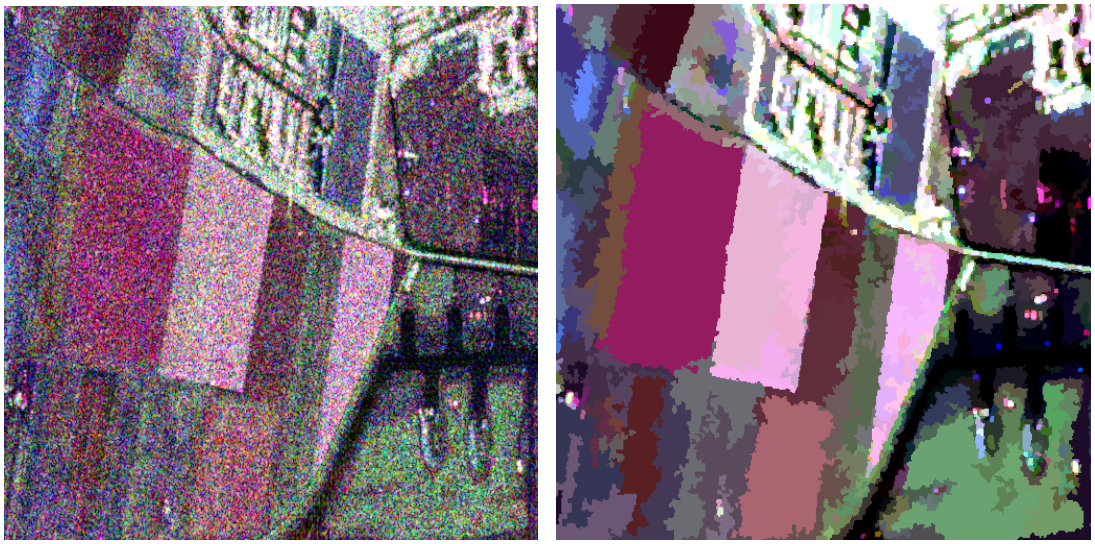

(a) Original crop (b) Filtered ($d_{sg}, \delta_p = -1dB$)

Figure 5.20: Original and filtered images of an agricultural area ($|S_{hh}+S_{vv}|$, $|S_{hv}+S_{vh}|$, $|S_{hh}-S_{vv}|$)

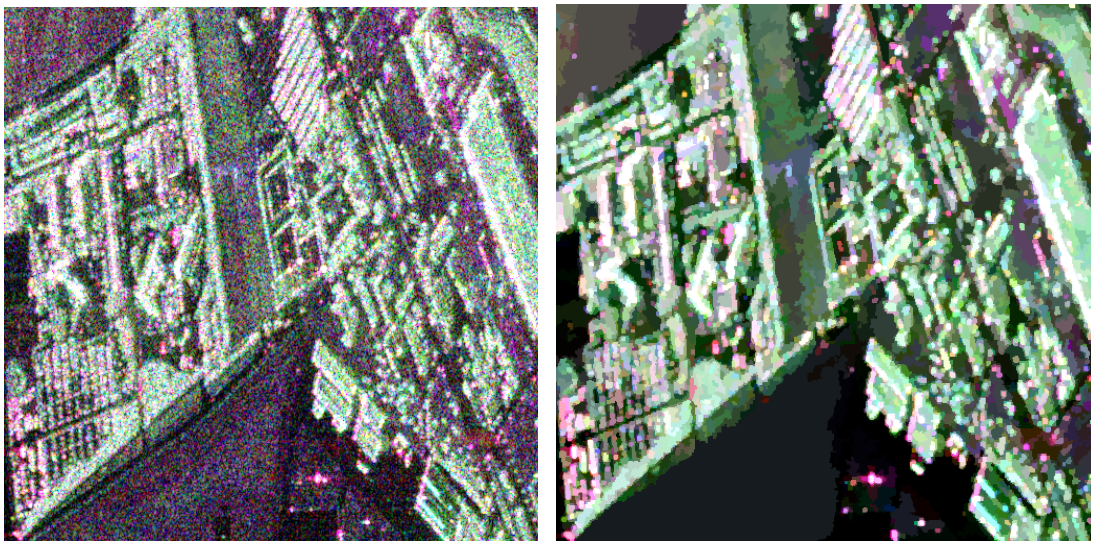

(a) Original crop (b) Filtered ($d_{sg}, \delta_p = -1dB$)

Figure 5.21: Original and filtered images of an urban area ($|S_{hh} + S_{vv}|$, $|S_{hv} + S_{vh}|$, $|S_{hh} - S_{vv}|$)

based filtering. However, they are a good choice to be used as a ground truth since they have regions of different sizes and their values are realistic since they are estimated over the original PolSAR image.

Note that the two selected crops as a ground truth represent completely different situations. The agricultural zone is dominated by large homogeneous regions corresponding to fields, although a small zone of urban area can be found at the top of the image to evaluate the ability to preserve regions with very different sizes. On the other hand, the

urban area is dominated by a large number of small regions very contrasted. In fact, the number of regions of the ground truth images are 1939 for the agricultural zone and 6869 for the urban zone.

With the synthetic ground truth established for the agricultural and urban areas, several realizations can be generated by simulating speckle noise following the estimated covariance matrix in every region. An example of a realization is shown in Fig. 5.22a and Fig. 5.23a. In turn, these realizations can be filtered with the proposed BPT-based technique, as presented in Fig. 5.22b and Fig. 5.23b. The availability of the ground truth for these images (Fig 5.20b and Fig 5.21b) makes possible a precise quantitative evaluation of the filtering process by comparing the results with the ground truth, similarly to the synthetic 4 region images evaluation.

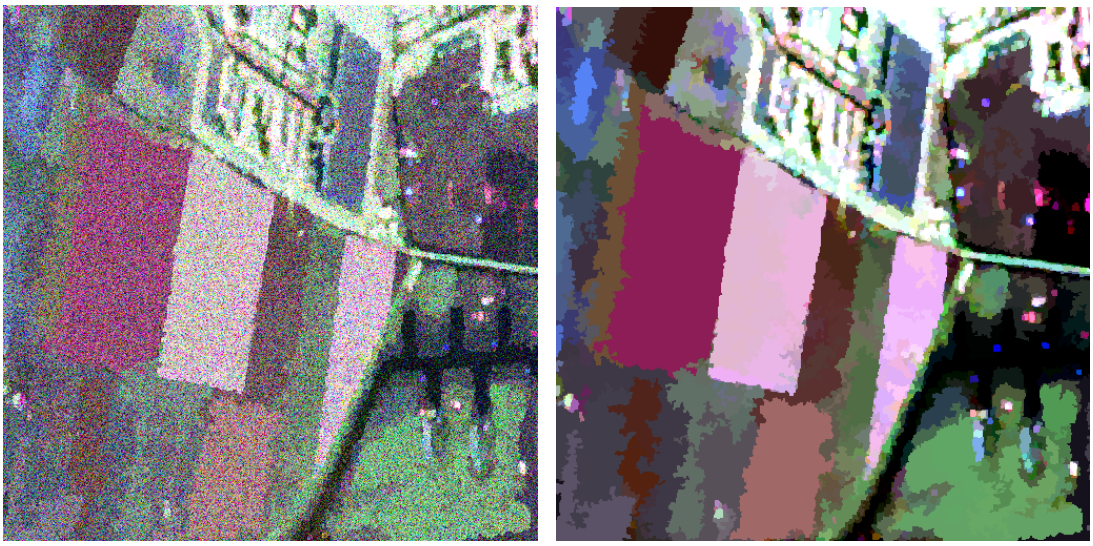

(a) One realization (b) Realization filtered ($d_{sg}, \delta_p = -5dB$)

Figure 5.22: Realization of the agricultural ground truth and the corresponding filtered image ($|S_{hh} + S_{vv}|$, $|S_{hv} + S_{vh}|$, $|S_{hh} - S_{vv}|$)

The evaluation process scheme is presented in Fig. 5.24. Different realizations are generated from a given ground truth image. These images are processed employing some filtering technique, in this case the region homogeneity BPT pruning and the multilook as a reference, and the filtered images are compared with the ground truth employing some quality measure $E(X, Y)$. The evolution of this measure E can be evaluated over all the simulated realizations and for different parameters of the filtering process. The proposed measure to evaluate the similarity of the filtered image X with the ground truth image Y is the relative error E_R, defined in (5.5).

As in the previous synthetic images, the relative error measure E_R has been calculated averaging the outcome of 25 different realizations of the ground truth image. Table 5.4

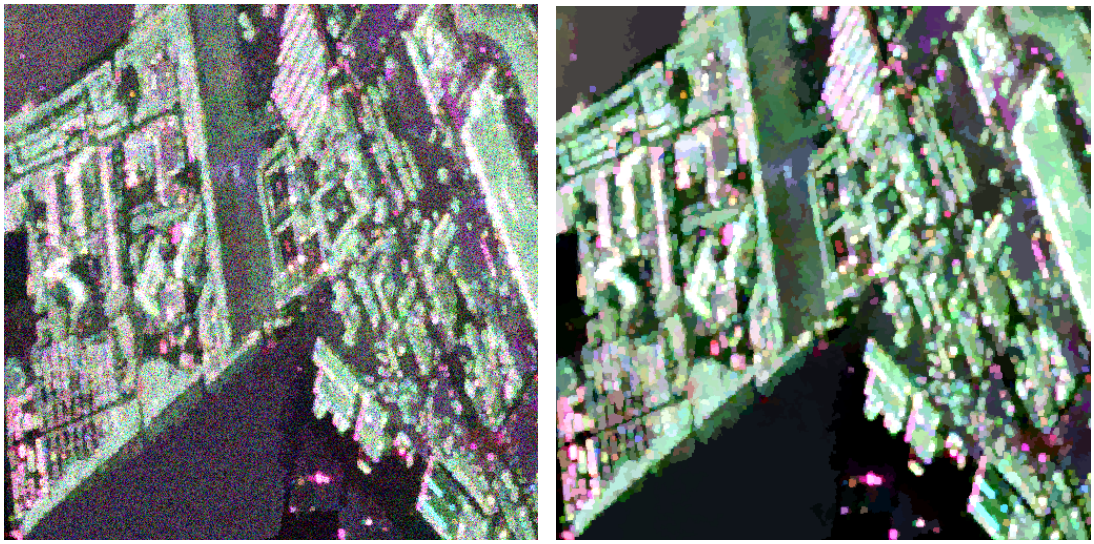

(a) One realization (b) Realization filtered ($d_{sg}, \delta_p = -5dB$)

Figure 5.23: Realization of the urban ground truth and the corresponding filtered image ($|S_{hh} + S_{vv}|$, $|S_{hv} + S_{vh}|$, $|S_{hh} - S_{vv}|$)

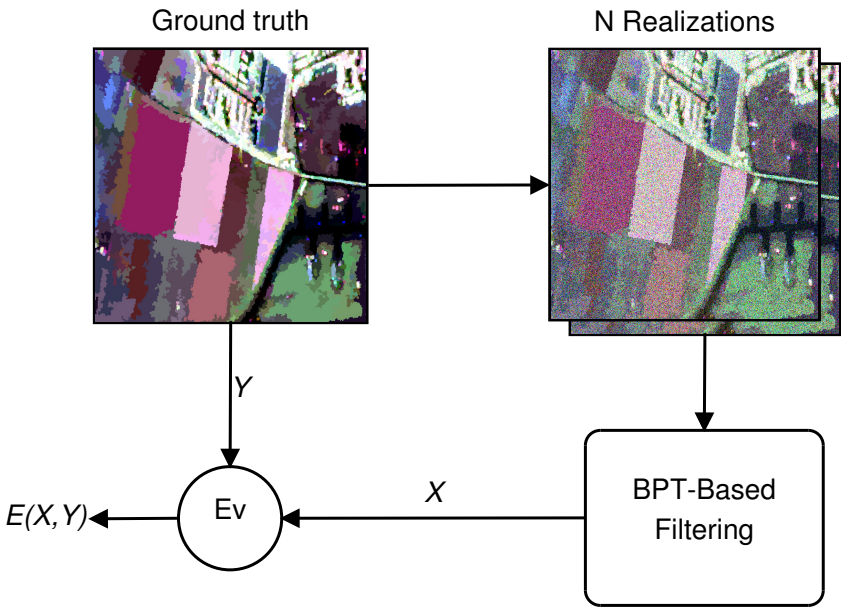

Figure 5.24: Evaluation process scheme

shows this measure for the original realizations and the filtered images with different sizes of square multilook filters.

Analyzing the results shown in Table 5.4 it can be seen that the best multilook filter size is 5x5 for the agricultural area and 3x3 for the urban area. This difference can be explained by the distinct composition of both zones. In the agricultural area, the effect of contour blurring and region mixture is compensated by a stronger filtering within homogeneous

	Agricultural zone	Urban zone
No filtering	1.451	1.565
3x3 multilook	-1.911	-0.251
5x5 multilook	-2.411	0.871
7x7 multilook	-1.895	2.616
9x9 multilook	-1.055	4.308

Table 5.4: Relative error E_R (in dB) for original and multilook filtered realizations

regions whereas in the urban area, the small regions mixture is dominant since they can not be properly filtered within a large window. It is worth to notice that the relative error measure obtains similar values for both cases when no filtering is applied.

This simulation process has been employed to examine the region homogeneity BPT pruning filtering. In this case, to simplify the evaluation process, only the region homogeneity based pruning strategy and the Wishart and geodesic families of dissimilarities will be employed, since they presented the better results in the previous analysis with real and simulated data. Fig. 5.25a shows the results obtained by the E_R measure for different pruning factors and for different trees, constructed with these dissimilarity measures.

As it can be seen, there is a clear minimum, located around $\delta_p = -5dB$, that is common for all the BPTs, independently of the dissimilarity measure employed for their construction. Additionally, better results than the multilook, presented in Table 5.4, are obtained for almost all values of δ_p, except for too high values of the pruning factor, in this case $\delta_p > -2dB$, where the region mixture becomes an important issue for the filtering application. Comparing results with different trees, it seems that, according to the E_R measure, the BPTs constructed employing the geodesic family of dissimilarities (d_{sg} and d_{dg}), obtain better results than the ones constructed with the Wishart based dissimilarities (d_{sw} and d_{dw}). Moreover, the relative error E_R for the trees employing the diagonal dissimilarities is slightly better than the ones obtained by employing the full matrix dissimilarities. This fact seems contradictory, since full matrix dissimilarities are employing the full polarimetric information under the Gaussian hypothesis and thus, it was expected that they could obtain better results. However, this fact can be related with the relative error measure E_R that is more sensitive to the power information, contained in the diagonal elements of the matrices, than to the off-diagonal information. Note that nowadays there is not a clear measure to evaluate properly the full matrix information preservation and probably the relative error measure E_R presents some limitations in this sense. Despite this, the full matrix dissimilarities have some important advantages that can be seen when analyzing other results shown in Fig. 5.25.

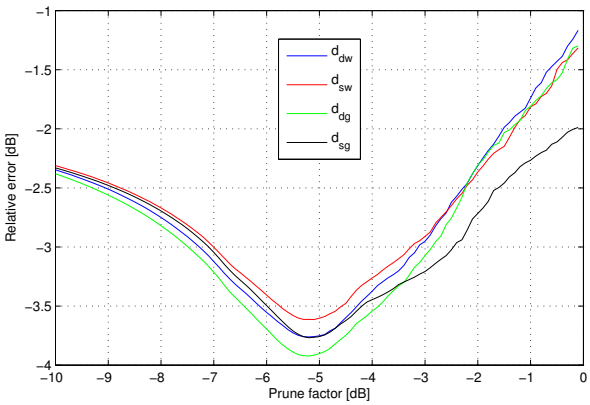

(a) E_R for different δ_p

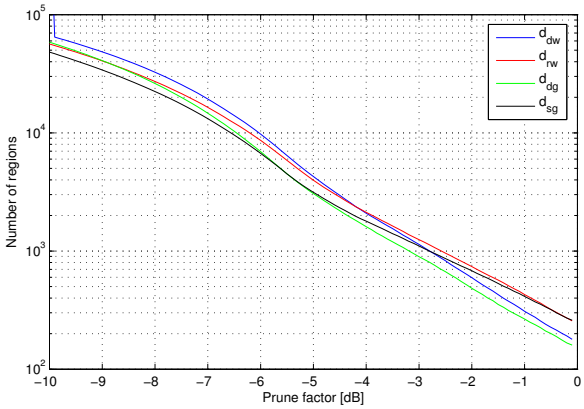

(b) Pruned regions for different δ_p

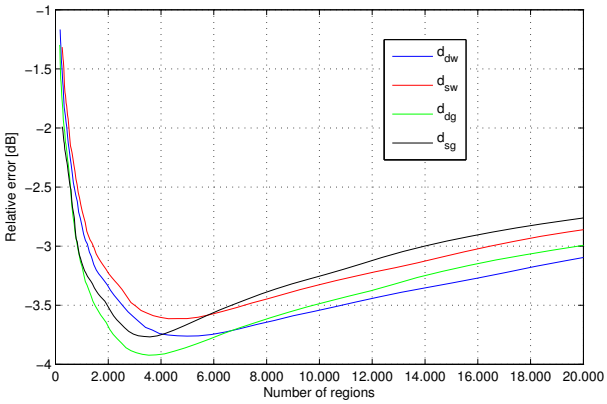

(c) E_R versus pruned regions

Figure 5.25: Parameter evolution for different values of δ_p and dissimilarity measures over the agricultural zone

Fig. 5.25b shows the number of pruned regions, that is, the number of leaves of the pruned tree, depending on the pruning factor δ_p. Note that the vertical axis, correspond-

ing to the number of regions is represented in logarithmic scale. The BPTs constructed with geodesic dissimilarities obtain a lower number of regions than the ones constructed with Wishart based dissimilarities. The pruning factor δ_p fixes the relative MSE of the pruned regions, as stated before, then this fact means that employing geodesic dissimilarities larger regions, that are equally homogeneous, can be obtained. In fact, this means that these dissimilarities can adapt better to the region contours by exploiting the off-diagonal information of the covariance matrices. When comparing full matrix with diagonal dissimilarity measures, that is d_{sg} with d_{dg} and d_{sw} with d_{dw}, a similar effect can be seen. Full matrix dissimilarities obtain a lower number of regions for $\delta_p < -5dB$ when, presumably there is not an important homogeneous regions mixture effect, and a larger number of regions for $\delta_p > -5dB$ when, passed the minimum error point, the homogeneous regions start to get mixed. As a consequence, dissimilarity measures employing the full matrix information obtain regions more homogeneous resulting in a better contour detection.

Fig. 5.25c combines the results of Fig. 5.25a and Fig. 5.25b to show the relative error versus the number of pruned regions. The values of E_R obtained are the same as in Fig. 5.25a, but it can be clearly seen that the number of regions for the minimum error point is different for the two families of dissimilarities. The trees constructed employing Wishart based dissimilarities obtain the best error values at about 5000 regions, but if geodesic dissimilarities are employed then this point is achieved at about 3500 regions. Remember that the number of regions of the ground truth for the agricultural zone is 1939. It can also be seen that the minimum point is attained at slightly lower number of regions for full matrix dissimilarities than for diagonal ones.

When comparing results from Fig. 5.25 and results obtained in Section 5.1.3 with real data, it can be seen that the values of δ_p differ substantially. Processing real data the typical values for the pruning factor where $-2dB < \delta_p < 0dB$ and for the simulated data in this section the best results are obtained in the range $-6dB < \delta_p < -4dB$. This effect can be related to additional region features in the real data that are not taken into account into the region model, which can be considered as the region texture. Then, since they are not properly modeled, the homogeneity threshold δ_p has to be increased to absorb these modeling errors when processing real data. Note that in the simulated data this region texture is not reproduced and then, it is not necessary to increase the pruning factor δ_p to assimilate the modeling errors. This explains why similar results are obtained for $\delta_p = -1dB$ and $\delta_p = -5dB$ in Fig. 5.20b and Fig. 5.22b, respectively.

Fig. 5.26 shows the results after processing 25 different realizations of the urban area crop presented in Fig. 5.21. The same plots than in Fig. 5.25 are shown for this area. Fig. 5.26a shows the E_R measure versus the pruning factor δ_p. With respect to Fig. 5.25a, there is a minimum for all the lines almost in the same position, at $-6dB < \delta_p < -5dB$,

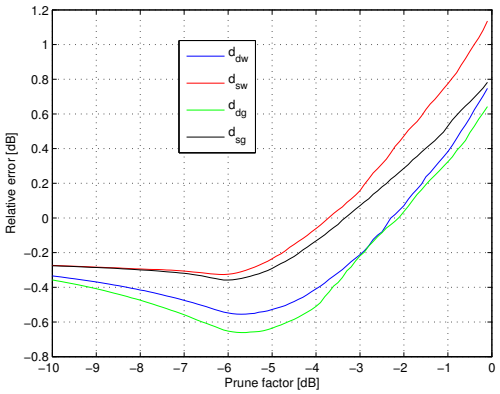

(a) E_R for different δ_p

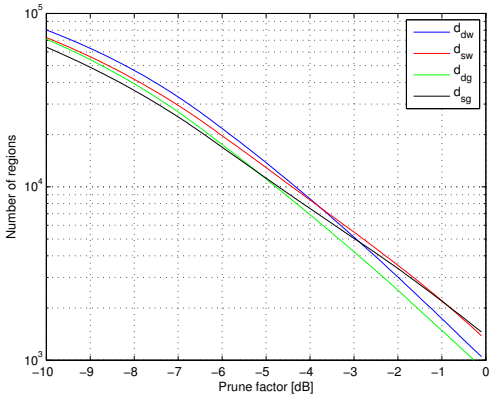

(b) Pruned regions for different δ_p

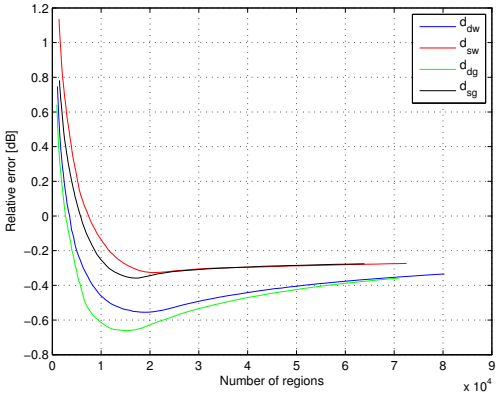

(c) E_R versus pruned regions

Figure 5.26: Parameter evolution for different values of δ_p and dissimilarity measures over the urban zone

but the values of these minimums in urban area are far in terms of E_R from the values over the agricultural area. Additionally, the difference between the value at $\delta_p = -10dB$

and the minimum point is not as large as in Fig. 5.25a. These differences are produced by the distinct structure of both images. Since the urban area is formed by a wide number of small homogeneous zones, there is no opportunity to achieve such a large filtering as in the agricultural area, because a smaller number of samples are available for each region. However, despite the minimum achieved is not so strong in the urban area as in the agricultural area, the values obtained for E_R are below those obtained for the multilook filter, as shown in Table 5.4. When comparing the results obtained employing different dissimilarity measures the same conclusions extracted for Fig. 5.25a apply, although over urban area the differences in term of E_R between diagonal and full matrix dissimilarities are larger.

Fig. 5.26b shows very similar trends to Fig. 5.25b, having almost the same shape. However, the vertical axis scale, corresponding to the number of regions, is different, since the structure of the urban areas is much more complex, resulting in a higher number of regions for a given pruning factor δ_p. The same effect can be seen on Fig. 5.26c: the best results in terms of E_R are achieved at about 15000 regions for the geodesic dissimilarities and at about 20000 for Wishart dissimilarities. As it has been stated before, the ground truth for the urban area contains 6869 regions, so there is approximately the same relation between the regions for the minimum E_R and the ground truth region number for the agricultural and the urban areas.

5.2 Coastline segmentation

In Section 5.1 the exploitation of the BPT structure has been defined and analyzed for the PolSAR speckle filtering application. However, as stated before, this representation contains a lot of useful information about the image structure that may be exploited for different applications. In this section a completely different application is introduced: coastline segmentation.

Fig. 5.27a shows a 1500 × 2500-pixel cut of a C-band Pauli RADARSAT-2 image of Barcelona, Spain, that was acquired in November, 18th 2008, in fine quad polarization mode, with nominal resolution of $5.2m \times 7.6m$. The figure also shows a detailed area corresponding to the Forum harbor of Barcelona. Fig. 5.27b shows a BPT-based coastline segmentation result. In this case, the revised Wishart dissimilarity d_{sw} (4.2) has been employed and a completely different and simpler pruning strategy has been applied, since the two most different regions, that is, the two child nodes of the root node, have been selected. The entropy (H) of this two regions is represented on Fig. 5.27b.

As it can be seen, the two child nodes of the root node represent the regions corresponding to the land and the sea. It is worth to notice that, due to the ability of the

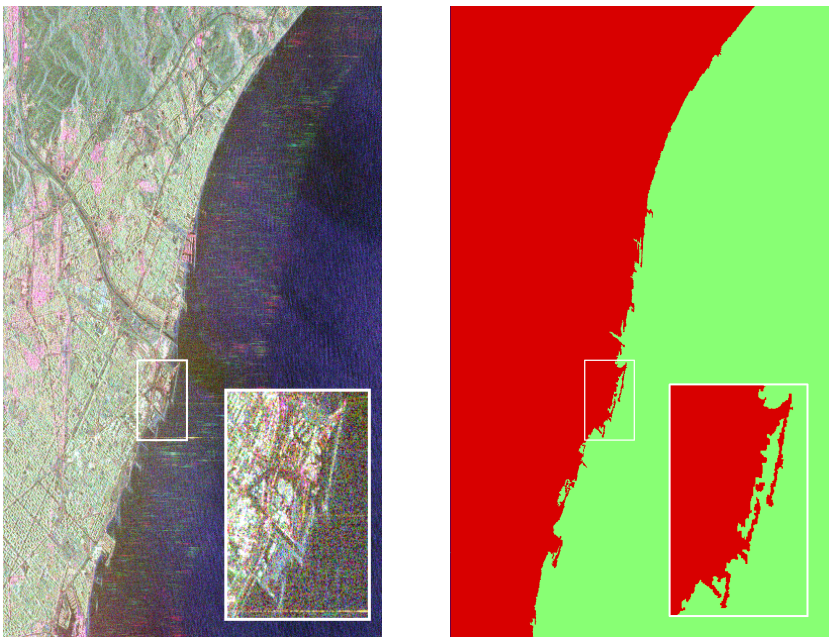

(a) Original Pauli (b) BPT based coastline segmentation

Figure 5.27: Pauli RGB image of Barcelona (a), and BPT-based coastline segmentation (b). The revised Wishart dissimilarity d_{sw} has been employed for the BPT construction

BPT representation to preserve small details of the image, the thin structures like the breakwaters of the Forum harbor are preserved in the segmentation. These small details are detected in the lower levels of the tree and, as a result, these features are transferred to the higher nodes of the tree, as shown in Fig. 5.27b. Note that, in this application, the higher nodes of the tree are employed, as opposite to the filtering application, focused on the lower levels of the tree, corresponding to homogeneous regions. This example shows the benefits of the multi-scale nature of the BPT PolSAR image representation.

In Section 4.2 it has been stated that the estimated covariance matrix $\mathbf{Z}$ is not a good model to represent inhomogeneous regions. In the coastline segmentation example presented in Fig. 5.27, the region corresponding to the land is strongly non-homogeneous, containing urban areas, field, mountains, etc. However, in this case the BPT structure is obtaining a meaningful image segmentation since the other region, in this case the sea, is quite homogeneous at this detail level. Nonetheless, for a proper segmentation over strongly non-homogeneous regions, more complex region models, capable of representing properly these areas, should be employed to obtain meaningful regions.

Chapter 6

BPT Processing of PolSAR image series

In Chapter 3, the BPT has been defined as a region-based and multi-scale data representation and in Chapters 4 and 5 it has been employed to process a PolSAR image, including different applications as speckle filtering and coastline segmentation. This representation has demonstrated its usefulness for PolSAR data, since it can adapt to the spatial contours of the image and it is able to separate the different homogeneous regions within the data.

In the last years, the presence of different PolSAR spaceborne systems has empowered the construction of PolSAR image datasets containing different acquisitions of the same scene at different times. In this chapter, this representation will be extended to the space-time domain, by applying it to a set of coregistered images, acquired by the same sensor at different dates. The idea is to obtain homogeneous regions in the space and time dimensions simultaneously, by adapting to the spatial and temporal contours on these dimensions. All the necessary concepts to construct a BPT representation with these datasets will be described on this chapter and its exploitation will be based on two different applications: speckle filtering and change detection.

6.1 BPT representation in the space-time domain

In this Chapter, the BPT data representation will be employed to process a three dimensional dataset, containing different PolSAR images of the same scene acquired at different dates. To simplify the processing of this dataset, it will be assumed that all the images are corregistered, that is, a pixel at position (i, j) in image k refers to the same physical

area in the scene that pixel (i, j) at image $m, \forall m \neq k$.

The dataset that will be employed on this Chapter corresponds to a RADARSAT-2 Fine Quad-Pol images of a test-site in Flevoland, Netherlands. The dataset was acquired during the ESA AgriSAR 2009 campaign, devoted to analyze the agricultural fields temporal evolution with PolSAR. The scene is composed mainly by an area of agricultural fields and some sea surface and urban areas. A subset of 8 images has been selected, corresponding to different acquisitions with the same incidence angle (beam FQ13) and ascending passes. The resulting subset is composed of images from April 4th, 2009 to September 29th, 2009 with an acquisition every 24 days. Two crops of these images are shown on Fig. 6.1, corresponding to two different acquisitions on April 14th, 2009 and June 25th, 2009. Each PolSAR image corresponds to a crop of size 4000 x 2000 pixel, thus, the full dataset corregistered contains 4000 x 2000 x 8 pixel, represented in Fig. 6.2.

In Chapter 3 the BPT construction process has been defined and separated into two different parts: the generation of the initial WRAG, Algorithm 3.1, and the construction of the BPT, Algorithm 3.2. As mentioned in Chapter 4, the following elements have to be defined to apply these algorithms over the space-time data:

1. Data elements and connectivity: to generate the initial WRAG, representing all the data elements and its relationships, the data has to be divided into data elements and define a neighborhood or connectivity for each data element. As in the previous chapters, devoted to process a single PolSAR image, the image pixels will be considered as the initial data elements, but a different neighborhood has to be defined over them, taking into account neighboring pixels in space and time dimensions. The 8-connectivity will be applied again over the space dimensions, but the two neighboring pixels at the same position in the time dimension will be added to the neighborhood, resulting in the 10 neighboring pixel scheme presented in Fig. 6.3. Since it is assumed that the dataset is corregistered, a pixel will only be related to the pixels in the same position, corresponding to the same physical area in the scene, over the time dimension.

2. A region model: as in the PolSAR image case, the estimated covariance matrix $\mathbf{Z}$ defined in (4.1) will be employed. This model will have the same advantages and drawbacks mentioned in Chapter 4. For an homogeneous region, under the Gaussian Polarimetric model, it will define completely the polarimetric behavior, but when the region is not homogeneous, it will not be a proper region model.

3. A dissimilarity measure on the region model space: since the region model for the space-time dataset presented is the same as for a single PolSAR image, all the

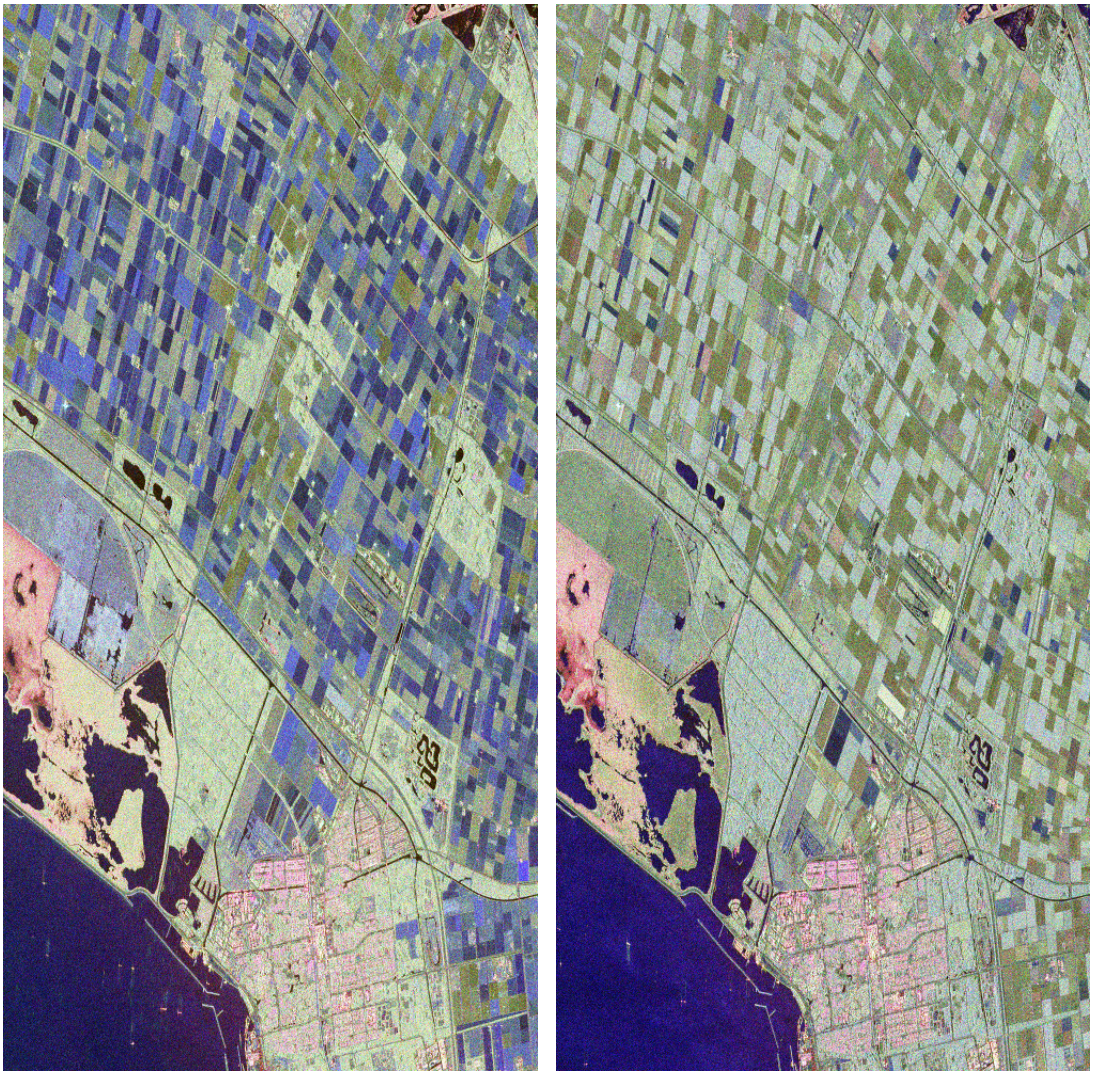

(a) April 14th, 2009 (b) June 25th, 2009

Figure 6.1: Pauli RGB crop images from acquisitions on April 14th, 2009 and June 25th, 2009 ($|S_{hh} + S_{vv}|$, $|S_{hv} + S_{vh}|$, $|S_{hh} - S_{vv}|$)

dissimilarity measures presented in Section 4.3 can be employed for the construction of the BPT in the space-time domain.

Once these elements have been defined, the BPT construction can be addressed directly by the construction algorithms presented in Chapter 3. In the following sections, this representation will be employed and analyzed for the speckle filtering application and also for the change detection applications over the dataset presented in Fig. 6.2. It is worth to notice that, due to the generic definition of the BPT-based processing scheme, only a new connectivity has to be defined to adapt the BPT representation to the time dimension.

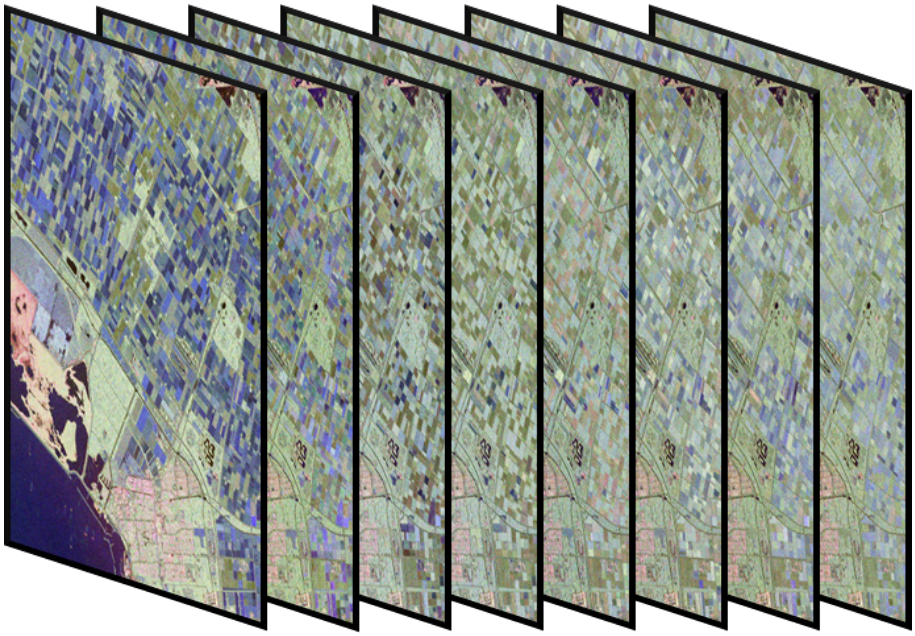

Figure 6.2: Composition with the Pauli RGB images of the full space-time dataset

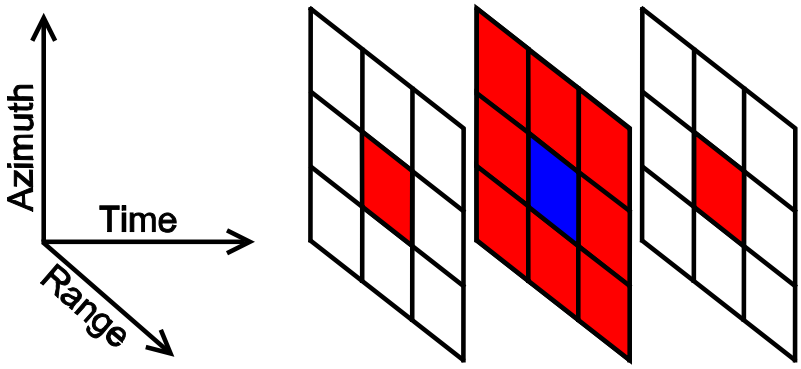

Figure 6.3: Pixel connectivity in the space-time domain. Each pixel, in blue, has 10 neighbors, in red

6.2 Speckle filtering

In Section 5.1 the BPT representation of a PolSAR image has been employed for the speckle filtering application. Two different tree pruning strategies were defined focused on this application: the pruning based on the number of regions and the region homogeneity based pruning. In this section, the region homogeneity based pruning will be employed over the space-time BPT representation, since it has proven to achieve better results than the pruning based on the number of regions with the only drawback of a larger complexity and computing time on some situations.

The pruning criteria ϕ in this case can be exactly the same as for the PolSAR case,

expressed in (5.1), since the same concept of homogeneity can be extended to the space-time regions. Note that the pruning process is defined over the BPT representation and, thus, it is not affected by the change of dimensionality of the underlying dataset, as shown in Fig. 3.9. As mentioned in the previous section, this dimensionality change will affect only the tree construction process. Once the BPT representation has been generated, the same pruning process, that is, the region homogeneity based pruning, for example, can be applied.

In fact, this advantage of the BPT-based processing scheme is related to an important consideration related to the application conceptualization. The BPT-based applications are defined over a data abstraction (the BPT) of the original data, by defining the interesting or meaningful regions, as stated before, then, the application rationale can be extracted from the particular data structure and layout to its most general and abstract form. For the speckle filtering application, this generic rationale can be expressed as "extracting the largest possible homogeneous regions of the dataset", in order to achieve the best possible estimation or characterization of a region model. Note that this is the main idea of the region homogeneity based pruning strategy.

After the tree pruning process, a set of regions Θ is obtained, corresponding to the homogeneous regions of the data into the space-time domain. Due to the difficulties in representing these tree dimensional regions, a cut of these regions at a specific time instant is shown in Fig. 6.4, corresponding to a BPT construction employing the geodesic dissimilarity measure d_{sg} (4.3). Results shown represent the regions intersecting the first image, that is, a cut of the tree dimensional regions over the first acquisition in time dimensions are shown. However, note that these regions are obtained employing samples of different acquisitions.

As a reference, the first image, corresponding to the acquisition on April 14th 2009, has been filtered with the BPT-based PolSAR image filtering defined in the previous chapter. Results are shown on Fig. 6.5 employing the same dissimilarity measure d_{sg} and the same pruning factors δ_p than on Fig. 6.4.

Comparing qualitatively the space-time PolSAR filtering over the first image, Fig. 6.4, with the single PolSAR image filtering of the first image, Fig. 6.5, there are small differences when the pruning factor δ_p is small and these differences become more noticeable as δ_p increases. This effect is produced by the region enlargement in the temporal dimension. It can be seen that the average region size increases in the spatial dimensions for larger values of the pruning factor δ_p, then, the same behavior is expected in the temporal dimension, generating more differences over both figures since the space-time filtering is employing a greater number of pixels from other acquisitions.

To assess the gain obtained when filtering an image employing the space-time dataset

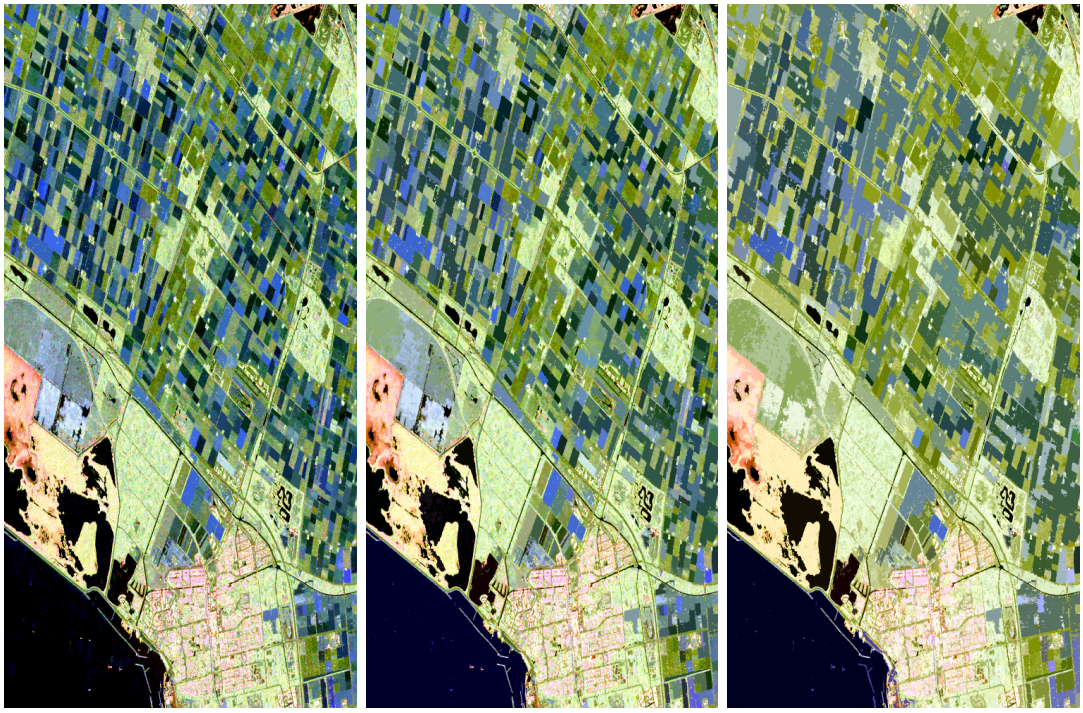

(a) $d_{sg}, \delta_p = -5dB$ (b) $d_{sg}, \delta_p = -3dB$ (c) $d_{sg}, \delta_p = -1dB$

Figure 6.4: BPT three-dimensional space-time filtering over the first image for different pruning factors δ_p ($|S_{hh} + S_{vv}|$, $|S_{hv} + S_{vh}|$, $|S_{hh} - S_{vv}|$)

with respect to a single PolSAR image dataset, the average region depth in the time dimension is shown in Table 6.1. This parameter is calculated as the relation between the number of pixels contained in all the regions intersecting the first acquisition and the pixels contained in a single image. The same BPT has been employed than on Fig. 6.4, constructed employing the geodesic dissimilarity d_{sg}. Note that as the pruning factor δ_p increases, the average region depth in the temporal domain increases, as shown in Fig. 6.4 and Fig. 6.5 for the spatial domain. As it can be seen, when $\delta_p = -3dB$ the first acquisition can be filtered employing approximately 4 times more samples than with a single acquisition, which is an important gain in terms of the speckle filtering application. It is worth to notice that, although regions are larger by means of including pixels from different acquisitions, the homogeneity of the resulting regions is the same as for the single image case, since the region homogeneity based pruning ensures that all the regions have a relative MSE below the pruning factor δ_p, as stated before.

Fig. 6.6 shows the results after applying the same BPT pruning as in Fig. 6.4b over other BPTs constructed employing various dissimilarity measures. As it can be seen, there are small differences among them, making difficult a qualitative comparison over them. To compare these results, Table 6.2 shows a detailed analysis of the pruned regions for

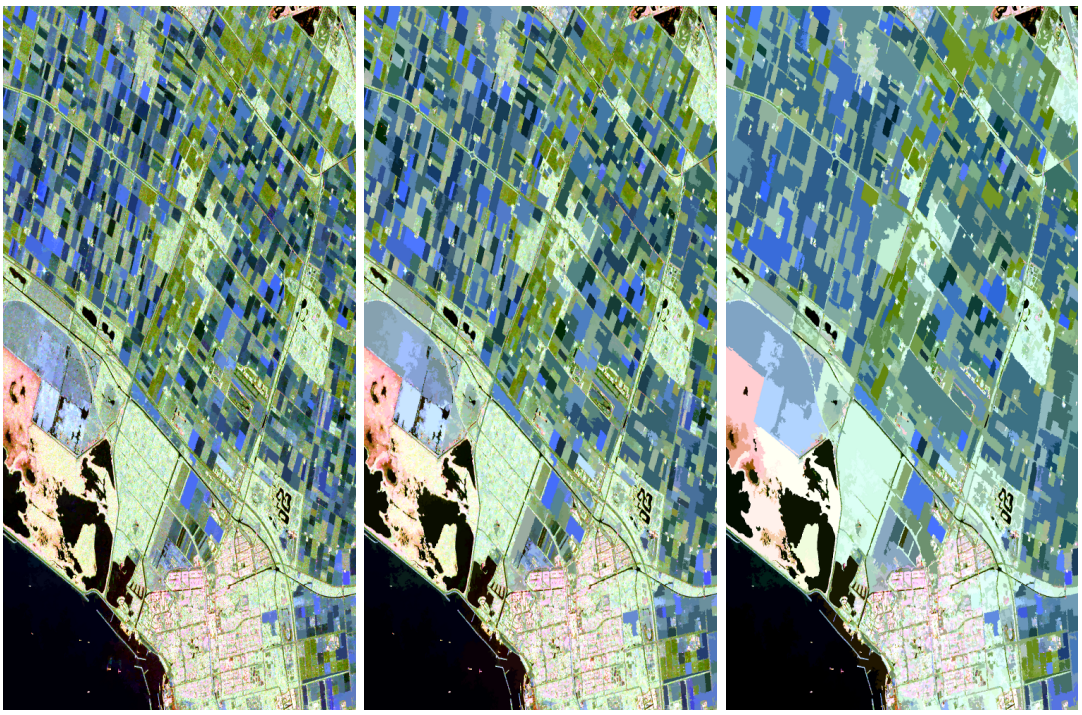

(a) $d_{sg}, \delta_p = -5dB$ (b) $d_{sg}, \delta_p = -3dB$ (c) $d_{sg}, \delta_p = -1dB$

Figure 6.5: BPT PolSAR single image filtering over the first image for different pruning factors δ_p ($|S_{hh} + S_{vv}|$, $|S_{hv} + S_{vh}|$, $|S_{hh} - S_{vv}|$)

δ_p	Pruned regions ∩ 1st acquisition	Average temporal depth
-5 dB	359371	2.067
-4 dB	223969	2.652
-3 dB	127957	4.068
-2 dB	52077	6.727
-1 dB	14660	7.758
0 dB	4666	7.921

Table 6.1: Number of regions intersecting the first acquisition and average region depth in time dimension over those regions for different pruning factors

these different BPTs. As stated for the two-dimensional filtering, the pruning over BPTs constructed employing the geodesic family of dissimilarities obtain a smaller number of regions, resulting in a better adaptation to the data contours. However, for the tree-dimensional filtering, it can be seen that employing the diagonal dissimilarities a smaller number of pruned regions is obtained than employing the full matrix dissimilarities. This behavior is completely different from the observed in the two-dimensional filtering, and it may be due to a larger regions on the temporal dimension, since the average region depth,

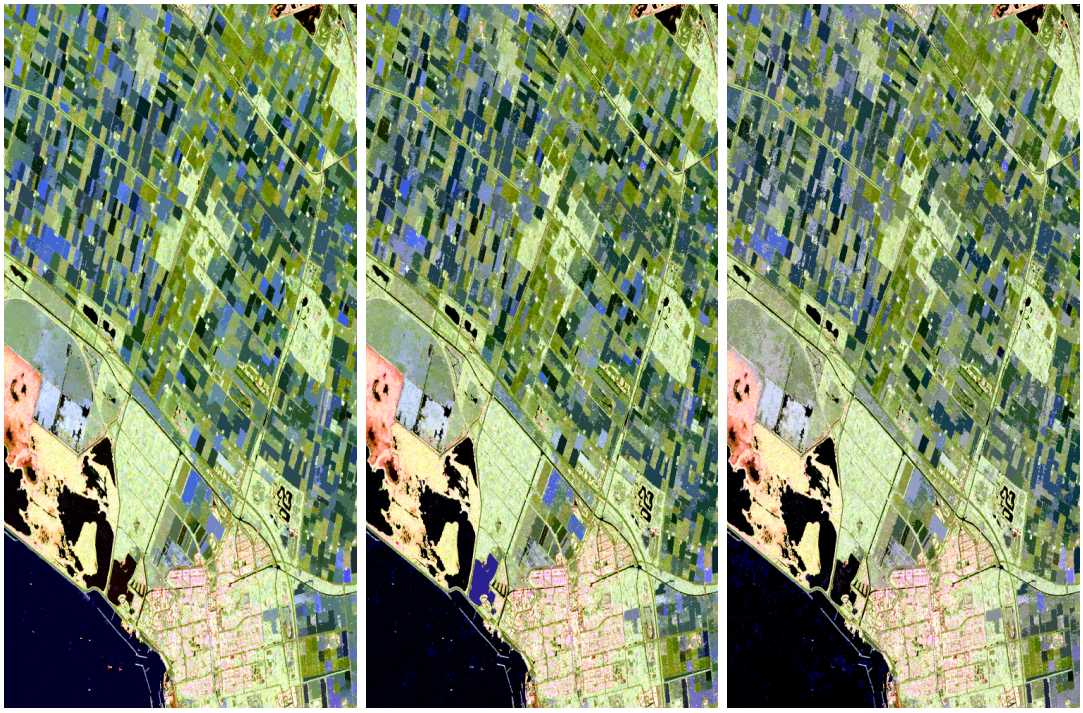

(a) $d_{sw}, \delta_p = -3dB$ (b) $d_{dw}, \delta_p = -3dB$ (c) $d_{dg}, \delta_p = -3dB$

Figure 6.6: BPT three-dimensional space-time filtering over the first image for different BPTs constructed employing various dissimilarity measures ($|S_{hh} + S_{vv}|$, $|S_{hv} + S_{vh}|$, $|S_{hh} - S_{vv}|$)

shown on Table 6.2, is larger when employing the diagonal dissimilarities. Then, it seems that the diagonal dissimilarities can adapt better to the temporal contours whereas the full matrix dissimilarities achieve better adaptation in the spatial domain. The rationale behind this fact is still an open question that may be studied further in the future.

Fig. 6.7 shows the temporal evolution of the entropy (H) and alpha ($\bar{\alpha}$) parameters for two different agricultural fields of potatoes and onions. The results obtained with the BPT for $\delta_p = 0dB$ and $\delta_p = -3dB$ are compared with those obtained with the 7x7 multilook. As it can be seen, qualitatively the evolution of the parameter is similar for all the cases. Differences are produced by estimating the parameter over regions of different sizes in space and time, and not only in space. The flat zones that appear with the BPT based processing are produced when the same region appears over different acquisitions, conforming an homogeneous region that spans various images in the time dimension.

6.3 Change detection

In the previous section, the space-time BPT representation has been employed for the speckle filtering application, as defined in Section 5.1. It has been demonstrated that

		d_{sw}	d_{dw}	d_{sg}	d_{dg}
$\delta_p = -5dB$	Pruned regions	2776493	3179675	2431602	2347080
	Regions ∩ 1st acquisition	397051	491433	359371	392471
	Avg depth 1st acquisition	1.7398	2.4436	2.0669	2.8271
$\delta_p = -3dB$	Pruned regions	603586	436332	495004	209970
	Regions ∩ 1st acquisition	146202	147115	127957	83814
	Avg depth 1st acquisition	3.4577	5.2418	4.0676	6.4275
$\delta_p = -1dB$	Pruned regions	33722	10316	28998	6707
	Regions ∩ 1st acquisition	16668	7673	14660	5243
	Avg depth 1st acquisition	7.8231	7.9654	7.7576	7.9352

Table 6.2: Number of total pruned regions, pruned regions intersecting the first acquisition and average region depth of those regions for different pruning factors δ_p over different BPTs constructed employing various dissimilarity measures

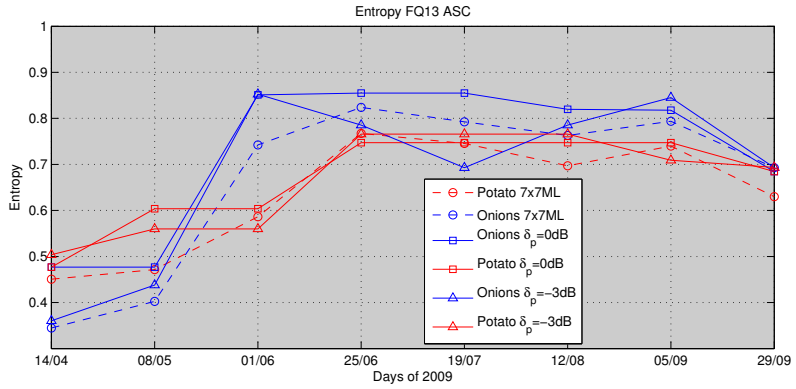

(a) Entropy (H) evolution

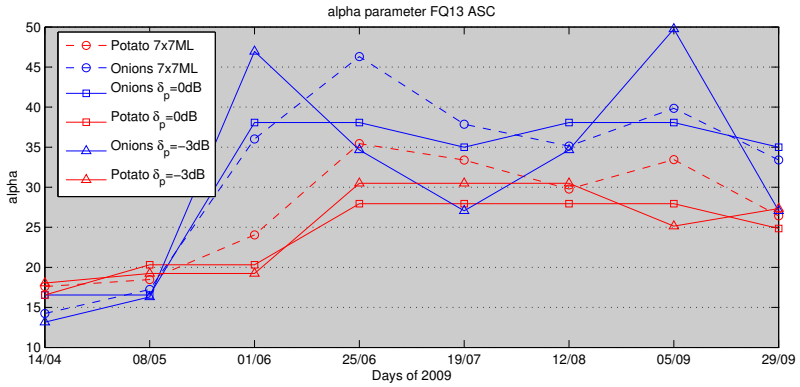

(b) Alpha ($\bar{\alpha}$) evolution

Figure 6.7: Estimated entropy (H) and alpha ($\bar{\alpha}$) temporal evolution over two different agricultural fields with 7x7 multilook and BPT homogeneity based pruning

the pruned regions obtained by the region homogeneity based pruning effectively contain pixels of different acquisitions, conforming homogeneous regions in the space-time domain.

Note that, as mentioned in Chapter 3, a BPT pruning conforms a segmentation of the data. Then, another application that automatically arises when segmenting a space-time dataset is the temporal change detection. In this case, the application is focused on the temporal contours, rather than on spatial contours.

Fig. 6.8 represents the number of contours in the temporal dimension, ranging from no changes, represented in blue, to 7 changes, represented in red color. Results are shown for different pruning factors δ_p and for the BPT constructed employing the geodesic dissimilarity measure d_{sg}, as in the previous figures.

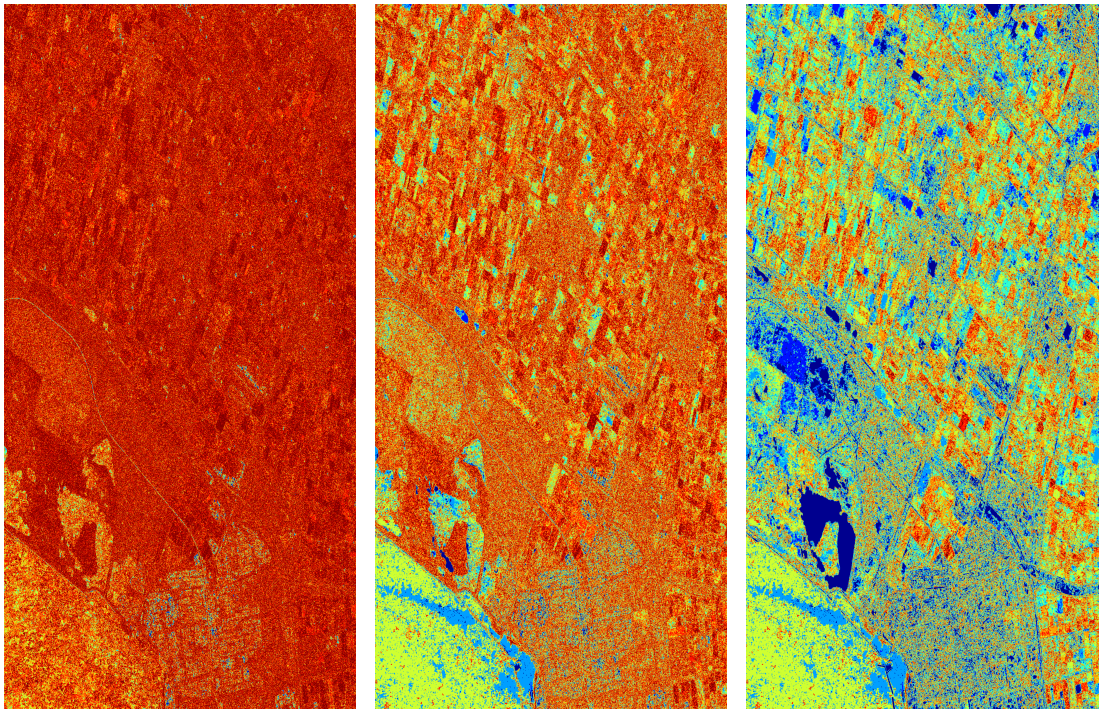

(a) $d_{sg}, \delta_p = -5dB$ (b) $d_{sg}, \delta_p = -3dB$ (c) $d_{sg}, \delta_p = -1dB$

Figure 6.8: Temporal changes detection for different pruning factors δ_p. No changes is represented in blue and 7 changes in red.

As seen before, incrementing the pruning factor δ_p results in bigger regions also in the temporal domain, represented by a smaller number of temporal changes on Fig. 6.8. Analyzing the results closely, it can be seen that there are small blue dots over urban area even for small values of the pruning factor, at $\delta_p = -5dB$. These small dots correspond to point scatters of the buildings or human-made structures that have no-change during the different acquisitions. A detailed image of an urban area and the changes detected for $\delta_p = -5dB$ is shown on Fig. 6.9.

As it can be seen, the agricultural fields area, at the top part of the image appears more reddish, indicating a large number of temporal changes at this detail scale ($\delta_p = -5dB$).

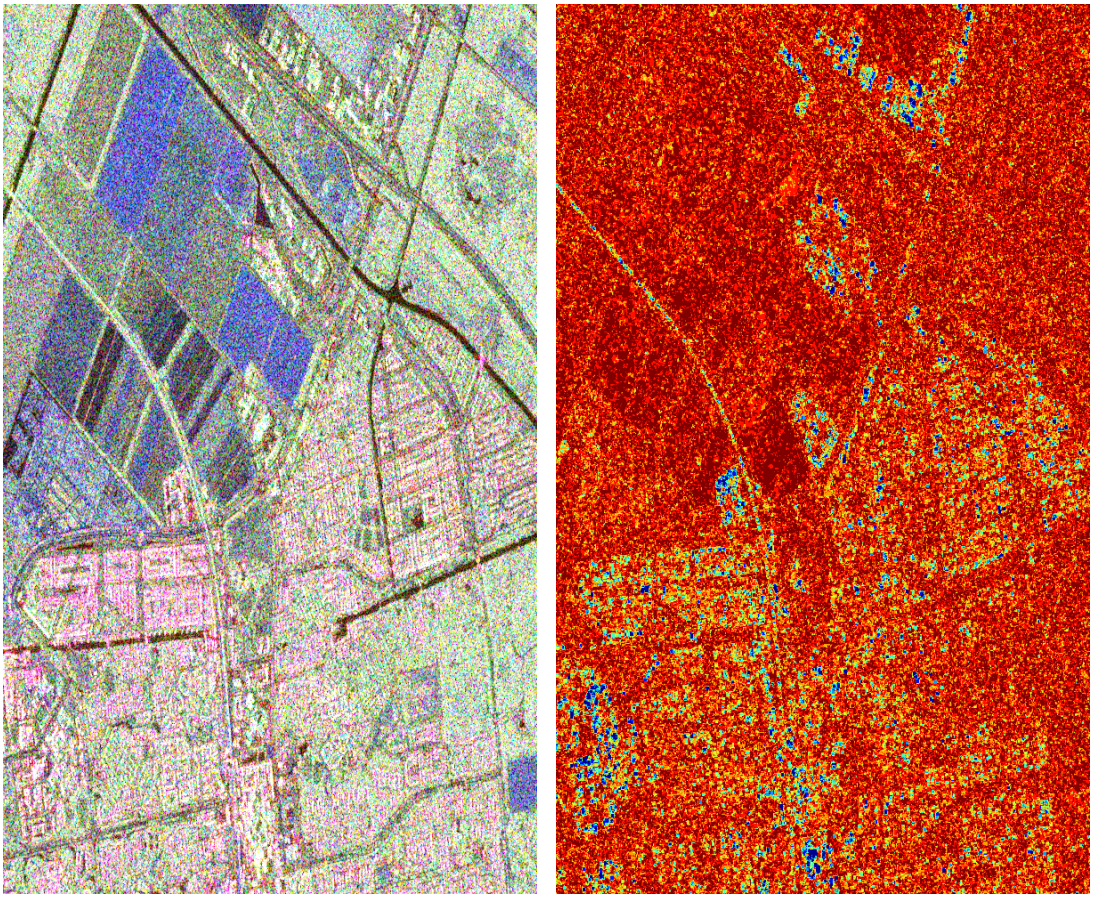

(a) Original Pauli RGB (b) Temporal changes, $d_{sg}, \delta_p = -5dB$

Figure 6.9: Pauli RGB detailed image of an urban area and the changes detected with $\delta_p = -5dB$

The urban areas, on the contrary, appears more yellowish, indicating a smaller number of changes, and, within these areas, there are small structures in blue, indicating no change in the whole sequence of acquisitions, as mentioned before.

When increasing the pruning factor to $\delta_p = -3dB$, as shown on Fig. 6.8b, some other areas appear also in blue, like closed water, which roughness is less affected in wind, having a stable polarimetric behavior. With this pruning factor, the agricultural fields also appear reddish and yellowish, having a large number of temporal changes. However, if the pruning factor is increased to $\delta_p = -1dB$, on Fig. 6.8c, then big differences in terms of temporal changes can be seen over the fields of the agricultural areas. This information can also be seen with the histogram of the region changes for different pruning factors, shown on Fig. 6.10.

Fig. 6.11 shows the same temporal change detection image presented in Fig. 6.8b for different BPTs constructed employing various dissimilarity measures. It can be seen, as stated before, that the images from diagonal dissimilarity measures (Figs. 6.11b and 6.11c)

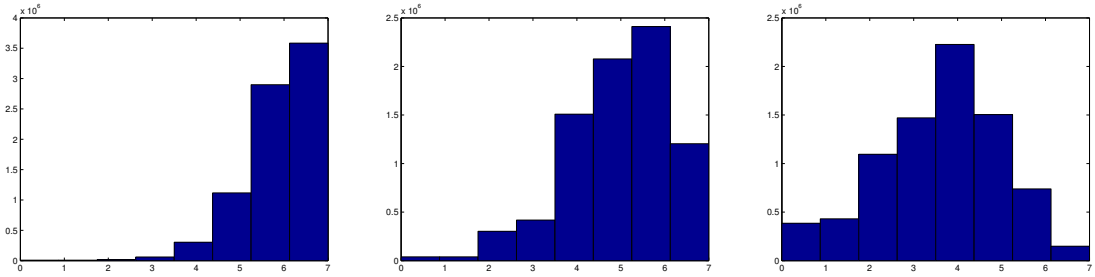

(a) $d_{sg}, \delta_p = -5dB$ (b) $d_{sg}, \delta_p = -3dB$ (c) $d_{sg}, \delta_p = -1dB$

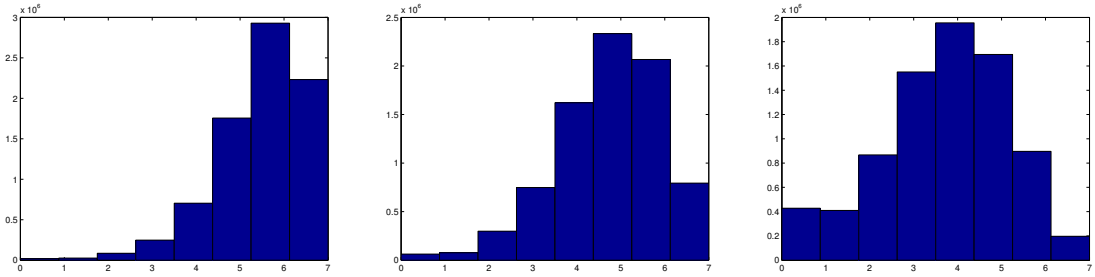

(d) $d_{dg}, \delta_p = -5dB$ (e) $d_{dg}, \delta_p = -3dB$ (f) $d_{dg}, \delta_p = -1dB$

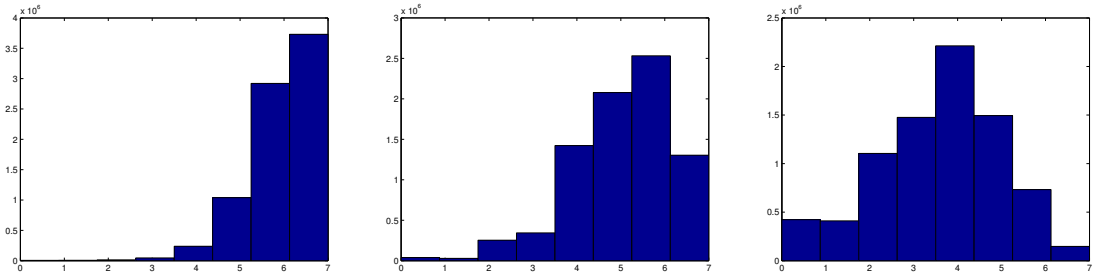

(g) $d_{sw}, \delta_p = -5dB$ (h) $d_{sw}, \delta_p = -3dB$ (i) $d_{sw}, \delta_p = -1dB$

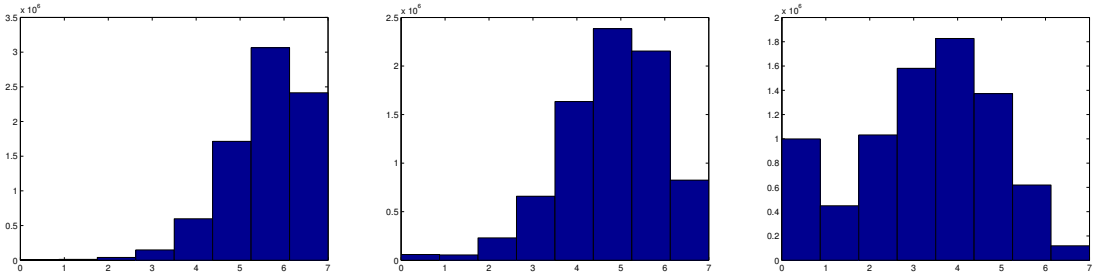

(j) $d_{dw}, \delta_p = -5dB$ (k) $d_{dw}, \delta_p = -3dB$ (l) $d_{dw}, \delta_p = -1dB$

Figure 6.10: Temporal changes histogram for different pruning factors δ_p and various dissimilarity measures

appear slightly more yellowish than the ones from full matrix dissimilarities (Figs. 6.8b and 6.11a). This is related with the fact that diagonal dissimilarities obtain larger regions

in the temporal dimension, as shown in Table 6.2 and on Fig. 6.10. However, the benefits of employing full matrix dissimilarity measures can be seen specially over the sea, which appears as a more contrasted region with respect to the land, on Figs. 6.8b and 6.11a. In fact, it is expected that the sea surface should have a more stable behavior than the earth surface, in terms of its polarimetric response, but this fact can only be properly observed when employing the full covariance matrix information.

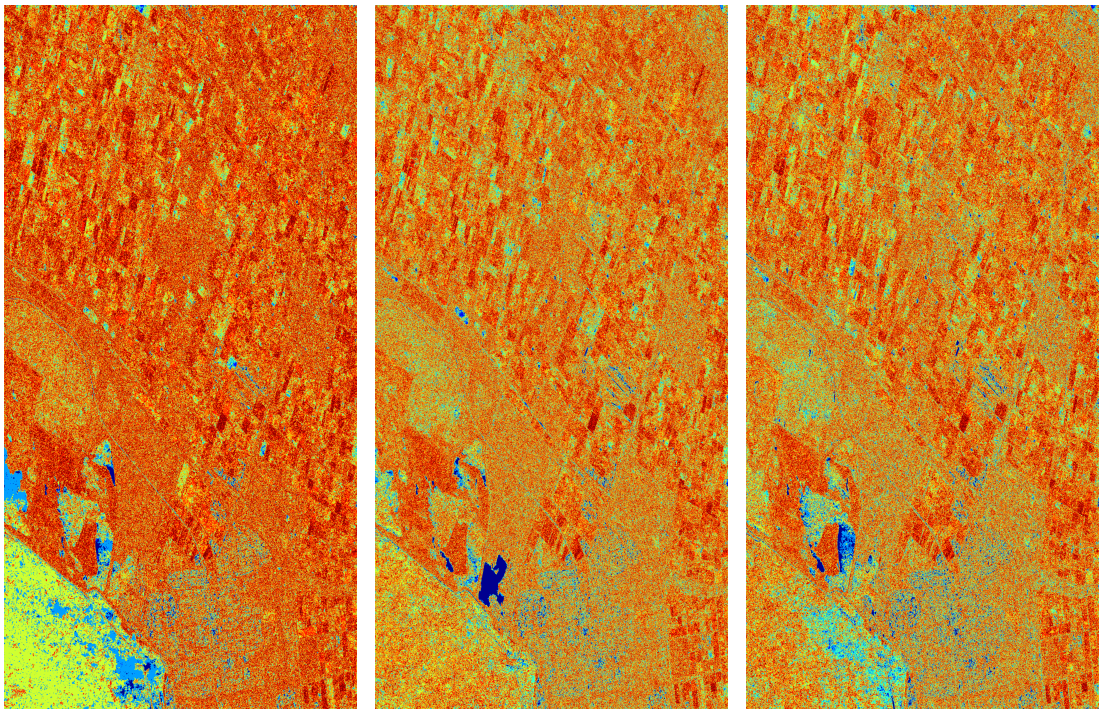

(a) $d_{sw}, \delta_p = -3dB$ (b) $d_{dw}, \delta_p = -3dB$ (c) $d_{dg}, \delta_p = -3dB$

Figure 6.11: Temporal changes detection for different BPTs constructed employing various dissimilarity measures. No changes is represented in blue and 7 changes in red

Note that, when employing full matrix dissimilarity measures, since the BPT construction process and the pruning strategy are exploiting all the polarimetric information in the covariance matrix, the proposed mechanism to detect temporal changes is also sensitive to all this information. Then, the concept of region temporal stability in terms of the whole polarimetric information is automatically obtained by the technique.

Chapter 7

Conclusions and future research lines

The objectives of this master thesis were the implementation and evaluation of the Binary Partition Tree (BPT) as a dataset abstraction of Polarimetric SAR images (PolSAR) and its exploitation for different applications. As a result, the BPT has proven its ability to properly represent the image structure at different scales, being a very useful data abstraction for different applications.

The BPT is a region-based and multi-scale data representation, containing information related to the data structure at different detail levels. A BPT-based processing scheme is proposed in Chapter 3, and it is divided into two main parts: the BPT construction, which is application independent, and the BPT exploitation, which is application dependent. The bottleneck of the whole process is the BPT construction, being the most time and space consuming process of the chain. However, as it is application independent, it is only necessary to do it once, since the BPT generated can be employed for different applications. The BPT hierarchical structure, adapted to the image morphology, enables the employment of fast and simple algorithms for its exploitation. The proposed strategy is through a tree pruning process, searching for the most useful nodes of the tree for the particular application. Moreover, another important property is that this data abstraction allows a generic definition of the application rationale. As an example, the same BPT pruning process, searching for the biggest homogeneous regions of the data, has been employed over a PolSAR image and over a temporal image series dataset without any change. In the same way, this property will allow in the near future the exploitation of the BPT for other applications, like, for instance, region classification, directly over a single image or a temporal image series without significant changes.

The speckle filtering application has been studied in detail, including a comparison

with some other state-of-the-art filtering techniques as the multilook Boxcar and IDAN filters. In this comparison, the BPT-based filtering has outperformed both filters being able to achieve strong filtering over large homogeneous areas while also preserving contours and small details of the data. Additionally, since the BPT construction process is based on a dissimilarity measure, when it employs all the polarimetric information contained within the covariance matrix, then a speckle filtering process sensitive to all this information may be defined. This is a significant improvement over most of the speckle filters present in the literature, like the IDAN filter, that only employ the information contained in the diagonal elements of the covariance matrix to adapt to the image morphology. In this sense, different dissimilarity measures, employing the full polarimetric information and only the diagonal elements of the covariance matrix have been defined and compared, to analyze the benefits of employing all this information. It has been stated that employing the full polarimetric information results in bigger regions equally homogeneous than with only the diagonal information, achieving, thus, a better adaptation and a more accurate representation of the spatial information of the data. Moreover, the full matrix dissimilarity measures are able to see contours in the off-diagonal elements, as seen in Chapter 5, being more robust and sensitive to all the polarimetric information. From all the proposed dissimilarity measures, the geodesic dissimilarity measure, based on the positive definite matrix cone geometry, has achieved the most promising filtering results. The proposed BPT-based filtering technique preserves all the polarimetric information without introducing any bias or distortion over the data, which is an important property for applications requiring a physical inversion of the covariance matrix.

On Chapter 6, this speckle filtering application has been employed over a dataset containing different acquisitions of the same scene at different dates. The same BPT pruning strategy previously defined has been applied directly over the BPT representation of this dataset, which has been constructed by defining a new connectivity over the space-time domain. In this sense, the extension of the BPT to the new domain has been very simple by defining the new pixel relation and handling the temporal dimension in the same manner as the space dimensions. In the speckle filtering context, the defined filter has improved substantially the amount of filtering by employing samples of different acquisitions, while preserving also the contours in the space-time domain. Furthermore, this representation has been employed for the change detection application, by inspecting the contours in the temporal dimension. Some maps representing the number of temporal changes have been generated by this application, and it has been shown that some structures, corresponding to buildings, within urban area are clearly detected as a stable regions by the BPT. On the contrary, the agricultural fields and other areas having significant changes along the temporal dimension appear as a less stable regions, with a large number of changes in this

dimension.

As mentioned in Chapter 3, all the BPT construction and exploitation is closely linked with the region model concept. The dissimilarity measures are defined over the region model space and the same applies to the pruning strategy. Assuming the complex Gaussian polarimetric hypothesis, the estimated covariance matrix has been employed as a region model, but, as stated, this region model is incomplete when representing inhomogeneous regions. Then, more complex region models could also be employed to obtain a better representation of these regions, since the BPT definition is not tied to any particular model.

In this thesis, two different BPT pruning strategies are proposed and evaluated: the BPT pruning based on the number of regions and the region homogeneity based pruning. However, only the region homogeneity based pruning effectively obtains good results independently of the image structure and the region sizes. In the future, more elaborated BPT pruning strategies can be defined for the speckle filtering application and also for different applications. In this sense, new applications can be developed by exploiting the BPT structure, like, for instance, region classification, taking advantage of the multi-scale nature of this data abstraction.

When generating the BPT structure of a space-time dataset, as seen on Chapter 6, different behaviors have been observed in the space and time dimensions with respect to employing the full covariance matrix or only the diagonal elements. This aspect needs a further analysis and probably may be caused as a result of having a completely different evolution in the temporal and the spatial dimensions of the data, that has to be taken into account when generating the BPT structure.

Appendix A

IEEE Transactions on Geoscience and Remote Sensing paper

Filtering and Segmentation of Polarimetric SAR Data Based on Binary Partition Trees

Alberto Alonso-González, Carlos López-Martínez, Senior Member, IEEE, and Philippe Salembier, Fellow Member, IEEE

***Abstract*—In this work, we propose the use of Binary Partition Trees (BPT) to introduce a novel region-based and multi-scale Polarimetric SAR (PolSAR) data representation. The BPT structure represents homogeneous regions in the data at different detail levels. The construction process of the BPT is based, firstly, on a region model able to represent the homogeneous areas, and, secondly, on a dissimilarity measure in order to identify similar areas and define the merging sequence. Depending on the final application, a BPT pruning strategy needs to be introduced. In this work, we focus on the application of BPT PolSAR data representation for speckle noise filtering and data segmentation on the basis of the Gaussian hypothesis, where the average covariance or coherency matrices are considered as a region model. We introduce and quantitatively analyze different dissimilarity measures. In this case, and with the objective to be sensitive to the complete polarimetric information under the Gaussian hypothesis, dissimilarity measures considering the complete covariance or coherency matrices are employed. When confronted to PolSAR speckle filtering, two pruning strategies are detailed and evaluated. As presented, the BPT PolSAR speckle filter defined filters data according to the complete polarimetric information. As shown, this novel filtering approach is able to achieve very strong filtering while preserving the spatial resolution and the polarimetric information. Finally, the BPT representation structure is employed for high spatial resolution image segmentation applied to coastline detection. The analyses detailed in this work are based on simulated, as well as on real PolSAR data acquired by the ESAR system of DLR and the RADARSAT-2 system.**

***Index Terms*—Binary Partition Tree, Polarimetry, Synthetic Aperture Radar, Speckle Filtering, Segmentation.**

I. Introduction

SAR Polarimetry (PolSAR) has demonstrated, specially during the last decade, its significance for the analysis and the characterization of the Earth surface, as well as for the quantitative retrieval of biophysical and geophysical parameters. The capability to explore the complete space of polarization states represents one of the most important properties of PolSAR data, as optimization procedures may be foreseen [1]. The second important property of PolSAR data is its inherent multidimensional nature that allows a more precise characterization of the scattering process at the resolution cell than single polarization data and eventually, a better characterization of the scatter or scatters within that resolution cell.

As a consequence of the coherent recording and processing of the scattered radar echoes, SAR systems are able to generate complex, high spatial resolution images of the observed area, independently of the day-night cycle and with little influence of atmospheric effects. The complex nature of SAR data, together with the fact that the scattering process in the resolution cell may be due to a certain number of elementary echoes, are on the origin of the speckle term. Despite speckle is determined by the scattering process itself, its complexity makes necessary to consider it from a stochastic point of view and then, to assume speckle as a noise term. The characterization of speckle noise must be carefully addressed, specially for PolSAR data, taking into account the nature of the scatters within the resolution cell. In the case of point scatters, as the scattered signal is only due to this single scatter, recorded data are speckle free and the value of the signal itself may be employed to characterize the scattering process and the scatter itself. For distributed scatters, speckle is said to be fully developed in the sense that it is produced from the coherent addition of a large number of individual echoes produced by the individual scatters in the resolution cell. Consequently, in the later case, the information to retrieve refers to the necessary knowledge to specify completely the probability density distribution (pdf) of the acquired PolSAR data. This information must be estimated from the recorded SAR data. In other words, speckle should be filtered from data to grant access to the information of interest.

SAR and PolSAR data are non-stationary as they reflect the complexity of the environment. Assuming that all the stochastic processes involved in the filtering process are ergodic, PolSAR filters must adapt to this non-stationarity. Most of the PolSAR speckle filters presented in the literature deal with non-stationarity by considering locally stationary data. Based on this hypothesis, two major questions arise. On the one hand, the statistical model or pdf under which stationarity shall be defined. On the other hand, the range of this stationarity. With respect to the statistical model, most of the filtering techniques, but also most of the techniques focused on the extraction of quantitative physical parameters, consider the multidimensional complex Gaussian speckle noise model. Under this hypothesis, the covariance, as well as the equivalent coherency or Muëller matrices, represent the most important radar observables, which maximum likelihood estimation (MLE) is the well-known boxcar or multilook filter. This filter privileges estimation accuracy at the cost of spatial resolution. However, the previous assumption of locally stationary data may be violated resulting in a loss of spatial resolution or a mixture of non-homogeneous areas. With the aim to avoid the breaking of the assumption of locally stationary data, a

The authors are with the Department of Signal Theory and Communications, Technical University of Catalonia, Barcelona, Spain, Email: alberto.alons@gmail.com, carlos.lopez@tsc.upc.edu, philippe.salembier@upc.edu

linear minimum mean square error (LMMSE) approach has been proposed in [3] where local statistics are estimated on the basis of edge aligned windows. This idea has been pursued in [4], where an adaptive neighborhood is constructed for every single pixel of the image, taking into account the statistical properties of the pixel itself.

Despite the techniques presented in [3] and [4] have been proved to result into a proper filtering, several questions must be answered in order to finally determine the filtering capabilities. One of the major concerns of the previous approaches is the way they determine local stationarity. On the basis of the Gaussian hypothesis, local stationarity is analyzed only in terms of the diagonal elements of the covariance matrix. Hence, they do not take into account the correlation information determined by the off-diagonal elements of the covariance matrix, despite it has been shown that if considered, optimized filtering capabilities result [5]. In addition, the way local neighbors are obtained in [4] does not guarantee that adjacent and stationary pixels result into the same local area of influence. A final aspect that must be also considered with respect to the estimation of physical information is that a minimum amount of independent samples are mandatory to secure a correct estimation of the information of interest [6].

In order to tackle these issues, we propose the use of Binary Partition Trees (BPT) [7] [22]. The BPT is an image representation that is region-based and multi-scale. The leaf nodes of the tree represent the pixels in the original image, whereas the remaining nodes represent regions that are obtained by the merging of the two neighboring regions represented by two child nodes. The root node corresponds to the entire image. The BPT can represent non-stationary signals because it is region-based, that is, each region can represent a locally stationary part of the signal. Moreover, it is a multi-scale representation allowing, at the same time, the description of very local information thanks to the nodes close the tree leaves and the description of global behavior thanks to the nodes close to the tree root as these nodes represent very large regions. In order to construct and to analyze the BPT in the context of applications, the tree nodes have to be described. An interesting feature of the BPT approach is its flexibility in the sense that it is not restricted to any particular model. In the case of PolSAR data, virtually any model representing the polarimetric information can be used. As it can be seen, the BPT can be considered as a first abstraction step with respect to the original image. The processing strategy involves therefore first, a tree construction and then, a tree pruning to extract either a simplified image for filtering applications or a partition for classification or segmentation applications.

The organization of this paper is as follows: Section II reviews the main characteristics of the PolSAR data and discusses its representation and processing with BPT. Section III analyses in details the tree construction process and focuses in particular on the definition of the similarity between regions used to define the merging order. Once the BPT has been computed, it can be used for many applications. In this paper we discuss filtering application in Section IV as well as a specific segmentation application in Section V. Finally, Section VI presents the conclusions.

II. Processing PolSAR data with BPT

A. SAR Polarimetry

A PolSAR system measures, for every resolution cell, the scattering matrix $\mathbf{S}$. By means of the lexicographic orthogonal basis for 2×2 complex matrices [2], and considering the backscattering direction under the BSA (Backscattering Alignment) convention, $\mathbf{S}$ leads to the target vector $\mathbf{k}$

$$\mathbf{k} = [S_{hh}, \sqrt{2}S_{hv}, S_{vv}]^T \tag{1}$$

where h and v denote the horizontal and vertical wave polarization states, respectively and ^{T} indicates vector transposition. In those cases in which the resolution cell contains only one scatter, or its scattering is largely dominated by a principal one, (1) characterizes completely the scattering process in the resolution, that is, (1) may be employed to characterize the target under study. When the resolution cell contains a certain number of single scatters, (1) corresponds to a coherent combination of the different contributions of this set of single scatters. This combination process receives the name of speckle. As indicated previously, speckle must be considered as a noise term. Under this hypothesis, the information of interest acquires sense only from a stochastic point of view, that is, this information refers to the set of parameters necessary to determine completely the pdf of (1).

The statistical characterization of (1) in case of distributed scatters involves the introduction of a particular pdf to describe its stochastic nature. This process is normally performed under certain simplifying approximations. Under the assumption that the return from a particular resolution cell is due to the coherent addition of the returns from a large number of individual scatters, none of which is dominant, the Central Limit Theorem applies [8], and $\mathbf{k}$ is distributed according to a multidimensional, zero-mean, complex Gaussian pdf

$$p_{\mathbf{k}}(\mathbf{k}) = \frac{1}{\pi^3 |\mathbf{C}|} \exp(-\mathbf{k}^H \mathbf{C}^{-1} \mathbf{k}) \tag{2}$$

where ^{H} is the complex conjugate transpose of a vector and $\mathbf{C}$ represents the covariance matrix

$$\begin{aligned} \mathbf{C} &= E\{\mathbf{k}\mathbf{k}^H\} \\ &= \begin{bmatrix} E\{S_{hh}S_{hh}^H\} & \sqrt{2}E\{S_{hh}S_{hv}^H\} & E\{S_{hh}S_{vv}^H\} \\ \sqrt{2}E\{S_{hv}S_{hh}^H\} & 2E\{S_{hv}S_{hv}^H\} & \sqrt{2}E\{S_{hv}S_{vv}^H\} \\ E\{S_{vv}S_{hh}^H\} & \sqrt{2}E\{S_{vv}S_{hv}^H\} & E\{S_{vv}S_{vv}^H\} \end{bmatrix} \end{aligned} \tag{3}$$

where $E\{x\}$ indicates the statistical expectation of the stochastic process x. It is clear that the approximations that led to (2) will limit its range of applications. Hence, (2) is usually considered as a multidimensional SAR signal model for homogeneous areas. Eq. (2) is not able to describe, for instance, textured scenarios. In these cases, it is necessary to increase the complexity of the statistical model in order to accommodate the texture information.

The MLE of $\mathbf{C}$, i.e., the multilook, under the assumption of statistical ergodicity and homogeneity, is obtained by substituting the statistical expectation by a spatial averaging

$$\mathbf{Z} = \langle \mathbf{k}\mathbf{k}^H \rangle_n = \frac{1}{n} \sum_{i=1}^{n} \mathbf{k}_i \mathbf{k}_i^H \tag{4}$$

where n indicates the number of independent looks or samples employed to estimate $\mathbf{C}$ and $\mathbf{k}_i$ corresponds to the target vector of the ith sample. The estimated covariance matrix $\mathbf{Z}$ receives the name of the sample covariance matrix, which is statistically determined by the Wishart distribution [9] [10] [11]

$$p_{\mathbf{Z}}(\mathbf{Z}) = \frac{n^{3n}|\mathbf{Z}|^{n-3}}{|\mathbf{C}|^n \widetilde{\Gamma}_3(n)} \text{etr}(-n\mathbf{C}^{-1}\mathbf{Z}) \quad (5)$$

where $\text{etr}(\mathbf{X})$ is the exponential of the matrix trace and

$$\widetilde{\Gamma}_3(n) = \pi^3 \prod_{i=1}^{3} \Gamma(n-i+1). \quad (6)$$

As given in (4), $\mathbf{C}$ is estimated from a finite number of samples n. Note that (5) is only valid if $\mathbf{Z}$ is a full rank matrix, which implies $n \geq 3$, otherwise the Wishart distribution cannot be defined. Since the estimated covariance matrix $\mathbf{Z}$ is itself a multivariate random variable, it will present an error with respect to the value to recover, i.e., $\mathbf{C}$. This error might be considered as being produced by a noise component. The advantage of such a characterization is that an optimized filtering might be envisaged.

B. BPT computation and processing strategy

We propose to tackle a large number of applications related to PolSAR data by performing initially a first step of abstraction from the original pixel-based representation of the image. This abstraction step is done through the computation of a BPT and should be as generic or application independent as possible. Once the BPT has been computed, its nodes are characterized and analyzed depending on the application of interest and the final result can generally be obtained through an application dependent tree pruning.

In order to be able to construct the BPT structure in an efficient manner, it would be interesting to decompose the process into simple steps making possible to tackle the process with an iterative algorithm. In this sense, the BPT construction process may be viewed as the introduction of all the hierarchical division-fusion relationships between the image pixels. Hence, this process can be decomposed in the inclusion of each hierarchical relationship, so the tree structure can be constructed iteratively computing one new division-fusion relationship between nodes per step.

In order to construct the BPT structure there are two main approaches:

1) One focused on division or *top-down* approach: In each construction process step a new division relationship is added to the structure, so a selected region of the image is separated into two connected and mutually disjoint regions that will become the two child nodes of the one containing the selected region.
2) One focused on fusion or *bottom-up* approach: Another conceptualization of the construction process is to add a fusion relationship between two neighboring regions of the image at each step. The merging of these two zones will produce a new bigger connected region represented by their parent node.

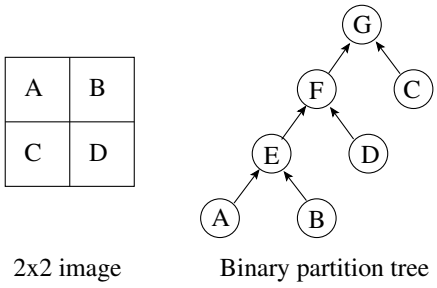

Fig. 1. Illustration of the BPT construction

For computational reasons, it is more feasible to address a *bottom-up tree construction* algorithm, since the number of possible new fusion relationships is more reasonable than the number of possible new divisions for a given construction step.

The BPT should be created in such a way that the most interesting or useful regions are represented. However, a possible solution, suitable for a large number of cases, is to create the tree by keeping track of the merging steps performed by a segmentation algorithm based on region merging, see [12], [13] for example. In the following, this information is referred to as the *merging sequence*. Starting from the initial partition, where each pixel is considered as an individual region, the algorithm merges neighboring regions following a similarity criterion until a single region is obtained.

To completely define the merging algorithm, one has to specify the region model and the merging order. The region model defines precisely how the set of pixels included in the regions are represented. As mentioned in the introduction, almost any model can be employed to represent polarimetric data. In this paper, we will use the average covariance matrix of the pixels included within the region as the region model, then assuming data to be distributed according to 2. The merging order defines the order in which pairs of neighboring regions are merged. In essence this criterion should assess the similarity between regions. Section III will propose, discuss and evaluate various families of criteria suitable for PolSAR data.

Once the tree has been computed, it can be processed or simplified by a pruning algorithm. This step is application dependent. Assume, for example, that we would like to filter the image to reduce the presence of noise. Then, the pruning should remove portions of the tree branches that are close to the original tree leaves in order to preserve as much as possible the image details. By contrast, if the application is based on segmenting or classifying the image, the pruning strategy should analyze each node of the tree looking for relevant segmentation or classification features and the resulting pruning may be much more severe. These cases will be analyzed respectively in Sections IV and V, respectively.

An illustration of the construction process is given in Fig. 1. The original 2x2 image involves four pixels: A, B, C and D. They are considered as initial regions and are represented as tree leaves. The algorithm merges the four regions in three steps. In the first step, the pair of most similar regions, A and B for example, are merged and create region E. Of course,

once E is created, its similarity with respect to its neighboring regions should be evaluated. Assume that after this evaluation, the pair of most similar regions are D and E. They are merged creating region F. Finally, region C is merged with region F and this creates a region corresponding to the region of support of the whole image. In this example, the merging sequence is: $(\{A, B, C, D\}, (A, B)|(D, E)|(C, F))$. This merging sequence defines the BPT as shown in Fig. 1.

III. Merging criteria for BPT construction for PolSAR data

A. Merging criteria and dissimilarity measures

As stated in Section II, the merging sequence determines the BPT construction. Since this process is performed iteratively, a *merging criterion* must be included in the construction process step in order to select the best fusion to perform among all the possible ones. The proposed criterion in Section II is to merge the pair of most similar regions.

In order to evaluate the similarity between regions, a measure has to be defined in the region model space. Actually, any distance in the region model space may be employed. However, other measures than distances can be used and the more general concept of *dissimilarity measure* will be employed in the following. Mathematically, a dissimilarity measure d is similar to a distance in concept, but it has less restrictive properties [17]:

1) $d(A, B) \geq d_0$ (generalized non-negativity)
2) $d(A, B) = d_0 \Leftrightarrow A = B$ (identity)
3) $d(A, B) = d(B, A)$ (symmetry)

where A and B are two region models and d_0 represents the absolute minimum value of the dissimilarity function d. Traditionally, as explained in Section II, in PolSAR the estimated covariance $\mathbf{C}$ or coherency $\mathbf{T}$ matrices are employed to characterize the scattering process over an homogeneous region, as defined in (4), then they may be employed as a region model in the BPT nodes.

In this context, the measure d establishes the similarity between each pair of adjacent regions. At each construction step, the two adjacent nodes with the lowest dissimilarity value are merged. Then, two dissimilarity measures d_1 and d_2 are equivalent if they define the same merging sequence. As a consequence, any monotonic function of the dissimilarity measure will lead to the same merging sequence and then it will produce the same BPT representation.

B. Dissimilarity measures

In this paper, five dissimilarity measures are proposed and analyzed for the BPT construction process. These measures are based on two region features: the polarimetric information, contained in the $\mathbf{Z}$ matrix, as defined in (4), and the region size. Nevertheless, more complex region models and the corresponding dissimilarity measures between them can be defined.

The proposed dissimilarity measures have been classified into two different groups: those using only the information contained in the diagonal elements of $\mathbf{Z}$ and those using the full estimated covariance matrix.

1) Dissimilarity measures using full $\mathbf{Z}$ information: These measures consider all the information contained in the estimated covariance matrix $\mathbf{Z}$ and thus require a complete characterization of the matrix. Note that this fact will induce the need for an initial filtering in order to get full rank matrices, as seen in (5). The dissimilarities are defined between two regions, X and Y, with average covariance matrices $\mathbf{Z}_X$ and $\mathbf{Z}_Y$ and sizes of n_x and n_y pixels, respectively.

- *Symmetric revised Wishart dissimilarity* (RW). The revised Wishart dissimilarity measure was defined in [15], and it is based on a statistical test assuming that the two regions follow a Wishart pdf and that one pdf is known. Thus, it is not symmetric as it depends on which region pdf is assumed to be known. In order to generate a dissimilarity measure, a modified symmetric version is proposed using $d_s(X, Y) = d(X, Y) + d(Y, X)$ and multiplying by the region size term

$$d_{RW}(X, Y) = \left(tr(\mathbf{Z}_X^{-1}\mathbf{Z}_Y) + tr(\mathbf{Z}_Y^{-1}\mathbf{Z}_X)\right) \cdot (n_x + n_y) \tag{7}$$

  where $tr(\mathbf{A})$ denotes the trace of the $\mathbf{A}$ matrix and $\mathbf{A}^{-1}$ its inverse.
- *Ward relative dissimilarity* (WR). In Ward hierarchical clustering [16], a measure based on the error sum-of-squares (ESS) was introduced in order to quantify the information loss when two clusters are joined. The same measure can be employed as the information loss of merging two neighboring regions. However, due to the multiplicative nature of the speckle noise, a modified relative version is proposed including a normalization matrix. The Ward relative dissimilarity d_{WR} (8) is then defined as

$$\begin{aligned} d_{WR}(X, Y) = n_x \cdot \left\| \mathbf{N}_{XY}^H \left(\mathbf{Z}_X - \mathbf{Z}_{XY}\right) \mathbf{N}_{XY} \right\|_F^2 + \\ n_y \cdot \left\| \mathbf{N}_{XY}^H \left(\mathbf{Z}_Y - \mathbf{Z}_{XY}\right) \mathbf{N}_{XY} \right\|_F^2 \end{aligned} \tag{8}$$

  where $\mathbf{Z}_{XY}$ denotes the average matrix of the region $X \cup Y$, $\mathbf{A}^H$ denotes matrix $\mathbf{A}$ hermitian transpose, $\mathbf{N}_A$ denotes the normalization matrix of $\mathbf{Z}_A$, defined as

$$\mathbf{N}_A = \begin{pmatrix} \sqrt{Z_{A11}} & 0 & 0 \\ 0 & \sqrt{Z_{A22}} & 0 \\ 0 & 0 & \sqrt{Z_{A33}} \end{pmatrix}, \tag{9}$$

  and $\|\mathbf{A}\|_F$ denotes the Frobenius matrix norm.

2) Dissimilarity measures using diagonal $\mathbf{Z}$ elements: These measures only employ the diagonal elements of the estimated covariance matrix $\mathbf{Z}$, corresponding to the power received at each polarization component. Consequently, they do not require any initial filtering, but they are not sensitive to the off-diagonal components of the covariance or coherency matrices.

- *Diagonal relative normalized dissimilarity* (DN) is based on the euclidean norm of the normalized difference of the diagonal vector. The difference of the diagonal vectors is normalized by their sum, which results in a value bounded in the interval $[-1, 1]$ for each diagonal element. The dissimilarity measure is obtained computing the euclidean

norm of the resulting vector and multiplying the resulting value by the sum of region sizes, as denoted in (10).

$$d_{DN}(X,Y) = \left(\sum_{i=1}^{3} \left(\frac{Z_{X\,ii} - Z_{Y\,ii}}{Z_{X\,ii} + Z_{Y\,ii}} \right)^2 \right)^{1/2} \cdot (n_x + n_y) \tag{10}$$

where A_{ij} is the index notation for the (i,j)th element of matrix $\mathbf{A}$.

- *Diagonal relative dissimilarity* (DR) is computed as the euclidean norm of the sum of relative errors between the diagonal elements multiplied by the size of the $X \bigcup Y$ region. Note that this dissimilarity measure d_{DR} (11) is not bounded, as opposite of d_{DN} (10) because the value interval of the resulting vector is open $[0, \infty)$

$$\begin{aligned} d_{DR}(X,Y) &= \left(\sum_{i=1}^{3} \left(\frac{Z_{X\,ii} - Z_{Y\,ii}}{Z_{Y\,ii}} + \frac{Z_{Y\,ii} - Z_{X\,ii}}{Z_{X\,ii}} \right)^2 \right)^{1/2} \\ &\quad \cdot (n_x + n_y) \\ &= \left(\sum_{i=1}^{3} \left(\frac{(Z_{X\,ii} - Z_{Y\,ii})^2}{Z_{X\,ii} Z_{Y\,ii}} \right)^2 \right)^{1/2} \cdot (n_x + n_y). \end{aligned} \tag{11}$$

- *Diagonal revised Wishart dissimilarity* (DW) is based on the symmetric revised Wishart dissimilarity as it is defined in (7), but only considering the diagonal elements and setting all off-diagonal elements to 0, which simplifies the matrix inversion as being the inverse of the diagonal elements. After some mathematic simplifications, it can be expressed as

$$d_{DW}(X,Y) = \left(\sum_{i=1}^{3} \left(\frac{Z_{X\,ii}^2 + Z_{Y\,ii}^2}{Z_{X\,ii} Z_{Y\,ii}} \right) \right) \cdot (n_x + n_y). \tag{12}$$

The objective of the previous division among distances will be to focus specifically on the analysis of the effects of considering the off-diagonal elements of the covariance and coherency matrices when processing PolSAR data under the Gaussian assumption. Additionally, it would be possible to determine and to establish those conditions that a distance should fulfill to perform a correct processing of PolSAR data, for speckle filtering or for any other different application. First of all, the distances should be invariant under similarity transformations of the special unitary group of matrices. For example, the approach followed by [3] would be congruent with this condition, since Span is invariant under these transformations. The distance function employed in [4] and the dissimilarity measures that consider only diagonal elements would not fulfill such a condition since only diagonal elements are considered. In this sense, only the distance d_{RW} would be invariant. Nevertheless, the invariance property is not sufficient to perform a correct processing of PolSAR data. A clear example is the approach in [3]. Despite this technique is invariant under similarity transformations, it is not sensitive to the off-diagonal information. Consequently, suitable distances, a part from being invariant under similarity transformations, should consider all the information provided by the covariance and coherency matrices, as for instance the d_{RW} distance.

IV. BPT pruning for PolSAR data filtering

As described in [7], the BPT is a very attractive representation since it proposes a reduced number of regions which are assumed to be the most homogeneous at different scales. This idea can be exploited to develop PolSAR advanced speckle noise filtering. The main purpose is to obtain a subset Θ of meaningful nodes, from the tree representing homogeneous regions, which can be used to have a better estimation of the region covariance matrix (4) maintaining the image spatial resolution. This process consisting of a selection of a subset Θ of nodes from the Binary Partition Tree is called *BPT pruning*.

In this section, two main strategies for tree pruning focused on PolSAR speckle filtering are discussed: pruning based on the number of regions and pruning based on the region homogeneity.

A. Pruning based on the number of regions

One of the simplest possible tree pruning strategy is to select the set Θ as a fixed number n_r of regions, corresponding to the most different regions of the tree. If the difference between regions is evaluated using the same dissimilarity measure used for the BPT construction process, then it is equivalent to stop the construction process when n_r regions are achieved. At that point, an image segmentation with the n_r most different regions, in terms of the employed dissimilarity measure, is obtained. Finally the filtered image is obtained by representing all pixels within each region with the mean covariance matrix, which corresponds to the region model. In the following, this process will be called *BPT pruning based on the number of regions*.

For a quantitative evaluation of this filtering process, a simulated 128x128 pixels PolSAR image is proposed in Fig. 2 with four square regions of equal size. Simulated data have been generated using the complex Gaussian polarimetric model presented in [14], assuming a reflection symmetric target since most of natural targets follow this model, with covariance matrix $\mathbf{C}$ of the form

$$\mathbf{C} = \sigma_{HH} \begin{pmatrix} 1 & 0 & \rho\sqrt{\gamma} \\ 0 & \varepsilon & 0 \\ \rho^*\sqrt{\gamma} & 0 & \gamma \end{pmatrix} \tag{13}$$

where * denotes complex conjugate.

Three sets of images have been simulated according to (13) with $\gamma_i = 1$ and $\varepsilon_i = 0.1$ and variations for σ_{HHi} and ρ_i in different regions $i = 1 \ldots 4$ as denoted in Fig. 2a

1) Variations in intensity: $\rho_i = 0.5$; $\sigma_{HH} = \{1,\ 9,\ 25,\ 49\}$
2) Variations in correlation: $\rho = \{0,\ 0.25e^{j\pi},\ -0.5,\ 0.75e^{-j\pi}\}$; $\sigma_{HHi} = 1$
3) Variations both in correlation and in intensity: $\rho = \{0,\ 0.25e^{j\pi},\ -0.5,\ 0.75e^{-j\pi}\}$; $\sigma_{HH} = \{1,\ 9,\ 25,\ 49\}$

A matrix relative error measure is also proposed in order to asses quantitatively the goodness of the processed image X in comparison with the ground truth Y

$$E_R(X,Y) = \frac{1}{n_h \cdot n_w} \sum_{i=1}^{n_h} \sum_{j=1}^{n_w} \frac{\|\mathbf{X}^{ij} - \mathbf{Y}^{ij}\|_F}{\|\mathbf{Y}^{ij}\|_F} \tag{14}$$

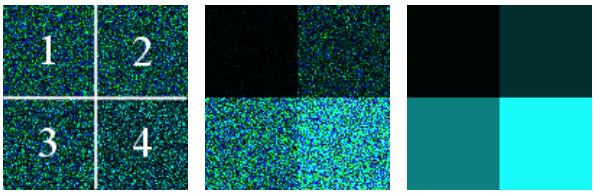

(a) (b) (c)

Fig. 2. Simulated PolSAR images with 4 equal size zones. C_{11}, C_{22} and C_{33} are assigned to blue, red and green channels. a) Zones shape and numeration, b) and c) one realization of the image with intensity variations and image ground-truth, respectively.

where n_h and n_w are the image height and width in pixels, respectively, $\mathbf{X}^{ij}$ represents the (i,j)th pixel value of image X and $\|\cdot\|_F$ denotes Frobenius matrix norm. Note that the relative error measure defined in (14) is based on the inverse signal to noise ratio (SNR^{-1}) averaged for all the pixels in the image.

Fig. 3 presents a filtering quality comparison, in terms of (14), of the proposed BPT pruning based on the number of regions with the dissimilarity measures defined in Section III. The number of regions n_r is shown in the upper horizontal axis with logarithmic scale. In the lower horizontal axis, the mean region area in pixels is stated, calculated as $(n_h \cdot n_w)/n_r$. The plot also compares the BPT pruning based on the number of regions with the multilook filter (4), for different window sizes. In this case, the mean region size corresponds to the nominal window size, i.e. n in (4). For the BPT based filtering, an initial 3x3 multilook has been applied in order to get full rank matrices needed for d_{RW} (7) and d_{WR} (8) dissimilarities. The results have been obtained averaging 25 different realizations of the simulated image. For the multilook and the d_{RW} cases the standard deviation values resulting from the 25 realizations are also included. The rest of the curves present similar values to the d_{RW} case.

When there are variations in intensity, Fig. 3a and 3c, for small values of region size the results of the BPT pruning based on the region number are very close to the Boxcar filter, as the region mixture is negligible. For region sizes in the order of 50-100 pixels (equivalent to 9x9 Boxcar filter) the error measure starts to increase rapidly for the Boxcar filter as the region mixture near the contours becomes appreciable. On the contrary, the BPT is able to adapt to the image morphology minimizing this region mixture effect and thus, the error measure keeps decreasing when the average region size increases, achieving the best error bounds near the 4 regions which should be the optimum as the simulated image has exactly four different regions.

In Fig. 3b the error plots are completely different since only the dissimilarity measures that use all the covariance matrix information are sensitive to the region contours. Therefore, the regions generated using d_{DN} (10), d_{DR} (11) and d_{DW} (12) rapidly start mixing non-homogeneous regions and never improve the multilook filter performance. On the other hand, full matrix dissimilarities d_{RW} (7) and d_{WR} (8) can adapt to the image morphology and overcome Boxcar error measures with higher region sizes. Note that, in Fig. 3b, the intensity

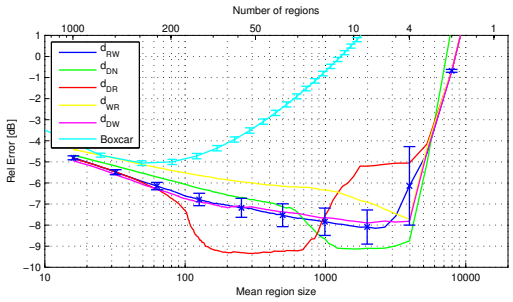

(a) Variation in intensity

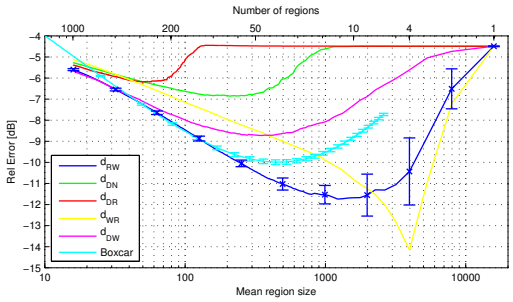

(b) Variation in correlation

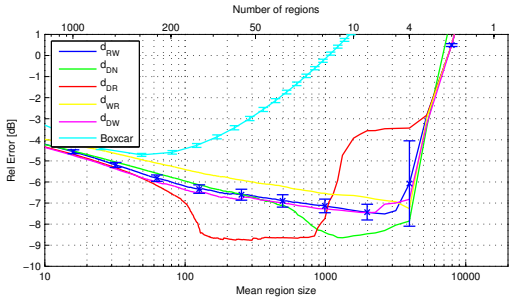

(c) Variations both in correlation and in intensity

Fig. 3. Relative matrix error for simulated images with 4 equal size zones filtered with a BPT pruning based on the region number. Results have been obtained averaging 25 realizations.

is constant over the entire image. As a result, the mixing of different regions has not a dramatic impact in the relative error as in Fig. 3a and 3c. This also explains why the minimum of the Boxcar error occurs at region sizes about 400-500 pixels (21x21 multilook filter).

Comparing the different proposed dissimilarity functions, when there are variations in intensity d_{DN} (10) and d_{DR} (11) can achieve better performance in terms of relative error, but the minimum can be far away from the 4 regions case. Wishart based dissimilarities, either diagonal d_{DW} (12) or full matrix d_{RW} (7), have very constant and stable behavior when increasing the mean region size and achieve the best results near the point corresponding to 4 regions. Ward based dissimilarity d_{WR} (8) can have poor performance when compared with other dissimilarities but it is the only one that presents a clear minimum always at exactly 4 regions. At this point, its performance in terms of relative error is comparable to the Wishart based dissimilarities. When intensity is constant, only

full matrix Wishart and Ward dissimilarities can adapt to the image morphology and outperform Boxcar performances. In this case, Ward dissimilarity performance at 4 regions is near 3 dB better than the Wishart minimum at about 10 regions.

Fig. 4 shows the results of applying the pruning based on the number of regions in one realization of the simulated data with variations both in correlation and in intensity compared with Boxcar filtering. As it may be seen in Fig. 4a, 4b and 4c, as the Boxcar filter size increases the amount of speckle noise reduction and the quality of the estimation increases. However, the spatial resolution is degraded considerably as the filter size increases, blurring completely the region contours. In Fig. 4d, 4e and 4f, the number of regions n_r is fixed to 100 and different dissimilarity measures for BPT construction are compared. All of them are able to detect the main contours of the four zones with this number of regions. The contours detected inside the main regions are completely random and they are due to the speckle noise present on the image. In Fig. 4g, 4h and 4i, the symmetric revised Wishart dissimilarity measure d_{RW} (7) has been employed and the results are shown for different number of regions. For n_r = 4, as it may be observed, there is a good preservation of the spatial resolution, but also of the polarimetric information under the Gaussian hypothesis. A comparison between Fig. 2c and Fig. 4i exhibits that the filtered image is quite close to the ideal one. This similarity is also supported by the fact that the relative error function (14), which is also sensitive to the polarimetric information, presents very low values. As detailed previously, each region is represented by the average covariance matrix which is the MLE under the Gaussian hypothesis [21]. Furthermore, as n_r decreases the number of contours in the filtered image decreases, reducing the effect of the speckle noise, but new contours never appear.

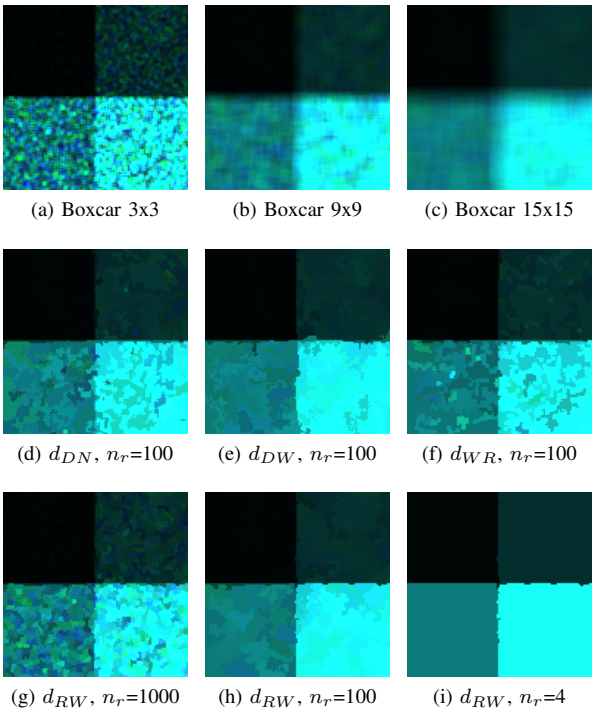

(a) Boxcar 3x3 (b) Boxcar 9x9 (c) Boxcar 15x15

(d) d_{DN}, n_r=100 (e) d_{DW}, n_r=100 (f) d_{WR}, n_r=100

(g) d_{RW}, n_r=1000 (h) d_{RW}, n_r=100 (i) d_{RW}, n_r=4

Fig. 4. Boxcar and BPT filtering (pruning based on the region number) in one of the simulated PolSAR images with variations in both correlation and intensity employing different dissimilarity functions. C_{11}, C_{22} and C_{33} are assigned to blue, red and green channels, respectively.

B. Region homogeneity based pruning

The previous pruning strategy is very simple since no new criterion nor evaluation are needed for pruning. The same dissimilarity measure employed for the BPT construction is employed for pruning, obtaining the n_r most different regions from the tree. However, it presents some drawbacks when applied to real images:

1) The averaged covariance matrix $\mathbf{Z}$ as a region model is a good representation of the region when it is homogeneous in the Gaussian case, but in the upper nodes of the tree, corresponding to larger regions of the image, this assumption is not true. Therefore, a pruning criterion based only on this model is not good for BPT pruning.
2) The optimum region number is completely dependent on the image structure and also on the employed dissimilarity measure, as seen in Fig. 3. In practical situations, it is almost impossible to fix a priori the optimum number of regions for a given PolSAR image.
3) The proposed dissimilarity functions have a strong dependence with the region sizes, which is needed for a good multiscale representation within the BPT. However, when employed as a pruning criterion, the obtained segmentation has also this strong dependence. This fact implies that, for example, it is very unlikely to obtain in the same segmentation point scatters and large homogeneous regions.

To solve the mentioned problems, the pruning criterion should not rely exclusively on the region model and it should be independent of the region size. A new BPT pruning strategy is proposed according to this principle with its pruning criterion focused on a region homogeneity measure ϕ.

The proposed criterion ϕ_R measures the average error produced at representing each region X by its model $\mathbf{Z}_X$:

$$\phi_R(X) = \frac{1}{n_x}\sum_{i=1}^{n_x}\frac{\|\mathbf{X}^i - \mathbf{Z}_X\|^2}{\|\mathbf{Z}_X\|^2} = \frac{1}{n_x\|\mathbf{Z}_X\|^2}\sum_{i=1}^{n_x}\|\mathbf{X}^i - \mathbf{Z}_X\|^2 \tag{15}$$

where $\mathbf{X}^i$ represents the covariance matrix for the ith pixel within region X and n_x is the number of pixels in X. It can also be interpreted as the mean loss of information that occurs when modeling the region by its estimated covariance matrix (4).

Then, the region homogeneity based pruning will select from the tree a set of regions Θ corresponding to the largest regions having a homogeneity value below a pruning threshold δ_p. This pruning process can be implemented using a top-down approach, selecting the first nodes X_i that fulfill the homogeneity criterion $\phi_R(X_i) < \delta_p$. Starting from the root node X_r, it will be checked for homogeneity. If it is not homogeneous, having $\phi_R(X_r) \geq \delta_p$, it will be split into its two child nodes, otherwise it will be added to Θ. Iteratively, each region will be checked for homogeneity and will be split or added to Θ depending on the result. Subsequently the set of

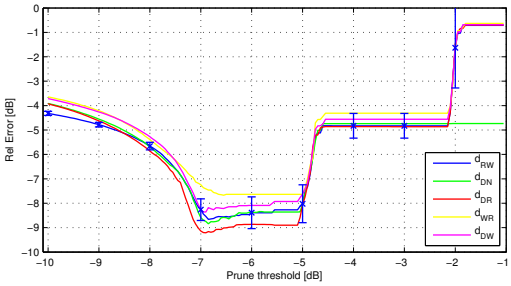

(a) Variation in intensity

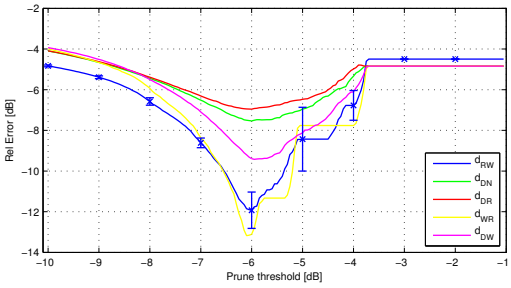

(b) Variation in correlation

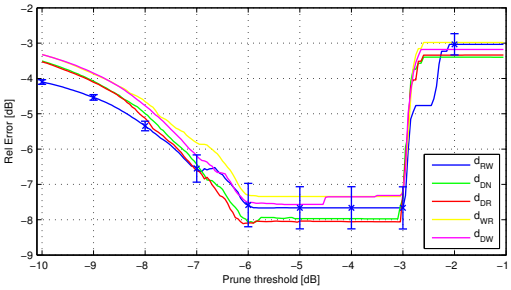

(c) Variations both in correlation and in intensity

Fig. 5. Relative matrix error for simulated images with 4 equal size zones filtered with a region homogeneity based pruning. Results have been obtained averaging 25 realizations.

regions Θ will conform a segmentation of the image having a mean information loss below the threshold δ_p for all regions.

This region homogeneity based pruning has been also evaluated as a PolSAR speckle filtering process with the same simulated images as the pruning based on the number of regions. The results in terms of relative error (14) for different pruning threshold values and dissimilarity measures are shown in Fig. 5. As for the BPT pruning based on the region number, the results have been obtained after averaging 25 different realizations of the simulated image, where the standard deviation values for the d_{RW} distance are included.

As it can be seen in Fig. 5, independently from the image structure, the homogeneity based pruning behavior versus the prune threshold is very similar for all the dissimilarity measures employed for BPT construction. There is always a minimum in terms of relative error located at the same position. There is also a value for the pruning threshold that is almost optimum for all the images at about -6 dB for δ_p.

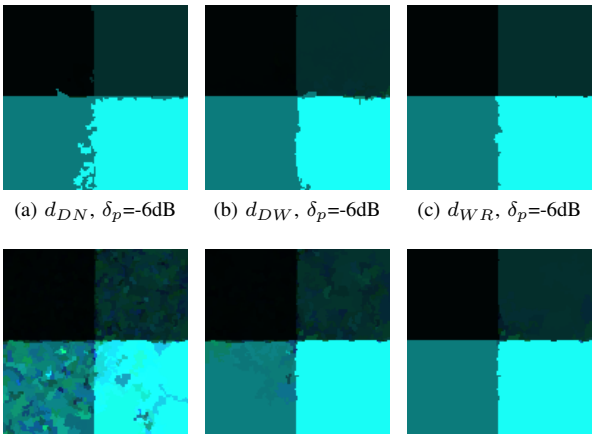

(a) d_{DN}, δ_p=-6dB (b) d_{DW}, δ_p=-6dB (c) d_{WR}, δ_p=-6dB

(d) d_{RW}, δ_p=-8dB (e) d_{RW}, δ_p=-7dB (f) d_{RW}, δ_p=-6dB

Fig. 6. BPT homogeneity pruning filtering in one of the simulated PolSAR images with variations in both correlation and intensity employing different dissimilarity measures and prune thresholds. C_{11}, C_{22} and C_{33} are assigned to blue, red and green channels, respectively.

When there are variations in intensity, in Fig. 5a and 5c, a wide set of values for δ_p, ranging from -6dB to -4dB or -3dB, are near optimum. When there are only variations in correlation, as seen in Fig. 5b, there is not such a wide optimum set of values, but a clear minimum is also located at -6 dB for δ_p.

Comparing Fig. 3 and Fig. 5, the minimum values in terms of relative error obtained in BPT pruning based on the number of regions are approximately preserved in the region homogeneity pruning. However, since the homogeneity measure in which pruning is based on is sensitive to all the covariance matrix elements, a small improvement can be observed when the dissimilarity measure is not sensitive to region changes, as seen in Fig. 5b for diagonal dissimilarities d_{DN} (10), d_{DR} (11) and d_{DW} (12), which contributes making the homogeneity based pruning more robust.

Fig. 6 shows the results of applying the BPT homogeneity based pruning in one realization of the simulated data with variations both in correlation and in intensity. In Fig. 6a, 6b and 6c the pruning threshold δ_p has been fixed to -6 dB, which is the optimum value for all the simulated images, as seen in Fig. 5. With this pruning threshold, the BPT homogeneity pruning employing all the dissimilarity measures obtain a filtered image very close to the ideal one shown in Fig. 2c, obtaining a good preservation of the polarimetric information under the Gaussian hypothesis. There are only small differences in the detected contours, which are more accurate for d_{WR} (8) and d_{RW} (7), since they are sensitive to all the covariance matrix information. In Fig. 6d, 6e and 6f, the symmetric revised Wishart dissimilarity measure d_{RW} has been employed and different pruning thresholds are shown. Comparing it with the pruning based on the region number results for the same image, in Fig. 4, they achieve similar results, specially for high pruning threshold values. Note that the region contours are exactly the same, since the two BPT pruning processes are performed over the same tree.

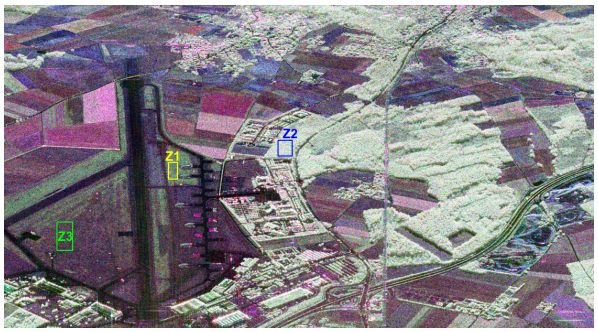

(a) Original

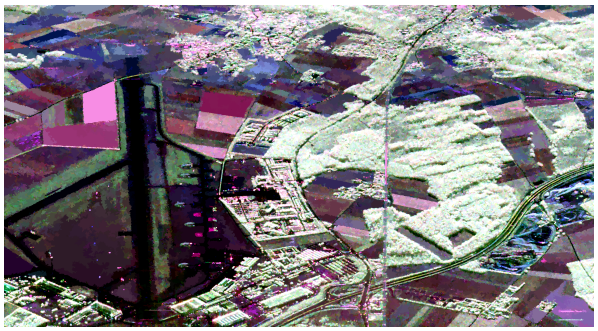

(b) d_{RW}, δ_p=-2dB

Fig. 7. Pauli original image of Oberpfaffenhofen (a) and processed image (b) employing homogeneity based pruning. RGB channels are assigned to $|hh - vv|$, $|hv + vh|$ and $|hh + vv|$, respectively. Selected homogeneous regions are marked over the original image.

Nevertheless, the most important properties of this new pruning strategy is to overcome the stated drawbacks of the BPT pruning based on the region number enumerated at the beginning of this section. This advantage can be seen more clearly with real data.

C. Real PolSAR data filtering

The BPT-based PolSAR filtering approach has been considered also with real PolSAR data acquired in a measurement campaign conducted by the DLR in 1999 with its experimental E-SAR system, over the Oberpfaffenhofen test-site, southern Germany. Data were collected at L-band, with a spatial resolution of $1.5m \times 1.5m$ in fully polarimetric mode. Fig. 7a presents the original Pauli RGB image of the mentioned data set.

The previous data set has been processed with a 7x7 multilook as a reference, the IDAN[1] [4] filter, and the discussed BPT pruning approaches: pruning based on the number of regions and region homogeneity based pruning. The IDAN approach has been considered in this work as it is very similar to the BPT-based approach, since it considers the selection of an adaptive neighborhood and filters it by assuming a multilook. As indicated by the authors [4], this approach is focused on data filtering, whereas they also introduce an approach based on the linear minimum square error when the

[1]The PolSARPro [18] IDAN implementation has been employed for this work, with a maximum window size parameter of 100 pixels.

(a) Original (b) 7x7 multilook (c) IDAN

Fig. 8. Detail Pauli RGB images. (a) Original, (b) filtered with 7x7 multilook and (c) filtered with IDAN.

focus is on spatial resolution preservation. Fig. 7b shows one processed image after applying an homogeneity based pruning with $\delta_p = -2dB$ over a BPT constructed employing the revised Wishart d_{RW} dissimilarity (7). Fig. 8 shows a detailed area of the image and results after applying the multilook and IDAN filters whereas Fig. 9 shows the same area processed with different BPT pruning strategies and parameters. The selected area contains some large homogeneous agricultural fields at the top left part of the image and an urban area with small details in the central part. The multilook filter implies a spatial resolution loss. The IDAN filter focuses specifically on data filtering by considering an adaptive neighborhood for every pixel of the data, in opposition to the BPT approach that considers homogeneous regions. As observed, neither the multilook nor the IDAN techniques can achieve such strong filtering as the proposed BPT-based filter. For the BPT construction process, the revised Wishart dissimilarity d_{RW} has been employed. Comparing both pruning criteria, the region homogeneity based pruning preserves more small details and point targets than the pruning based on the number of regions, as can be seen in urban zones, while, at the same time, it produces larger areas for homogeneous fields. This effect is caused by the strong dependence of the dissimilarity measures with the region sizes, as mentioned before.

One of the main features of the BPT is its multiscale nature, as it has been indicated. This aspect can be deduced from figures 9a to 9f. Note that all of these images have been generated from the same tree, just changing the pruning strategy and parameters. Then, the BPT contains all the information presented in the images at different detail levels. This property is exploited to obtain within the same image strong filtering in case of homogeneous areas whereas the spatial resolution and details of the image are maintained. Decreasing the number of regions n_r or increasing the pruning factor δ_p modifies the strength of the filter, but is worth to notice that new contours never appear, since bigger regions are always generated by fusion of smaller ones. To illustrate the ability of the region homogeneity based pruning to obtain within the same image regions with very different sizes, Fig. 10 shows a small homogeneous area of the original image with corner reflectors, close to the runway. BPT based filtering can achieve very strong filtering while preserving the corner reflectors as small spatial details. Multilook and IDAN do not achieve such a strong filtering and multilook implies a spatial resolution loss, resulting in larger spots.

Fig. 9 also shows that the polarimetric information is main-

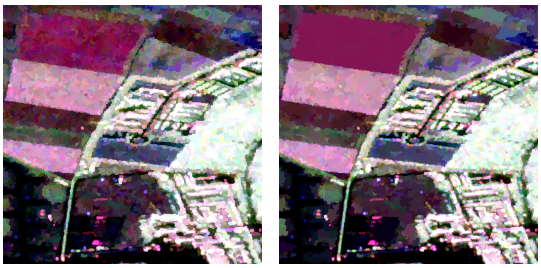

(a) $d_{RW}, n_r = 50000$ (b) $d_{RW}, \delta_p = -2dB$

(c) $d_{RW}, n_r = 10000$ (d) $d_{RW}, \delta_p = -1dB$

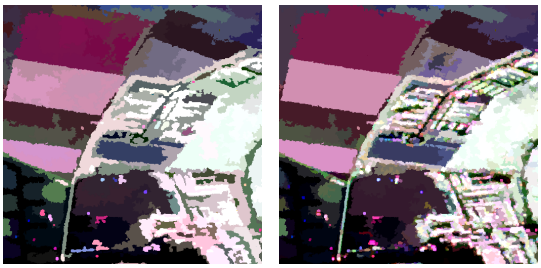

(e) $d_{RW}, n_r = 2000$ (f) $d_{RW}, \delta_p = 0dB$

Fig. 9. Detail Pauli RGB images. (a), (c), (e) filtered with pruning based on the number of regions and (b), (d), (f) filtered with region homogeneity based pruning.

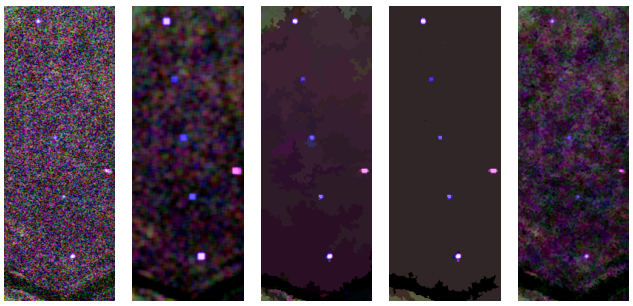

(a) Original (b) 7x7 ML (c) $\delta_p = -2dB$ (d) $\delta_p = 0dB$ (e) IDAN

Fig. 10. Detail Pauli RGB images of corner reflectors preservation. For BPT homogeneity based pruning the revised Wishart d_{RW} dissimilarity has been employed. For IDAN filter, the maximum window size is 100 pixels.

tained in the Gaussian case, since the Pauli representations do not vary between the original image Fig. 8a and the BPT filtered images. As stated before, the region model employed within the BPT nodes consists of the estimated covariance matrix (4), which represents the MLE of the covariance matrix, assuming a complex Gaussian distribution [21].

Fig. 11 presents the results for the same image obtained after applying a region homogeneity based pruning with $\delta_p = -1dB$ over different trees, changing the dissimilarity function employed for the BPT construction process. As one may observe, all the proposed dissimilarity measures are sensitive to the main contours of the image, obtaining large regions over homogeneous areas while preserving contours and small details. However, there are some differences between them. The contours detected employing d_{WR} dissimilarity (8) are noisy (see Fig. 11a), as it can be seen specially in the fields, appearing as a rough line. The BPT obtained with diagonal dissimilarities d_{DN} (10) and d_{DR} (11), figures 11b and 11c, present clear region contours but some small spots can be seen inside homogeneous regions that corresponds to the image speckle noise. This effect is more obvious inside the upper fields for d_{DR} dissimilarity. The obtained results with d_{DW} (12), in Fig. 11d, are very close to the revised Wishart d_{RW} results, shown in Fig. 9d, since the two dissimilarities are based on the same principles, but some large areas are better characterized with d_{RW}, as it is sensitive to all the covariance matrix elements.

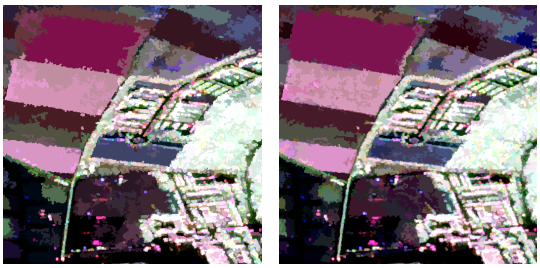

(a) $d_{WR}, \delta_p = -1dB$ (b) $d_{DN}, \delta_p = -1dB$

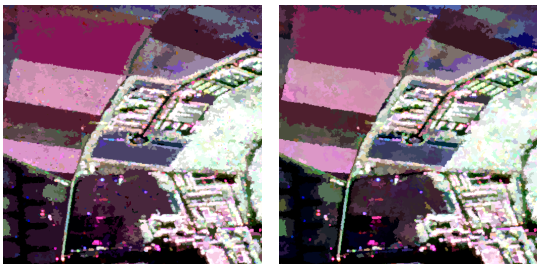

(c) $d_{DR}, \delta_p = -1dB$ (d) $d_{DW}, \delta_p = -1dB$

Fig. 11. Detail Pauli RGB images processed using region homogeneity based pruning with $\delta_p = -1dB$ over different trees constructed employing various dissimilarity functions.

To illustrate the capability to retain the polarimetric information of the proposed BPT filtering approach under the Gaussian hypothesis, the eigendecomposition parameters of the covariance matrix, Entropy (E), Anisotropy (A) and the averaged alpha angle ($\bar{\alpha}$), are shown in Fig. 12 in comparison with the 7x7 multilook and IDAN filtering. An initial qualitative comparison of the images shows that they obtain the same values. However, there are differences for large homogeneous areas in the agricultural fields, where the BPT approach can obtain these parameters with larger filtering than multilook, reducing the estimation errors for distributed scatters. Moreover, in the case of point targets and small details of the image, for example inside the urban areas, it is able to maintain a higher spatial resolution, since smaller regions of

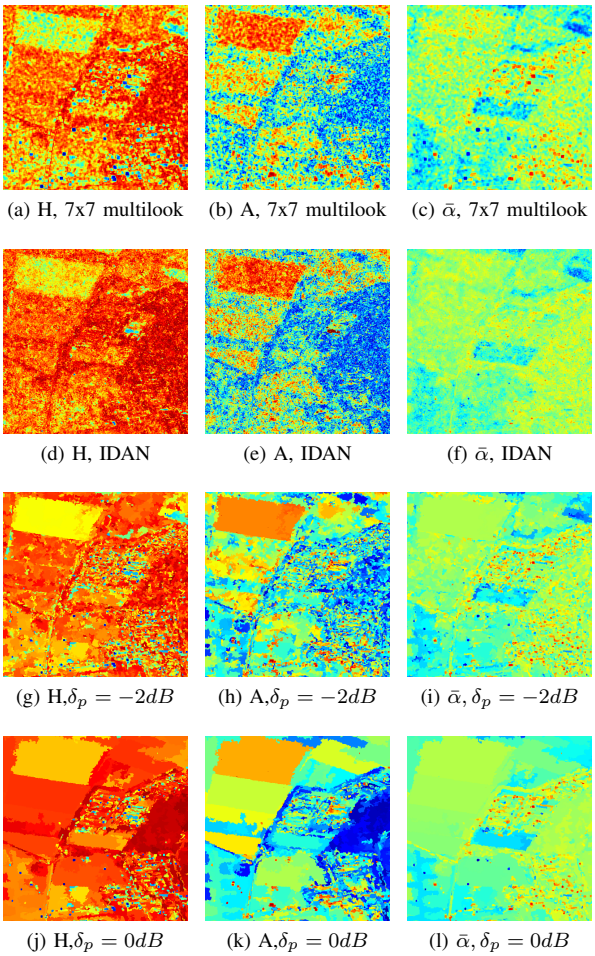

(a) H, 7x7 multilook (b) A, 7x7 multilook (c) $\bar{\alpha}$, 7x7 multilook

(d) H, IDAN (e) A, IDAN (f) $\bar{\alpha}$, IDAN

(g) H,$\delta_p = -2dB$ (h) A,$\delta_p = -2dB$ (i) $\bar{\alpha}, \delta_p = -2dB$

(j) H,$\delta_p = 0dB$ (k) A,$\delta_p = 0dB$ (l) $\bar{\alpha}, \delta_p = 0dB$

Fig. 12. H/A/$\bar{\alpha}$ from processed images with multilook, IDAN and using region homogeneity based pruning for different pruning threshold values and d_{RW} dissimilarity.

the tree are obtained. As a consequence, the proposed BPT filtering approach improves the estimation of the polarimetric information, both, in point as well as in distributed scatters.

To be able to make a quantitative evaluation of the polarimetric information preservation, three homogeneous areas from the image have been selected and some mean estimated parameters are calculated over them, regarding the covariance matrix elements and the eigendecomposition parameters H/A/$\bar{\alpha}$. The selected areas are shown in Fig. 7a and the mean estimated values are presented in Table I. A comparison is made between the original values, 7x7 multilook, IDAN filtering and BPT homogeneity based pruning for different δ_p. As it can be seen, in the case of multilook and BPT filtering the estimated covariance matrix elements are very similar to the original values. However, IDAN filtering introduces appreciable bias in the covariance matrix elements although the eigendecomposition parameters H/A/$\bar{\alpha}$ are close to the other filtering values. The presence of this bias has been discussed in [19] and compensate up to a certain point by the authors [20]. With BPT-based filter and $\delta_p = 0dB$ the values start to diverge from the original ones because of the inhomogeneous region mixture effect due to excessive

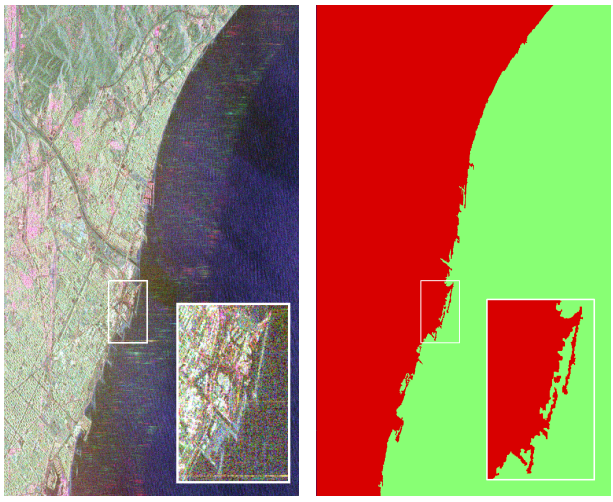

(a) Original Pauli (b) BPT based coastline segmentation

Fig. 13. Pauli RGB image of Barcelona (a), and coastline segmentation with BPT (b). The revised Wishart d_{RW} dissimilarity has been employed for the BPT construction.

filtering. The H/A/$\bar{\alpha}$ parameters cannot be estimated over the original image since its estimated covariance matrices are singular, and then a filtering process is needed. Note that these estimated parameters are biased [6]; increasing the pruning factor means increasing the filtering and the number of looks per region and then reducing the estimation biases for all the eigendecomposition parameters. As expected, as the number of looks increases the bias is reduced and the estimated entropy increases while anisotropy is reduced.

V. BPT PRUNING FOR COASTLINE DETECTION

In Section IV, the BPT representation of the image has been employed for PolSAR filtering. However, the BPT structure contains a lot of useful information about image structure that may be employed for other applications. Fig. 13 is an example where the BPT is employed to obtain an image segmentation over the coastline. Fig. 13a shows a 1500×2500-pixel cut of a C-band Pauli RADARSAT-2 image of Barcelona, Spain, that was acquired in November, 18th 2008, in fine quad polarization mode, with nominal resolution of $5.2m \times 7.6m$. The figure also shows a detailed area corresponding to the Forum harbor of Barcelona. Fig. 13b shows two regions of the BPT corresponding to land and sea. In this case, the two most different regions (that is the two child nodes of the root node) were selected. Note that, for coastline detection, upper nodes of the tree, closer to the root, are selected, in opposition to the filtering application, where lower nodes of the tree, closer to the leaves, are interesting. It is worth to notice that, due to the ability of the BPT to preserve small details, the thin structures in the coastline like breakwaters are preserved.

VI. CONCLUSIONS

A new PolSAR data processing approach, based on a Binary Partition Tree (BPT) image representation is presented. The BPT contains a large number of regions that may be extracted

Region	Filtering	C_{11}	C_{22}	C_{33}	$\Re(C_{13})$	$\Im(C_{13})$	H	A	$\bar{\alpha}$
Z1 5000 px	Original	28.27	16.06	18.34	5.242	5.504	-	-	-
	ML 7x7	28.21	15.97	18.36	5.321	5.465	0.8012	0.3543	48.29
	IDAN	18.73	9.661	12.03	2.471	2.595	0.8558	0.3050	49.48
	BPT -2dB	28.15	16.10	18.17	5.466	5.605	0.8271	0.2873	48.27
	BPT -1dB	28.20	15.20	18.08	5.558	5.612	0.8618	0.2036	47.91
	BPT 0dB	27.76	14.47	16.96	5.813	5.211	0.8694	0.1630	47.74
Z2 5950 px	Original	279.3	159.1	172.8	49.80	-14.37	-	-	-
	ML 7x7	280.8	159.3	172.9	49.18	-15.27	0.8598	0.2907	49.06
	IDAN	173.0	102.4	105.8	20.59	-7.978	0.9003	0.2501	51.29
	BPT -2dB	278.1	158.4	171.5	48.05	-16.12	0.8475	0.2984	49.50
	BPT -1dB	280.4	157.7	172.4	50.24	-15.42	0.8925	0.2269	49.41
	BPT 0dB	292.2	160.8	177.0	50.74	-13.42	0.9305	0.1307	49.61
Z3 18000 px	Original	10.70	2.782	13.13	2.644	5.599	-	-	-
	ML 7x7	10.70	2.789	13.14	2.662	5.593	0.6781	0.4248	42.62
	IDAN	7.123	1.864	8.678	1.433	2.896	0.7438	0.4505	44.39
	BPT -2dB	10.33	2.713	12.94	2.498	5.255	0.7370	0.3755	43.32
	BPT -1dB	10.36	2.799	13.23	2.434	5.136	0.7445	0.3881	43.60
	BPT 0dB	11.76	3.405	13.59	2.556	5.351	0.7852	0.3471	44.34

TABLE I
MEAN ESTIMATED VALUES OVER HOMOGENEOUS AREAS FOR DIFFERENT FILTERING STRATEGIES.

from the data, that are organized in a hierarchical structure, corresponding to different scales or detail levels. Consequently, this data representation contains a lot of useful information related to data structure. Thus, the BPT is a powerful tool for developing non-linear, region-based and multi-scale PolSAR applications.

The BPT construction process has been analyzed, employing a bottom-up approach. In this case, a region model and a dissimilarity measure need to be defined. The estimated covariance matrix has been selected as a region model, assuming a complex Gaussian model, and different dissimilarity measures have been proposed and analyzed. It is worth to notice that this construction process employs all the elements of the covariance matrix and then exploits all the polarimetric information. Nevertheless, other region models accounting, for instance, for data texture or characterizing high resolution data are possible. The BPT is a general representation of the data, which construction process should be application independent, conforming a common part for all the BPT-based applications.

The processing of the BPT typically involves the identification of the tree nodes that are useful for a particular application. The main application considered in this work is PolSAR speckle filtering. The target for speckle filtering application is to detect the largest homogeneous regions within the image. Two tree pruning strategies for the filtering application have been proposed, the pruning based on the number of regions and the homogeneity based pruning. The proposed BPT based PolSAR speckle filtering process has shown to achieve very high level of noise filtering while preserving small details and spatial resolution. Furthermore, the proposed technique is able to exploit all the polarimetric information under the Gaussian assumption, unlike most state-of-the-art filtering techniques, that are only based on radiometric information. The number of regions n_r or the pruning factor δ_p may be employed to adjust the strength of the filtering. Additionally, it has been observed that no bias or distortion is introduced in the polarimetric information as the region model that has been employed, the average covariance or coherency matrices, corresponds to the MLE of these matrices.

Secondarily, another BPT-based application of PolSAR data processing is presented: coastline detection. In this case, the goal is to detect the two most different regions corresponding to sea and land and then identify the coastline as their contour. Due to the ability of the BPT to preserve small details and spatial resolution, this coastline detection can detect thin structures in the coastline like breakwaters.

ACKNOWLEDGMENT

This work has been supported by the Spanish MICINN project TEC2008-06764-C02-01 and the CUR of the DIUE of the Autonomous Government of Catalonia and the European Social Fund. The authors would like to thank to DLR and to MDA for providing the ESAR and the RADARSAT-2 datasets, respectively. The authors would like also to acknowledge the reviewers for their valuable comments and Dr. Jordi Mallorquí for his support in the development of this work.

REFERENCES

[1] A. B. Kostinski and W. M. Boerner, "On foundations of radar polarimetry," *Antennas and Propagation, IEEE Transactions on*, vol. AP-34, no. 12, pp. 1395 – 1403, Dec. 1986.

[2] S. Cloude and E. Pottier, "A review of target decomposition theorems in radar polarimetry," *Geoscience and Remote Sensing, IEEE Transactions on*, vol. 34, no. 2, pp. 498–518, March 1996.

[3] J.-S. Lee, M. Grunes, and G. de Grandi, "Polarimetric SAR speckle filtering and its implication for classification," *Geoscience and Remote Sensing, IEEE Transactions on*, vol. 37, no. 5, pp. 2363–2373, Sept. 1999.

[4] G. Vasile, E. Trouve, J.-S. Lee, and V. Buzuloiu, "Intensity-driven adaptive-neighborhood technique for polarimetric and interferometric SAR parameters estimation," *Geoscience and Remote Sensing, IEEE Transactions on*, vol. 44, no. 6, pp. 1609–1621, June 2006.

[5] C. López-Martínez and X. Fàbregas, "Model-based polarimetric sar speckle filter," *Geoscience and Remote Sensing, IEEE Transactions on*, vol. 46, no. 11, pp. 3894–3907, Nov. 2008.

[6] C. López-Martínez, E. Pottier, and S. Cloude, "Statistical assessment of eigenvector-based target decomposition theorems in radar polarimetry," *Geoscience and Remote Sensing, IEEE Transactions on*, vol. 43, no. 9, pp. 2058–2074, Sept. 2005.

[7] P. Salembier and L. Garrido, "Binary partition tree as an efficient representation for image processing, segmentation and information retrieval," *Image Processing, IEEE Transactions on*, vol. 9, no. 4, pp. 561-576, April 2000.
[8] J. W. Goodman, "Some fundamental properties of speckle," *J. Opt. Soc. Am*, vol. 66, no. 11, pp. 1145 – 1149, Nov. 1976.
[9] N. R. Goodman, "Statistical analysis based on a certain multivariate complex gaussian distribution (an introduction)," *Ann. Mathemat. Statist.*, vol. 34, pp. 152 – 177, 1963.
[10] R. J. A. Tough, D. Blacknell, and S. Quegan, "A statistical description of polarimetric and interferometric synthetic aperture radar data," *Proc. R. Soc. Lond. A*, pp. 567–589, 1995.
[11] J.-S. Lee, K. Hoppel, S. Mango, and A. Miller, "Intensity and phase statistics of multilook polarimetric and interferometric SAR imagery," *Geoscience and Remote Sensing, IEEE Transactions on*, vol. 32, no. 5, pp. 1017–1028, Sept. 1994.
[12] O. Morris, M. Lee and A. Constantinidies, "Graph theory for image analysis: an approach based on the shortest spanning tree," *IEE Proceedings, F*, vol. 133, no. 2, pp. 146-152, April 1986.
[13] L. Garrido, P. Salembier and D. Garcia, "Extensive operators in partition lattices for image sequence analysis," *Signal Processing (Elsevier)*, vol. 66, no. 2, pp. 157-180, April 1998.
[14] L.M. Novak and M.C. Burl, "Optimal speckle reduction in polarimetric SAR imagery", *Aerospace and Electronic Systems, IEEE Transactions on*, vol. 26, no. 2, pp. 293-305, March 1990
[15] P.R. Kersten, J.-S. Lee and T.L. Ainsworth, "Unsupervised Classification of Polarimetric Synthetic Aperture Radar Images Using Fuzzy Clustering and EM Clustering", *Geoscience and Remote Sensing, IEEE Transactions on*, vol. 43, no. 3, pp. 519-527, March 2005
[16] J.H. Ward, "Hierarchical grouping to optimize an objective function", *Journal of the American Statiscal Association*, 58(301), pp. 236-244, 1963
[17] S. Normann, R. Jenssen and T. Eltoft, "Spectral clustering of Polarimetric SAR data with Wishart-derived distance measures", *PolInSAR 2007*, January 2007.
[18] PolSARPro v. 4.0.3, http://earth.esa.int/polsarpro
[19] G. Vasile, J.-P. Ovarlez, F. Pascal and C. Tison, "Coherency matrix estimation of heterogeneous clutter in high-resolution polarimetric SAR images", *Geoscience and Remote Sensing, IEEE Transactions on*, vol. 48, No. 4, pp. 1809-1826, 2010
[20] G. Vasile, J.-P. Ovarlez, F. Pascal, C. Tison, L. Bombrun, M. Gay and E. Trouv, "Normalized coherency matrix estimation under the SIRV model" - Alpine glacier POLSAR data analysis, *IEEE International Geoscience and Remote Sensing Symposium IGARSS*, Boston, USA, July 2008, Vol. 1, pp. I74-I77
[21] R. J. Muirhead, Aspects of Multivariate Statistical Theory, John Wiley & Sons, Inc., New York, USA, 1982
[22] A. Alonso-González, C. López-Martínez and P. Salembier, "Filtering and segmentation of Polarimetric SAR images with Binary Partition Trees", *IEEE International Geoscience and Remote Sensing Symposium IGARSS*, Honolulu, Hawaii, USA, July 2010, pp. 4043-4046

Appendix B

IEEE IGARSS 2010 conference paper

FILTERING AND SEGMENTATION OF POLARIMETRIC SAR IMAGES WITH BINARY PARTITION TREES

Alberto Alonso-González, Carlos López-Martínez, Philippe Salembier

Universistat Politècnica de Catalunya (UPC), Signal Theory and Communications Dept. (TSC)
Jordi Girona 1-3, 08034 Barcelona, Tlf. +34 934016785 Email: alberto.alons@gmail.com

ABSTRACT

A new multi-scale PolSAR data filtering technique, based on a Binary Partition Tree (BPT) representation of the data, is proposed. Different alternatives for the construction and the exploitation of the BPT for filtering and segmentation are presented. Results with simulated and experimental PolSAR data are presented to shown the capabilities of the BPT-filtering strategy to maintain both spatial details and the polarimetric information.

Index Terms— SAR, SAR Polarimetry, Speckle filtering, Binary Partition Tree, Segmentation

1. INTRODUCTION

SAR Polarimetry (PolSAR) has demonstrated, specially during the last decade, its significance for the analysis and the characterization of the Earth surface, as well as for the quantitative retrieval of biophysical and geophysical parameters. A set of complex radar scattered echoes are coherently processed in order to achieve high spatial resolution. As a consequence, the received signal is affected by a speckle term. Despite speckle is determined by the scattering process itself, its complexity makes necessary to consider it from a stochastic point of view and then, to assume the speckle term as a noise term. The speckle is a handicap in SAR imagery processing and information extraction and consequently some speckle filtering process is needed.

SAR and PolSAR data are non stationary as they reflect the complexity of the environment. Assuming that all the stochastic processes involved in the filtering process are ergodic, PolSAR filters must adapt to this non stationarity. Most recent state-of-the-art filtering techniques [1][2] are based on this approach, tending to define a different homogeneity neighborhoods for each image pixel. In this paper, we propose to tackle this issue by relying on a region-based multi-scale representation of the image by means of a Binary Partition Tree (BPT) and to perform filtering or segmentation tasks directly by pruning the BPT.

The authors thank DLR for providing the PolSAR data. This work has been supported by the Ramón-y-Cajal programm and the TEC2007-65690/TCM Spanish MICINN project.

2. BINARY PARTITION TREE

The Binary Partition Tree (BPT) was introduced in [3] as a region-based and multi-scale image representation. It contains information about image structure at different detail levels in a tree. Each node represents a region of the image. The tree leaves correspond to single pixels of the image and the remaining nodes represent the merging of the two child regions. Finally, the root node represents the whole image. The tree edges describe the inclusion relationship between nodes. From the leaves to the root, many regions with different sizes may be found. This multi-scale representation contains a lot of information about the image structure and may be exploited for PolSAR filtering and segmentation and for many other applications.

The BPT construction process can be performed in an efficient manner by an iterative algorithm [3] in a bottom-up approach. In the initial state, every pixel of the image will conform a single region. Iteratively the two most similar neighbor regions will be merged until a single region is achieved, keeping full track of the *merging sequence* within the tree structure. Thus, in order to be able to construct a BPT representation from a PolSAR image, the following elements have to be defined:

1. A region model: traditionally, under the complex Gaussian PolSAR model, the 3x3 estimated covariance matrix $\mathbf{Z}$ is employed to measure the region polarimetric information

$$\mathbf{Z} = \langle \mathbf{k}\mathbf{k}^H \rangle_n = \frac{1}{n} \sum_{i=1}^{n} \mathbf{k}_i \mathbf{k}_i^H \qquad (1)$$

   where $\mathbf{k}_i$ represents the scattering vector of the i-th pixel and n represents the region size in pixels.

2. A similarity measure on the region model space to compare two neighboring regions $d(X, Y)$. The revised Wishart distance measure [4] d_w is based on a statistical test assuming Wishart distributions and that one region statistics are known. However, since this measure is not symmetric, a modified symmetric version

will be applied

$$d_{sw}(X,Y) = \left(tr(\mathbf{Z}_X^{-1}\mathbf{Z}_Y) + tr(\mathbf{Z}_Y^{-1}\mathbf{Z}_X)\right)\cdot(n_x+n_y) \quad (2)$$

where $\mathbf{Z}_X$ and $\mathbf{Z}_Y$ represent the estimated covariance matrices for regions X and Y, respectively, and n_x and n_y represent their number of pixels.

For comparison purposes a new version of the symmetric revised Wishart dissimilarity will be used, only taking into account the diagonal elements of the $\mathbf{Z}$ matrix and assuming all off-diagonal values equal to zero

$$d_{dw}(X,Y) = \left(\sum_{i=1}^{3}\left(\frac{Z_{X\,ii}^{\,2} + Z_{Y\,ii}^{\,2}}{Z_{X\,ii}Z_{Y\,ii}}\right)\right)\cdot(n_x+n_y) \quad (3)$$

where $Z_{X\,ij}$ and $Z_{Y\,ij}$ represent the (i,j)th element of the estimated covariance matrices $\mathbf{Z}_X$ and $\mathbf{Z}_Y$, respectively.

3. BPT PRUNING

As stated in [3] an image segmentation may be obtained performing a tree pruning over the BPT. This pruning process is application dependent. In this paper two BPT pruning criteria are proposed focused on the speckle filtering application.

- *Pruning based on the region number.* The number of regions n_r of the segmentation is fixed and the n_r most different regions of the tree are obtained. If this decision relies on the same similarity measure employed for the BPT construction, then it is equivalent to stop the BPT construction process when n_r regions are obtained.
- *Homogeneity based pruning.* A new homogeneity criteria is introduced to evaluate the region homogeneity. The main goal is to obtain a set of regions from the BPT that represent the largest homogeneous regions on the image.

The pruning based on the region number has the advantage of being simpler and faster than the homogeneity based pruning, since no new criteria nor evaluation are needed for pruning. However, in practical situations, it is almost impossible to fix a priori the optimum number of regions for a given PolSAR image.

For the homogeneity based pruning, the following homogeneity criteria is proposed

$$\phi_R(X) = \frac{1}{n_x}\sum_{i=1}^{n_x}\frac{\|\mathbf{X}^i - \mathbf{Z}_X\|_F^2}{\|\mathbf{Z}_X\|_F^2} \quad (4)$$

where $\mathbf{X}^i$ is the estimated covariance matrix for the i-th pixel within region X and $\|.\|_F$ represents the Frobenius matrix norm.

Note that the homogeneity measure (4) depends on the values of all the region pixels and not only on the region model, as the similarity measure. The measure (4) may be interpreted as the information loss when modeling all the region pixels by its estimated covariance matrix. Thus, in order to determine if a region is homogeneous or not, a maximum value for the homogeneity measure will be defined, called *pruning threshold*.

4. RESULTS

To be able to make a quantitative evaluation of the proposed BPT pruning processes, a simulated 128x128 pixels PolSAR image is proposed in Fig. 1. Simulated data have been generated using the complex Gaussian PolSAR pdf assuming a reflection symmetric target

$$\mathbf{C} = \sigma_{HH}\begin{pmatrix} 1 & 0 & \rho\sqrt{\gamma} \\ 0 & \varepsilon & 0 \\ \rho^*\sqrt{\gamma} & 0 & \gamma \end{pmatrix} \quad (5)$$

where * denotes complex conjugate.

Two sets of images has been generated according to (5) with values $\gamma_i = 1$ and $\varepsilon_i = 0.1$ and variations for σ_{HHi} and ρ_i in different regions $i = 1\ldots4$ as denoted in Fig. 1a

1. Variations in correlation: $\rho = \{0,\ 0.25e^{j\pi},\ -0.5,\ 0.75e^{-j\pi}\};\ \sigma_{HHi} = 1$
2. Variations in both correlation and intensity: $\rho = \{0,\ 0.25e^{j\pi},\ -0.5,\ 0.75e^{-j\pi}\};\ \sigma_{HH} = \{1,\ 9,\ 25,\ 49\}$

(a) (b) (c)

Fig. 1: Simulated image with variations in both correlation and intensity. C_{22}, C_{33} and C_{11} are assigned to RGB channels. (a) Zone numeration; BPT pruning at -6dB with (b) d_{sw} and (c) d_{dw}.

To assess qualitatively the goodness of the processed image X compared with the ground truth Y a relative error measure is used

$$E_R(X,Y) = \frac{1}{n_h\cdot n_w}\sum_{i=1}^{n_h}\sum_{j=1}^{n_w}\frac{\|\mathbf{X}^{ij} - \mathbf{Y}^{ij}\|_F^2}{\|\mathbf{Y}^{ij}\|_F^2} \quad (6)$$

where n_h and n_w are the image height and width in pixels, respectively, $\mathbf{X}^{ij}$ represents the (i,j)th pixel value of image X.

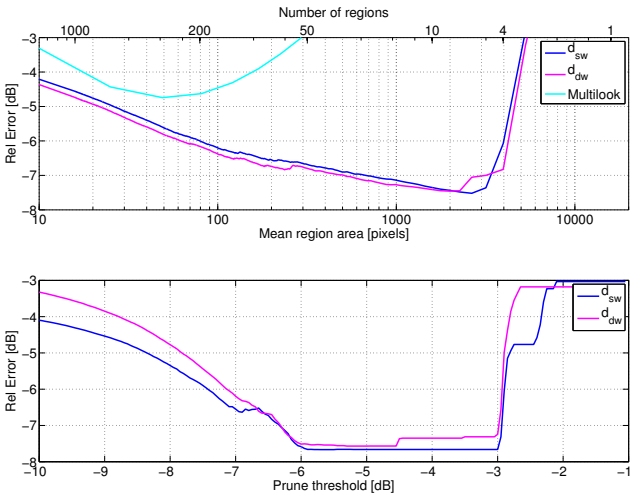

Fig. 2: Relative error for simulated images with variations in both correlation and intensity. BPT number of regions based pruning (top) and homogeneity based pruning (down).

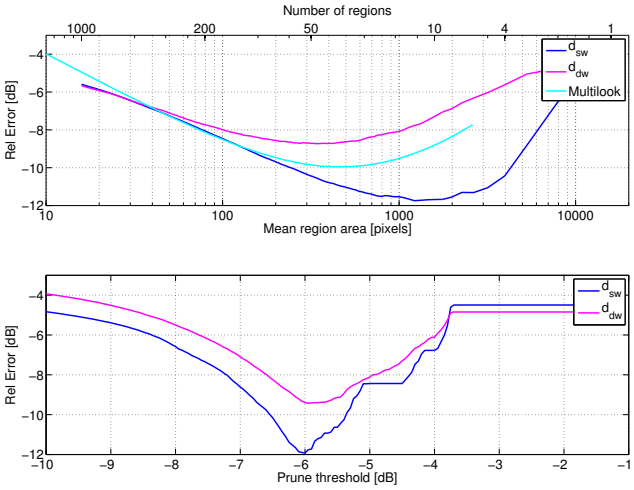

Fig. 3: Relative error for simulated images with variations in correlation. BPT number of regions based pruning (top) and homogeneity based pruning (down).

Note that the relative error measure (6) is based on the inverse signal to noise ratio (SNR^{-1}) averaged for all the image pixels.

Fig. 2 shows the relative error over the image with variations in both correlation and intensity for the two proposed BPT pruning strategies. Fig. 3 shows the relative error over the image with variations in correlation only. The upper plot of the figures corresponds to the pruning based on the region number and the lower plot corresponds to region homogeneity based pruning. As observed in Fig. 2, in all the cases the BPT-filtering approach obtains lower values that the multilook, specially for large areas, without the alteration of the

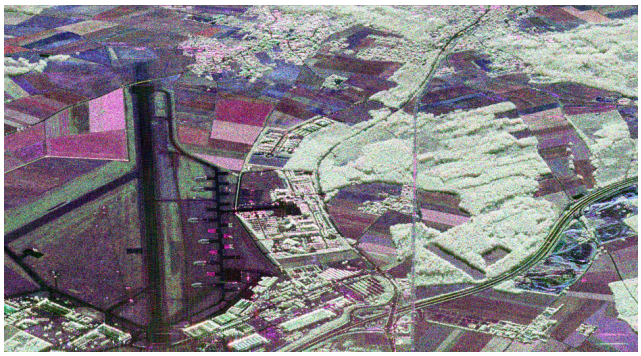

(a)

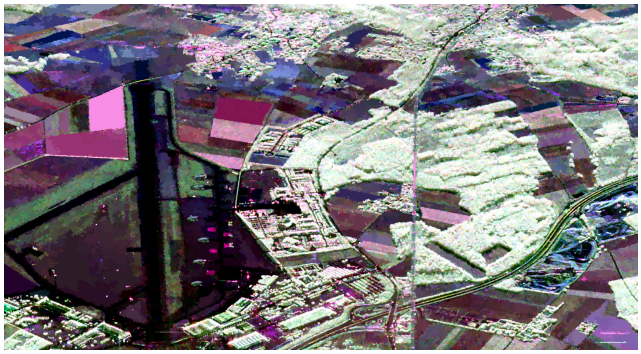

(b)

Fig. 4: Pauli RGB images: (a) original and (b) processed.

image contours. When there are variations only in the off-diagonal matrix elements, as in Fig. 3, the d_{dw} similarity measure is not sensitive to contours and only d_{sw} can exploit all the polarimetric information and improve the multilook filtering.

Complementarily, the application of the BPT-filtering strategy for PolSAR filtering has been considered with experimental PolSAR data that was acquired in a measurement campaign conducted by the DLR in 1999 with its experimental SAR system, E-SAR, over the Oberpfaffenhofen test-site, southern Germany. Data were collected at L-band, with a spatial resolution of $1.5m \times 1.5m$ in fully polarimetric mode.

Fig. 4 presents the original Pauli RGB image of the previous data set, compared with Pauli RGB image obtained from the speckle filtered data set considering the previous BPT approach. In this case, the distance d_{sw} has been considered for the construction process and the *homogeneity based pruning* with a *pruning threshold* of -2 dB has been assumed. As one may observe, the BPT-based filtering does not introduce neither new contours nor artifacts on the filtered data set. It is worth to mention that the proposed BPT-filtering approach makes it possible to retain almost the original spatial resolution in case of point and man-made targets, whereas it allows a large filtering in case of distributed targets such agricultural and forest areas.

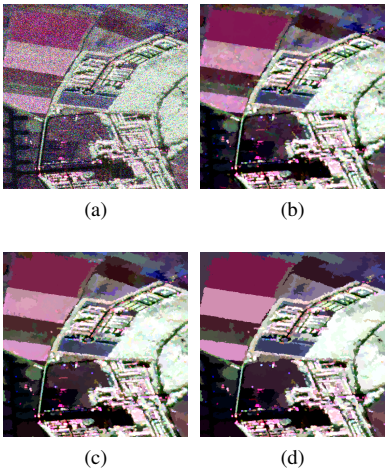

(a) (b) (c) (d)

Fig. 5: Detail Pauli RGB images: (a) original and processed with *pruning threshold* (b) -2 dB (c) -1 dB and (d) 0 dB.

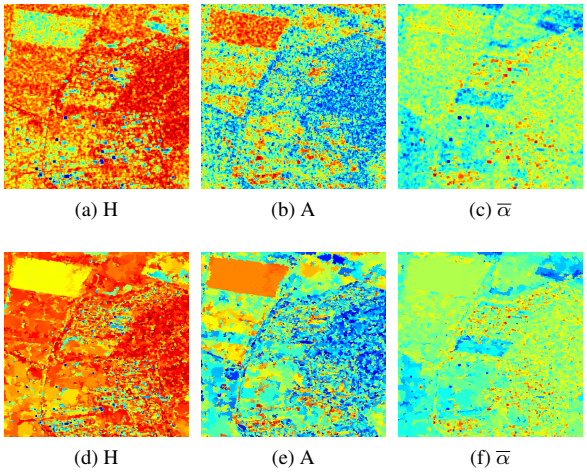

(a) H (b) A (c) $\overline{\alpha}$ (d) H (e) A (f) $\overline{\alpha}$

Fig. 6: H/A/$\overline{\alpha}$ with 7×7 multilook (a), (b) and (c), and with BPT employing a *pruning threshold* of -2 dB (d), (e) and (f).

As it has been indicated, one of the main features of the BPT-based filtering approach is the capability to perform a multi-scale analysis. Fig. 5 demonstrates this capability by changing the *pruning threshold* from -2 dB to 0 dB. As observed, the multi-scale capability allows different levels of filtering, specially on homogeneous areas, but without the introduction of new contours or artifacts. This feature allows to introduce strong filtering in case of homogeneous areas whereas maintaining the spatial resolution and details of the data.

Additionally to the maintenance of the spatial resolution and spatial details of the image, Figs. 4 and 5 also shown that the BPT-filtering approach is able to maintain the polarimetric information, as the Pauli representations do not vary between the original and the filtered images. As indicated, the model for the nodes of the BPT consists of (1), which represents the *Maximum Likelihood Estimation* of the covariance matrix to represent the data with the complex Gaussian pdf. Consequently, no global biases are introduced in the filtered signal since given a segmentation, a pixel can only belong to one region. In order to demonstrate the capability to retain the polarimetric information, the parameters of the eigendecomposition of the covariance matrix, namely, Entropy (H), Anisotropy (A) and the average alpha angle $\overline{\alpha}$ have been obtained with a 7×7 multilook filters and compared with the ones obtained through the BPT-filtering approach. As observed in Fig. 6, both approaches obtain qualitatively the same values. Nevertheless, the BPT-approach is able to obtain these parameters with larger filtering in case of distributed targets reducing estimation errors. additionally, in case of distributed scatterers, the BPT-filtering approach is able to maintain the spatial resolution. Consequently, the proposed filtering approach improves the estimation of the polarimetric information, both, in point as well as in distributed scatterers.

5. CONCLUSIONS

This paper proposes a novel multi-scale polarimetric speckle filtering strategy, based on a BPT representation of the data, that is able to maintain spatial resolution and details in case of point scatterers, while introducing large filtering in case of homogeneous ones. This filtering strategy adapts to the complete covariance matrix which represents the main difference with respect to previous approaches that only rely on its diagonal elements. As demonstrated, the proposed strategy also maintains the polarimetric information without the introduction of biases.

Furthermore, it has been proved that the BPT representation can be employed to extract useful information in PolSAR images, and it can be employed for many other applications.

6. REFERENCES

[1] Jong-Sen Lee, M. R. Grunes, and G. de Grandi, "Polarimetric sar speckle filtering and its implication for classification," *IEEE TGRS*, vol. 37, no. 5, pp. 2363–2373, 1999.

[2] G. Vasile, E. Trouve, Jong-Sen Lee, and V. Buzuloiu, "Intensity-driven adaptive-neighborhood technique for polarimetric and interferometric sar parameters estimation," *IEEE TGRS*, vol. 44, no. 6, pp. 1609–1621, 2006.

[3] P. Salembier and L. Garrido, "Binary partition tree as an efficient representation for image processing, segmentation, and information retrieval," *IEEE TIP*, vol. 9, no. 4, pp. 561–576, 2000.

[4] P. R. Kersten, Jong-Sen Lee, and T. L. Ainsworth, "Unsupervised classification of polarimetric synthetic aperture radar images using fuzzy clustering and em clustering," *IEEE TGRS*, vol. 43, no. 3, pp. 519–527, 2005.

Appendix C

IEEE IGARSS 2011 conference paper

BINARY PARTITION TREE AS A POLARIMETRIC SAR DATA REPRESENTATION IN THE SPACE-TIME DOMAIN

Alberto Alonso-González, Carlos López-Martínez, Philippe Salembier

Universistat Politècnica de Catalunya (UPC), Signal Theory and Communications Dept. (TSC)
Jordi Girona 1-3, 08034 Barcelona, Tlf. +34 934016785 Email: alberto.alonso@tsc.upc.edu

ABSTRACT

The aim of this paper is to present a Polarimetric Synthetic Aperture Radar data processing technique on the space-time domain. This approach is based on a Binary Partition Tree (BPT), which is a region-based and multi-scale data representation. Results with series of RADARSAT-2 real data are analyzed from the point of view of speckle filtering and change detection applications, to illustrate the capabilities to detect and preserve spatial and temporal contours.

Index Terms— SAR, SAR Polarimetry, Binary Partition Tree, Segmentation, Change detection

1. INTRODUCTION

Within the last decade Polarimetric Synthetic Aperture Radar (PolSAR) has demonstrated its capabilities to extract useful geophysical and biophysical information from the Earth surface. A set of complex radar echoes are coherently processed to achieve a high spatial resolution image. As a consequence of this coherent processing and the fact that the resolution cell contains a certain number of elementary targets, the received signal is the coherent sum of all these echoes inducing the speckle term. Despite the speckle term is determined by the scattering process itself, its complexity makes necessary to consider it from a stochastic point of view and then, to assume the speckle term as a noise term. The speckle is a drawback in SAR imagery processing and information extraction and consequently some speckle filtering process is needed.

An important point in PolSAR image processing is that the data are non stationary since they reflect the complexity of the environment. Therefore, PolSAR filters must adapt to this non stationarity. Some recent state-of-the-art filtering techniques are based on this approach [1][2] by defining a homogeneous neighborhood for each pixel. In [3] a new PolSAR data filtering scheme was introduced based on a Binary Partition Tree (BPT) representation of the image [4]. This processing strategy employs a region-based and multi-scale data representation which is able to detect homogeneous regions of the data at different detail levels.

This work has been funded by the Spanish MICINN project TEC2008-06764-C02-01 and the Catalan FI-DGR program. The authors would like also to acknowledge the ESA AgriSAR 2009 campaign.

In the last years, the presence of a number of PolSAR space-borne systems has empowered the construction of PolSAR image datasets containing images of the same scene at different times. In this work we propose an extension of the BPT technique to employ series of coregistered PolSAR images to construct a representation of the data in the space-time domain. This data representation considers the full dataset as a single three-dimensional figure of the same scene. This novel representation is useful to identify homogeneous regions over space and time, allowing a better characterization and a temporal evolution analysis of the scatters, by means of merging efficiently all the data in the different time acquisitions.

2. BINARY PARTITION TREE REPRESENTATION

The Binary Partition Tree (BPT) was introduced in [4] as an image representation. Recently, it has been employed for PolSAR data filtering and segmentation in [3][5]. BPT is a region-based and multi-scale data representation. It is a hierarchical structure containing information about the data structure at different detail levels. Each node of the tree represents a region of the data; the tree leaves represent single pixels, whereas other nodes represent the merging of its two child regions. Consequently, the root node of the tree represents the whole data. The edges of the tree describe the inclusion relationship between regions. The BPT contains a large number of regions between the leaves and the root, having useful information about the data structure that may be employed for different applications.

In this paper, the BPT representation is extended to the time dimension represented by a series of images of the same site acquired at different dates. As a consequence, a region of the tree will represent a set of pixels covering different images. Then, a region conceptually represents a space-time area of the data.

3. BPT PROCESSING

In this paper, the proposed BPT space-time representation has been employed to process a RADARSAT-2 Fine Quad-Pol dataset corresponding to a test-site in Flevoland, Nether-

lands. The dataset was acquired during the ESA AgriSAR 2009 campaign, devoted to analyze the agricultural fields temporal evolution with PolSAR. The scene is composed mainly by an area of agricultural fields and some sea surface and urban areas. A subset of 8 images has been selected, corresponding to different acquisitions with the same incidence angle (beam FQ13) and ascending passes. The resulting subset is composed of images from April 4th, 2009 to September 29th, 2009 with an acquisition every 24 days.

3.1. Pre-processing

To process the dataset correctly, a 4000 by 2000 pixel cut of the original image has been selected and a coregistration process has been done to ensure that all the pixels are aligned in the time dimension. The full dataset coregistrated, containing 4000 x 2000 x 8 pixel is represented in Fig. 1.

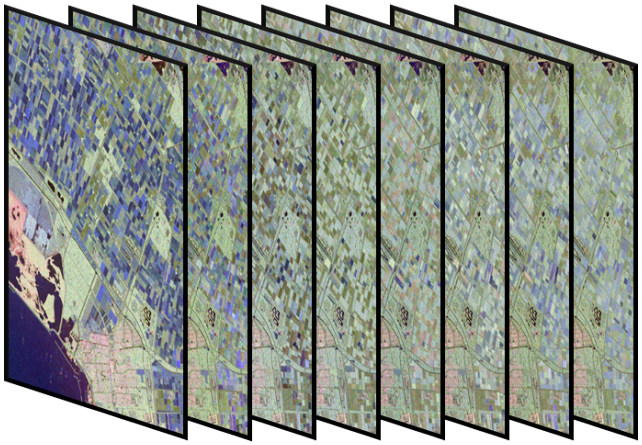

Fig. 1: Full 3-dimensional data set

3.2. BPT Construction

The BPT can be constructed with an iterative algorithm in a bottom-up approach [4]. In the initial state of the algorithm every pixel of the dataset becomes a one-pixel region. At each step of the construction process the two most similar neighboring regions are merged. This process is repeated iteratively until the root of the tree is generated. In this case, since the dataset is covering the space and time dimensions, a neighborhood has to be defined within this context. In this work, we propose the 10 connectivity shown in Fig. 2. Each pixel is connected with its 8 neighbors in space, to be able to preserve small diagonal details properly, and with the pixel in the same position in the images immediately before and after in the time dimension.

As mentioned in [3], the following additional elements have to be defined to apply the BPT construction process:

1. A region model: traditionally, under the complex Gaussian PolSAR model, the 3x3 estimated covariance matrix $\mathbf{Z}$ is employed to measure the region polarimetric information

$$\mathbf{Z} = \langle \mathbf{k}\mathbf{k}^H \rangle_n = \frac{1}{n}\sum_{i=1}^{n} \mathbf{k}_i \mathbf{k}_i^H \tag{1}$$

where $\mathbf{k}_i$ represents the scattering vector of the *i*-th pixel and n represents the region size in pixels.

2. A similarity measure on the region model space to compare two neighboring regions $d(X,Y)$. In this work we will employ the d_{sg} measure based on the positive definite matrix cone geometry [6]. Different similarity measures were analyzed and compared in [5], where d_{sg} resulted into the best performance in the case of spatial BPT-based PolSAR data filtering

$$d_{sg}(X,Y) = \|log\left(\mathbf{Z}_X^{-1/2}\mathbf{Z}_Y\mathbf{Z}_X^{-1/2}\right)\|_F + \\ + ln\left(\frac{2n_x n_y}{n_x + n_y}\right) \tag{2}$$

where $\mathbf{Z}_X$ and $\mathbf{Z}_Y$ represent the estimated covariance matrices for regions X and Y, respectively, n_x and n_y represent their number of pixels, $\|.\|_F$ represents the Frobenius matrix norm, $log(.)$ represents the matrix logarithm and $ln(.)$ represents the natural logarithm.

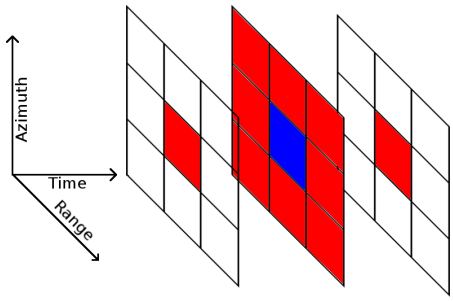

Fig. 2: Pixel connectivity for the dataset. Each pixel, in blue, has 10 neighbors, in red

3.3. BPT Pruning

A data processing may be obtained by a tree pruning process over the full BPT, as stated in [4]. This is an application dependent process. For filtering and segmentation, a homogeneity based tree pruning has been proposed and evaluated in [3][5]. A homogeneity criterion is introduced and the biggest regions of the tree that fulfill this criterion are selected from the BPT

$$\phi_R(X) = \frac{1}{n_x}\sum_{i=1}^{n_x} \frac{\|\mathbf{X}^i - \mathbf{Z}_X\|_F^2}{\|\mathbf{Z}_X\|_F^2} < \delta_p \tag{3}$$

where $\mathbf{X}^i$ is the estimated covariance matrix for the *i*-th pixel within region X and δ_p is the pruning factor, usually expressed in dB.

Note that the region model, the similarity measure and the pruning criterion employed for the BPT based processing are sensitive to the full estimated covariance matrix, so this processing is employing systematically all the polarimetric information, assuming the complex Gaussian PolSAR model.

4. RESULTS

The mentioned BPT processing strategy has been employed with the full dataset presented in Fig. 1. In this case, because of the dimensionality of the original data, a space-time segmentation is obtained, representing homogeneous regions in this domain.

In the following, the results obtained will be interpreted from the point of view of speckle filtering application and change detection.

4.1. Filtering results

For the speckle filtering application, the BPT processing can benefit from a space-time segmentation, since additional samples can be employed from different images to estimate the covariance matrix if the region is homogeneous in time.

Fig. 3 shows filtering results for the first image, corresponding to the first acquisition image, for different pruning factors δ_p. As expected, when increasing the pruning factor δ_p bigger regions are obtained since less homogeneous regions are accepted and pruned. Note that, as discussed before, these filtering results are obtained by averaging pixels corresponding to different acquisitions, depending on the region extent in the time dimension.

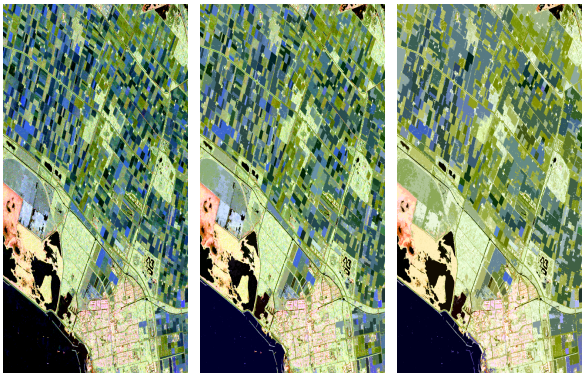

(a) $\delta_p = -5dB$ (b) $\delta_p = -3dB$ (c) $\delta_p = -1dB$

Fig. 3: First image processed with space-time filtering for different pruning factors δ_p

To assess the gain obtained when filtering an image employing the full dataset with respect to a 2 dimensional case, the average region depth in the time dimension is shown in Table 1. This parameter is calculated as the relation between the number of pixels contained in all the regions intersecting the first acquisition and the pixels contained in a single image. Note that, for example, when $\delta_p = -3dB$ the first acquisition can be filtered employing approximately 4 times more samples than with a single acquisition.

δ_p	Regions	Average depth
-5 dB	359371	2.067
-4 dB	223969	2.652
-3 dB	127957	4.068
-2 dB	52077	6.727
-1 dB	14660	7.758
0 dB	4666	7.921

Table 1: Number of regions and average region depth in time dimension over homogeneous regions intersecting the first acquisition for different pruning factors

Fig. 4 shows the temporal evolution of the entropy (H) parameter for two different agricultural fields of potatoes and onions. The results obtained with the BPT for $\delta_p = 0dB$ and $\delta_p = -3dB$ are compared with those obtained with the 7x7 multilook. As it can be seen, qualitatively the evolution of the parameter is similar for all the cases. Differences are produced by estimating the parameter over regions of different sizes in space and time, and not only in space. The flat zones that appear with the BPT based processing are produced when the same region appears over different acquisitions, conforming an homogeneous region that spans various images in the time dimension.

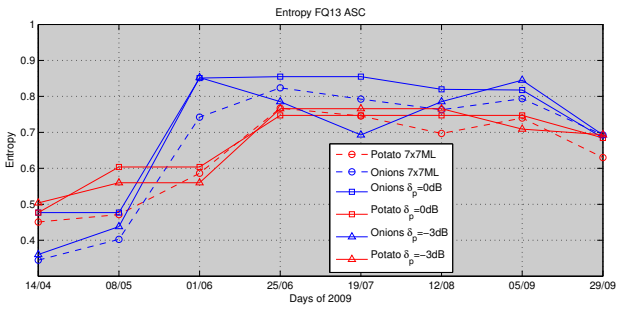

Fig. 4: Estimated entropy (H) temporal evolution over two different agricultural fields with 7x7 multilook and BPT homogeneity based pruning

4.2. Change detection results

In the previous section some filtering results have been presented showing the spatial contours of the homogeneous areas within the BPT corresponding to the first acquisition. In this section we will focus on the contours in the time dimension, interpreted as changes between different acquisitions.

Fig. 5 shows, for different δ_p, the number of changes, or contours in the time dimension, for each pixel, ranging from no changes, represented in blue, to 7 changes, in red. Again, increasing the pruning factor δ_p results in bigger regions also

in the time domain, and a smaller number of changes is detected for each pixel. Analyzing the results closely, some small blue dots can be seen over urban areas even at $\delta_p = -5dB$, corresponding to point scatters of the buildings that have no change in time. When increasing the pruning factor some other areas appear also in blue, as some regions of closed water, which roughness is less affected by wind. On the other hand, some agricultural fields appear more reddish, indicating that they are changing substantially along different acquisitions. A detailed area showing this behavior is shown in Fig. 6.

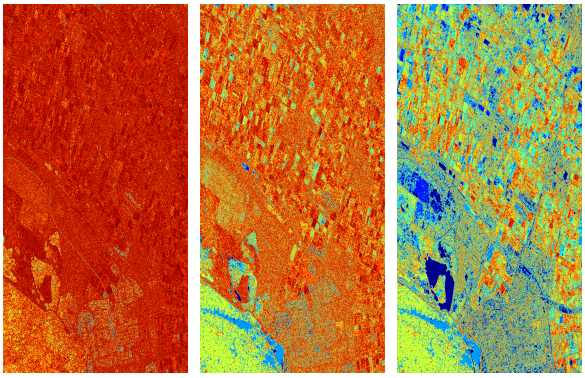

(a) $\delta_p = -5dB$ (b) $\delta_p = -3dB$ (c) $\delta_p = -1dB$

Fig. 5: Temporal changes detection for different pruning factors δ_p. No changes is represented in blue and 7 changes in red.

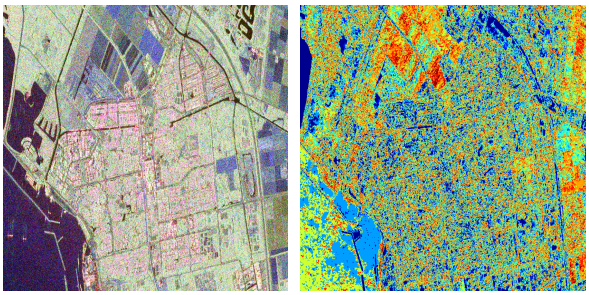

(a) Pauli image (b) Changes detected

Fig. 6: Detail of changes detection around urban area

Note that, since this processing strategy is employing all the information within the covariance matrix, the change detection application is also sensitive to all this information, identifying indirectly a concept of region temporal stability in terms of all the polarimetric information assuming the Gaussian polarimetric model.

5. CONCLUSIONS

In this paper a region-based and multi-scale data representation has been proposed simultaneously in the space and time dimensions. It is based on a BPT representation extended to the temporal dimension. Region homogeneity based pruning has been applied to obtain homogeneous regions of the tree in the space-time domain. It has proven to be able to adapt to the spatial and temporal information, preserving the polarimetric information. For the filtering application, this technique is able to increase the number of samples of homogeneous regions by efficiently employing pixels of different acquisitions, conforming an important gain in terms of the speckle filtering application.

Another application that automatically arises when segmenting a space-time dataset is temporal change detection. Some maps have been generated showing the number of changes detected in the time dimension. Although this changes cannot be physically confirmed, because of the absence of ground-truth, the temporal evolution of the entropy (H) parameter over some fields has shown to follow similar trends than the individual images filtered.

Consequently, a new processing tool has been introduced that systematically exploits PolSAR image series. Due to the BPT processing generic formulation, the same BPT construction and pruning algorithms can be employed for a single image or a set of images; only a new pixel neighboring scheme is needed to generate the initial state of the construction process. Moreover, the BPT based processing is not restricted to any region model, similarity measure or pruning criterion.

6. REFERENCES

[1] Jong-Sen Lee, M. R. Grunes, and G. de Grandi, "Polarimetric sar speckle filtering and its implication for classification," *IEEE TGRS*, vol. 37, no. 5, pp. 2363–2373, 1999.

[2] G. Vasile, E. Trouve, Jong-Sen Lee, and V. Buzuloiu, "Intensity-driven adaptive-neighborhood technique for polarimetric and interferometric sar parameters estimation," *IEEE TGRS*, vol. 44, no. 6, pp. 1609–1621, 2006.

[3] Alberto Alonso-Gonzalez, Carlos Lopez-Martinez, and Philippe Salembier, "Filtering and segmentation of polarimetric sar images with binary partition trees," in *Proc. IEEE Int. Geoscience and Remote Sensing Symp. (IGARSS)*, 2010, pp. 4043–4046.

[4] P. Salembier and L. Garrido, "Binary partition tree as an efficient representation for image processing, segmentation, and information retrieval," *IEEE TIP*, vol. 9, no. 4, pp. 561–576, 2000.

[5] Alberto Alonso-Gonzalez, Carlos Lopez-Martinez, and Philippe Salembier, "Polsar speckle filtering and segmentation based on binary partition tree representation," in *Proc. ESA Int. Workshop on Science Applications of SAR Polarimetry and Polarimetric Interferometry. (PolInSAR)*, 2011.

[6] Frederic Barbaresco, "Interactions between symmetric cone and information geometries: Bruhat-tits and siegel spaces models for high resolution autoregressive doppler imagery," in *Emerging Trends in Visual Computing*, Frank Nielsen, Ed., vol. 5416 of *Lecture Notes in Computer Science*, pp. 124–163. Springer Berlin / Heidelberg, 2009.

Appendix D

ESA PolInSAR 2011 conference paper

POLSAR SPECKLE FILTERING AND SEGMENTATION BASED ON BINARY PARTITION TREE REPRESENTATION

Alberto Alonso-González, Carlos López-Martínez, and Philippe Salembier

Universitat Politècnica de Catalunya (UPC), Signal Theory and Communications Dept. (TSC), Jordi Girona 1-3, 08034, Barcelona, Spain. Email: alberto.alonso@tsc.upc.edu

ABSTRACT

A region-based and multi-scale image representation is proposed in this work, the Binary Partition Tree (BPT), for different polarimetric SAR image processing applications. This structure contains a lot of information about the image structure at different detail levels. The BPT construction process and its exploitation for PolSAR data filtering and segmentation is analyzed in this work. Results with real and simulated data are presented to illustrate the capability of the BPT based filtering to maintain spatial resolution and small details of the image while, at the same time, strong filtering is performed over large homogeneous regions.

Key words: SAR, PolSAR, speckle filtering, segmentation, Binary Partition Tree.

1. INTRODUCTION

Synthetic Aperture Radar (SAR) is a technique that coherently combines the echoes received by a moving radar to form a high resolution image. In the las decade, multidimensional SAR data, specially polarimetric SAR data (PolSAR), have demonstrated its importance for characterization and classification of the earth surface. Some geophysical and biophysical information can be extracted by inversion of the polarimetric data.

However, SAR data are contaminated by speckle noise, produced by the coherent processing of received echoes. The speckle term can be reduced by estimation over homogeneous regions. However, SAR data are vastly non-homogeneous, as they reflect the structure of the scene. Some state-of-the-art techniques try to adapt to this non-stationarity, either with predefined directional windows [LGdG99] or defining an adaptive neighborhood for each pixel [VTLB06].

In this work we propose a Binary Partition Tree (BPT) [SG00] representation of the image to extract its spatial information in order to segment the data into homogeneous regions, where the polarimetric information can be estimated precisely. The BPT is a fully region-based and multi-scale PolSAR data representation. Additionally this representation can be exploited for many different PolSAR processing applications. The BPT was introduced for PolSAR data processing in [AGLMS10]. In this paper, we introduce some new similarity criteria, and we do a more extensive evaluation with more complex and realistic synthetic data. Furthermore, we present results of coastline segmentation as a new application based on the BPT.

2. BINARY PARTITION TREE

The Binary Partition Tree (BPT) was introduced in [SG00] as a region-based and multi-scale image representation. It contains information of the image structure at different details levels within a tree. In this hierarchical structure each node represents a connected region of the image. The tree leaves represent single pixels and all the other nodes represent the region composed by merging its two son nodes. Finally, the root node represents the whole image. Thus, the tree edges describe the inclusion relationship between nodes. Between the leafs and the root there are a wide number of nodes representing regions of the image with different detail level. This multi-scale representation contains a lot of useful information about the image structure that can be exploited for different applications.

To construct the BPT representation from an image, an iterative algorithm is employed in a bottom-up approach [SG00]. In the initial state, every pixel of the image becomes a one-pixel region. At every step, the two most similar regions are merged and this process is repeated until the root of the tree, containing the whole image, is generated. In order to apply this algorithm, two important concepts have to be defined [AGLMS10]:

1. A region model: traditionally, under the complex Gaussian PolSAR model, the estimated covariance matrix $\mathbf{Z}$ is employed to measure the region polari-

metric information

$$\mathbf{Z} = \langle \mathbf{k}\mathbf{k}^H \rangle_n = \frac{1}{n}\sum_{i=1}^{n} \mathbf{k}_i \mathbf{k}_i^H \quad (1)$$

where $\mathbf{k}_i$ represents the scattering vector of the i-th pixel and n represents the region size in pixels.

Additionally, since during the BPT construction process regions of different sizes coexist, the region size information should be taken into account and will be included in the region model.

2. A similarity measure on the region model space to compare two neighboring regions $d(X, Y)$. Two types of measures are analyzed in this work, ones based on the statistical distribution (the Wishart distribution) and others based on the covariance matrix subspace geometry. The revised Wishart measure [KLA05] d_w is based on a statistical test assuming Wishart distributions and that one region statistics are known. However, since this measure is not symmetric, a modified symmetric version will be applied

$$d_{sw}(X,Y) = \left(tr(\mathbf{Z}_X^{-1}\mathbf{Z}_Y) + tr(\mathbf{Z}_Y^{-1}\mathbf{Z}_X)\right) \cdot \cdot(n_x + n_y) \quad (2)$$

where $tr(.)$ represent the matrix trace, $\mathbf{Z}_X$ and $\mathbf{Z}_Y$ represent the estimated covariance matrices for regions X and Y, respectively, and n_x and n_y represent their number of pixels.

For comparison purposes a new version of the symmetric revised Wishart dissimilarity will be used, only taking into account the diagonal elements of the $\mathbf{Z}$ matrix and assuming all off-diagonal values equal to zero

$$d_{dw}(X,Y) = \left(\sum_{i=1}^{3}\left(\frac{Z_{X\,ii}^2 + Z_{Y\,ii}^2}{Z_{X\,ii}Z_{Y\,ii}}\right)\right) \cdot (n_x + n_y) \quad (3)$$

where $Z_{X\,ij}$ and $Z_{Y\,ij}$ represent the (i,j)-th element of the estimated covariance matrices $\mathbf{Z}_X$ and $\mathbf{Z}_Y$, respectively.

Another family of dissimilarities is proposed and analyzed on this paper based on the positive definite matrix cone geometry [Bar09]

$$d_{sg}(X,Y) = \|log\left(\mathbf{Z}_X^{-1/2}\mathbf{Z}_Y\mathbf{Z}_X^{-1/2}\right)\|_F + + ln\left(\frac{2n_x n_y}{n_x + n_y}\right) \quad (4)$$

where $\|.\|_F$ represents the Frobenius matrix norm, $log(.)$ represents the matrix logarithm and $ln(.)$ represents the natural logarithm.

As for the Wishart dissimilarities, a new version is defined employing only the information contained in the diagonal elements of the covariance matrix

$$d_{dg}(X,Y) = \sqrt{\sum_{i=1}^{3} ln^2\left(\frac{Z_{X\,ii}}{Z_{Y\,ii}}\right)} + ln\left(\frac{2n_x n_y}{n_x + n_y}\right) \quad (5)$$

3. BPT PRUNING

The BPT is a hierarchical representation of the image structure at different details levels. Thus, it depends only on the image and consequently it is application independent. One possible approach to develop BPT-based applications is to select a set of meaningful regions within the tree. As mentioned in [SG00], an image segmentation can be obtained by tree pruning.

For the filtering application, the main target is to obtain the biggest possible homogeneous regions of the image. The BPT and its multi-scale nature can be exploited for this application. Then, an homogeneity-based tree pruning can be performed. A region homogeneity measure ϕ has to be defined to be able to define a pruning process. In [AGLMS10], is proposed the criterion based on the Frobenius matrix norm

$$\phi_R(X) = \frac{1}{n_x}\sum_{i=1}^{n_x} \frac{\|\mathbf{X}^i - \mathbf{Z}_X\|_F^2}{\|\mathbf{Z}_X\|_F^2} \quad (6)$$

where $\mathbf{X}^i$ is the estimated covariance matrix for the i-th pixel within region X.

Note that this measure depends on all the pixel values within the X region and not only on its model, as the dissimilarity measure. Additionally, ϕ_R is independent of the region size, since it is an average over all the region pixels. This is an important property of the homogeneity measure in order to define the region homogeneity independently of its size. The measure (6) can be seen as the mean information loss when modeling all the pixels within a region with its estimated covariance matrix. Finally, to determine if a region is homogeneous or not, a maximum value δ_p for the homogeneity measure has to be defined, called *pruning threshold*. Then, the bigger regions X_i having $\phi_R(X_i) < \delta_p$ will be selected from the tree. In this paper δ_p will be expressed in dB scale, corresponding to $10 \cdot log_{10}(\phi_R)$.

4. FILTERING RESULTS

The described homogeneity based BPT pruning for filtering has been tested with real and simulated PolSAR data. Fig. 1 shows one real image corresponding to PolSAR data that was acquired in a measurement campaign conducted by the DLR in 1999 with its experimental SAR system, E-SAR, over the Oberpfaffenhofen test-site, southern Germany. Data were collected at L-band, with a spatial resolution of $1.5m \times 1.5m$ in fully polarimetric mode.

On Fig. 2 different pruning results are shown over the same BPT constructed with the d_{sw} dissimilarity (2). Increasing the pruning threshold δ_p results in bigger regions of the tree pruned, as less homogeneous regions are accepted. Note that all of this regions are contained within

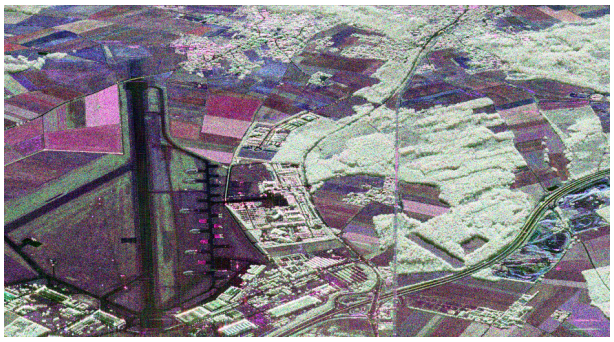

Figure 1: Pauli RGB original E-SAR image

the same tree and thus, they reflect the multi-scale nature of the BPT.

It is worth to notice that in the same image there are regions with very different sizes. Large homogeneous areas, as the agricultural fields in the left part of the image, appear as big regions whereas point scatters or details from the urban area in the center of the image are preserved as small regions. The value for each region is the estimated covariance matrix, as expressed in (1), over all the pixels within the region. This means that very strong filtering can be achieved while, at the same time, spatial resolution and small details of the image are preserved.

A 512x512 pixels cut of the original data, shown in Fig. 3a, is selected to see a more detailed view of the results. The 7x7 multilook is shown in Fig. 3b for comparison purposes. In Figs. 3c-3f different results are shown corresponding to the same tree pruning process over different BPTs constructed with the different similarity measures proposed. Compared with the 7x7 multilook, the BPT based filtering preserves much better original image spatial resolution and small details. Comparing the results obtained with different similarity measures there are very subtle differences. This fact gives an idea of robustness of the technique respect to the similarity measure employed for the BPT construction.

To analyze the capability of the BPT based filtering approach to retain the polarimetric information without distortion, the eigendecomposition parameters of the estimated covariance matrix, Entropy (E), Anisotropy (A) and the averaged alpha angle ($\bar{\alpha}$), are shown in Fig. 4. Different pruning thresholds are compared with the 7x7 multilook over the image cut presented in Fig. 3a. A qualitative analysis of these parameters shows that they obtain the same values. However, the BPT based filtering can take profit of the very large regions over homogeneous areas to enhance the covariance matrix estimation. This effect can be seen specially in the agricultural fields in the left part of the image. In the forest, in the right part of the image, the same effect can be found; increasing the pruning factor to $\delta_p = 0dB$ results in a better estimation of H and A, tending to 1 and 0 respectively, which fits with the theoretical response for random volume scattering. The capability to preserve small details can also be seen in urban areas, in the center of the image, specially

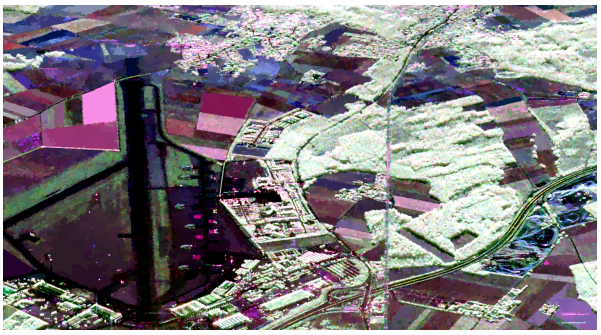

(a) $\delta_p = -2dB$

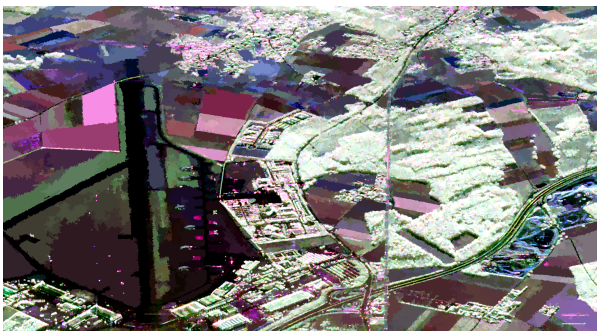

(b) $\delta_p = -1dB$

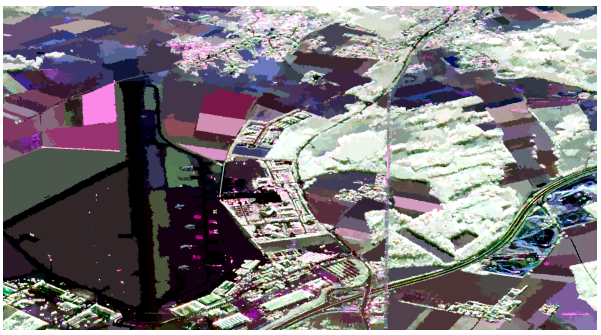

(c) $\delta_p = 0dB$

Figure 2: Pauli RGB processed images

in H and $\bar{\alpha}$ in comparison with the multilook, which has an important spatial resolution loss.

Additionally, a quantitative evaluation of the polarimetric information preservation has been made taking into account some homogeneous regions of the image presented in Fig. 5. Over these regions some parameters corresponding to covariance matrix elements and H/A/$\bar{\alpha}$ decomposition have been estimated. The results for the original image, 7x7 multilook and BPT based filtering are shown in Table 1. The covariance matrix elements calculated for the original image and the filtered image are very similar for both filtering strategies. On some regions, the BPT pruning with $\delta_p = 0dB$ start to diverge from the original values due to inhomogeneous region mixture. The H/A/$\bar{\alpha}$ parameters cannot be calculated over original data since it needs full-rank matrices and some filtering process is needed. The estimation of H and A parameters is biased [LMPC05] and, as stated

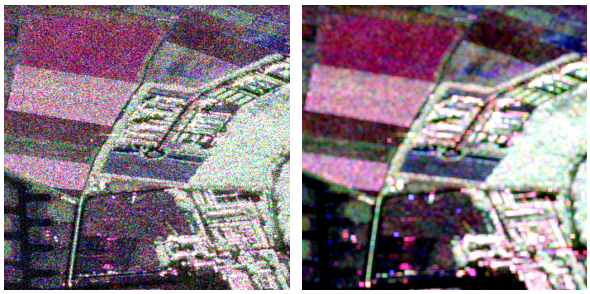

(a) Original (b) 7x7 multilook

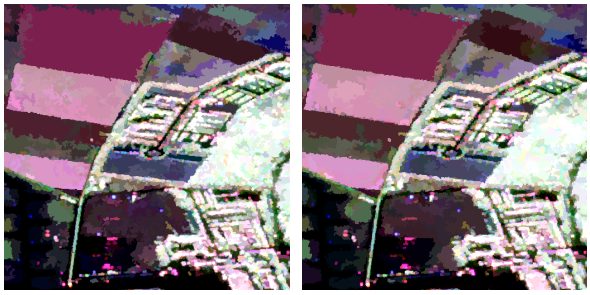

(c) $d_{dw}, \delta_p = -1dB$ (d) $d_{sw}, \delta_p = -1dB$

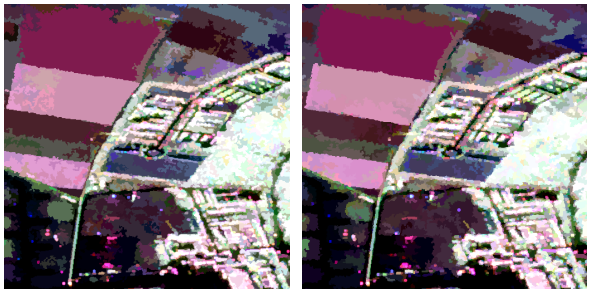

(e) $d_{dg}, \delta_p = -1dB$ (f) $d_{sg}, \delta_p = -1dB$

Figure 3: Detail Pauli RGB original and BPT processed images with $\delta_p = -1dB$ over different trees constructed employing various similarity criteria

before, the BPT based filtering can achieve a better estimation of the H/A/$\bar{\alpha}$ parameters due to the estimation of the covariance matrix over larger number of homogeneous samples. This explains the evolution observed for H and A, with are always underestimated and overestimated, respectively, when increasing δ_p.

To be able to make a quantitative evaluation of the BPT based filtering over the whole image a simulated data has been generated from a segmentation of a real image. A 512x512 pixels cut has been selected, Fig. 6a, containing mainly agricultural fields and some urban area, and it has been filtered using a BPT pruning with d_{sg} similarity measure and $\delta_p = -1dB$, Fig. 6b. This data has been used as a ground truth to generate simulated PolSAR images. A filtered image is employed in order to obtain a ground truth with realistic polarimetric and spatial information. As an example, one realization is shown in Fig. 6c and one BPT filtered image in Fig. 6d with d_{sg} similarity measure and $\delta_p = -5dB$.

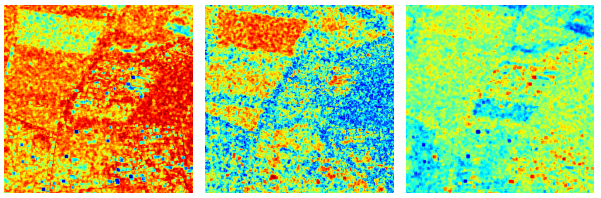

(a) H, 7x7 multilook (b) A, 7x7 multilook (c) $\bar{\alpha}$, 7x7 multilook

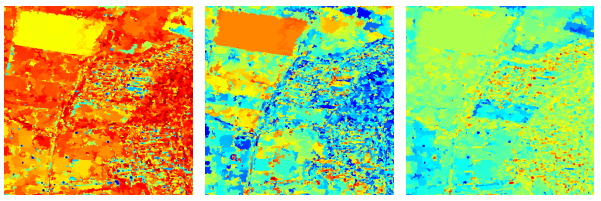

(d) H,$d_{sw}, \delta_p = -2dB$ (e) A,$d_{sw}, \delta_p = -2dB$ (f) $\bar{\alpha}, d_{sw}, \delta_p = -2dB$

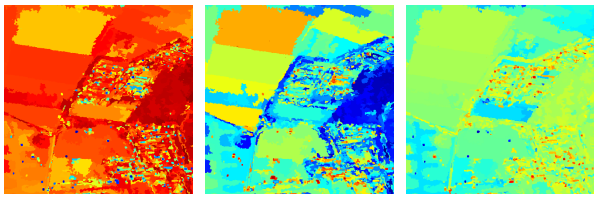

(g) H,$d_{sw}, \delta_p = 0dB$ (h) A,$d_{sw}, \delta_p = 0dB$ (i) $\bar{\alpha}, d_{sw}, \delta_p = 0dB$

Figure 4: H/A/$\bar{\alpha}$ from processed images with multilook and BPT based pruning for different δ_p

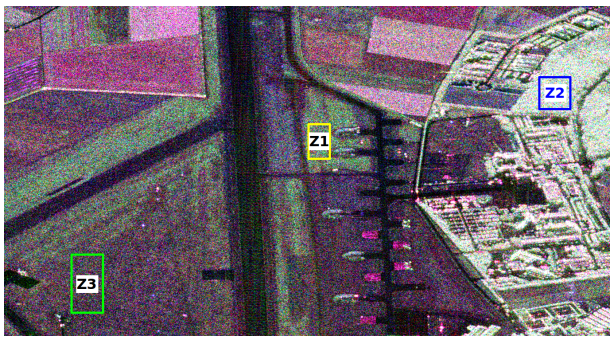

Figure 5: Homogeneous zones selected over the image

Several different realizations are generated and filtered with different techniques. These results are compared with the ground truth, Fig. 6b, to asses numerically the goodness of the filtering technique. As an error measure, $E_R(X, Y)$ is defined between two images X and Y

$$E_R(X,Y) = \frac{1}{n_h \cdot n_w} \sum_{i=1}^{n_h} \sum_{j=1}^{n_w} \frac{\|\mathbf{X}^{ij} - \mathbf{Y}^{ij}\|_F}{\|\mathbf{Y}^{ij}\|_F} \qquad (7)$$

where n_h and n_w are the image height and width in pixels, respectively, $\mathbf{X}^{ij}$ represents the (i, j)th pixel value of image X and $\|\cdot\|_F$ denotes Frobenius matrix norm. Note that the relative error measure defined in (7) is based on the inverse signal to noise ratio (SNR^{-1}) averaged for all the pixels in the image.

Region	Filtering	C_{11}	C_{22}	C_{33}	$\Re(C_{13})$	$\Im(C_{13})$	H	A	$\bar{\alpha}$
Z1 5000 px	Original	28.27	16.06	18.34	5.242	5.504	-	-	-
	ML 7x7	28.21	15.97	18.36	5.321	5.465	0.8012	0.3543	48.29
	BPT -2dB	28.15	16.10	18.17	5.466	5.605	0.8271	0.2873	48.27
	BPT -1dB	28.20	15.20	18.08	5.558	5.612	0.8618	0.2036	47.91
	BPT 0dB	27.76	14.47	16.96	5.813	5.211	0.8694	0.1630	47.74
Z2 5950 px	Original	279.3	159.1	172.8	49.80	-14.37	-	-	-
	ML 7x7	280.8	159.3	172.9	49.18	-15.27	0.8598	0.2907	49.06
	BPT -2dB	278.1	158.4	171.5	48.05	-16.12	0.8475	0.2984	49.50
	BPT -1dB	280.4	157.7	172.4	50.24	-15.42	0.8925	0.2269	49.41
	BPT 0dB	292.2	160.8	177.0	50.74	-13.42	0.9305	0.1307	49.61
Z3 18000 px	Original	10.70	2.782	13.13	2.644	5.599	-	-	-
	ML 7x7	10.70	2.789	13.14	2.662	5.593	0.6781	0.4248	42.62
	BPT -2dB	10.33	2.713	12.94	2.498	5.255	0.7370	0.3755	43.32
	BPT -1dB	10.36	2.799	13.23	2.434	5.136	0.7445	0.3881	43.60
	BPT 0dB	11.76	3.405	13.59	2.556	5.351	0.7852	0.3471	44.34

Table 1: Mean estimated values over homogeneous areas for different filtering strategies

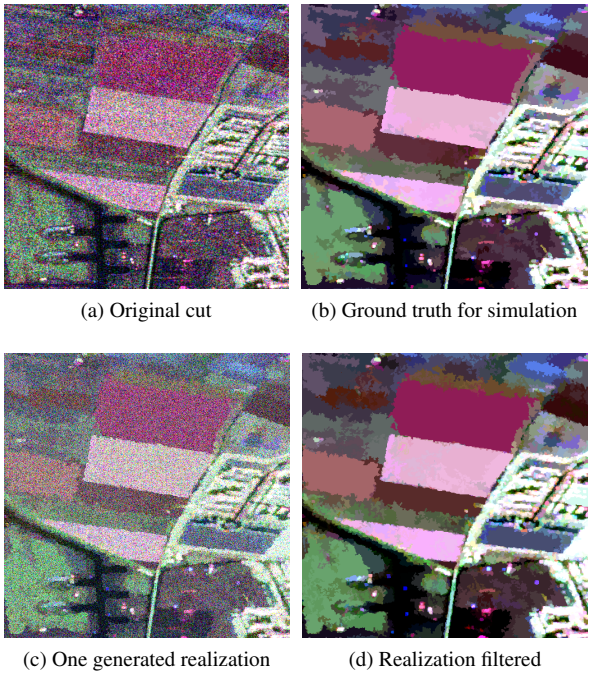

(a) Original cut (b) Ground truth for simulation

(c) One generated realization (d) Realization filtered

Figure 6: Simulated data generation from a real image segmentation

Fig. 7 shows the evolution of the relative error E_R defined in (7) when changing the pruning threshold δ_p for the defined similarity measures in Section 2. Note that the error axis is expressed in logarithmic scale (dB). To make a clearer plots, results over 25 different realization of the ground truth have been averaged. As it can be seen, the behavior when changing the pruning factor is the same for all the BPTs constructed with different criteria. There is always a clear minimum located at about -5dB. According to the relative error E_R criterion, employing the diagonal similarity measures for BPT construction seems to achieve better results than full-matrix ones. However,

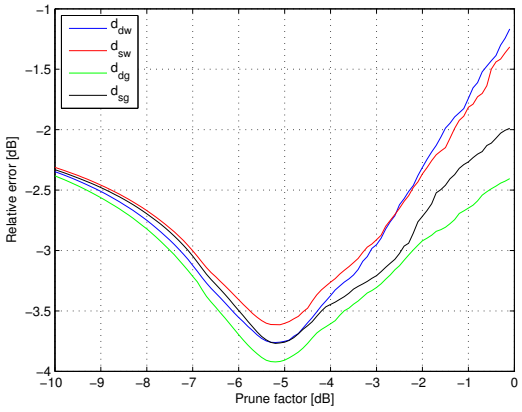

Figure 7: Relative error E_R versus pruning factor δ_p plot over simulated images

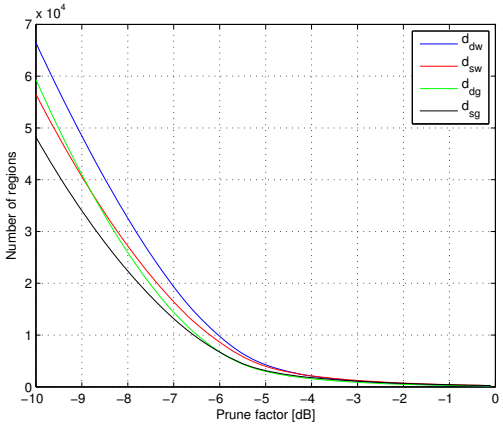

Figure 8: Number of regions versus pruning factor δ_p plot over simulated images

the E_R measure is more sensitive to power, corresponding to the diagonal elements of the covariance matrix,

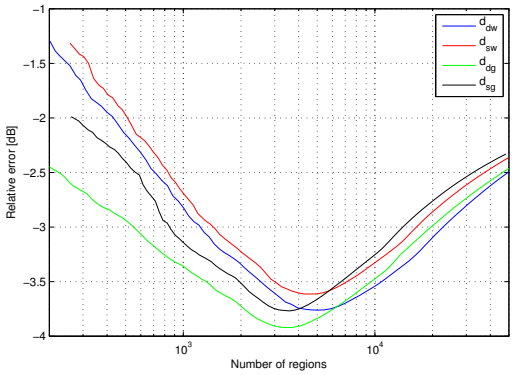

Figure 9: Relative error E_R versus number of regions plot over simulated images

than to the correlation information. In the lack of a clear measure to correctly quantify the polarimetric information loss, an alternative evaluation is made by means of analysis of the number of regions attained by different BPT pruning in Fig. 8. Note that the number of regions pruned is automatically found when fixing the maximum accepted homogeneity per region δ_p. This plot shows that for a specific value of δ_p, the number of regions attained by full-matrix similarity measures is always lower than for the diagonal ones. This means that full-matrix similarity measures produce trees having bigger regions with the same level of homogeneity and, thus, they can achieve better adaptation to the spatial information. Additionally, it reflects that similarity measures based on the positive definite covariance matrix cone geometry leads to better adaptation to this spatial information than the ones based on the Wishart distribution statistical test.

Moreover, Fig. 9 shows the relative error E_R versus the number of regions pruned. Similarity measures based on the positive define matrix cone geometry attain better results in terms of relative error and also they achieve the best results with a lower number of regions than the Wishart based ones. As a reference, the ground truth image, Fig. 6b, has 1939 regions, whereas the minimum error is attained at 3000-4000 regions for d_{dg} and d_{sg} and over 5000 for d_{dw} and d_{sw} measures. This difference reflects the accuracy of the different segmentations obtained by means of BPT pruning and, consequently, the quality attainable for the filtering application.

Analyzing the results with real and simulated data an important point arises. Similar results are obtained by means of BPT based filtering in Fig. 6b and Fig. 6d in real and simulated images. However, the pruning threshold in both cases differs significantly: -1dB and -5dB, respectively. In the view of the authors, this fact can be related to additional region features in the real data not taken into account inside the model, which can be considered as the region texture. The homogeneity threshold has to be increased to absorb these modeling errors with real data. For the simulated data, since this texture is not reproduced, it is not necessary to increase δ_p and the same results are obtained with lower homogeneity thresholds.

5. SEGMENTATION RESULTS

In Section 4 the BPT has been analyzed to develop a filtering application. However, the BPT is an application independent image representation that can be useful for many other applications. As an example, in this section some results will be shown that employ the BPT for a segmentation application, concretely to coastline segmentation. For filtering purposes, the pruned nodes are usually homogeneous regions that are relatively close to the tree leaves. For this application, bigger regions are interesting, strongly non-homogeneous, closer to the tree root.

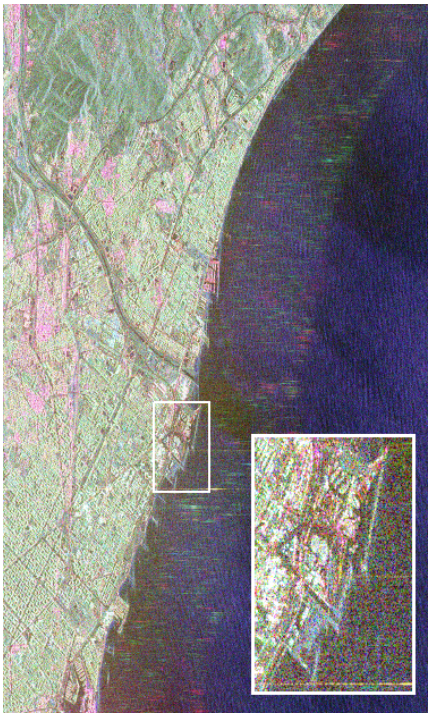

Figure 10: Pauli RGB for the original image of Barcelona

Fig. 10 shows the original image corresponding to 1500×2500-pixel cut of a C-band Pauli RADARSAT-2 image of Barcelona, Spain, that was acquired in November, 18th 2008, in fine quad polarization mode with nominal resolution of $5.2m \times 7.6m$. The figure also shows a detailed area corresponding to the Forum harbor of Barcelona. Fig. 11 shows the resulting coastline segmentation result. Two regions can be clearly seen, corresponding to the land and the sea on the original image. In this case the pruning process is based on selecting the two bigger regions of the tree, corresponding to the two sons of the root node. Fig. 11 represents the entropy H of the two regions. The d_{sw} criteria has been used for BPT construction, defined in (2). As can be seen, specially in the zoom over the Forum harbor, the segmentation preserves the spatial resolution of the original image and small details and thin structures like breakwaters are preserved.

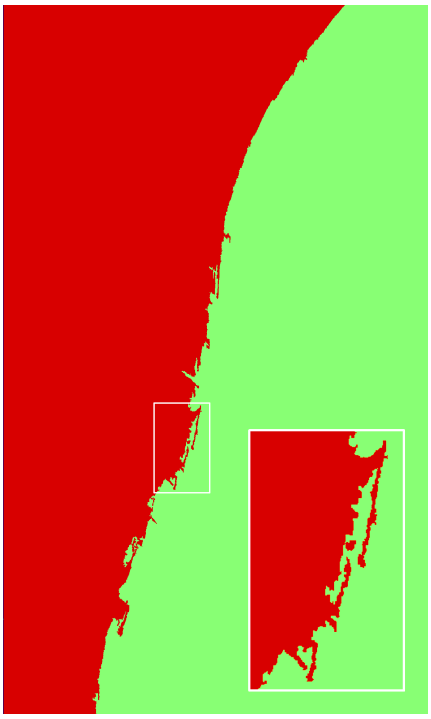

Figure 11: Coastline segmentation, where colors represent the region entropy H

6. CONCLUSIONS

In this work, a region-based and multi-scale image representation has been employed for PolSAR data representation [AGLMS10]. This BPT representation contains information about the image structure and is application independent. It has proved to be able to extract spatial information of the image at different detail levels, ranging from small details close to the tree leaves to big regions close to the root, as the land and the sea on the segmentation example.

An iterative algorithm is employed to construct a BPT from a PolSAR image, based on a region model and a similarity measure. The region model is based on the polarimetric information contained in the covariance matrix and several similarity criteria are presented. Analyzing the results obtained for the filtering application, it seems that the proposed family of measures based on the positive definite matrix cone geometry perform better for BPT construction since a better adaptation to the spatial information is achieved.

In addition, a BPT based processing approach is analyzed, based on an application dependent tree pruning, which produces a segmentation of the image. The speckle filtering application has been studied in detail, by defining a BPT pruning based on the region homogeneity. It has proved to attain good results with real and simulated data, being able to obtain at the same time large regions over homogeneous areas while preserving spatial resolution and small details. Moreover, this filtering technique is able to adapt to the full polarimetric information without introducing any kind of bias or distortion. Additionally, the segmentation application itself has been presented with a coastline segmentation example. On this example a simpler pruning process is employed: select the two bigger regions of the BPT, corresponding to the soon nodes of the tree root. Furthermore, the BPT representation contains a lot of information about the image that can be useful for many other applications.

ACKNOWLEDGMENT

The authors would like to thank to DLR and to MDA for providing the ESAR and the RADARSAT-2 datasets, respectively.

REFERENCES

[AGLMS10] Alberto Alonso-Gonzalez, Carlos Lopez-Martinez, and Philippe Salembier. Filtering and segmentation of polarimetric sar images with binary partition trees. In *Proc. IEEE Int. Geoscience and Remote Sensing Symp. (IGARSS)*, pages 4043–4046, 2010.

[Bar09] Frederic Barbaresco. Interactions between symmetric cone and information geometries: Bruhat-tits and siegel spaces models for high resolution autoregressive doppler imagery. In Frank Nielsen, editor, *Emerging Trends in Visual Computing*, volume 5416 of *Lecture Notes in Computer Science*, pages 124–163. Springer Berlin / Heidelberg, 2009.

[KLA05] P. R. Kersten, Jong-Sen Lee, and T. L. Ainsworth. Unsupervised classification of polarimetric synthetic aperture radar images using fuzzy clustering and em clustering. *IEEE TGRS*, 43(3):519–527, 2005.

[LGdG99] Jong-Sen Lee, M. R. Grunes, and G. de Grandi. Polarimetric sar speckle filtering and its implication for classification. *IEEE TGRS*, 37(5):2363–2373, 1999.

[LMPC05] C. Lopez-Martinez, E. Pottier, and S. R. Cloude. Statistical assessment of eigenvector-based target decomposition theorems in radar polarimetry. 43(9):2058–2074, 2005.

[SG00] P. Salembier and L. Garrido. Binary partition tree as an efficient representation for image processing, segmentation, and information retrieval. *IEEE TIP*, 9(4):561–576, 2000.

[VTLB06] G. Vasile, E. Trouve, Jong-Sen Lee, and V. Buzuloiu. Intensity-driven adaptive-neighborhood technique for polarimetric and interferometric sar parameters estimation. *IEEE TGRS*, 44(6):1609–1621, 2006.

Bibliography

[1] A.B. Carlson, P.B. Crilly, J.C. Rutledge, B. Carlson, and PB Crilly, *Communication systems*, vol. 492, McGraw-Hill New York etc., 1986.

[2] G.L. Turin, "An introduction to digital matched filters," *Proceedings of the IEEE*, vol. 64, no. 7, pp. 1092–1112, 1976.

[3] J.C. Curlander and R.N. McDonough, *Synthetic aperture radar: systems and signal processing*, Wiley New York, 1991.

[4] W.M. Brown, "Synthetic aperture radar," *Aerospace and Electronic Systems, IEEE Transactions on*, , no. 2, pp. 217–229, 1967.

[5] C. Elachi, "Spaceborne radar remote sensing: applications and techniques," *New York, IEEE Press, 1988, 285 p.*, vol. 1, 1988.

[6] M.I. Skolnik, *Introduction to radar systems*, McGraw-Hill (New York), 1980.

[7] A. Cardama, L.J. Roca, J.M. Rius, J. Romeu, and S. Blanch, *Antenas*, Edicions UPC, Edicions de la Universitat Politècnica de Catalunya, 1993.

[8] F.T. Ulaby, R.K. Moore, and A.K. Fung, *Microwave remote sensing: Active and passive. Volume 2 - Radar remote sensing and surface scattering and emission theory*, Reading, MA, Addison-Wesley Publishing Co., 1982.

[9] G. Franceschetti and R. Lanari, *Synthetic aperture radar processing*, CRC, 1999.

[10] F.K. Li and R.M. Goldstein, "Studies of multibaseline spaceborne interferometric synthetic aperture radars," *Geoscience and Remote Sensing, IEEE Transactions on*, vol. 28, no. 1, pp. 88–97, 1990.

[11] P. Beckmann and A. Spizzichino, "The scattering of electromagnetic waves from rough surfaces," *Norwood, MA, Artech House, Inc., 1987, 511 p.*, vol. 1, 1987.

[12] W.H. McCrea and F.J.W. Whipple, "Random paths in two and three dimensions," in *Proc. Roy. Soc. Edinburgh*, 1940, vol. 60, pp. 281–298.

[13] J.L. Doob, L.S. Ornstein, G.E. Uhlenbeck, S.O. Rice, M. Kac, and S. Chandrasekhar, *Selected papers on noise and stochastic processes*, Dover Publications, 1954.

[14] "Analysis and applications related to synthetic aperture radar data," .

[15] J.A. Ogilvy and H.M. Merklinger, "Theory of wave scattering from random rough surfaces," *The Journal of the Acoustical Society of America*, vol. 90, pp. 3382, 1991.

[16] J.W. Goodman, *Statistical optics*, New York, Wiley-Interscience, 1985, 567 p., 1985.

[17] A. Papoulis, S.U. Pillai, and S. Unnikrishna, *Probability, random variables, and stochastic processes*, vol. 196, McGraw-hill New York, 1965.

[18] J.W. Goodman, "Some fundamental properties of speckle," *JOSA*, vol. 66, no. 11, pp. 1145–1150, 1976.

[19] C. Oliver and S. Quegan, *Understanding synthetic aperture radar images*, SciTech Publishing, 2004.

[20] J.S. Lee, "Speckle analysis and smoothing of synthetic aperture radar images," *Computer graphics and image processing*, vol. 17, no. 1, pp. 24–32, 1981.

[21] A. Lopes, R. Touzi, and E. Nezry, "Adaptive speckle filters and scene heterogeneity," *Geoscience and Remote Sensing, IEEE Transactions on*, vol. 28, no. 6, pp. 992–1000, 1990.

[22] W. M. Boerner, "Optimal polarization concept in radar imaging," Tech. Rep., May 1981.

[23] C.A. Balanis, *Advanced engineering electromagnetics*, Wiley New York, 1989.

[24] F.D. Ortín, D.A. García, and J.R. Martos, *Campos electromagnéticos*, vol. 70, Edicions UPC, 1998.

[25] F.T. Ulaby and C. Elachi, *Radar polarimetry for geoscience applications*, Artech House on Demand, 1990.

[26] L. Tsang, J.A. Kong, and R.T. Shin, *Theory of microwave remote sensing*, Wiley-Interscience, 1985.

[27] J.S. Lee, K.W. Hoppel, S.A. Mango, and A.R. Miller, "Intensity and phase statistics of multilook polarimetric and interferometric sar imagery," *Geoscience and Remote Sensing, IEEE Transactions on*, vol. 32, no. 5, pp. 1017–1028, 1994.

[28] RJA Tough, D. Blacknell, and S. Quegan, "A statistical description of polarimetric and interferometric synthetic aperture radar data," *Proceedings of the Royal Society of London. Series A: Mathematical and Physical Sciences*, vol. 449, no. 1937, pp. 567, 1995.

[29] I.R. Joughin, D.P. Winebrenner, and D.B. Percival, "Probability density functions for multilook polarimetric signatures," *Geoscience and Remote Sensing, IEEE Transactions on*, vol. 32, no. 3, pp. 562–574, 1994.

[30] A. Nuttall, "High-order covariance functions for complex gaussian processes (corresp.)," *Information Theory, IRE Transactions on*, vol. 8, no. 3, pp. 255–256, 1962.

[31] I. Reed, "On a moment theorem for complex gaussian processes," *Information Theory, IRE Transactions on*, vol. 8, no. 3, pp. 194–195, 1962.

[32] S.R. Cloude and E. Pottier, "A review of target decomposition theorems in radar polarimetry," *Geoscience and Remote Sensing, IEEE Transactions on*, vol. 34, no. 2, pp. 498–518, 1996.

[33] NR Goodman, "Statistical analysis based on a certain multivariate complex gaussian distribution (an introduction)," *The Annals of Mathematical Statistics*, vol. 34, no. 1, pp. 152–177, 1963.

[34] R. Touzi, A. Lopes, J. Bruniquel, and P.W. Vachon, "Coherence estimation for sar imagery," *Geoscience and Remote Sensing, IEEE Transactions on*, vol. 37, no. 1, pp. 135–149, 1999.

[35] C. Lopez-Martinez, *Multidimensional Speckle Noise, Modelling and Filtering Related to SAR Data*, Ph.D. thesis, Technical University of Catalonia (UPC), Barcelona, June 2003.

[36] J.S. Lee, K.P. Papathanassiou, T.L. Ainsworth, M.R. Grunes, and A. Reigber, "A new technique for noise filtering of sar interferometric phase images," *Geoscience and Remote Sensing, IEEE Transactions on*, vol. 36, no. 5, pp. 1456–1465, 1998.

[37] J.R. Huynen, "Measurement of the target scattering matrix," *Proceedings of the IEEE*, vol. 53, no. 8, pp. 936–946, 1965.

[38] E. Krogager, "New decomposition of the radar target scattering matrix," *Electronics Letters*, vol. 26, no. 18, pp. 1525–1527, 1990.

[39] W.L. Cameron and L.K. Leung, "Feature motivated polarization scattering matrix decomposition," in *Radar Conference, 1990., Record of the IEEE 1990 International*. IEEE, 1990, pp. 549–557.

[40] A. Freeman and S.L. Durden, "A three-component scattering model for polarimetric sar data," *Geoscience and Remote Sensing, IEEE Transactions on*, vol. 36, no. 3, pp. 963–973, 1998.

[41] R. Touzi, "Target scattering decomposition of one-look and multi-look sar data using a new coherent scattering model: The tsvm," in *Geoscience and Remote Sensing Symposium, 2004. IGARSS'04. Proceedings. 2004 IEEE International*. IEEE, 2004, vol. 4, pp. 2491–2494.

[42] S.R. Cloude and E. Pottier, "An entropy based classification scheme for land applications of polarimetric sar," *Geoscience and Remote Sensing, IEEE Transactions on*, vol. 35, no. 1, pp. 68–78, 1997.

[43] Jong-Sen Lee, M. R. Grunes, and G. de Grandi, "Polarimetric sar speckle filtering and its implication for classification," *IEEE Transactions on Geoscience and Remote Sensing*, vol. 37, no. 5, pp. 2363–2373, 1999.

[44] G. Vasile, E. Trouve, Jong-Sen Lee, and V. Buzuloiu, "Intensity-driven adaptive-neighborhood technique for polarimetric and interferometric sar parameters estimation," *IEEE Transactions on Geoscience and Remote Sensing*, vol. 44, no. 6, pp. 1609–1621, 2006.

[45] R. Gordon and R.M. Rangayyan, "Feature enhancement of film mammograms using fixed and adaptive neighborhoods," *Applied Optics*, vol. 23, no. 4, pp. 560–564, 1984.

[46] D. Gonzalez-Asensio, "Análisis de técnicas basadas en el crecimiento de regiones aplicadas a datos sar multidimensionales," M.S. thesis, Technical University of Catalonia (UPC), Barcelona, 2008.

[47] J.S. Lee, "Digital image smoothing and the sigma filter," *Computer Vision, Graphics, and Image Processing*, vol. 24, no. 2, pp. 255–269, 1983.

[48] P. Salembier and L. Garrido, "Binary partition tree as an efficient representation for image processing, segmentation, and information retrieval," *IEEE Transactions on Image Processing*, vol. 9, no. 4, pp. 561–576, 2000.

[49] F. Harary, *Graph Theory*, Addison-Wesley, Reading, MA, 1969.

[50] S.N. Anfinsen, R. Jenssen, and T. Eltoft, "Spectral clustering of polarimetric sar data with wishart-derived distance measures," in *PolInSAR 2007*.

[51] C.H. Papadimitriou, *Computational complexity*, John Wiley and Sons Ltd., 2003.

[52] A. Alonso-Gonzalez, C. Lopez-Martinez, and P. Salembier, "Filtering and segmentation of polarimetric sar images with binary partition trees," in *Proc. IEEE Int. Geoscience and Remote Sensing Symp. (IGARSS)*, 2010, pp. 4043–4046.

[53] A. Alonso-Gonzalez, C. Lopez-Martinez, and P. Salembier, "Polsar speckle filtering and segmentation based on binary partition tree representation," in *Proc. ESA Int. Workshop on Science Applications of SAR Polarimetry and Polarimetric Interferometry. (PolInSAR)*, 2011.

[54] J.S. Lee and E. Pottier, *Polarimetric radar imaging: from basics to applications*, CRC Press, 2009.

[55] S. Cloude, *Polarisation: applications in remote sensing*, Oxford University Press, USA, 2009.

[56] P. R. Kersten, Jong-Sen Lee, and T. L. Ainsworth, "Unsupervised classification of polarimetric synthetic aperture radar images using fuzzy clustering and em clustering," *IEEE Transactions on Geoscience and Remote Sensing*, vol. 43, no. 3, pp. 519–527, 2005.

[57] F. Barbaresco, "Interactions between symmetric cone and information geometries: Bruhat-tits and siegel spaces models for high resolution autoregressive doppler imagery," in *Emerging Trends in Visual Computing*, Frank Nielsen, Ed., vol. 5416 of *Lecture Notes in Computer Science*, pp. 124–163. Springer Berlin / Heidelberg, 2009.

[58] J.H. Ward, "Hierarchical grouping to optimize an objective function," *Journal of the American statistical association*, vol. 58, no. 301, pp. 236–244, 1963.

[59] "Polsarpro v. 4.0.3," http://earth.esa.int/polsarpro.

[60] G. Vasile, J.-P. Ovarlez, F. Pascal, and C. Tison, "Coherency matrix estimation of heterogeneous clutter in high-resolution polarimetric sar images," *IEEE Transactions on Geoscience and Remote Sensing*, vol. 48, no. 4, pp. 1809–1826, 2010.

[61] G. Vasile, J.-P. Ovarlez, F. Pascal, C. Tison, L. Bombrun, M. Gay, and E. Trouve, "Normalized coherency matrix estimation under the sirv model. alpine glacier polsar

data analysis," in *Proc. IEEE Int. Geoscience and Remote Sensing Symp. IGARSS 2008*, 2008, vol. 1.

[62] C. Lopez-Martinez, E. Pottier, and S. R. Cloude, "Statistical assessment of eigenvector-based target decomposition theorems in radar polarimetry," *IEEE Transactions on Geoscience and Remote Sensing*, vol. 43, no. 9, pp. 2058–2074, 2005.

[63] L. M. Novak and M. C. Burl, "Optimal speckle reduction in polarimetric sar imagery," *IEEE Transactions on Aerospace and Electronic Systems*, vol. 26, no. 2, pp. 293–305, 1990.

[64] R.J. Muirhead and Inc ebrary, *Aspects of multivariate statistical theory*, Wiley Online Library, 1982.